VOL. 687 NO. 2 23 DECEMBER 1994
THIS ISSUE COMPLETES VOL. 687

JOURNAL OF CHROMATOGRAPHY A

INCLUDING ELECTROPHORESIS AND OTHER SEPARATION METHODS

ELSEVIER

JOURNAL OF CHROMATOGRAPHY A

INCLUDING ELECTROPHORESIS AND OTHER SEPARATION METHODS

Scope. The *Journal of Chromatography A* publishes papers on all aspects of **chromatography, electrophoresis** and related methods. Contributions consist mainly of research papers dealing with chromatographic theory, instrumental developments and their applications. In the *Symposium volumes*, which are under separate editorship, proceedings of symposia on chromatography, electrophoresis and related methods are published. *Journal of Chromatography B: Biomedical Applications* —This journal, which is under separate editorship, deals with the following aspects: developments in and applications of chromatographic and electrophoretic techniques related to clinical diagnosis or alterations during medical treatment; screening and profiling of body fluids or tissues related to the analysis of active substances and to metabolic disorders; drug level monitoring and pharmacokinetic studies; clinical toxicology; forensic medicine; veterinary medicine; occupational medicine; results from basic medical research with direct consequences in clinical practice.

Submission of Papers. The preferred medium of submission is on disk with accompanying manuscript (see *Electronic manuscripts* in the Instructions to Authors, which can be obtained from the publisher, Elsevier Science B.V., P.O. Box 330, 1000 AH Amsterdam, Netherlands). Manuscripts (in English; *four* copies are required) should be submitted to: Editorial Office of *Journal of Chromatography A*, P.O. Box 681, 1000 AR Amsterdam, Netherlands, Telefax (+31-20) 485 2304, or to: The Editor of *Journal of Chromatography B: Biomedical Applications*, P.O. Box 681, 1000 AR Amsterdam, Netherlands. Review articles are invited or proposed in writing to the Editors who welcome suggestions for subjects. An outline of the proposed review should first be forwarded to the Editors for preliminary discussion prior to preparation. Submission of an article is understood to imply that the article is original and unpublished and is not being considered for publication elsewhere. For copyright regulations, see below.

Publication information. *Journal of Chromatography A* (ISSN 0021-9673): for 1995 Vols. 683–714 are scheduled for publication. *Journal of Chromatography B: Biomedical Applications* (ISSN 0378-4347): for 1995 Vols. 663–674 are scheduled for publication. Subscription prices for *Journal of Chromatography A*, *Journal of Chromatography B: Biomedical Applications* or a combined subscription are available upon request from the publisher. Subscriptions are accepted on a prepaid basis only and are entered on a calendar year basis. Issues are sent by surface mail except to the following countries where air delivery via SAL is ensured: Argentina, Australia, Brazil, Canada, China, Hong Kong, India, Israel, Japan, Malaysia, Mexico, New Zealand, Pakistan, Singapore, South Africa, South Korea, Taiwan, Thailand, USA. For all other countries airmail rates are available upon request. Claims for missing issues must be made within six months of our publication (mailing) date. Please address all your requests regarding orders and subscription queries to: Elsevier Science B.V., Journal Department, P.O. Box 211, 1000 AE Amsterdam, Netherlands. Tel.: (+31-20) 485 3642; Fax: (+31-20) 485 3598. Customers in the USA and Canada wishing information on this and other Elsevier journals, please contact Journal Information Center, Elsevier Science Inc., 655 Avenue of the Americas, New York, NY 10010, USA, Tel. (+1-212) 633 3750, Telefax (+1-212) 633 3764.

Abstracts/Contents Lists published in Analytical Abstracts, Biochemical Abstracts, Biological Abstracts, Chemical Abstracts, Chemical Titles, Chromatography Abstracts, Current Awareness in Biological Sciences (CABS), Current Contents/Life Sciences, Current Contents/Physical, Chemical & Earth Sciences, Deep-Sea Research/Part B: Oceanographic Literature Review, Excerpta Medica, Index Medicus, Mass Spectrometry Bulletin, PASCAL-CNRS, Referativnyi Zhurnal, Research Alert and Science Citation Index.

US Mailing Notice. *Journal of Chromatography A* (ISSN 0021-9673) is published weekly (total 52 issues) by Elsevier Science B.V., (Sara Burgerhartstraat 25, P.O. Box 211, 1000 AE Amsterdam, Netherlands). Annual subscription price in the USA US$ 5389.00 (US$ price valid in North, Central and South America only) including air speed delivery. Second class postage paid at Jamaica, NY 11431. **USA POSTMASTERS**: Send address changes to *Journal of Chromatography A*, Publications Expediting, Inc., 200 Meacham Avenue, Elmont, NY 11003. Airfreight and mailing in the USA by Publications Expediting.

See inside back cover for Publication Schedule, Information for Authors and information on Advertisements.

0021-9673/94 $07.00

Printed in the Netherlands

VOL. 687, NO. 2 JOURNAL OF CHROMATOGRAPHY A 23 DECEMBER 1994

CONTENTS

(Abstracts/Contents Lists published in Analytical Abstracts, Biochemical Abstracts, Biological Abstracts, Chemical Abstracts, Chemical Titles, Chromatography Abstracts, Current Awareness in Biological Sciences (CABS), Current Contents/Life Sciences, Current Contents/Physical, Chemical & Earth Sciences, Deep-Sea Research/Part B: Oceanographic Literature Review, Excerpta Medica, Index Medicus, Mass Spectrometry Bulletin, PASCAL-CNRS, Referativnyi Zhurnal, Research Alert and Science Citation Index)

REGULAR PAPERS

Column Liquid Chromatography

Field-Flow Fractionation

Gas Chromatography

(Continued overleaf)

Contents (continued)

ELSEVIER

Journal of Chromatography A, 687 (1994) 179–200

JOURNAL OF CHROMATOGRAPHY A

Properties of some C_{18} stationary phases for preparative liquid chromatography I[☆]. Equilibrium isotherms

Hong Guan[a,b], Georges Guiochon[a,b,*]

[a]*Department of Chemistry, University of Tennessee, Knoxville, TN 37996-1600, USA*

[b]*Division of Chemical and Analytical Sciences, Oak Ridge National Laboratory, Oak Ridge, TN 37831-6120, USA*

First received 17 May 1994; revised manuscript received 10 August 1994

Abstract

Isotherm data were measured by frontal analysis and elution by characteristic points for 2,6-dimethylphenol, 3-phenyl-1-propanol and methyl benzoate on six columns packed with two commercial octadecyl silicas, using methanol–water solutions as the mobile phase. The retention factors and isotherm coefficients depend on the packing density. This density varies markedly from column to column, at least with some phases for which it is also a function of the column length. The determination of the thermodynamic data required for the modelling of chromatography must be done with an accuracy which seems to exceed what the current level of column to column reproducibility of these data permits at present, even when care is taken to control the experimental parameters, make precise measurements and report the data to the mass of silica.

1. Introduction

Reversed-phase liquid chromatography is by far the domineering technique in analytical chromatography [1]. Octadecyl-bonded silica adsorbents (ODS), used as the non-polar stationary phase of choice in this method, have been extensively studied for the last twenty years [2–16]. ODS adsorbents are also widely used in preparative chromatography, unless the feed components are too poorly soluble in the strongly polar solvents which must be used as the mobile phase to ensure significant retention. In spite of a most abundant literature discussing the use of these phases, their analytical applications and their chromatographic properties, some important questions remain unanswered, especially regarding their behavior under overloading conditions and the reproducibility of their performance in preparative chromatography.

Much fundamental work has been done on the comparison of the properties of columns packed with ODS and with other packing materials [6–8], of columns packed with ODS prepared with different reagents [9], and of columns packed with ODS produced by different manufacturers [10–12]. However, almost all these studies were undertaken using methods of linear chromatography, with the single aim to facilitate its ana-

* Corresponding author. Address for correspondence: Department of Chemistry, University of Tennessee, TN 37996-1600, USA.

☆ For Part II, see Ref. [33].

0021-9673/94/$07.00
SSDI 0021-9673(94)00773-X

lytical applications. Accordingly, they are mainly focused on the retention characteristics of the columns being compared, on the dependence of the retention factor on various experimental parameters, and on the column efficiency. While this last parameter depends mostly on the packing method used and on the skill of the operator and, with proper care, can be improved to a certain extent, the other two have been found to depend essentially on the origin of the material used, to be most difficult to adjust, and uneasy to reproduce. Considerable attention has been paid to the column-to-column, batch-to-batch, and manufacturer-to-manufacturer reproducibilities of analytical performance [17–19]. The first has generally been found to be excellent, the second acceptable, the third poor, as if the ODS materials produced using different processes were almost entirely different products.

Except for a recent report discussing the performance of overloaded chromatographic columns [13], little attention has been paid to the column characteristics which are important in preparative chromatography. These are the kinetics of mass transfer and of adsorption–desorption in the column and the equilibrium isotherms of the components of interest between the stationary and the mobile phases. The column efficiency is a measure of the rate of the mass-transfer kinetics in the column but it must be used with caution. The initial slope of the isotherm is proportional to the retention factor, so many of the conclusions of analytical studies are applicable to this isotherm parameter. The nature of the isotherm, its initial curvature, and its saturation capacity are other parameters of importance for preparative chromatography. There is at present little comparative information on these parameters.

The goal of this work is an investigation of the feasibility of a comparison of the performance of stationary phases for preparative liquid chromatography. A number of issues must be clarified, such as (i) which compounds should be chosen for comparative studies; (ii) what is the reproducibility of column parameters when several similar columns are prepared at the same time; (iii) how close are the parameters of columns of different lengths, packed at the same time; (iv) are classical mass-transfer kinetics data, such as plots of the reduced column efficiency versus the reduced velocity, relevant in preparative chromatography and how could they be used. The amount of data required for a thorough comparison could be considerable. The scope of the work has to be limited to the essential if the approach is to be useful for the selection of the best stationary phase for practical applications. For example, it has been shown theoretically [14,15] that, in analytical chromatography, the use of 2-μm particles would be optimal for the separation of complex mixtures. It has also been proven that the practical difficulties experienced when trying to prepare and operate columns packed with such small particles are serious [16]. Preparative chromatography is best carried out with particles between 10 and 40 μm in diameter [20]. We have limited the present study to 10-μm particles.

In this paper, we discuss only the data of thermodynamics nature. Emphasis is placed on the column-to-column reproducibility of the data obtained with a given material. In order to be able to measure thermodynamic data on analytical columns and use these data to predict accurately band profiles on large-size preparative columns, relative differences between the values of the numerical coefficients of the isotherm not exceeding a few percents are desirable. Otherwise, a proper correction would be needed.

2. Theory

Adsorption isotherms were measured by frontal analysis (FA) and by the elution by characteristic point (ECP) method. The ECP method is based on the ideal model of chromatography [20], which assumes that the column efficiency is infinite. In this case, each concentration has a retention time which is simply related to the slope of the isotherm. A large sample is injected in the column. The peak recorded has a sharp

shock layer, usually at the front, and a diffuse boundary [20]. The equation which relates the profile of the diffuse boundary, $V(C)$, the amount of the compound adsorbed on the stationary phase at equilibrium, q, and the mobile phase concentration, C, can be written as follows

$$q = \frac{1}{V_a} \cdot \sum_{0}^{C} (V - V_0)\delta_i C \quad (1)$$

where V_a is the volume of adsorbent in the column, V_0 is the column hold-up volume, V is the retention volume of the characteristic point of the diffuse profile at concentration C, and $\delta_i C$ is the concentration increment (with $\sum \delta_i C = C$). Since all actual columns have a finite efficiency, the ECP method introduces a model error, as shown by Huber and Gerritse [21,22]. In a previous publication [23], we have made a numerical study of this error and shown that an efficiency of approximately 5000 theoretical plates is required to reduce below 1% the systematic error made on the determination of the isotherm coefficients.

When the column efficiency is not as high as required by ECP for accurate determinations, FA [20–22,24–27] is used. This method requires the measurement of the retention times of successive abrupt step changes of increasing (for peaks with self-sharpening fronts) or decreasing (for peaks with self-sharpening rear boundaries) sample concentration. The isotherm is derived by using the following equation for each concentration step:

$$q_{i+1} = q_i + \frac{(C_{i+1} - C_i)(V_{F,i+1} - V_0)}{V_a} \quad (2)$$

where q_i and q_{i+1} are the amounts of compound adsorbed by the column packing at equilibrium, after the end of the ith and $i + 1$th breakthrough curves and $V_{F,i+1}$ is the retention volume of the breakthrough curve obtained when the concentration is raised from C_i to C_{i+1}.

The FA method has serious advantages over ECP. The retention volumes measured are independent of the column efficiency, no detector calibration is needed since the solutions used have known concentrations, and measurements can easily be carried out at mobile phase concentrations which are much higher than in ECP. The main drawbacks of the FA method are that it requires considerable amount of time and sample and it gives only a small number of data points. Although frontal analysis by characteristic point (FACP) [20,28,29], which uses the diffuse boundary of a negative step in the frontal analysis mode, permits the determination of isotherm data points at high concentrations, the need of calibrating the detector and the model error associated with the ECP method subsist while the requirement for a large amount of sample common to all FA methods remains. We have used both the FA and the ECP methods in the present work.

Statistical thermodynamics suggests the following general equation for liquid–solid isotherms [20]

$$q = q_S \cdot \frac{C(b_1 + 2b_2C + \cdots + nb_nC^{n-1})}{1 + b_1C + b_2C^2 + \cdots + b_nC^n} \quad (3)$$

where q_S is the saturation capacity of the adsorbent and the coefficients b_i are numerical coefficients related to the adsorbate–adsorbent and the adsorbate–adsorbate interaction energies. Eq. 3 must be used with few coefficients only. Otherwise, it is too flexible. The popular Langmuir isotherm is obtained for $n = 1$

$$q = \frac{q_S b_1 C}{1 + b_1 C} \quad (4)$$

The quadratic isotherm is obtained for $n = 2$

$$q = q_s \cdot \frac{C(b_1 + 2b_2C)}{1 + b_1C + b_2C^2} \quad (5)$$

It is the simplest isotherm with an inflection point. It has been used previously with success to account for the isotherm data of components which exhibit anti-Langmuir behavior [30].

The coefficients of the isotherm were obtained

by least-square fit of the data to minimize the square of the relative difference between the experimental data points and the corresponding points of the fitted isotherm [20,31,32].

3. Experimental

3.1. Equipment

The ECP determinations were performed using a Perkin-Elmer (Norwalk, CT, USA) Model 400 liquid chromatograph solvent-delivery system, a VICI (Valco, Houston, TX, USA) 6-port motor-driven sample injection valve with 0.25-, 0.50- and 1-ml sample loops, and a Spectra-Flow 757 UV absorbance detector (Kratos, Ramsey, NJ, USA). Data were acquired simultaneously with a Spectra-Physics (San Jose, CA, USA) SP 4270 integrator, for the real-time display of the chromatograms during the experiment, and an Autolab software (Spectra-Physics part No. A0099-207 10/86 A), for storing data files in an IBM personal computer for further analysis or for downloading to one of the VAX computers at the University of Tennessee Computer Center.

The frontal analysis measurements were performed using a Hewlett-Packard (Palo Alto, CA, USA) HP1090 liquid chromatograph, equipped with a multisolvent delivery system, a diode-array UV detector, and a computer data acquisition system.

3.2. Columns

Two samples of spherical ODS, both 10 μm average particle size, were obtained from YMC (Wilmington, NC, USA) with catalog No. BS-1010 S-10 120A ODS and lot No. EC03817, and Vydac (Hesperia, CA, USA) with catalog No. 201HSB10 and lot No. 910611-12-1, respectively. Six stainless columns (Alltech, Deerfield, IL, USA), all 0.46 cm I.D., were packed in our laboratory, using the slurry technique and a maximum pressure of 6000 p.s.i. (1 p.s.i. = 6894.76 Pa). Two 10 cm long and two 25 cm long columns were packed with the Vydac ODS material, one 10 cm long and one 25 cm long columns were packed with the YMC ODS material.

3.3. Chemicals

2,6-Dimethylphenol, 99% pure, solid, formula weight (FW) 122.17 [CAS Ref. No. 576-26-1], catalog No. D17,500-5 and methyl benzoate, 99%, liquid, FW 136.15 [93-58-3], catalog No. M2,990-8 were obtained from Aldrich (Milwaukee, WI, USA). 3-Phenyl-1-propanol, >98% (GC), liquid, FW 136.20, catalog No. 79 000 was obtained from Fluka (Buchs, Switzerland).

The mobile phase was a mixture of 40% methanol (Baker Analyzed HPLC reagent, catalog No. 9093-33; J.T. Baker, Phillipsburg, NJ, USA) and 60% water. Deionized water was freshly made in the laboratory using a Barnstead/Thermolyne (Dubuque, IA, USA) water-deionizing system consisting in two cartridges, one HN high-capacity DI cartridge (catalog No. D8901) and one HG organic-removal cartridge (catalog No. D8904).

3.4. Procedures

Sample preparation

For each compound, the most concentrated solution possible to prepare, based on its solubility in a methanol–water (40:60) mixture, was made first. Weighed amounts of the compounds studied were introduced into volumetric flasks with known volumes of mobile phase (methanol–water, 40:60) and thoroughly shaken in a sonic water bath, until all the solute dissolves or for 30 min. Failure for the solute to dissolve resulted in the addition of a small volume of fresh solvent and the procedure was repeated. This allowed the preparation of nearly saturated solutions. More dilute solutions were prepared by introducing weighted amounts of the solutes into known volumes of mobile phase. There was no secondary dilution of standard solutions to avoid errors due to sample loss during transfers. Solutions in the following concentration ranges were prepared: 2,6-dimethylphenol from 18.50 to

Table 1
Characteristics of the columns studied

	YMC		Vydac			
	YS (10 cm long)	YL (25 cm long)	VS1 (10 cm long)	VS2 (10 cm long)	VL1 (25 cm long)	VL2 (25 cm long)
ϵ_1	0.680	0.671	0.692	0.722	0.682	0.674
ϵ_2	0.754	0.753	0.755	0.749	0.686	0.724
ϵ_3	0.694	0.671	0.729	0.744	0.669	0.646
W_{Si}/V_c	0.64	0.67	0.61	0.58	0.71	0.70

ϵ_1 = Total porosity from uracil retention time; ϵ_2 = total porosity from the mass of dry silica (silica density = 2.21 g/ml) in the column; ϵ_3 = total porosity from the mass of methanol in the column; W_{Si}/V_c (g/ml) = ratio of the mass of stationary phase in the column and the column volume, as results from the average porosity.

4.609 mg/ml; 3-phenyl-1-propanol from 25.336 to 5.606 mg/ml; methyl benzoate from 11.76 to 2.52 mg/ml.

Detector calibration

The output of the detector is an electrical voltage. It is converted into the concentration (mg/ml) of the corresponding solute using a detector calibration curve obtained by flushing the detector cell with each solution prepared until a stable signal is obtained. For each of the three compounds studied, a third-order polyno-

Table 2
Column hold-up times (t_0), efficiency (N_0) and sample capacity factor (k') at infinite sample dilution

Compound	Parameter	Columns					
		YS	YL	VS1	VS2	VL1	VL2
	t_0 (min)	1.26	2.94	1.26	1.31	2.93	2.95
PP	k'	9.74	9.85	6.52	6.27	7.11	7.25
	Reproducibility[a]	0.01		0.06			
	$k'/(W_{Si}L)$			10.47			
	Reproducibility		−0.04				0.03
	N_0	1860	3050	1250	1640	3160	4070
DMP	k'	11.2	12.1	7.13	6.99	7.91	8.08
	Reproducibility[a]		0.07				0.06
	$k'/(W_{Si}L)$						11.61
	Reproducibility		0.03				0.03
	N_0	1890	3000	1290	1650	3210	3630
MB	k'	13.2	14.1	8.79	8.60	9.81	10.3
	Reproducibility[a]		0.06				0.07
	$k'/(W_{Si}L)$			14.43			
	Reproducibility		0.02				0.03
	N_0	1680	3130	1240	1360	3320	3220

For columns, see Table 1. PP = 3-Phenyl-1-propanol; DMP = 2,6-dimethylphenol; MB = methyl benzoate; L = column length.
[a] Reproducibility for YMC columns: $(k'_{YL} - k'_{YS})/k'_{YL}$; for Vydac columns: σ of the four results.

mial gave a close fit to the experimental data. The best coefficients of the fit were obtained by applying the polynomial regression in SigmaPlot (Jandel, San Rafael, CA, USA) to the experimental data points. The calibration data were used to convert the recorded chromatograms into the plots of concentration versus time shown below.

Column parameters

The column porosity was derived by three different methods, using the column holdup volume, the amount of silica contained in the column and the amount of methanol. The column hold-up time (t_0) was derived from the retention time of uracil. A solution of 0.15 mg uracil in 1.0 ml mobile phase was used for these measurements. Samples of 0.010 and 0.020 ml were injected into the 10 and 25 cm long columns, respectively. After completion of all the experiments reported here and in the companion paper [33], the columns were dried under a stream of nitrogen for 15 h, then filled with pure methanol and weighed again, giving the amount of methanol filling the pores. Finally, the columns were dried again, weighed and emptied. The mass of silica contained in the column permits the calculation of the porosity from the density of silica (2.21 g/ml). These results are summarized in Table 1.

The retention factor of each compound (k') and its limit efficiency for a zero-size sample (N_0) were measured by injecting the same volumes of the least concentrated solution used, at a flow-rate of 1.0 ml/min. The efficiency was derived from the conventional equation

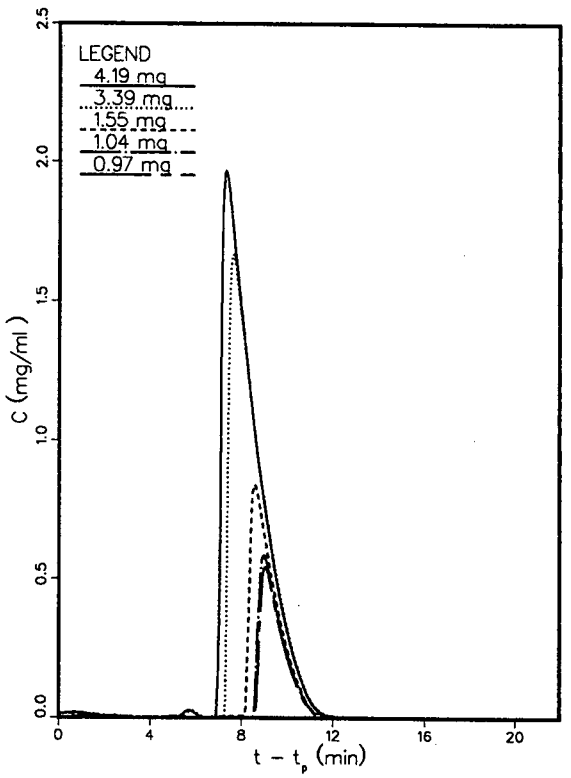

Fig. 1. Experimental chromatogram for sample 2,6-dimethylphenol on column VS2 ($L = 10$ cm, Vydac ODS). t_p = Duration of the injection.

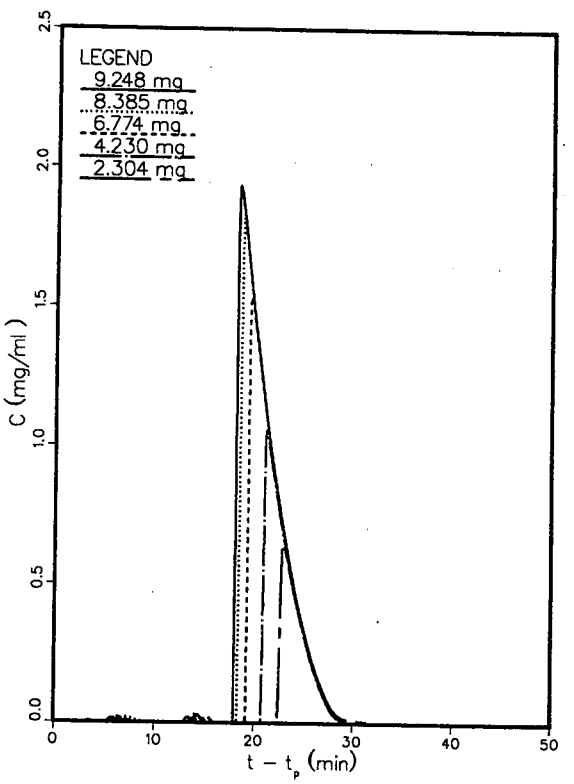

Fig. 2. Experimental chromatogram for sample 2,6-dimethylphenol on column VL2 ($L = 25$ cm, Vydac ODS).

$$N_0 = 5.54\left(\frac{t_R}{W_{0.5}}\right)^2 \quad (6)$$

The retention factor k' of each compound was calculated from

$$k' = \frac{t_{R,0} - t_0}{t_0} \quad (7)$$

The results obtained are summarized in Table 2. The retention factors of all three components are nearly the same on the two Vydac columns having the same length, but they are systematically lower on the shorter columns, by a few percents on the YMC column, by around 13% on the Vydac columns. By contrast, the height equivalent to a theoretical plate (HETP) at 1.0 ml/min (reduced velocities between 12 and 15) is nearly the same on the Vydac columns of different lengths (i.e., the plate number is proportional to the column length), but almost 50% higher on the longer YMC column than on the shorter one. While column-to-column fluctuations of efficiency are common and are usually attributed to fluctuations in packing homogeneity, variations in retention factors between columns packed with the same material can be easily explained only by variations in the packing density, which affect the phase ratio. Indeed, the amount of adsorbent introduced in the longer Vydac columns is approximately 2.75 times as large as the amount packed in the shorter columns, corresponding to an average packing density 10% larger.

ECP Measurements

The large samples required by this method

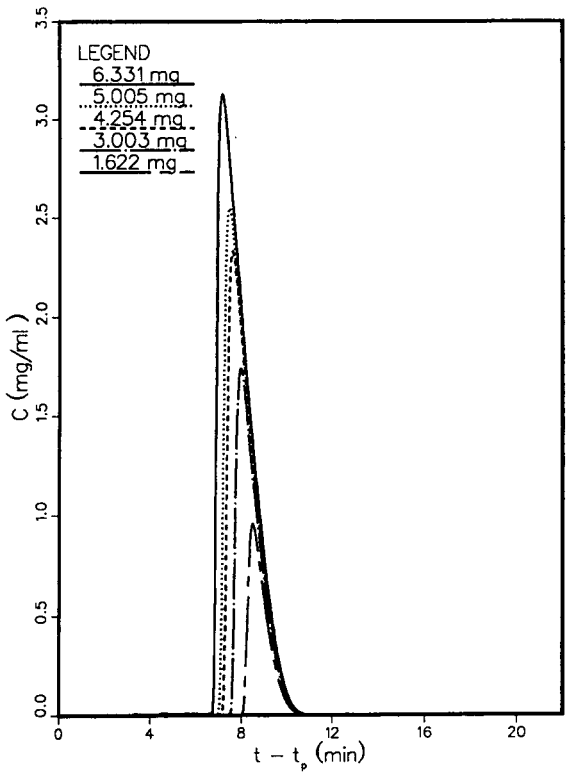

Fig. 3. Experimental chromatogram for sample 3-phenyl-1-propanol on column VS2 (L = 10 cm, Vydac ODS).

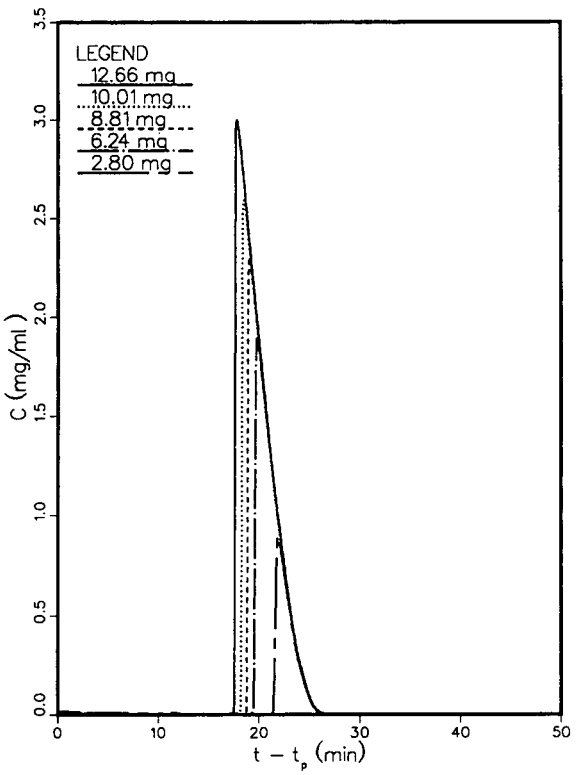

Fig. 4. Experimental chromatogram for sample 3-phenyl-1-propanol on column VL2 (L = 25 cm, Vydac ODS).

were obtained by injecting 0.25 ml of each solution on the 10 cm long columns, 0.50 ml of the concentrated 2,6-dimethylphenol and 3-phenyl-1-propanol solutions, and 1.0 ml of the concentrated methyl benzoate solution on the 25 cm long columns. In each of these experiments, the flow-rate was set at 1.0 ml/min. The use of large sample volumes in ECP is conventional. The proper correction was applied by taking the end of the injection as time origin.

4. Results and discussion

The experimental results in Table 1 lead to several unexpected conclusions. First, the packing density of columns is not very reproducible. Second, the three methods used to determine the column porosity do not agree closely. Third, the packing density varies with the length of the column, the longer columns having, rather surprisingly, a higher packing density. The trend is only marginal with the YMC material, with a packing density nearly 5% higher for the longer column. The difference is important for the columns packed with the Vydac ODS, a material which is known for being difficult to pack. Both 25 cm long columns and both 10 cm long ones have nearly the same packing density, but the former are nearly 15% denser than the latter. Since the columns were packed with the same material, using the same method, it is unlikely that the specific surface area of the adsorbent be different. Then the thermodynamic properties should be reported to the mass of packing in the column rather than to its volume.

The lack of close agreement between the three methods used to determine the column porosity

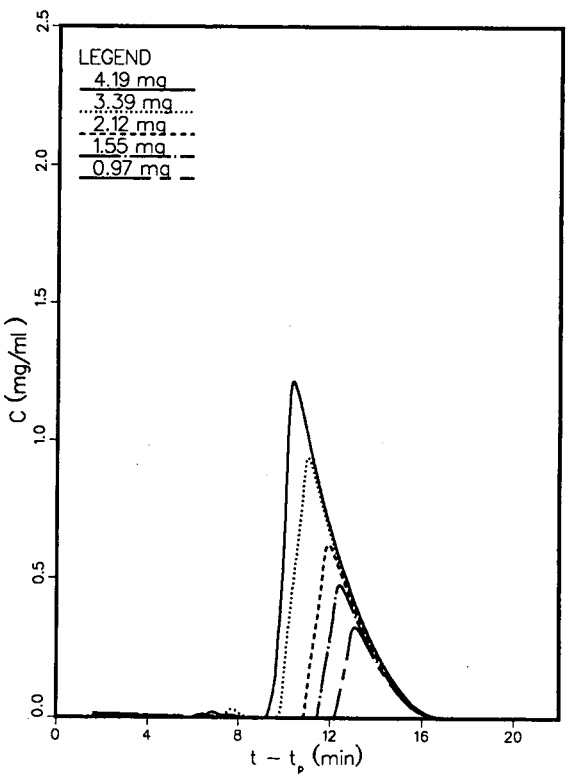

Fig. 5. Experimental chromatogram for sample 2,6-dimethylphenol on column YS (L = 10 cm, YMC ODS).

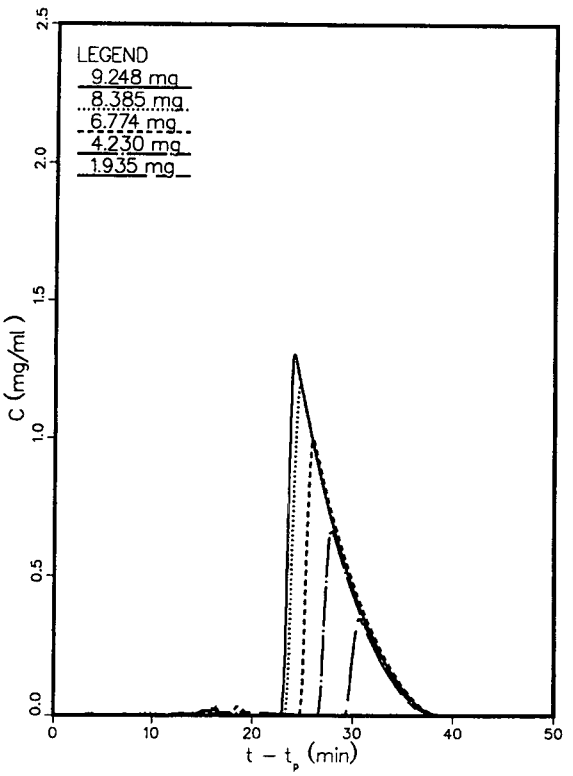

Fig. 6. Experimental chromatogram for sample 2,6-dimethylphenol on column YL (L = 25 cm, YMC ODS).

is not surprising. There is no guarantee that uracil is a non-retained, non-excluded tracer. The calculation of the volume of solid stationary phase using 2.21 g/ml for the density of silica is approximate, as this number is not universally accepted for amorphous silica and it neglects the contribution of the C_{18} bonded groups. Finally, the retention volume of uracil in methanol–water (40:60) may differ slightly from the volume of pure methanol contained in the column if the wettability of silica by the two liquids is different.

The retention factors of the three probes at infinite dilution[1] are reported in Table 2. The standard deviation of the measurement of k' on any single column is 0.5 to 1%. If the data for the four Vydac columns are not corrected for the variable packing density, the standard deviation for the four values of k' is 6 to 7% (Table 2). If the data are corrected, it is only 3%. A similar but less conclusive result is observed for the two YMC ODS columns, the relative difference of the two values being used instead. This result confirms the importance of taking the column packing density into account when comparing thermodynamic data acquired on different columns. This should be of major concern when trying to predict elution band profiles on preparative columns using data acquired with analytical size columns [34].

2,6-Dimethylphenol and 3-phenyl-1-propanol were found to have a near-Langmuirian equilibrium behavior on all six columns, while methyl benzoate has an anti-Langmuirian behavior. The

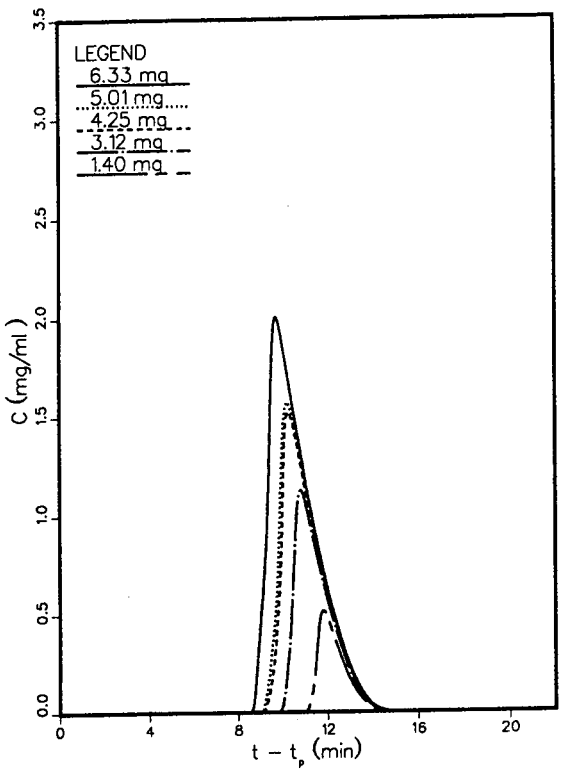

Fig. 7. Experimental chromatogram for sample 3-phenyl-1-propanol on column YS ($L = 10$ cm, YMC ODS).

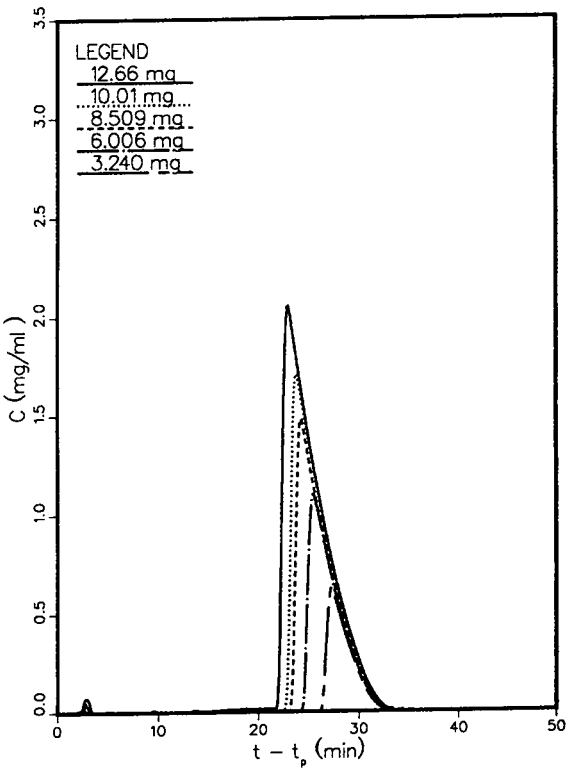

Fig. 8. Experimental chromatogram for sample 3-phenyl-1-propanol on column YL ($L = 25$ cm, YMC ODS).

[1] If we refer to Eq. 4, we see that we can consider the isotherm as linear as long as b_1C is negligible compared to 1. Values of C were such that b_1C was smaller than 0.001.

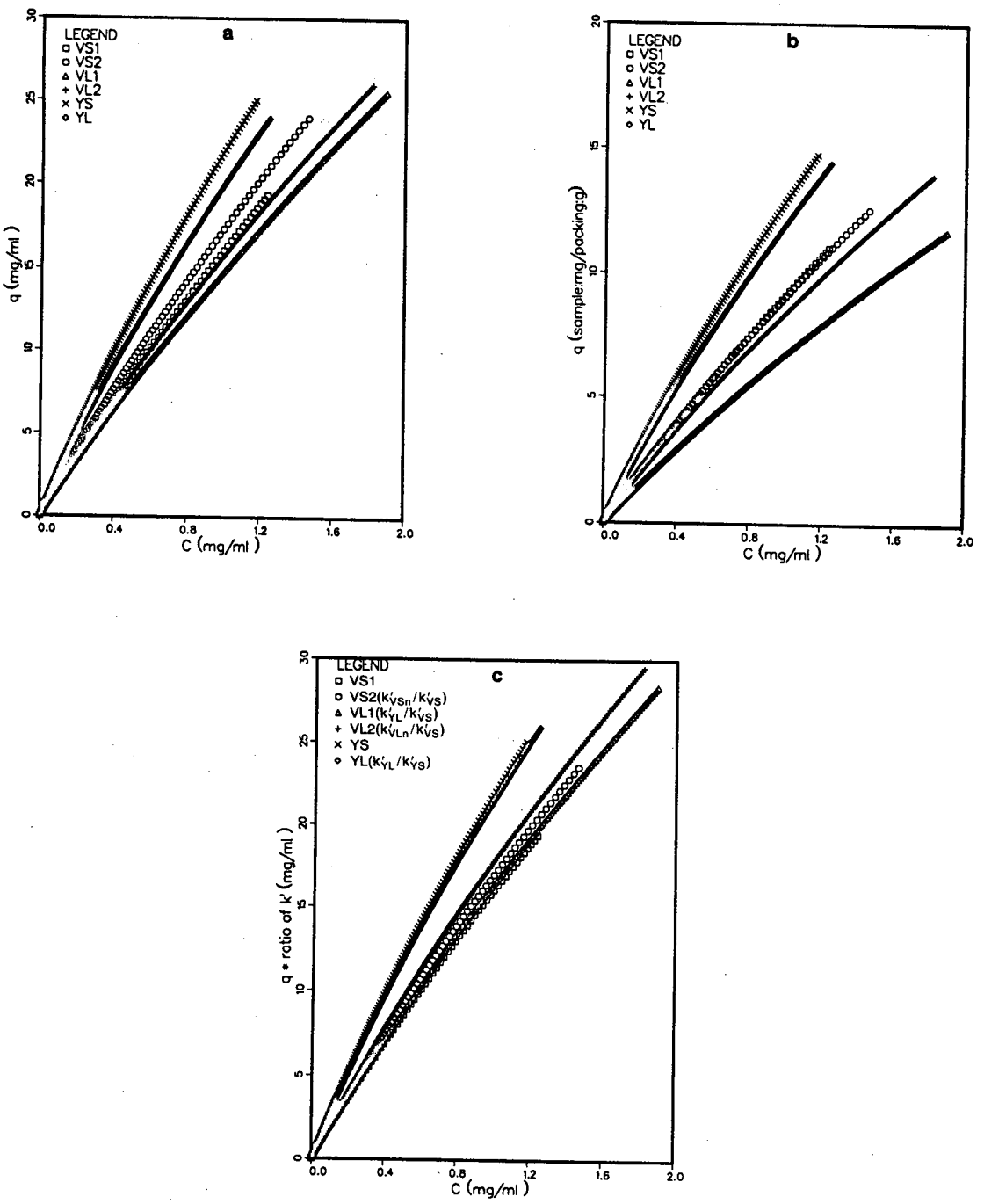

Fig. 9. Isotherms measured by ECP for 2,6-dimethylphenol on all six columns examined. (a) Isotherm data reported to the volume of the column. (b) Isotherm data reported to the mass of silica. (c) Isotherm data reported to the retention factor under analytical conditions.

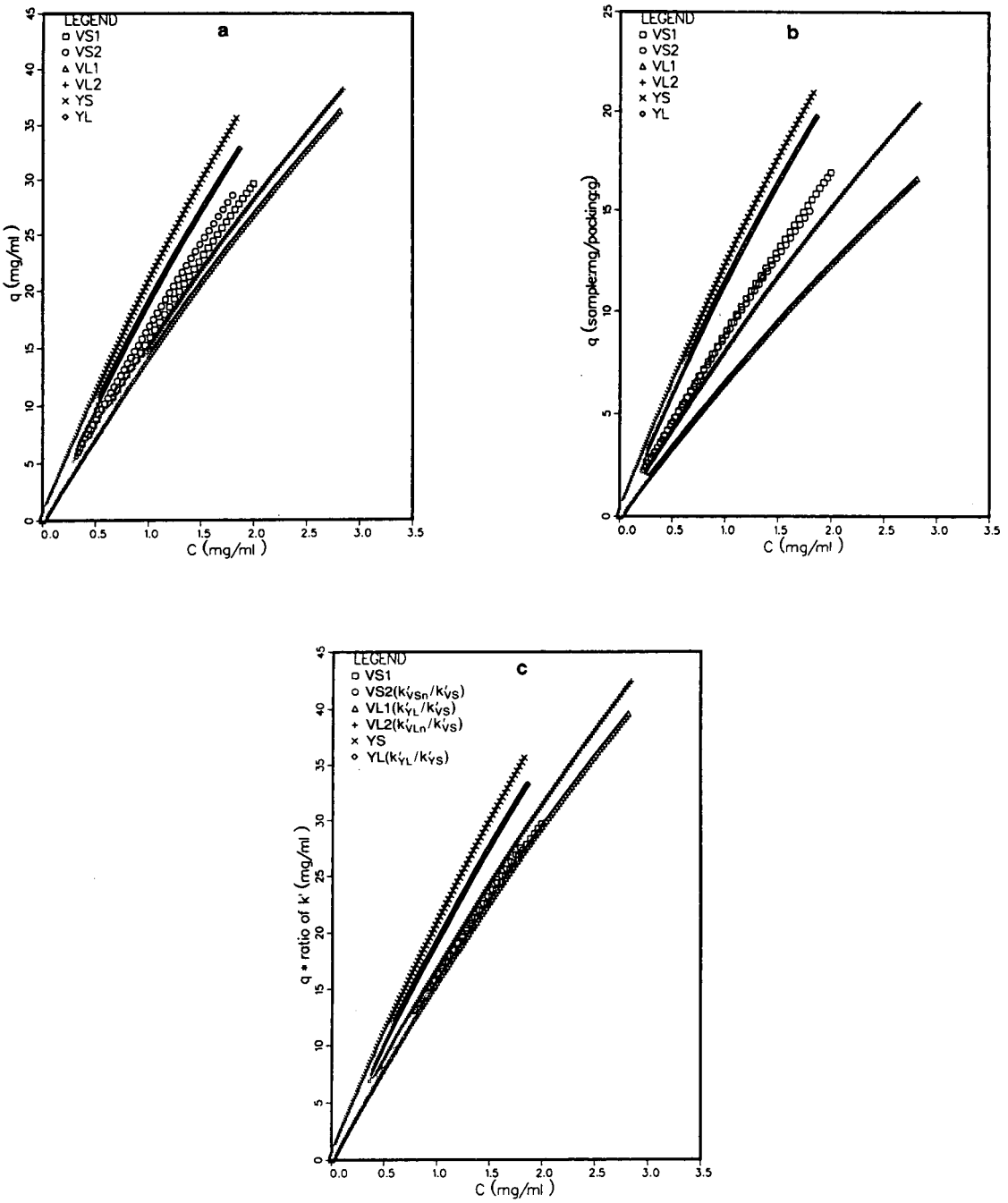

Fig. 10. Isotherms measured by ECP for 3-phenyl-1-propanol on all six columns examined. (a) Isotherm data reported to the volume of the column. (b) Isotherm data reported to the mass of silica. (c) Isotherm data reported to the retention factor under analytical conditions.

major differences in this behavior and in the procedures required for the modeling of the equilibrium isotherms and of the band profiles justify the separate discussion of these two sets of results.

4.1. Langmuirian compounds

The Langmuir isotherm is most popular because it is simple and it accounts quite well for the single-component equilibrium data obtained in a vast majority of the cases encountered in liquid chromatography and particularly in reversed-phase HPLC. The behavior of 2,6-dimethylphenol and 3-phenyl-1-propanol on the Vydac and YMC ODS are cases in point.

Both compounds exhibit Langmuirian band profiles on all six columns. Data are reported only for one set of Vydac columns (Figs. 1–4) and for the YMC columns (Figs. 5–8). In all cases, the front of the profiles obtained with the 25 cm long columns (Figs. 2, 4, 6 and 8) are steeper than those recorded with the 10 cm long columns (Figs. 1, 3, 5 and 7), in relation to the higher efficiency of the former, longer columns. The front of the band profiles tend to be steeper and the profiles to be narrower on the Vydac ODS columns.

The ECP method was applied to each of the profiles obtained and the experimental isotherms were calculated. The results are shown in Figs. 9 and 10. In Figs. 9a and 10a, the amounts adsorbed at equilibrium are reported to the volume of column, as classical in the chromatographic determination of isotherms. The curves obtained

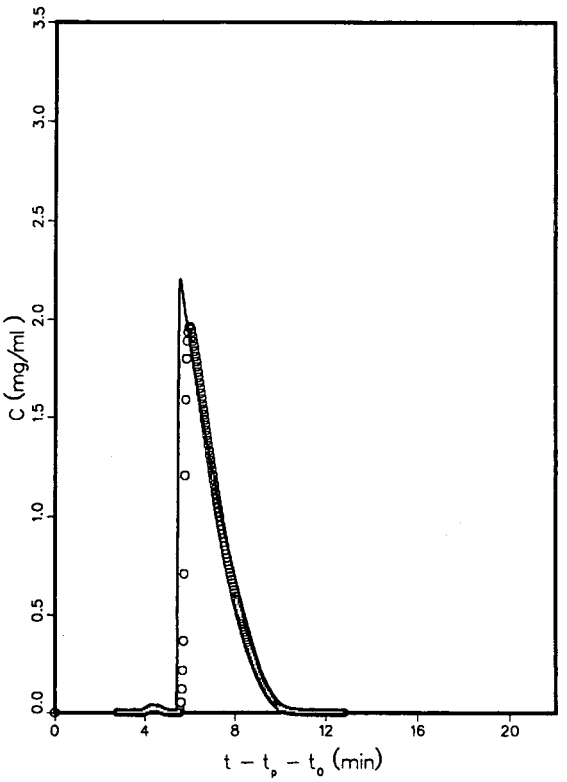

Fig. 11. Comparison between calculated (solid line) and experimental (symbols) band profiles on column VS2 ($L = 10$ cm, Vydac ODS). Sample: 2,6-dimethylphenol; amount: 4.2 mg. Mobile phase: methanol–water (40:60, v/v). Langmuir isotherm coefficients, $q_s = 144$ and $b = 0.14$.

are spread and no patterns emerge. In Figs. 9b and 10b, the amounts adsorbed have been reported to the mass of packing contained in the column. The curves corresponding to the six

Table 3
Isotherm coefficients for 2,6-dimethylphenol

2,6-Dimethylphenol	Columns					
	YS	YL	VS1	VS2	VL1	VL2
q_s from ECP	119	113	136	144	131	124
b_1 from ECP	0.226	0.213	0.134	0.144	0.128	0.145

For columns, see Table 1.

Table 4
Isotherm coefficients for 3-phenyl-1-propanol

3-Phenyl-1-propanol	Columns					
	YS	YL	VS1	VS2	VL1	VL2
q_S from ECP	208.96	199.79	264.33	264.84	228.88	225.68
b_1 from ECP	0.1117	0.1052	0.0632	0.0708	0.0668	0.0715
q_S from FA	203.83	196.36	246.11	265.81	232.48	220.03
b_1 from FA	0.1009	0.0960	0.0514	0.0626	0.0584	0.0643

For columns, see Table 1.

columns now form two better defined clusters, corresponding to the two different adsorbents. Inside each cluster, there is still a significant difference between the isotherms obtained for different columns packed with the same stationary phase. This difference is small, about 5%, in the case of the two YMC columns, YS and YL. It is negligible in the case of the two short columns packed with the Vydac material, VS1 and VS2 (less than 1%). Column VL2 gives an isotherm which is close to those given by columns VS1 and VS2 (the difference is 6%) but the isotherm derived from column VL1 is quite different, with an amount adsorbed at equilibrium with the same mobile phase concentration nearly 20% lower. The same conclusions apply to both compounds. It seems unlikely that such a large error could be made on the determination of the amount of stationary phase in the column. It is at least as unlikely that the specific surface area of the material contained in the two columns be that different. There is a possibility that the adsorbent surface in column VL1 has been modified but this is dubious, artifacts of that kind being common in normal-phase chromatography but rare in reversed-phase chromatography. The reason for the spread of the isotherm data still eludes us. In our opinion, the solution to this problem is an important prerequisite for the systematic use of isotherm data for the optimization of the experimental conditions in preparative chromatography.

In Figs. 9c and 10c, the amounts adsorbed have been reported to the retention factor measured under analytical conditions (very small sample amount, so the product b_1C (Eq. 4) is negligible compared to unity). The lines obtained for the columns of both series become much closer. In all cases, for the YMC and the Vydac columns, for PP and for DMP, the range of amounts adsorbed for a given mobile phase

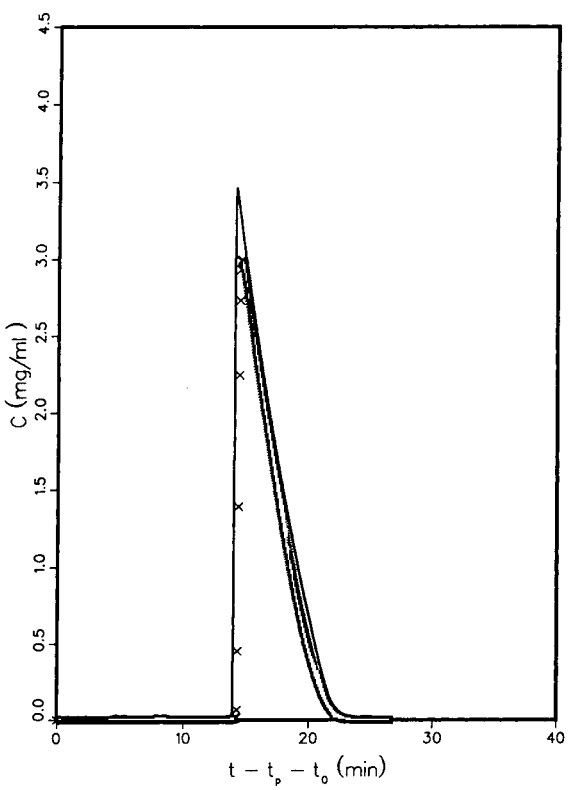

Fig. 12. Comparison between calculated (solid line) and experimental (symbols) band profiles on column VL2 ($L = 25$ cm, Vydac ODS). Sample: 3-phenyl-1-propanol; amount: 12.7 mg. Mobile phase: methanol–water (40:60, v/v). Langmuir isotherm coefficients: $q_S = 225.7$ and $b = 0.072$.

concentration is ± 4%, which is quite satisfactory. The rationale for this correction is that the retention factor at infinite dilution, k', is equal to $Fa = Fb_1q_s$ where F is the phase ratio $[(1 - \varepsilon)/\varepsilon$, ε is the total porosity of the column the product of the phase ratio and the initial slope of the isotherm. So, if the isotherm is a characteristic of the stationary phase which depends only on the chemistry of the surface and the specific surface area, the differences between isotherms measured on different columns should be proportional to the differences between retention factors, because they are due to differences in packing density, hence in phase ratio. This assumption seems to prove approximately correct.

Since each of these isotherms appears to be Langmuirian, the experimental data were fitted to this model (Eq. 4). The coefficients q_S and b_1 were calculated for the isotherm derived from the elution band profile of the largest sample, as previously described [23]. The values obtained are reported in Tables 3 (2,6-dimethylphenol) and 4 (3-phenyl-1-propanol). The values corresponding to the two phases are significantly different, with the Vydac phase exhibiting a higher saturation capacity and a higher retention factor than the YMC phase. Inside each group, there is a spread of the numerical results, with a relative standard deviation of 6% for both q_S and b_1 on the Vydac material (the only one for which a meaningful relative standard deviation

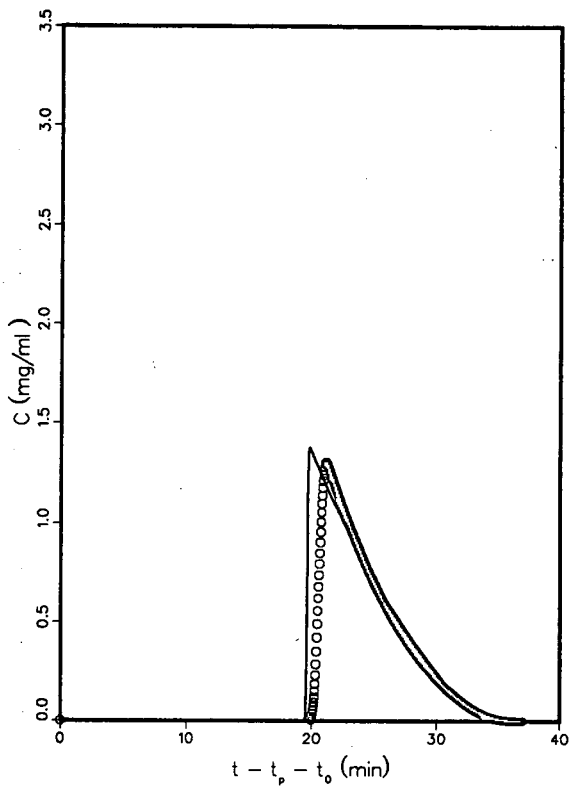

Fig. 13. Comparison between calculated (solid line) and experimental (symbols) band profiles on column YL ($L = 25$ cm, YMC ODS). Sample: 2,6-dimethylphenol; amount injected: 9.25 mg; amount used in the calculation: 8.40 mg. Mobile phase: methanol–water (40:60, v/v). Langmuir isotherm coefficients: $q_S = 113.6$ and $b = 0.21$.

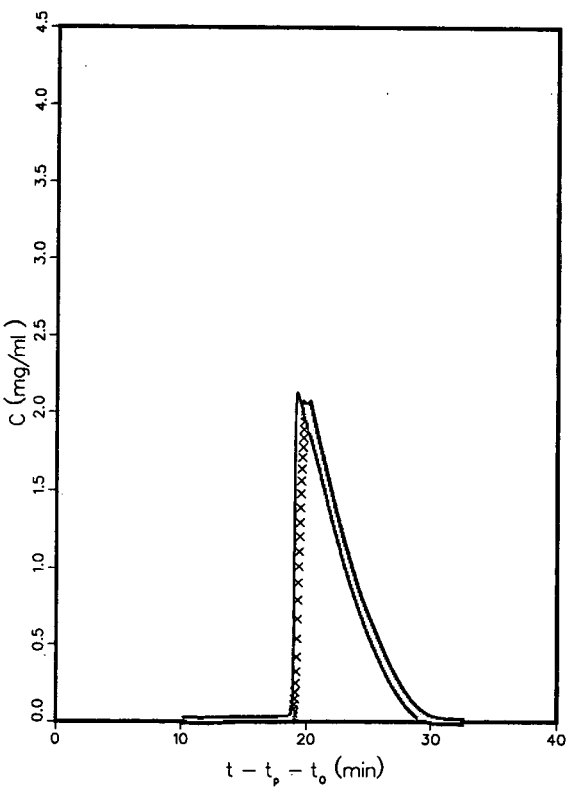

Fig. 14. Comparison between calculated (solid line) and experimental (symbols) band profiles on column YL2 ($L = 25$ cm, YMC ODS). Sample: 3-phenyl-1-propanol; amount injected: 12.7 mg; amount used in the calculation: 10.50 mg. Mobile phase: methanol–water (40:60, v/v). Langmuir isotherm coefficients: $q_S = 199.8$ and $b = 0.11$.

can be calculated). This error appears to be reasonable for experimental results involving complex determinations. Unfortunately, it is too large to permit accurate calculations of band profiles.

Isotherm data were also determined using the method of upward-staircase frontal analysis for 3-phenyl-1-propanol. The values obtained for the coefficients of the Langmuir equation are also given in Table 4. There is a very good general agreement with the results of the ECP method.

Knowing the isotherm and the column efficiency, it is possible to calculate band profiles using the equilibrium-dispersive model of chromatography [20,35,36]. Some of the results obtained are compared with the experimental band profiles in Figs. 11–14. In principle, this comparison is a circular argument. However, two model errors are made, one in each part of the circular argument. The first error is made in the ECP method which assumes the column efficiency to be infinite. Its consequences on the accuracy of the isotherm coefficients and on the selection of an isotherm model have been discussed previously [23]. In this earlier study based on the simulation of the measurement process using a Langmuir isotherm, we showed that there is a systematic difference between the values of the amount adsorbed at equilibrium given by the best-fit Langmuir isotherm and by the ECP isotherm at the same mobile phase concentration. In Figs. 15 and 16, these residuals are plotted versus the mobile phase concentration (C) for the two compounds studied. The shape of the curves obtained matches the result reported earlier.

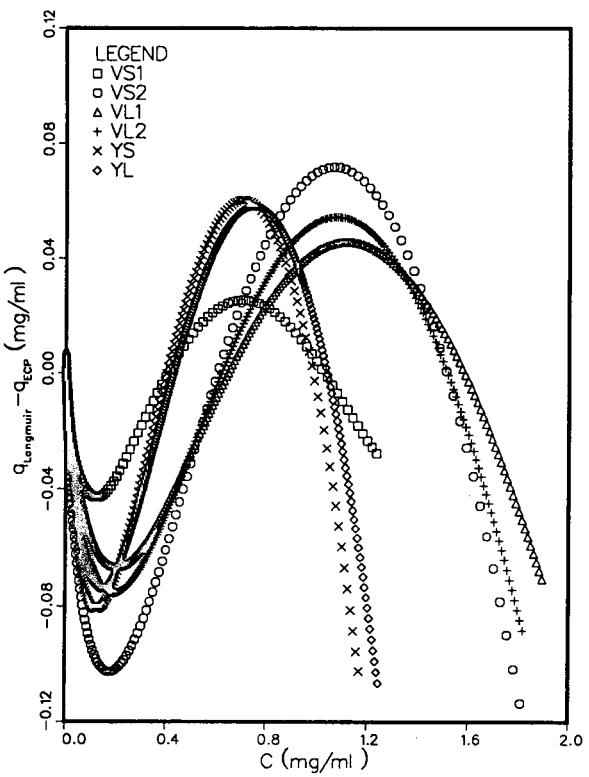

Fig. 15. Illustration of the model error caused by the use of ECP to derive the isotherm of 2,6-dimethylphenol on the six columns studied.

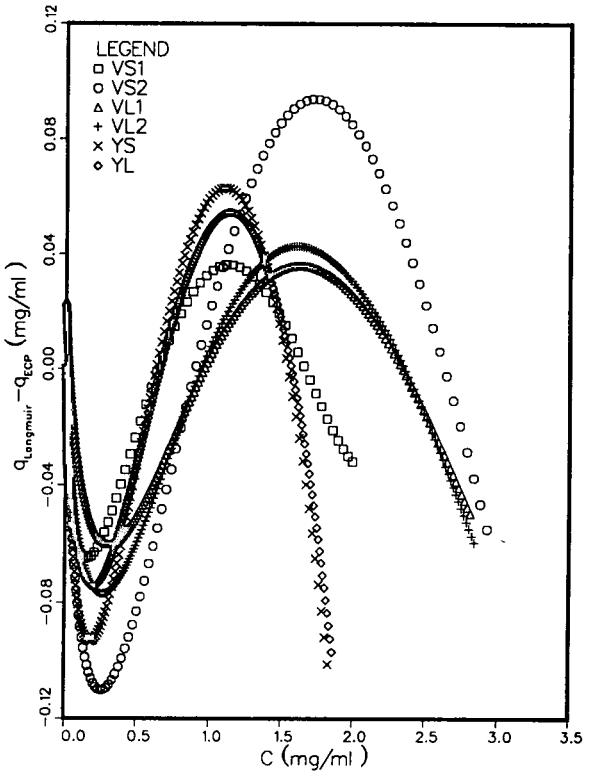

Fig. 16. Illustration of the model error caused by the use of ECP to derive the isotherm of 3-phenyl-1-propanol on the six columns studied.

A second model error is made in the equilibrium-dispersive model itself. This model assumes that the effect of a finite column efficiency on the band profile can be accounted for by a constant coefficient of apparent axial dispersion [20]. However, this coefficient varies with the solute concentration, causing a difference between the actual and the calculated band profiles. This difference is small if the rate constant of the mass-transfer kinetics is large, as is usually the case in reversed-phase chromatography of low-molecular-mass molecules [20]. Comparison between the calculated and experimental band profiles permits an assessment of the importance of these errors and of the possibility to correct them.

The agreement between calculated and experimental band profiles is very good for both compounds on the columns packed with both ODS phases (Figs. 11–14). However, the calculated peaks have a steeper front, are sharper at the peak maximum and less diffused at the rear of the tail. The difference in the steepness of the band front is slightly more important with the YMC than with the Vydac columns, suggesting a slower rate of mass transfer. Also, comparison of peak areas shows a slightly lower response on the former phase, suggesting a small sample loss on these columns.

4.2. Anti-Langmuirian compound

The behavior of the third compound studied, methyl benzoate, is opposite to that of the other two compounds. All overloaded bands of methyl benzoate exhibit a self-sharpening rear and a front diffuse boundary, a typical anti-Langmuirian behavior. The same type of profile was

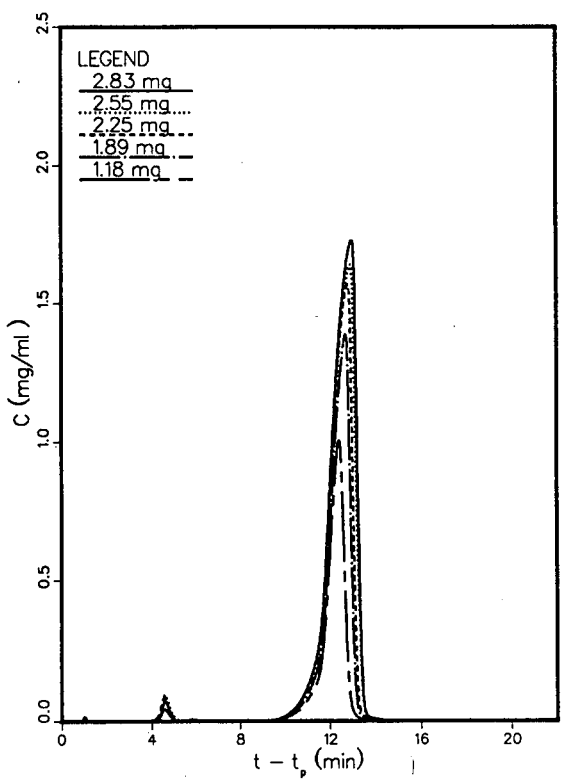

Fig. 17. Experimental chromatogram of methyl benzoate on column VS1 (L = 10 cm, Vydac ODS).

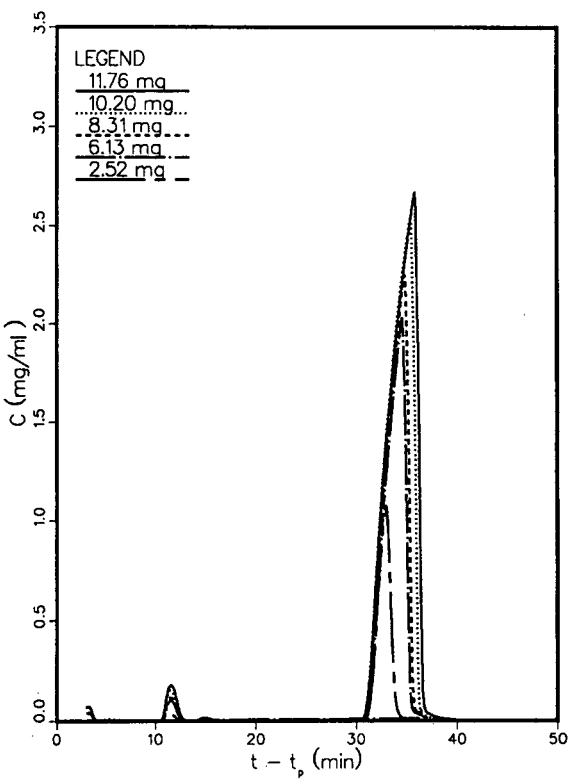

Fig. 18. Experimental chromatogram of methyl benzoate on column VL2 (L = 25 cm, Vydac ODS).

observed on all six columns, regardless of their length and of the nature of the stationary phase, as shown in Figs. 17–20. As a result of the shape of the isotherm, the elution time of the peak maximum increases and the rear shock becomes sharper with increasing sample size. Such an effect has rarely been reported in reversed-phase liquid chromatography and never studied in detail.

The isotherm of methyl benzoate was determined by applying the ECP method to the diffuse front of the band profiles obtained under overloading conditions. To verify this isotherm, determinations of the solute amount adsorbed at various mobile phase concentrations were carried out by FA, using negative concentration steps to generate self-sharpening rear shock layers. The isotherms obtained for all six columns are shown in Figs. 21 and 22. Difficulties

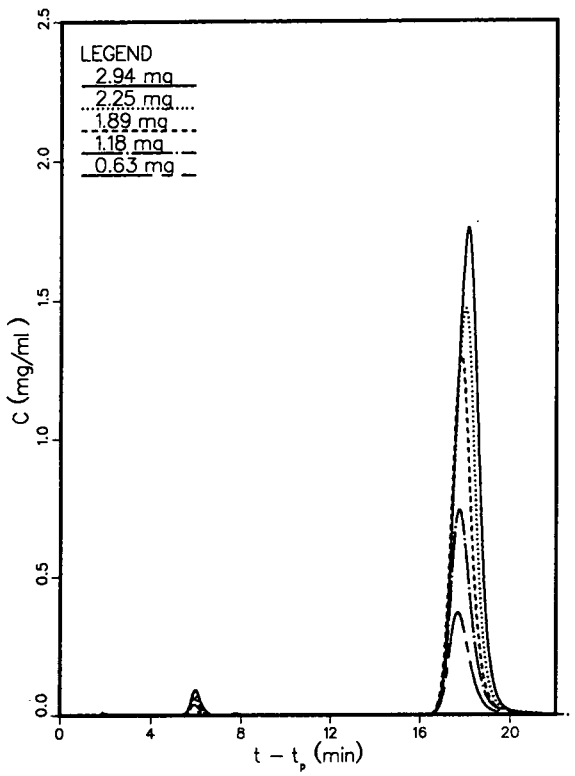

Fig. 19. Experimental chromatogram of methyl benzoate on column YS (L = 10 cm, YMC ODS).

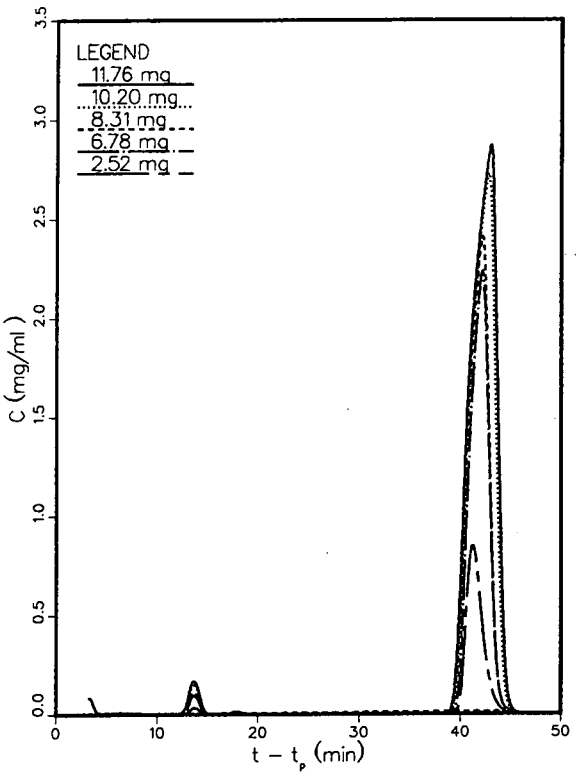

Fig. 20. Experimental chromatogram of methyl benzoate on column YL (L = 25 cm, YMC ODS).

arise for the determination of the isotherm at high concentrations because of the poor solubility of methyl benzoate in methanol–water solutions, which is probably related with the shape of the isotherm. In a methanol–water (40:60) mobile phase, the solubility is approximately 11.7 mg/ml. It was not possible to inject large enough samples and carry out the ECP determinations for concentrations exceeding 2.5 mg/ml (Fig. 21). By contrast, FA determinations could be done at concentrations up to 11.5 mg/ml (Fig. 22). This explains why the ECP isotherms appear to be almost linear while the curvature of the FA isotherms is apparent. Measurements were also made in a methanol–water (60:40) mixture in which the methyl benzoate solubility is much larger, ca 71.1 mg/ml. As seen in Fig. 23, the ECP and FA results are in excellent agreement in the low and medium

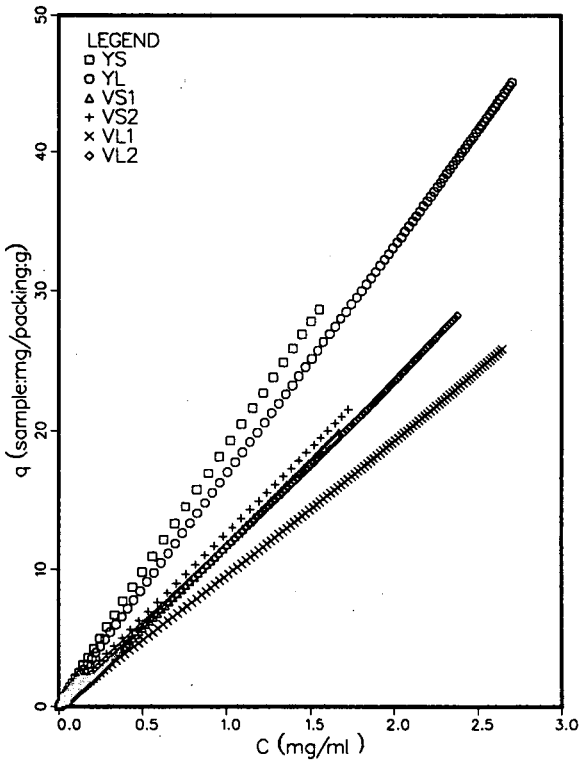

Fig. 21. Isotherms measured by ECP for methyl benzoate on the six columns studied. Mobile phase: methanol–water (40:60, v/v). Data reported to the mass of silica in the column.

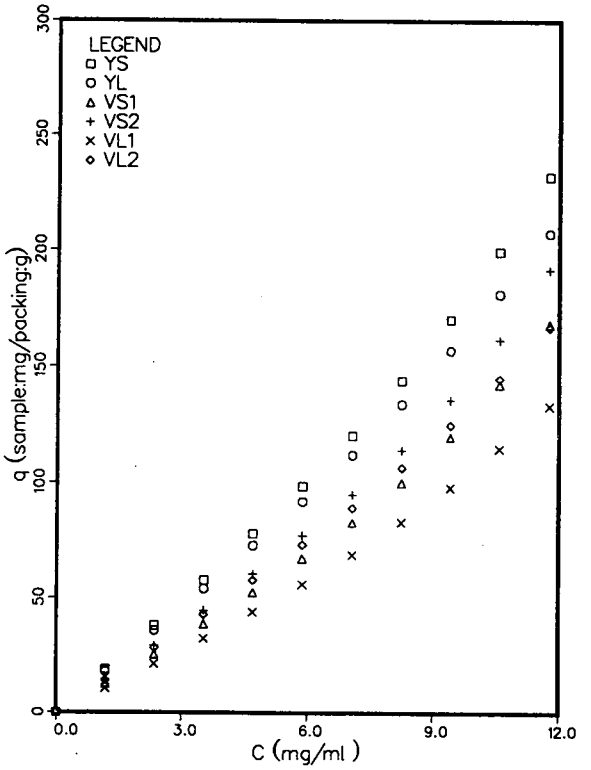

Fig. 22. Isotherms measured by FA for methyl benzoate on the six columns studied. Data reported to the mass of silica in the column. Mobile phase: methanol–water (40:60, v/v).

range of concentrations but diverge above approximately 30 mg/ml.

A convex-downward isotherm can be accounted for by accepting a negative value of b in Eq. 4 (Langmuir isotherm) or by using the second-order approximation of the general isotherm (Eq. 3). The former approach is purely empirical as it leads to an infinite value of the amount adsorbed for some finite mobile phase concentration, a conclusion which is physically meaningless. It also results in negative values of q_S (Table 5). Isotherms of type III in the Brunauer–Emmett–Teller classification are not encountered in liquid–solid equilibria. More probably, a convex-downward isotherm is an isotherm of type V whose inflection point is not accessible because it takes place at a concentration higher than the solubility. Accordingly, the true saturation capacity, q_S, is difficult to estimate.

The experimental adsorption data derived by ECP and FA were fitted to the two models listed above. The numerical coefficients obtained are reported in Table 5. There seems to be as much fluctuations between coefficients obtained for columns packed with the same phase as differences between the results obtained for columns packed with different phases.

Using these isotherm data, band profiles of methyl benzoate were calculated using a forward-backward algorithm [20,35]. The program aborted for instability reasons when the Langmuir equation with a negative b value was used. The results of two different calculations are reported here. The first used a four-term Taylor expansion of the Langmuir equation, the second used the three-term isotherm (Eq. 5). Com-

parison between experimental and calculated band profiles on two columns are illustrated in Figs. 24 and 25. The results obtained with the other four columns were similar. There are two major differences between these profiles. First, the calculated peak tends to be much higher than the experimental one. Second, the experimental band front is more diffuse than calculated, and its steep rear elutes slightly earlier. The differences in time and profile are less significant, however, when band profiles are calculated with the second isotherm (Eq. 5).

The simplest possible reason to explain the difference between experimental and calculated profiles around their maximum would be a decrease in the solubility of methyl benzoate in methanol–water solutions with increasing pressure. The injection of a saturated solution would result in the precipitation of the excess amount injected followed by its slow redissolution in the mobile phase. This would effectively widen the injection profile, decrease its maximum concentration and increase the retention time of the rear part of the profile. However, the rear shock layer originating from the end of the injection profile would be dispersed in the process, which is not the case. Furthermore, practically the same difference between calculated and mea-

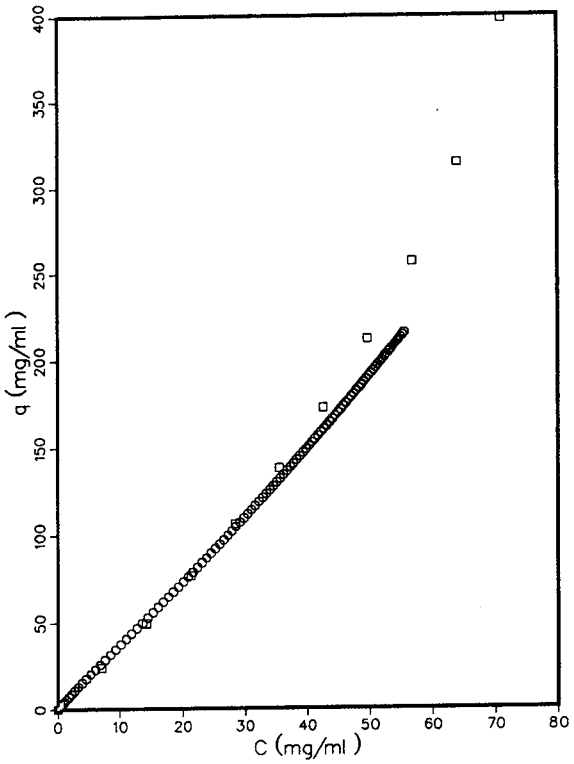

Fig. 23. Comparison of the isotherms derived from ECP (○) and FA (□) for methyl benzoate on column VL2 (L = 25 cm, Vydac ODS). Mobile phase: methanol–water (60:40, v/v).

Table 5
Isotherm coefficients for methyl benzoate

	Columns					
	YS	YL	VS1	VS2	VL1	VL2
ECP[a] q_S	na	na	−533	815	−1510	−1740
ECP[b] b_1	na	na	−0.037	0.032	−0.0136	−0.0123
FA[c] q_S	−1160	−1420	−601	−813	−794	−1160
FA[d] b_1	−0.021	−0.0165	−0.028	−0.027	−0.023	−0.018
FA[e] q_S	−600	−511	−285	−401	−368	−660
FA[f] b_1	−0.039	−0.041	−0.053	−0.054	−0.045	−0.031
FA[g] b_2	0.0003	0.0003	0.0005	0.0007	0.0004	0.0002

For columns, see Table 1. na = Not available.
[a] q_S obtained by ECP; first-order approximation isotherm.
[b] b_1 obtained by ECP; first-order approximation isotherm.
[c] q_S obtained by FA; first-order approximation isotherm.
[d] b_1 obtained by FA; first-order approximation isotherm.
[e] q_S obtained by FA; second-order approximation isotherm.
[f] b_1 obtained by FA; second-order approximation isotherm.
[g] b_2 obtained by FA; second-order approximation isotherm.

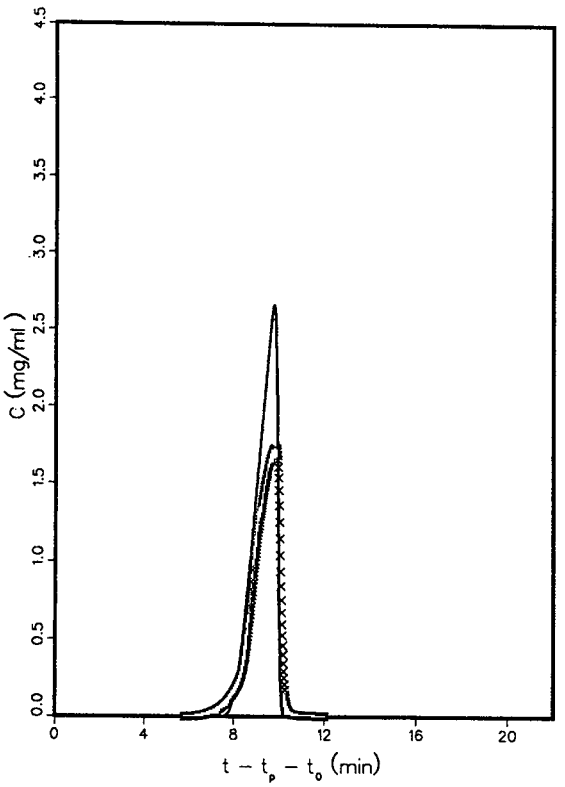

Fig. 24. Comparison between calculated (solid line) and experimental (symbols) band profiles for column VS1 ($L = 10$ cm, Vydac ODS). Sample: methyl benzoate; amount 2.83 mg. Mobile phase: methanol–water (40:60, v/v). Langmuir isotherm coefficients: $q_S = -640.5$ and $b_1 = -0.028$.

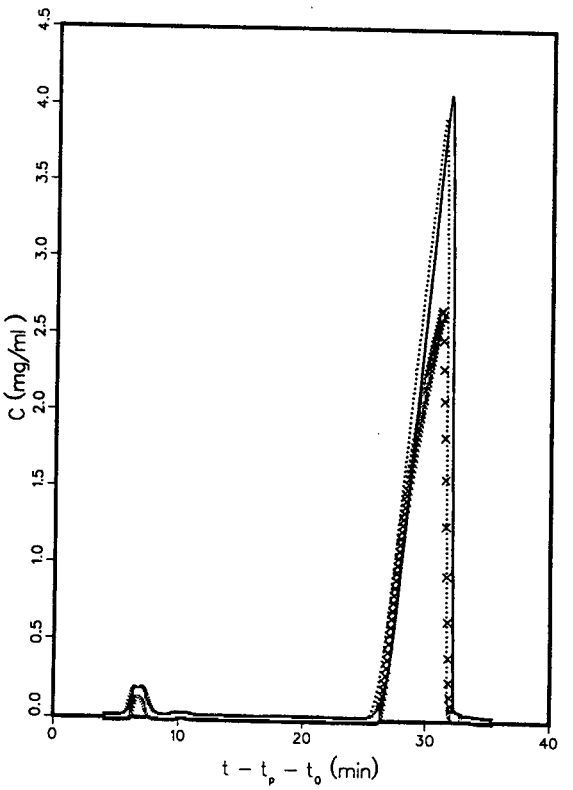

Fig. 25. Comparison between experimental (symbols) and calculated band profiles using isotherm data measured by FA and the Langmuir (solid line) or the quadratic (dotted line) isotherm models, for column VL2 ($L = 25$ cm, Vydac ODS). Sample: methyl benzoate; amount 11.76 mg. Mobile phase: methanol–water (40:60, v/v). Isotherm coefficients, Langmuir: $q_S = -1158.05$ and $b_1 = -0.018$; quadratic isotherm: $q_S = -660.66$, $b_1 = -0.031$ and $b_2 = 0.0002$.

sured profiles is observed with less concentrated solutions (Fig. 26).

5. Conclusions

The conclusions of a study based on the determination of isotherm data of three compounds on six chromatographic columns packed with ODS from two different companies can only be very limited. It is noteworthy, however, that the behavior of these two stationary phases is very similar. Both give Langmuir isotherms for 2,6-dimethylphenol and 3-phenyl-1-propanol and anti-Langmuir isotherms for methyl benzoate. The sharpness of the shock layers and the extent of dispersion of the diffuse boundary vary from column to column only in relation with their efficiency.

If allowance is made for the differences in the packing density of the different columns packed with the same stationary phase, the column-to-column reproducibility of isotherm data is markedly improved for the components giving a Langmuir isotherm. It is also better, although not as satisfactory, for methyl benzoate which gives an anti-Langmuir isotherm. The ratio of the retention factors of the compounds studied on the two phases investigated is close in spite of the important differences between these adsorbents.

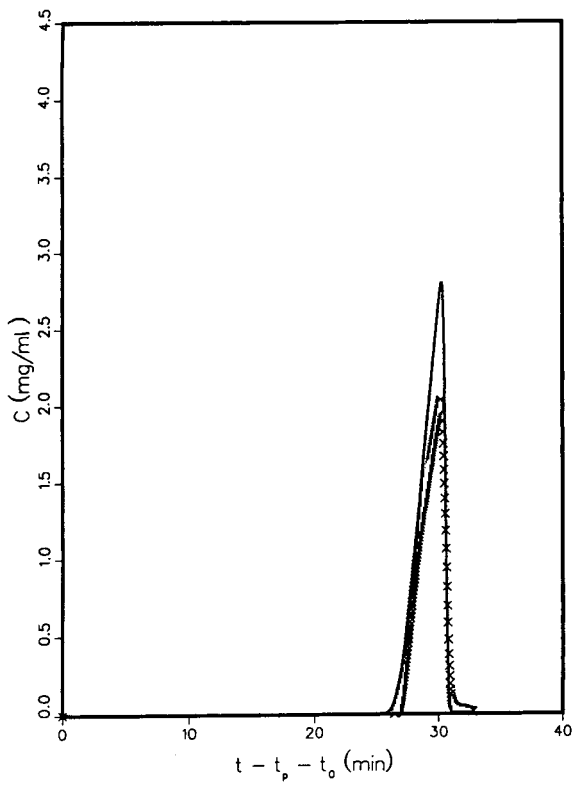

Fig. 26. Same comparison as in Fig. 25, except sample amount, 6.1 mg.

The isotherm data obtained by the ECP and FA methods are in excellent agreement for components giving Langmuir isotherms, as often reported previously [21,22]. However, this agreement is only fair for methyl benzoate at high concentrations. It is unclear whether the differences observed are due to experimental problems related to the anti-Langmuirian nature of the isotherm or to the low solubility of the compound.

Acknowledgements

We are grateful to YMC and Vydac companies for the gift of the ODS packing materials used throughout our studies. This work was supported in part by grant CHE-9201663 from the National Science Foundation and by the cooperative agreement between the University of Tennessee and the Oak Ridge National Laboratory. We acknowledge support of our computational effort by the University of Tennessee Computing Center.

References

[1] C.F. Poole and S.K. Poole, *Chromatography Today*, Elsevier, Amsterdam, The Netherlands, 1991.
[2] E. Grushka (Editor), *Bonded Stationary Phases in Chromatography*, Ann Arbor Sci. Publ., Ann Arbor, MI, 1974.
[3] D.C. Locke, *J. Chromatogr. Sci.*, 11 (1973) 120.
[4] R.E. Majors, *Int. Lab.*, July–August (1972) 25.
[5] H. Colin, J.C. Diez-Masa and G. Guiochon, *J. Chromatogr.*, 167 (1978) 41.
[6] R.I. Greyson and A.M. Patch, *J. Chromatogr.*, 242 (1982) 349.
[7] H. Colin, N. Ward and G. Guiochon, *J. Chromatogr.*, 149 (1978) 169.
[8] H. Colin and G. Guiochon, *J. Chromatogr.*, 158 (1978) 183.
[9] P. Roumeliotis and K.K. Unger, *J. Chromatogr.*, 149 (1978) 211.
[10] R.D. Smillie, D.T. Wang and O. Merez, *J. Environ. Sci. Health*, A13 (1978) 47.
[11] K. Ogan, E. Katz and W. Slavin, *Anal. Chem.*, 51 (1979) 1315.
[12] K. Ogan and E. Katz, *J. Chromatogr.*, 188 (1980) 115.
[13] N.T. Miller, *J. Chromatogr.*, 550 (1991) 301.
[14] J.H. Knox and M. Saleem, *J. Chromatogr. Sci.*, 12 (1969) 614.
[15] M. Martin, C. Eon and G. Guiochon, *J. Chromatogr.*, 110 (1975) 213.
[16] K.K. Unger, W. Messer and K.F. Krebs, *J. Chromatogr.*, 149 (1978) 1.
[17] S.A. Wise and W.E. May, *Anal. Chem.*, 55 (1983) 1479.
[18] L.C. Sander and S.A. Wise, *J. Chromatogr.*, 316 (1984) 163.
[19] M. Olsson, L.C. Sander and S.A. Wise, *J. Chromatogr.*, 477 (1989) 277.
[20] G. Guiochon, S. Golshan-Shirazi and A.M. Katti, *Fundamentals of Preparative and Nonlinear Chromatography*, Academic Press, Boston, MA, 1994.
[21] J.F.K. Huber and R.E. Gerritse, *J. Chromatogr.*, 58 (1971) 138.
[22] R.E. Gerritse and J.F.K. Huber, *J. Chromatogr.*, 71 (1972) 173.
[23] H. Guan, B.J. Stanley and G. Guiochon, *J. Chromatogr. A*, 659 (1994) 27.
[24] G. Schay and G. Szekely, *Acta Chim. Hung.*, 5 (1954) 167.

[25] D.H. James and C.S.G. Phillips, *J. Chem. Soc.*, (1954) 1066.
[26] Y.A. Eltekov, Y.V. Kazakevitch, A.V. Kiselev and A.A. Zhuchkov, *Chromatographia*, 20 (1985) 525.
[27] Y.A. Eltekov and Y.V. Kazakevitch, *J. Chromatogr.*, 365 (1986) 213.
[28] E. Glueckauf, *Trans. Faraday Soc.*, 51 (1955) 1540.
[29] J. Jacobson, J. Frenz and Cs. Horváth, *J. Chromatogr.*, 316 (1984) 53.
[30] M. Diack and G. Guiochon, *Langmuir*, 8 (1992) 1587.
[31] D.W. Marquardt, *J. Soc. Appl. Math.*, 11 (1963) 431.
[32] A. Seidel-Morgenstern and G. Guiochon, *Chem. Eng. Sci.*, 48 (1993) 2787.
[33] H. Guan and G. Guiochon, *J. Chromatogr. A*, 687 (1994) 201.
[34] M. Sarker and G. Guiochon, *J. Chromatogr. A*, 683 (1994) 293.
[35] S. Golshan-Shirazi and G. Guiochon, in F. Dondi and G. Guiochon (Editors), *Theoretical Advancements in Chromatography and Related Separation Techniques (NATO ASI, Series C*, Vol. 383), Kluwer, Dordrecht, 1992, p. 35.
[36] S. Golshan-Shirazi and G. Guiochon, in F. Dondi and G. Guiochon (Editors), *Theoretical Advancements in Chromatography and Related Separation Techniques (NATO ASI, Series C*, Vol. 383), Kluwer, Dordrecht, 1992, p. 1.

ELSEVIER

Journal of Chromatography A, 687 (1994) 201–212

JOURNAL OF CHROMATOGRAPHY A

Properties of some C_{18} stationary phases for preparative liquid chromatography
II. Column efficiency

Hong Guan[a,b], Georges Guiochon[a,b,*]

[a]*Department of Chemistry, University of Tennessee, Knoxville, TN 37996-1600, USA*

[b]*Division of Chemical and Analytical Sciences, Oak Ridge National Laboratory, Oak Ridge, TN 37831-6120, USA*

First received 17 May 1994; revised manuscript received 10 August 1994

Abstract

Apparent column efficiencies were measured for 2,6-dimethylphenol, 3-phenyl-1-propanol, *m*-cresol and methyl benzoate on six columns packed with two commercial octadecyl silica, using methanol–water solutions as the mobile phase. The columns having the less dense packing are also the most efficient (the long-term stability problem conventionally associated with low packing-density columns has not been studied). The dependence of the column efficiency on the sample size is well accounted for by the Knox–Pyper model, using the isotherm data previously determined and the solution of the ideal model to account for the thermodynamic contribution to band broadening.

1. Introduction

In a companion paper [1], we discussed the results of measurements of isotherm data for 2,6-dimethylphenol, 3-phenyl-1-propanol and methyl benzoate on six different columns prepared with two different octadecyl silica adsorbents for reversed-phase liquid chromatography. The first two components give Langmuirian isotherms on both stationary phases, the last one gives an anti-Langmuirian isotherm. Calculated and measured band profiles were generally in good agreement, showing that the model errors have been properly corrected or accounted for.

For each component, the same isotherm model could be used to account for the adsorption data on the different columns, the Langmuir model for the first two compounds, the quadratic model for the last one. The parameters of these isotherms are quite different on the two stationary phases. For each stationary phase, the parameters determined for each column are somewhat different, but most of the differences can be explained by the differences in density of the column packing.

The aim of the present paper is to compare the efficiency data acquired in the same time on the different columns studied, and the dependence of the apparent column efficiency on the sample size.

* Corresponding author. Address for correspondence: Department of Chemistry, University of Tennessee, Knoxville, TN 37996-1600, USA.

0021-9673/94/$07.00
SSDI 0021-9673(94)00774-8

2. Theory

Classically, the column efficiency is a measure of the relative bandwidth of elution peaks

$$N_0 = 5.54 \cdot \left(\frac{t_R}{W_{0.5}}\right)^2 \quad (1)$$

where N_0 is the number of theoretical plates of the column, t_R is the retention time of the peak and $W_{0.5}$ is its width at half height. In linear chromatography, the column efficiency is simply related to the design and operation parameters of the column. In non-linear chromatography, the apparent efficiency is also a function of the sample size.

The column efficiency has also been related to the second statistical moment of the band, proportional to the band variance. The definitions are equivalent for nearly symmetrical peaks. Column efficiency being an empirical parameter [2], the choice is a matter of convenience. With the protocol defined in the Experimental section, the precision obtained by measuring the width at half height (ca. 1%) is an order of magnitude better than could be achieved for the determination of the second moment because of the uncertainty, due to the signal noise, regarding the time when the integration should be stopped.

2.1. Linear chromatography

In linear chromatography, the elution bandwidth observed for small samples injected in a short time depends only on the axial dispersion and on the mass-transfer kinetics. A correlation between the height equivalent to a theoretical plate (HETP: $H = L/N_0$, with L = column length), which characterizes the relative band width, and the mobile phase flow velocity (u) has been described by Done et al. [3] who defined the *reduced plate height* h as

$$h = \frac{H}{d_p} \quad (2)$$

and the *reduced velocity* ν or particle Peclet number (see [4]) as

$$\nu = \frac{d_p u}{D_m} \quad (3)$$

where d_p is the average diameter of the packing particles and D_m is the diffusion coefficient of the compound in the mobile phase. The universal correlation is given by

$$h = \frac{b}{\nu} + a\nu^n + c\nu \quad (4)$$

where b characterizes axial diffusion, due to the concentration gradient along the column axis, at the boundaries of the band, a the eddy diffusion, a function of the homogeneity of the column packing, and c the mass-transfer kinetics. The exponent n is commonly assigned a value of 1/3 to best fit experimental results [3]. The Knox equation predicts that the column efficiency reaches a maximum at a certain flow velocity, i.e., that there is a minimum in the h vs. ν plot.

2.2. Apparent efficiency in overloaded elution

In non-linear chromatography, the bandwidth depends also on the thermodynamics of phase equilibrium. Knox and Pyper [5] have suggested that the kinetic contribution to the column efficiency (due to axial dispersion and to mass-transfer resistances) can be separated from the thermodynamic contribution (due to the non-linear behavior of the equilibrium isotherm). This assumes that the mass-transfer resistances are independent of the solute concentration [2].

With this assumption, the apparent column efficiency, N, under overloaded conditions is given by

$$N = \frac{N_0 N_{th}}{N_0 + N_{th}} = \frac{N_0}{1 + \frac{N_0}{N_{th}}} \quad (5)$$

where N_0 refers to the column efficiency at infinite dilution (i.e., it is the plate number resulting from axial dispersion and the mass-transfer kinetics only, as given by Eq. 4) and N_{th}

Table 1
Column hold-up times and capacity factors

	Columns[a]					
	YS	YL	VS1	VS2	VL1	VL2
t_0 (min)	1.26	2.95	1.25	1.30	2.95	2.95
MC: k'	5.60	6.15	3.70	3.60	4.0	4.1
PP: k'	9.7	9.8	6.5	6.3	7.1	7.2
DMP: k'	11.2	12.1	7.1	7.0	7.9	8.1
MB: k'	13.2	14.1	8.8	8.6	9.8	10.3

MC = *m*-Cresol; PP = 3-phenyl-1-propanol; DMP = 2,6-dimethylphenol; MB = methyl benzoate.
[a]All columns, I.D. 4.6 mm. YS: L = 10 cm, YMC ODS; YL: L = 25 cm, YMC ODS; VS1: L = 10 cm, Vydac ODS; VS2: L = 10 cm, Vydac ODS; VL1: L = 25 cm, Vydac ODS; VL2: L = 25 cm; Vydac ODS.

is the apparent plate number of an infinitely efficient column at finite concentration, resulting from the non-linear behavior of the isotherm. N_{th} can be derived from the band profile calculated in ideal chromatography [2]. It is given by

$$N_{th} = 5.54 \cdot \frac{(2 - L_f^{1/2})^4}{(4L_f^{1/2} - L_f)^2} \cdot \left[1 + \frac{t_p + t_0}{k_0' t_0} \cdot \frac{1}{(1 - L_f^{1/2})^2}\right]^2 \quad (6)$$

where t_p is the duration of the injection, k_0' is the limit retention factor of the component (or retention factor at infinite dilution) and L_f its loading factor, defined as the ratio of the amount of component injected to the column saturation capacity for that component:

$$L_f = \frac{n}{q_S} = \frac{nb}{SLk'} \quad (7)$$

where n is the amount of component injected, S and L are the column geometrical cross-section area and length, respectively, and b is the second coefficient of the Langmuir equation. The loading factor as defined above is meaningless for an isotherm which has no horizontal asymptote.

The dependence of the apparent column efficiency on the sample size has been discussed previously, using the theoretical approach outlined above [2,6,7] or a more empirical method [8,9]. Lucy and Carr [7] have shown that, in spite of some fundamental reservations [10], the method gives correct results at moderate and high loading factors, a result also in agreement with experimental determinations [6].

3. Experimental

The same equipment (Perkin-Elmer, Norwalk, CT, USA), the same columns, the same chemicals and the same procedures were used in this work as in the work described in the companion paper [1], except that column efficiencies were also measured for *m*-cresol, 99%, liquid (Aldrich, Milwaukee, WI, USA), formula weight (FW) 108.14 [CAS Ref. No. 108-39-4], catalog No. C8,572-7. Solutions of *m*-cresol with concentrations between 172.5 and 4.22 mg/ml were prepared.

3.1. Measurement of the column efficiency

To determine the efficiency under linear conditions, the retention times and bandwidths at half height were measured as a function of the flow velocity for the four components using the most dilute solutions prepared, to avoid column overloading. The choice of measuring the band width at half height rather than at the baseline or

any other fractional height is arbitrary. From previous, independent studies [11], however, the width at half height seems to afford the most precise measurement of the column bandwidth. It is also readily amenable to automatic determination using a simple calculation procedure.

At each flow-rate, a 0.010-ml (for 10 cm long columns) or a 0.020-ml (for 25 cm long columns) sample was injected. The calibration curves reported independently [1] were used. Apparent efficiencies under overloaded conditions were determined following the same procedure, but using larger volume loops and more concentrated solutions, as needed.

The retention data under linear conditions are listed in Table 1. The other column characteristics are reported in the companion paper [1], Table 1.

3.2. Numerical treatment of the data

The determination of the column efficiency from recorded experimental band profiles requires the measurement of the retention time and the bandwidth at half height (Eq. 1). To reduce the contribution of the experimental errors and particularly that of the signal noise and of a non-linear detector response, the following procedure was used. First, the chromatograms [1] were transformed from records of the detector output (i.e., electrical voltage) versus the running time into plots of component concentration in the mobile phase, C, versus time t. Second, the data points in the following three groups were extracted into separate files.

Group I contains all the data points ranging between 90 and 100% of the peak maximum and will be processed to derive the retention time of the peak and its height. Groups II and III contain the data points ranging between 45 and 55% of the peak maximum, with the signal increasing or decreasing with increasing time, respectively. They will be processed together to derive the bandwidth at half height.

The data points of the first group are fitted to a parabolic model

$$C = a_2 t^2 + a_1 t + a_0 \quad (8)$$

Table 2
Parameters used in the Wilke–Chang equation

	Compounds			
	MC	DMP	PP	MB
M_A (g/mol)	108.1	136.2	122.2	136.1
d_A (g/ml)	1.034	1.001	1.025	1.094
V_A (ml/mol)	104.6	136.1	119.2	124.5
$D_m \times 10^6$	6.06	5.17	5.60	5.46

For compound abbreviations, see Table 1.

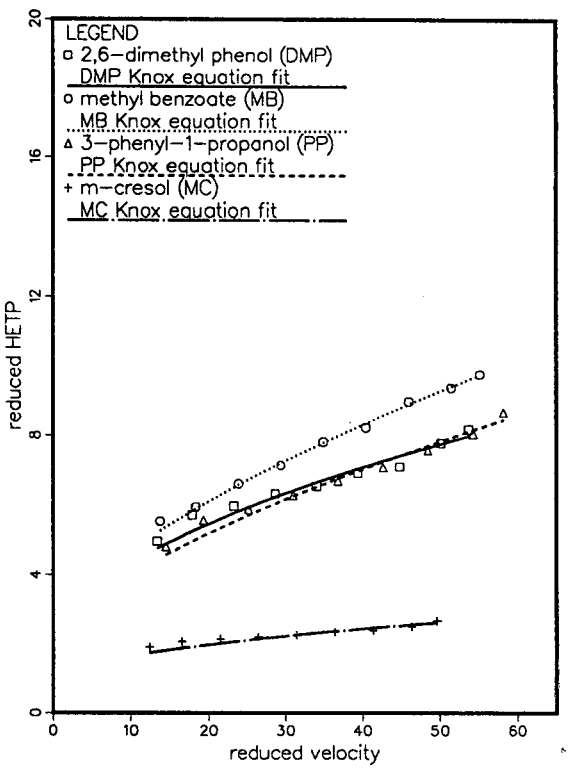

Fig. 1. Comparison between the experimental data for the column efficiency (symbols) and the best fit to the Knox equation (lines). Column YS (L = 10 cm, YMC ODS).

Table 3
Calculated coefficients for the Knox equation

Sample	Coefficient	Columns					
		YS	YL	VS1	VS2	VL1	VL2
MC	*a*	0.71	1.80	0.81	0.45	1.87	1.88
	c	0.000	0.000	0.006	0.099	0.003	0.000
DMP	*a*	1.60	2.88	2.88	1.94	2.85	2.55
	c	0.038	0.000	0.002	0.029	0.059	0.012
PP	*a*	1.85	3.18	2.70	2.11	3.56	2.82
	c	0.018	0.000	0.015	0.008	0.012	0.000
MB	*a*	1.89	2.50	2.03	2.48	2.43	2.17
	c	0.045	0.078	0.035	0.000	0.018	0.030

For columns and compound abbreviations, see Table 1.

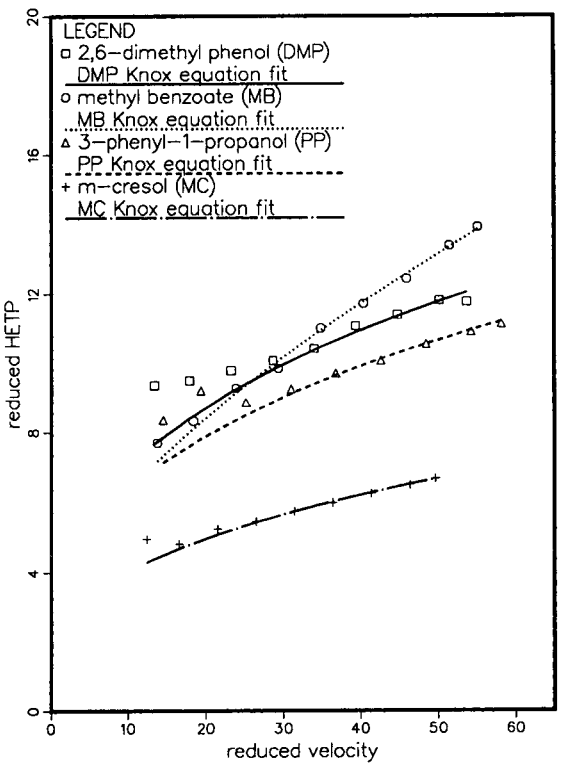

Fig. 2. Same as Fig. 1, but column YL ($L = 25$ cm, YMC ODS).

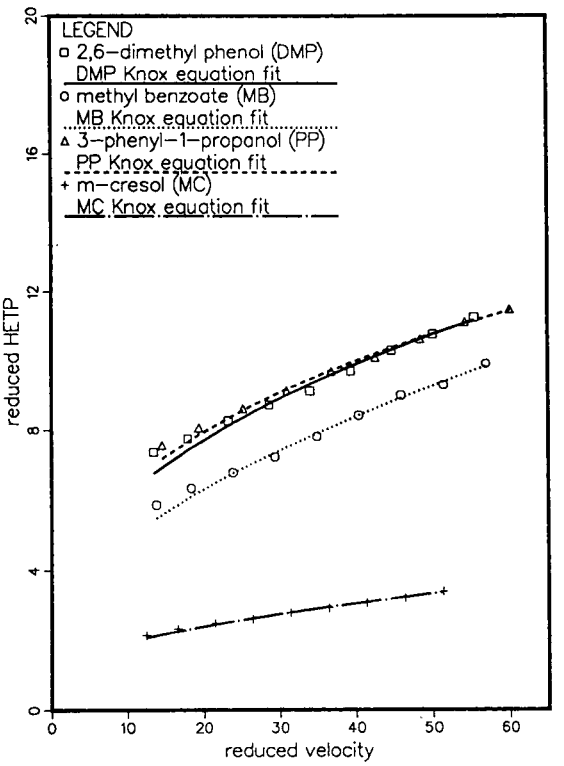

Fig. 3. Same as Fig. 1, but column VS1 ($L = 10$ cm, Vydac ODS).

using a least-square method. From the best coefficients a_2, a_1 and a_0 the coordinates of the peak maximum, hence the retention time, t_R and the maximum concentration of the peak, C_M, are calculated.

The data points of each of the other two groups are fitted to a linear equation

$$C = b_1 t + b_0 \tag{9}$$

Using the best values of the coefficients b_1 and b_0, the times corresponding to the elution of the concentration $C_M/2$ on each side of the band are determined by interpolation. This gives the bandwidth at half height.

This procedure of data smoothing is carried out entirely by software which eliminates human judgment and errors and ensures the maximum reproducibility.

3.3. Determination of the reduced velocity

Finally, the mobile phase flow velocity was measured as $u = L/t_0$, with L = column length and t_0 = retention time of uracil. For all compounds, this velocity is converted into a reduced velocity, using Eq. 3, with the known particle size (10 μm) and the diffusion coefficients derived from the classical Wilke and Chang equation [12]

$$D_{A,B} = 7.4 \cdot 10^{-8} \cdot \frac{\sqrt{\psi_B M_B} T}{\eta_B V_A^{0.6}} \tag{10}$$

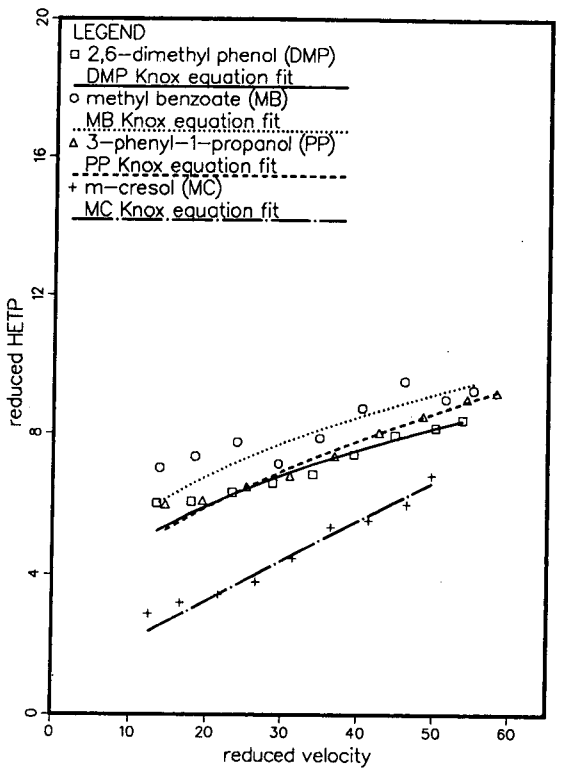

Fig. 4. Same as Fig. 1, but column VS2 (L = 10 cm, Vydac ODS).

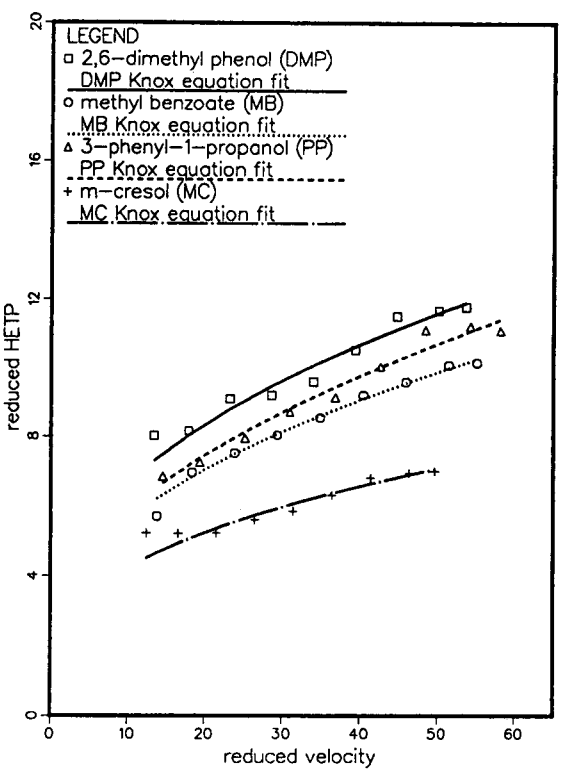

Fig. 5. Same as Fig. 1, but column VL1 (L = 25 cm, Vydac ODS).

where ψ_B is an association constant for the solvent, M_B is the molecular mass of the solvent (g/mol), η_B its viscosity (cP), V_A the molar volume (ml/mol) of the liquid solute at its normal boiling point, and T the absolute temperature (K). Recommended ψ_B values are 1.9 for methanol and 2.6 for water [12]. The value for V_A can be calculated from group contributions [13,14]. Since the solvent used is a solution of methanol–water (40:60) ($M_{methanol} = 32.04$ g/mol, $M_{water} = 18.00$ g/mol), the value of $\psi_B M_B$ was taken as the weighed average, i.e.

$$\psi_B M_B = 60\% \psi_{water} M_{water} + 40\% \psi_{methanol} M_{methanol} = 52.4304 \quad (11)$$

Temperature T was taken as 298.13 K and the solvent viscosity 1.62 cP [2]. The value of V_A for each compound studied was taken as the quotient of that molecular mass M_A divided by its density d_A. The data used are summarized in Table 2.

3.4. Representation of the efficiency data

The values of the reduced efficiency and reduced velocity are fitted to the Knox equation [3] using a linear regression and setting $b = 1.5$ for the lack of data at low values of the reduced efficiency. In a few instances, this procedure leads to negative values of c, in which case c was set to 0 and the procedure repeated for the determination of a. The coefficients obtained are reported in Table 3 and used to draw the lines in the figures.

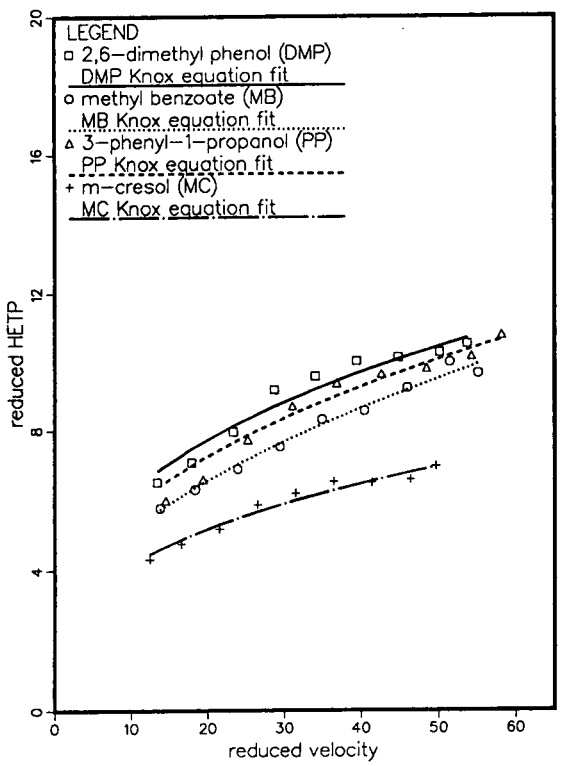

Fig. 6. Same as Fig. 1, but column VL2 ($L = 25$ cm, Vydac ODS).

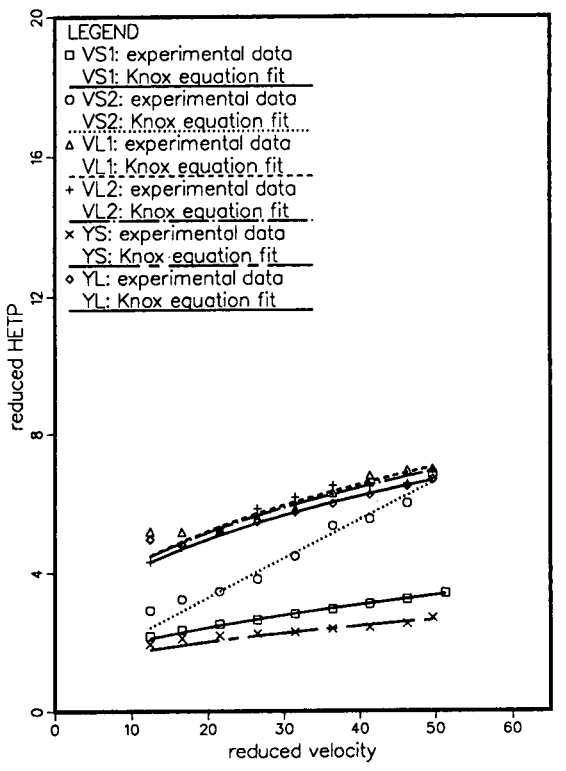

Fig. 7. Comparison between the experimental data for column efficiency (symbols) and the best fit to the Knox equation (lines). Data for *m*-cresol.

4. Results and discussion

4.1. Effect of the mobile phase flow-rate on the column efficiency

The experimental results are shown in Figs. 1–6 (symbols) as plots of the reduced HETP versus the reduced velocity for the six columns studied. No data were collected in the velocity range where axial dispersion controls the band width because this effect is well known. We are mainly interested in the mass-transfer resistances which constitute the main contribution to band broadening at the high flow velocities at which preparative columns must be operated. So no minima are observed on the curves. In all cases, the reduced efficiency increases with increasing reduced velocity in a manner consistent with the Knox equation (Eq. 4). As expected, there is a good agreement between the experimental data points (symbols) and the curves derived from the best coefficients obtained by fitting these results to the Knox equation (Table 3).

Two different trends are observed when comparing the data in Tables 1 and 3 and in Figs. 1–6. For the three components (*m*-cresol, 3-phenyl-1-propanol and 2,6-dimethylphenol) whose adsorption follows Langmuir behavior, the reduced plate height increases with increasing capacity factor k', leveling at high values: on any given column, there is little difference between the efficiencies for 3-phenyl-1-propanol and 2,6-dimethylphenol. On the other hand, the column efficiency for methyl benzoate does not seem to depend on its retention factor.

The reproducibility of efficiency data on any single column is excellent. For example, based on six measurements done with *m*-cresol, the

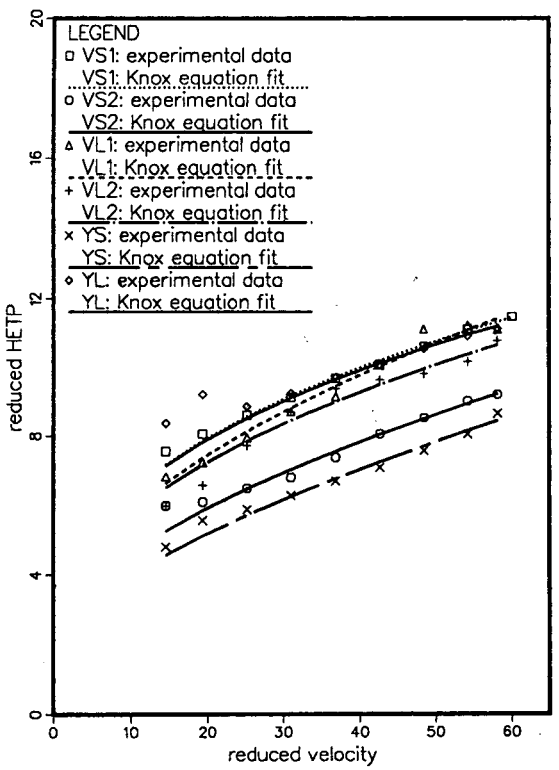

Fig. 8. Same as Fig. 7, except data for 3-phenyl-1-propanol.

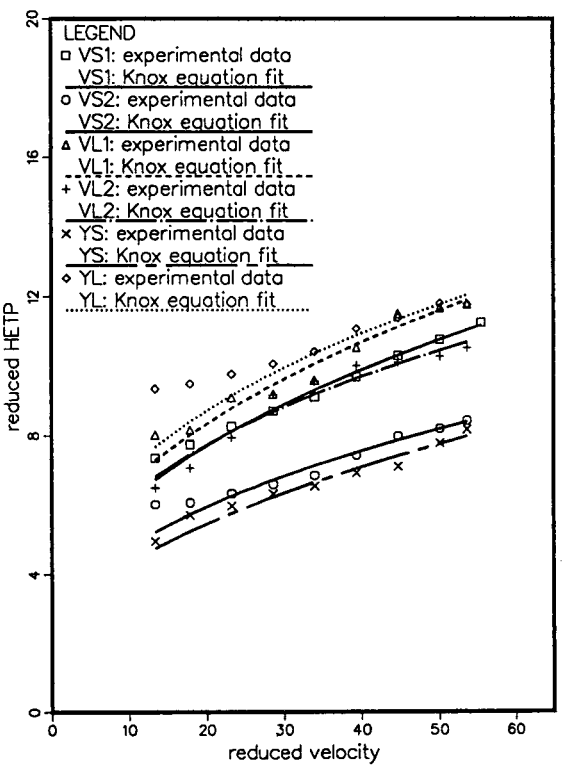

Fig. 9. Same as Fig. 7, except data for 2,6-dimethylphenol.

relative standard deviation (R.S.D.) on the HETP is 1%. This is in large part because of the rigorous procedure adopted for the determination of the width at half height (R.S.D. of $W_{0.5}$, 0.4%), the column-to-column reproducibility is not necessarily so and deserves a more detailed study. While Figs. 1–6 showed the efficiency data obtained on each column and revealed interesting trends regarding the dependence of the efficiency on the retention factor, Figs. 7–10 show the same data for each component and permit a comparison of the performance of the different columns.

The data in Table 3 confirm that the Knox equation (Eq. 4) is an empirical correlation, not the mathematical expression of a rigorous model based on first principles. This is clear from the origin of this equation [2] and was explained by Done et al. [3]. The constant a characterizes eddy diffusion and the lack of homogeneity of the packing. On this basis, the values of a on a given column, for compounds which have very similar diffusivities (Table 2) are expected to be very close. As seen in Table 3, they are not but, depending on the column, vary as 1 to 1.5 (VL2) or 1 to 5 (VS2). Similarly, c characterizes the mass-transfer kinetics through the particles. The values of c for a given compound should be the same on a given packing material since column-to-column variations in the packing density should not affect mass transfer inside particles. Nevertheless, c varies from column to column for a given component.

The general conclusion is that the data obtained with a given stationary phase are poorly

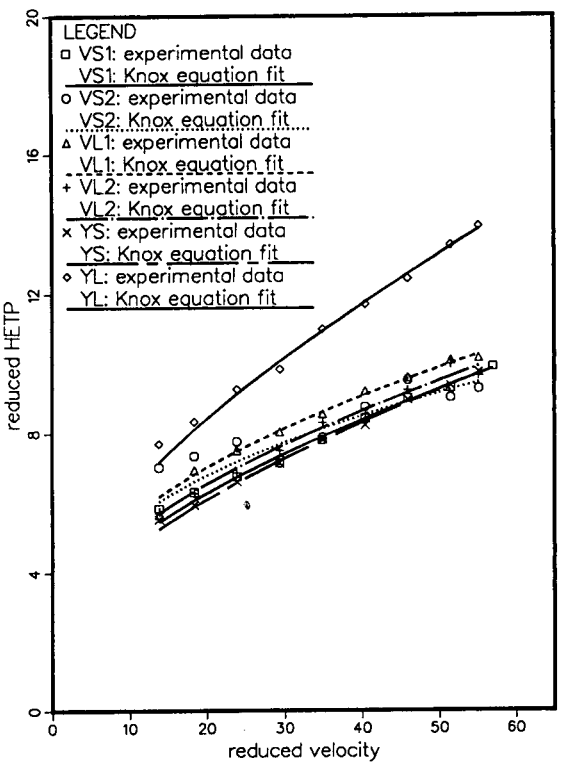

Fig. 10. Same as Fig. 7, except data for methyl benzoate.

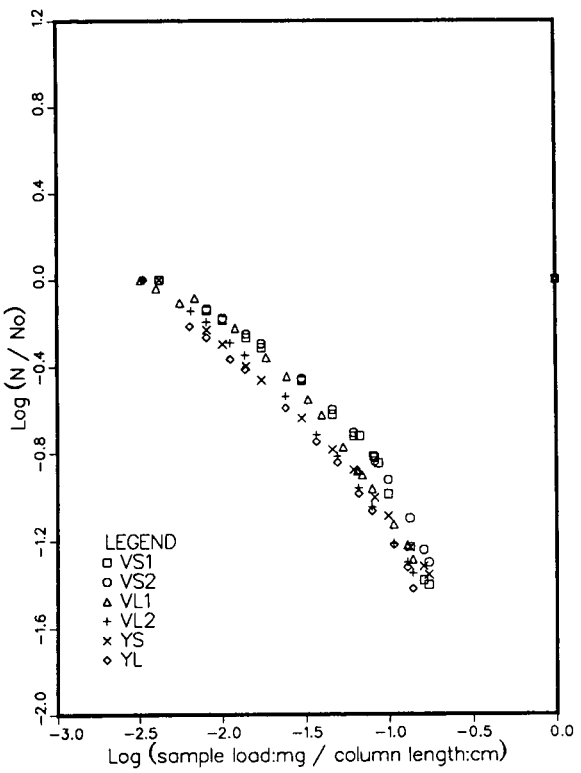

Fig. 11. Plot of the logarithm of the ratio of the apparent column efficiency (N) and the column efficiency at zero-sample size (N_0) vs. the logarithm of the ratio of the injected sample (mg) and the column length (cm) for m-cresol.

reproducible from column to column, which is most probably related to the packing procedure employed and must be correlated with the fluctuations of the packing density previously reported. The scattering of the curves obtained does not seem to depend on the nature of the packing material used. However, it seems that the short columns (10 cm long) tend to have lower reduced plate heights than the long ones (25 cm long) for all the compounds studied, effectively pointing to a packing problem. It should not be concluded hastily, however, that a low packing density should be preferred. First, the experimental results presented here are insufficient to warrant a strong correlation between column efficiency and packing density. Second, there are some serious doubts regarding the long-term stability of columns which have a low packing density. Under the influence of a constant stream of eluent, slow consolidation of the packing is bound to take place.

4.2. Apparent column efficiency and sample size

The apparent column efficiency was measured as a function of the amount of sample injected at a constant flow-rate of 1.0 ml/min. The data are plotted (Figs. 11–14) in logarithmic coordinates. In order to eliminate the trivial effect of the column length, the logarithm of the ratio of the column efficiency to its limit efficiency at zero sample size is plotted versus the logarithm of the ratio of the sample size to the column length. The logarithm of the loading factor would be more appropriate for compounds with a Langmuir adsorption isotherm, but there is no saturation capacity for an anti-Langmuir isotherm.

The behavior of the components whose adsorption follows a Langmuirian isotherm (Figs. 11–13) is strikingly different from that of methyl benzoate (Fig. 14) which has an anti-Langmuirian isotherm. For the first three compounds, the column efficiency decreases monotonically

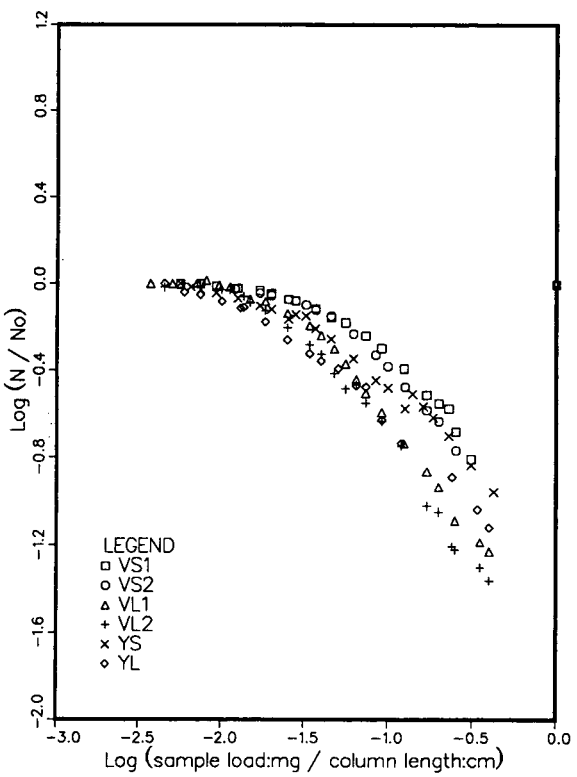

Fig. 12. Same as Fig. 11, except 3-phenyl-1-propanol.

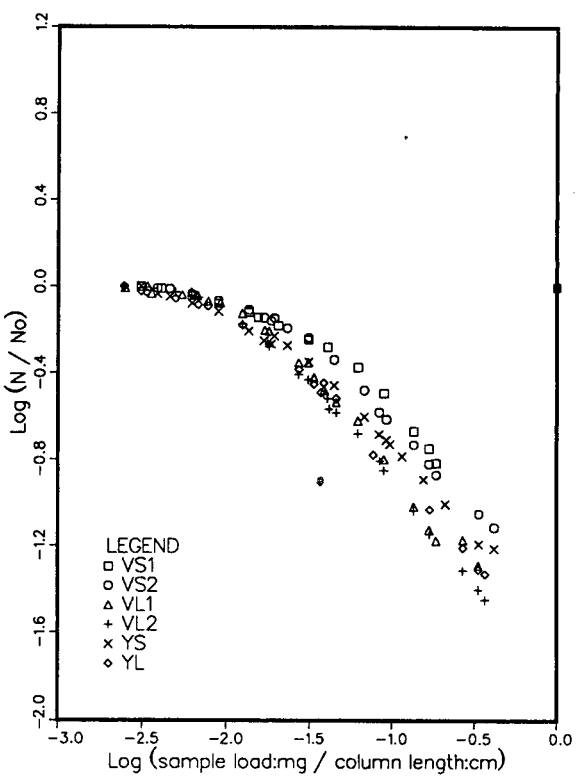

Fig. 13. Same as Fig. 11, except 2,6-dimethylphenol.

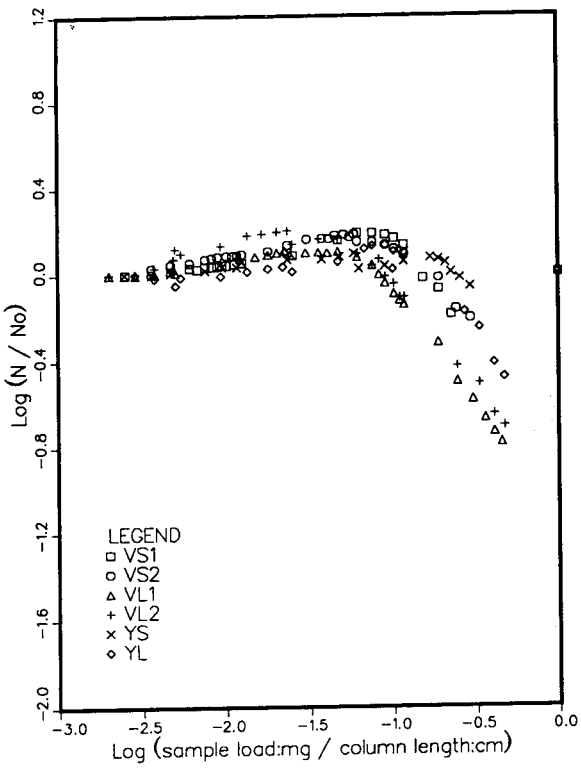

Fig. 14. Same as Fig. 11, except methyl benzoate.

with increasing sample amount. For the last one, the efficiency begins to increase at low sample sizes and goes through a maximum. This anomalous behavior is explained by the initial increase in the retention time of methyl benzoate when the sample amount is increased. Note that for *m*-cresol it was not possible to make a precise measurement of the column efficiency at a sample size small enough to ensure linear behavior of the retention mechanism.

Using the model of Knox and Pyper [5] described in the Theory section and the band profile given by the ideal model, it is possible to account simply for these results in the case of the compounds whose adsorption behavior follows the Langmuir model [5,6]. Because the width of a Gaussian profile and that of an ideal model profiles are related to the fractional height in a different way, different equations must be used, depending on which fractional height is used. The width at half height can be measured with better accuracy and precision than the baseline width and has been used here. Golshan-Shirazi and Guiochon [6] have shown that, in the case of a component following the Langmuir adsorption model, the thermodynamic contribution to the column efficiency is given by Eq. 6. When the loading factor is moderate, this equation can be simplified and becomes

$$N_{th} = \frac{5.54}{L_f} \cdot \left[\frac{1+k'_0}{k'_0}\right]^2 \cdot \left[1 + \left(2.5 - \frac{4k'_0}{1+k'_0}\right) \cdot \sqrt{L_f}\right] \quad (12)$$

In Figs. 15 and 16 the experimental results (symbols) obtained with the different columns

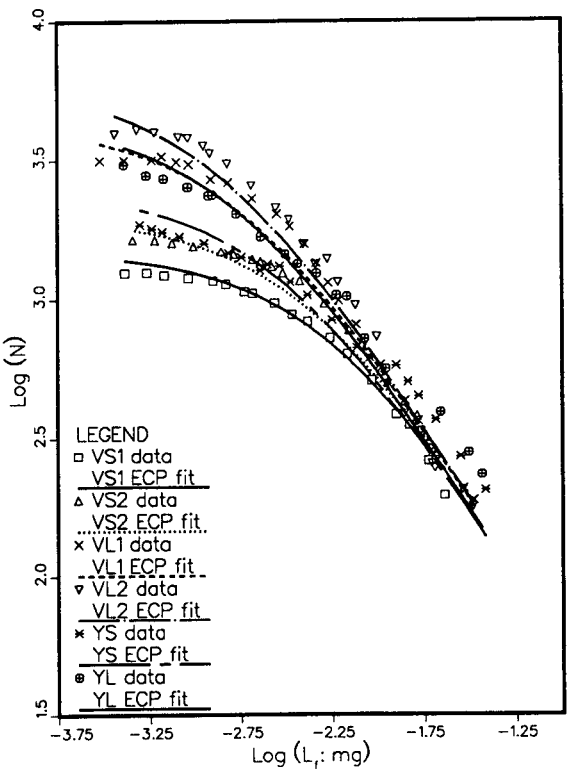

Fig. 15. Comparison between experimental results and theoretical dependence of the column efficiency on the sample size. 3-Phenyl-1-propanol.

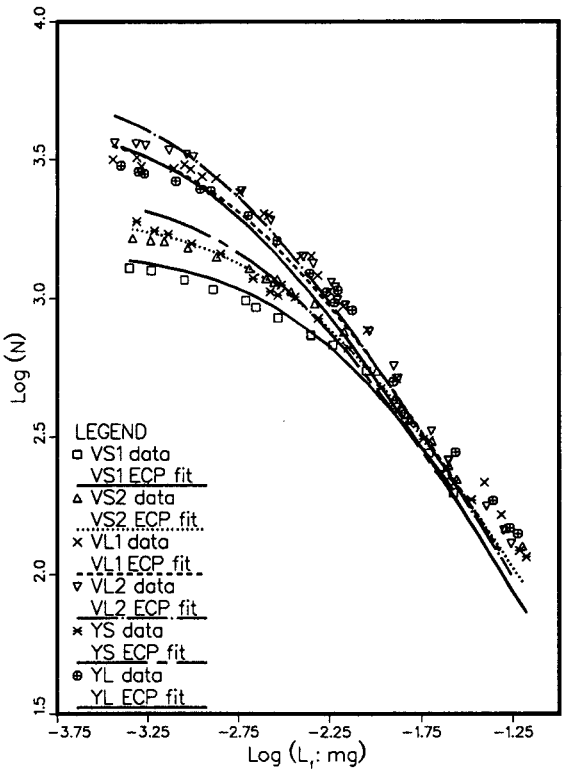

Fig. 16. Same as Fig. 15, except 2,6-dimethylphenol.

for 3-phenyl-1-propanol and 2,6-dimethylphenol have been replotted as log N versus log L_f, using the equilibrium isotherm data determined in the companion paper to calculate L_f. The values calculated from Eq. 12 are also given (lines). There is an excellent general agreement between the theoretical prediction and the experimental results. The deviations observed at high values of the loading factor are due to inaccuracies in the estimate of the width of the injection (i.e., of t_p in Eq. 6), which is neglected in Eq. 12, although it becomes significant for large sample sizes.

Acknowledgements

We acknowledge the gift of samples of stationary phases by YMC and Vydac. This work was supported in part by grant CHE-9201663 from the National Science Foundation and by the cooperative agreement between the University of Tennessee and the Oak Ridge National Laboratory. We acknowledge support of our computational effort by the University of Tennessee Computing Center.

References

[1] H. Guan and G. Guiochon, *J. Chromatogr. A*, 687 (1994) 179.
[2] G. Guiochon, S. Golshan-Shirazi and A.M. Katti, *Fundamentals of Preparative and Nonlinear Chromatography*, Academic Press, Boston, MA, 1994.
[3] J.N. Done, G.J. Kennedy and J.H. Knox, in E.S. Perry (Editor), *Gas Chromatography 1972*, Applied Science, London, 1973, p. 145.
[4] J.C. Giddings, *J. Chromatogr.*, 13 (1964) 301.
[5] J.H. Knox and H.M. Pyper, *J. Chromatogr.*, 363 (1986) 1.
[6] S. Golshan-Shirazi and G. Guiochon, *Anal. Chem.*, 60 (1988) 2364.
[7] C.A. Lucy and P.W. Carr, *J. Chromatogr.*, 556 (1991) 159.
[8] H. Colin, *Sep. Sci. Technol.*, 22 (1987) 1953.
[9] N.T. Miller, *J. Chromatogr.*, 550 (1991) 301.
[10] E.V. Dose and G. Guiochon, *Anal. Chem.*, 62 (1990) 1723.
[11] D.L. Ball, W.E. Harris and H.W. Habgood, *J. Gas Chromatogr.* 5 (1966) 613.
[12] C.R. Wilke and P. Chang, *AIChE J.*, 1 (1955) 264.
[13] R.C. Reid, J.M. Prausnitz and B.E. Poling, *The Properties of Gases and Liquids*, McGraw-Hill, New York, 4th ed., 1987.
[14] A.L. Hines and R.N. Maddox, *Mass Transfer: Fundamentals and Applications*, Prentice-Hall, Englewood Cliffs, NJ, 1985.

ELSEVIER

Journal of Chromatography A, 687 (1994) 213–221

JOURNAL OF CHROMATOGRAPHY A

Patching in reversed-phase high-performance liquid chromatographic materials studied by solid-state NMR spectrometry

Harry A.M. Verhulst[a], Leo J.M. van de Ven[a], Jan W. de Haan[a,*], Henk A. Claessens[a], Friedhelm Eisenbeiss[b], Carel A. Cramers[a]

[a]*Laboratory of Instrumental Analysis, Eindhoven University of Technology, P.O. Box 513, 5600 MB Eindhoven, Netherlands*
[b]*E. Merck, Darmstadt, Germany*

First received 10 February 1994; revised manuscript received 22 August 1994

Abstract

The distribution of silane chains over the silica gel surface in reversed-phase high-performance liquid chromatographic (RP-HPLC) phases was investigated with special attention being paid to surface homogeneity: there might be areas with high coverage and areas with low coverage of silane chains, hence clustering or patching of the silane chains can occur. Two RP phases were studied before and after well conditioned ageing, together with four silylated silica gels, serving as models. Two solid-state NMR techniques, namely ^{1}H–^{29}Si dipolar dephasing ^{29}Si cross-polarization magic angle spinning NMR and ^{13}C spin–lattice relaxation in the rotating frame, were used. For the four model compounds with varying degrees of coverage only differences in the NMR time constants were observed between the maximally covered phase and the three less densely covered silica gels. This proves that silane chains on an RP phase with maximum coverage are restricted in their mobilities with respect to the less densely packed materials. For the two non-aged RP phases the silane chains are probably homogeneously distributed over the silica gel surface. Further, the non-aged RP phases were compared with their counterparts, aged under well defined experimental conditions. After ageing, no differences were found between the original and the aged phases, now indicating however, that patching had developed upon ageing.

1. Introduction

Nowadays over 75% of all high-performance liquid chromatographic (HPLC) separations are carried out using reversed-phase (RP)-type stationary materials [1]. The reasons for this widespread use are the great variety of RP phases [2–4], the large number of possibilities of influencing the chromatographic separation by influencing the composition of the mobile phase [5] and the fast equilibrium of the phase system [6].

The production process for these phases, however, is not always very reproducible, i.e., even nominally identical RP materials from the same manufacturer may show batch-to-batch variations [7,8]. Moreover, the practical use of RP-HPLC phases is limited to only mild acidic or

* Corresponding author.

0021-9673/94/$07.00
SSDI 0021-9673(94)00808-6

basic conditions (pH 4–7). Under more severe conditions (pH < 3), needed, for example, in the separation of basic compounds, the chromatographic performance decreases dramatically in a short time [9]. This decrease in chromatographic performance is seen as a decrease in the capacity factor (k') and plate number and a deteriorated peak shape.

For the future development of RP materials of more constant quality and with better chemical stability, a thorough knowledge of the properties of the RP materials and of the supporting silica gels is needed. Also, a detailed study of the changes in RP materials during usage (ageing) is required [10].

In our laboratory, the study of artificial ageing of RP columns under well defined experimental conditions began some time ago. Hetem [11] studied the influence of chain length and type of anchoring (mono-, bi- or tridentate) of the silane groups on the stability of the RP materials towards these ageing conditions. Other investigations, concerning the influence of the pretreatment of the support silica gel (e.g., hydrothermal, acid) on the chromatographic performance of the corresponding RP columns have been reported [12–14].

Recently, several papers have appeared dealing with the question of whether the distribution of the silane chains over the silica gel surface in RP-HPLC materials is homogeneous [15,16]. One can imagine areas with a high coverage of silane chains as opposed to areas with low coverage. Conceivably, some forms of clustering (i.e., patching) might exist. Surface inhomogeneity of stationary phases will exert a negative influence on the chromatographic behaviour in many cases [13]. Hence investigations on whether this patching occurs in RP-HPLC materials are desirable.

Several routes leading to the formation of surface inhomogeneities (patching) in RP materials, before or after ageing, are conceivable. These routes are illustrated in Fig. 1 (routes I–VI) and explained in the Results and Discussion section. In HPLC practice, most RP separations are carried out using fully silylated silica gels. Therefore, in this paper only completely silylated silica gels are considered as genuine RP-HPLC stationary phases.

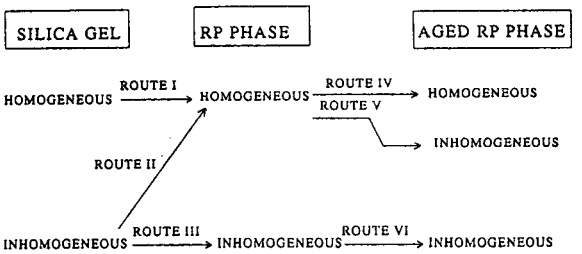

Fig. 1. The six different routes, possibly leading to patching in RP materials (aged and non-aged). For the explanation of this scheme, see Results and discussion.

Conventional characterization methods and calculations involve bulk properties and thus only give an average measure of surface coverage. These approaches are not able to give the extent of patching on a molecular level. Very recently, multiple quantum (MQ) NMR was used to study the extent of clustering of some RP materials [17]. However, no patching could be shown in the investigated RP materials.

Two solid-state NMR techniques, namely ^{1}H–^{29}Si dipolar dephasing ^{29}Si cross-polarization (CP) magic angle spinning (MAS) NMR [18–20] and ^{13}C spin–lattice relaxation measurements in the rotating frame [$T_{1\rho}$ (^{13}C)] [19,21–23], commonly used in mobility studies of polymers, are in principle also useful in order to study patching.

In dipolar dephasing experiments, the decrease of the X signal (in this case ^{29}Si) is, in principle, caused by dipolar interactions between protons and X nuclei. The dipolar interaction is a function of the distance [$\propto 1/(\text{distance})^3$] between the nuclei and of mobility (large mobilities diminish the efficiency of the ^{1}H–^{29}Si dipolar interactions in causing the ^{29}Si NMR signal to decay). The rate of decrease of the X signal depends on the distance to the nearest protons and the mobility of the X–H vector (100–1000 Hz range). The dipolar dephasing technique was first used to distinguish protonated from non-protonated carbons [24–26]. Dipolar dephasing

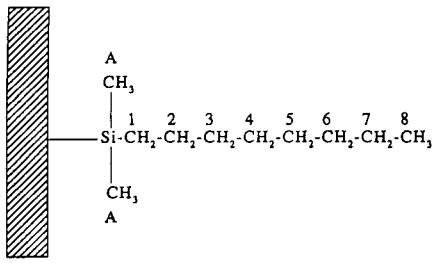

Fig. 2. Structure of the monofunctionally dimethyloctyl RP phases used in this study. The carbon atoms are numbered and this notation will be used throughout the text.

was also used to discriminate crystalline from amorphous regions in polymers [27].

The $T_{1\rho}$ (^{13}C) relaxation time yields information about mobilities in the mid-kilohertz range (10–100 kHz). In many rigid systems (e.g., polymers), both spin–lattice and spin–spin processes contribute to the $T_{1\rho}$ (^{13}C) parameter [22]. In this study, the mobilities of the silane chains are very rapid in comparison with many chain motions in polymer samples, so major contributions from spin–spin interactions are not expected. Many papers have appeared using $T_{1\rho}$ (^{13}C) in the study of mobilities of different alkyl groups in various compounds [28].

In the present study, four monofunctionally derivatized dimethyloctylsilica gels, Zorbax materials RX-1–RX-4 (see Fig. 2), with different coverages, including a sample with maximum coverage, were investigated with the two NMR techniques. These materials serve as models for the RP phases. The non-aged RP phases (M-1 and M-2) were compared with their counterparts, aged under well defined experimental conditions (M-1A and M-2A). These phases are based on a different support silica gel.

2. Experimental

2.1. Materials

Four monofunctionally derivatized dimethyloctylsilane materials with different degrees of coverage (Zorbax materials) were a gift from Rockland Technologies (Newport, DE, USA). For the ageing, two special dimethyloctylsilane research phases were compared with the same phases aged under well defined experimental conditions (0.05 *M* phosphate buffer of pH 2.2 for 10 days) [11]. These two phases (non-aged) were specially prepared by the Research and Development Laboratory of E. Merck (Darmstadt, Germany). Table 1 summarizes the ligand densities (μmol/m^2) for all non-aged materials as specified by the manufacturers. Subsequently in this paper, these RP phases will be coded as in Table 1. All samples were dried in vacuum at 110°C for 6 h prior to NMR analysis.

2.2. NMR measurements

^{13}C and ^{29}Si CP-MAS-NMR

Solid-state ^{13}C and ^{29}Si NMR measurements were carried out on a Bruker MSL 400 Fourier transform NMR spectrometer at 100.58 and 79.46 MHz, respectively. Samples of 200–250 mg were measured in 7 mm O.D. rotors made of ZrO_2 of the Bruker double-bearing type. Air (dew point −70°C) was used as the bearing and driving gas. Rotors and caps provided a reasonable seal against air moisture (checked with highly hygroscopic samples). The proton 90° pulse length was 6.6 μs and the repetition time 4 s. CP was used with spin temperature inversion [29] and a contact time of 5 ms for ^{13}C and 6 ms for ^{29}Si. The Hartmann–Hahn condition for CP was adjusted by varying the radio frequency (RF) power and maximizing the CP-MAS sig-

Table 1
Ligand densities (μmol/m^2) for the non-aged materials

Notation	Ligand density (μmol/m^2)
RX-1	1.14
RX-2	1.83
RX-3	2.18
RX-4	3.65
M-1	3.39
M-2	2.61

nal for known samples $\{Q_8M_8 = Si_8O_{12}[OSi(CH_3)_3]_8$ for ^{29}Si and adamantane for $^{13}C\}$ at their optimum contact times. The MAS spinning rates were 2.0 and 2.5 kHz for ^{29}Si and ^{13}C, respectively; 2000 free induction decays with an acquisition time of 25 ms were accumulated in 1024 data points. During acquisition ^1H decoupling was carried out.

^1H–^{29}Si dipolar dephasing ^{29}Si CP-MAS-NMR

The pulse sequence used is the modification by Bodenhausen et al. [29]. The CP part of this sequence used the same parameters as given above. Typically, 2000 free induction decays with 22 different values of the dephasing delay τ between 4 μs and 4 ms were accumulated. To eliminate long-term experimental artifacts, block averaging was used to spread out over time the individual measurements. All dipolar dephasing data were analysed using a combined Gaussian–Lorentzian decay, given by the equation

$$I(T_{dd}) = I_G e^{-0.5(T_{dd}/T_G)^2} + I_L e^{(-T_{dd}/T_L)} \quad (1)$$

where $I(T_{dd})$ is the intensity of the X signal after a dephasing time T_{dd}, I_G and I_L are the weighting factors for the Gaussian and Lorentzian parts, respectively, and T_G and T_L are the time constants for the Gaussian and Lorentzian parts, respectively.

^{13}C $T_{1\rho}$ CP-MAS-NMR

For the CP part, see the parameters given in the section on ^{13}C CP-MAS-NMR. Typically, 1280 free induction decays with 15 different values of the spin-lock time τ between 0.6 μs and 300 ms were accumulated. To eliminate long-term experimental artifacts, block averaging was used to spread out over time the individual measurements. All $T_{1\rho}$ (^{13}C) data were analysed using a Lorentzian decay function.

For all measurements after applying a Lorentzian line broadening of 20 Hz, the 1024 data points were zero-filled to 8192 prior to Fourier transformation. All ^{13}C and ^{29}Si chemical shifts, in parts per million, are relative to liquid tetramethylsilane (Me_4Si), using adamantane and Q_8M_8, respectively as secondary external references.

3. Results and discussion

3.1. Zorbax (non-aged) materials

The ^{29}Si CP-MAS-NMR spectra for RX-1, RX-2, RX-3 and RX-4 (Table 1) are given in Fig. 3. These spectra show four signals: the silane groups M^1, the geminal silanediol groups Q^2, the silanol groups Q^3 and the siloxane groups Q^4 at +13, −91, −100 and −110 ppm, respectively [30]. From Fig. 3 the effect of a higher loading with silane chains (going from RX-1 to RX-4) is clearly visible: the intensities of the silane and siloxane signals increase, whereas those of the geminal silanediol and silanol signals decrease.

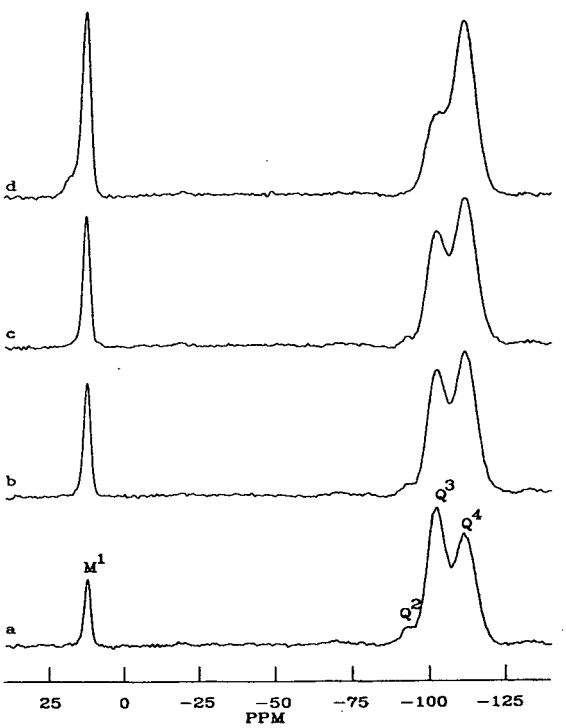

Fig. 3. ^{29}Si CP-MAS-NMR spectra (9.4 T) for the four Zorbax materials with the different degrees of coverage: (a) RX-1; (b) RX-2; (c) RX-3; (d) RX-4 (see Table 1).

3.2. ^{1}H-^{29}Si dipolar dephasing ^{29}Si CP-MAS-NMR

The ^{1}H–^{29}Si dipolar dephasing ^{29}Si CP-MAS-NMR spectra for RX-1 for four selected values of the dipolar dephasing time τ are given in Fig. 4. The intensities of all ^{29}Si NMR signals decrease with increasing τ, as expected from the theory [19]. The siloxane signal (Q^4) without protons dephases more slowly than the silanol signals (Q^3) with one closely attached hydroxyl proton. The signal of the silane groups (M^1) with an octyl group and two methyl groups bonded to the silicon nucleus dephases most quickly.

For all four Zorbax samples the intensity of the M^1 signal was measured as a function of the dipolar dephasing time τ and the data were analysed using Eq. 1.

For the Gaussian part (4–100 μs), the natural logarithm of the intensity of the M^1 signals was plotted versus the square of the dipolar dephasing time τ. These fits gave poor correlation coefficients, typically 0.95 for all four samples. An explanation of why the Gaussian part does not fit so well is probably that in the Gaussian part of the equation other effects such as the ^{1}H–^{1}H dipolar interactions and/or ^{29}Si chemical shift anisotropy also play an important role [18]. Therefore, these initial, fast Gaussian decays are not considered further. For the Lorentzian part (200 μs–4 ms), a plot of the natural logarithm of the intensity of the M^1 signals versus the dipolar dephasing time τ gave good correlation coefficients (typically >0.99). Fig. 5 gives a typical plot of the Lorentzian decay for RX-1. Now the question is which ^{1}H–^{29}Si dipolar interactions cause the Gaussian and the Lorentzian decay, respectively. Two assumptions were made: the Gaussian part (fast decay) is caused by the dipolar interactions between the silicon nuclei and the protons of the CH_2 group of the octyl chain (Fig. 2, carbon atom 1). These CH_2 groups will be less mobile than the methyl groups on the silicon atom (unhindered rotation around the threefold axis). The Lorentzian decay (slow decay) is caused by the dipolar interaction between the silicon nuclei and the protons of the two methyl groups bonded directly to these silicon nuclei (Fig. 2, carbon atoms A). To support this assumption a contact time of 15 ms was used instead of 6 ms for sample RX-4. A

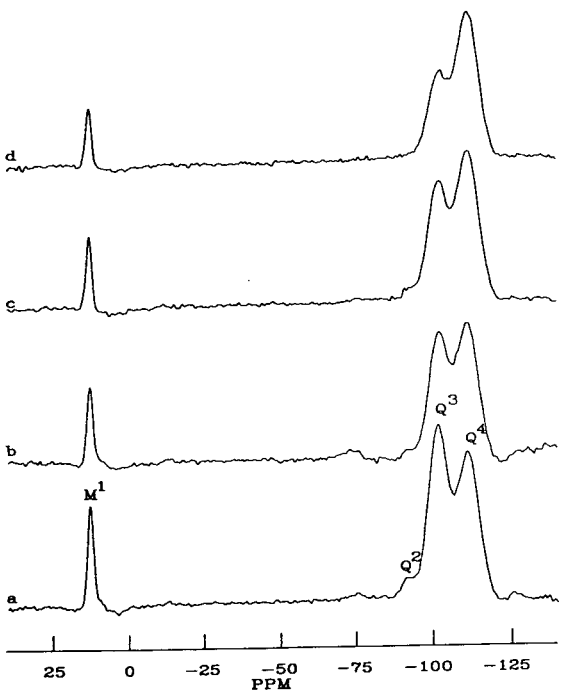

Fig. 4. ^{1}H–^{29}Si dipolar dephasing ^{29}Si CP-MAS-NMR spectra for RX-1 (see Table 1) for four selected dipolar dephasing times τ: (a) 4 μs; (b) 100 μs; (c) 500 μs; (d) 1 ms.

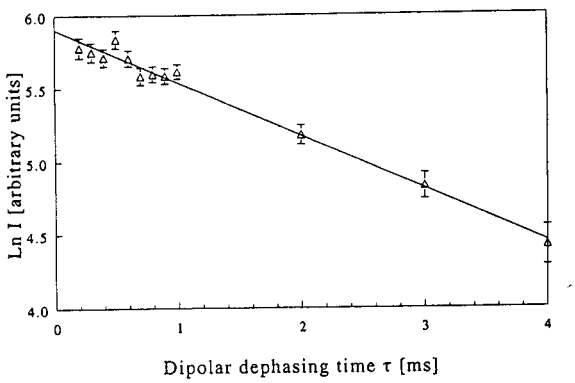

Fig. 5. Plot of the Lorentzian part of Eq. 1 for the sample RX-1, created by plotting the natural logarithm of the intensity of the M^1 signals versus the dipolar dephasing time τ. The uncertainties in the y values are given by error bars.

longer contact time yields a relatively larger contribution from the faster rotating methyl groups. This is due to the less efficient $^{1}H-^{29}Si$ cross-polarization, caused by smaller dipolar interactions with protons. A longer contact time should therefore decrease the Gaussian–Lorentzian ratio (I_G/I_L). This is indeed the case, as for a contact time of 15 ms this ratio is 0.50 compared with 0.80 for a contact time of 6 ms. Hence the assumptions made above are probably justified.

The Lorentzian time constants for the M^1 groups of the four Zorbax materials are summarized in Table 2. It is clear that the Lorentzian time constants are the same (within the accuracy limits) for RX-1, RX-2 and RX-3. Only the Lorentzian time constant of the maximally covered RP material RX-4 is clearly smaller. This is caused by a larger dipolar interaction, which is caused, in turn, by decreased mobilities of the methyl groups A (Fig. 2) as a consequence of steric hindrance in RX-4. It seems logical to assume that steric interactions between neighbouring chains are felt primarily by these methyl groups, protruding sidewards from the main chains. This means that close-packed silane chains can be distinguished from less densely packed silane chains.

For all four samples, only monoexponential Lorentzian decays were found, although extensive tests for biexponential behaviour were carried out. In all instances, either the time constants merge to a single value in the iteration process or the contribution of only one time constant in the plot is significant. This means that in each Zorbax material only one type of silane chain can be found, at least from the point of view of mobilities in the 100–1000 Hz range. The implications are discussed in Section 3.4 on aged phases.

Table 2
Lorentzian and $T_{1\rho}$ (^{13}C) time constants for the four Zorbax samples (RX-1–RX-4)

Notation	Lorentzian time constant[a] (ms) (±0.2)	$T_{1\rho}$ (^{13}C)[b] (ms) (±7)
RX-1	3.0	190
RX-2	3.0	185
RX-3	2.9	–[c]
RX-4	1.7	112

[a] For the silane groups (M^1).
[b] For the carbon atoms A (Fig. 2).
[c] Not determined.

3.3. ^{13}C spin–lattice relaxation in the rotating frame [$T_{1\rho}$ (^{13}C)]

Fig. 6 shows typically $T_{1\rho}$ (^{13}C) spectra for RX-1 for four selected values of the spin-lock time τ. The natural logarithm of the intensity of the carbon signals A (Fig. 2) plotted versus the spin-lock time τ gave correlation coefficients of typically 0.99 and higher for all four Zorbax samples. The corresponding fit for RX-1 is shown in Fig. 7. Table 2 gives the $T_{1\rho}$ (^{13}C) time constants of the carbon atoms A for the Zorbax materials. The $T_{1\rho}$ (^{13}C) time constants are identical, within the accuracy limits, for the two derivatized silica gels RX-1 and RX-2. The time constant for the maximally covered sample RX-4 is again different. Hence the $T_{1\rho}$ (^{13}C) measure-

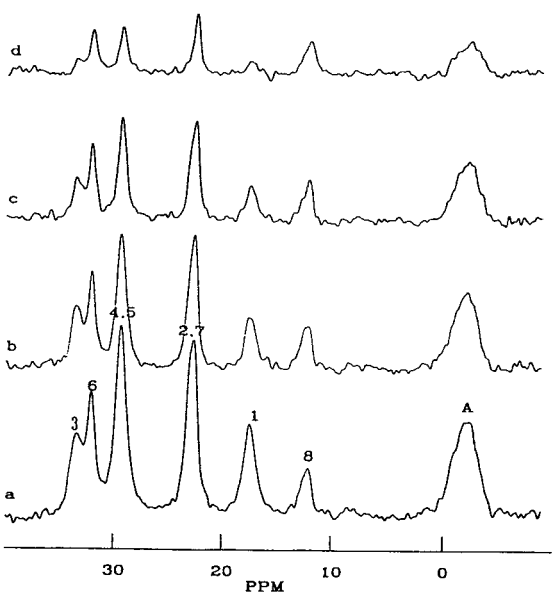

Fig. 6. $T_{1\rho}$ (^{13}C) NMR spectra for RX-1 for four selected values of the spin-lock time τ: (a) 0.6 μs; (b) 50 ms; (c) 100 ms; (d) 200 ms. For the numbering of the carbon atoms, see Fig. 2.

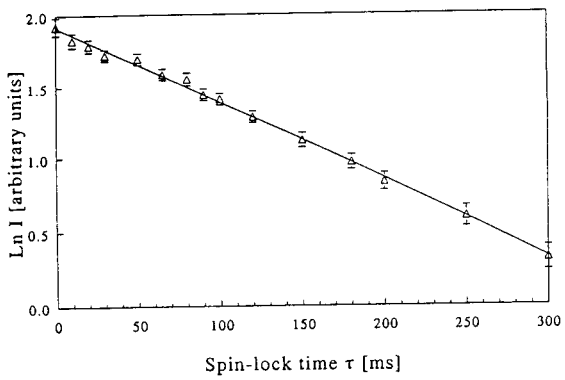

Fig. 7. Plot of the natural logarithm of the intensity of the carbon atoms A (see Fig. 2) versus the spin-lock time τ for sample RX-1. The uncertainties in the y values are given by error bars.

ments are in line with the $^{1}H-^{29}Si$ dipolar dephasing measurements, i.e. no multi-exponential behaviour can be found. However, the influence of the close packing on the mobilities can be seen clearly again.

3.4. Aged phases

The surface of the silica gel substrate can be either homogeneous or inhomogeneous with respect to the distribution of reactive silanol groups, which participate in reactions with functionalized silanes in the formation of an RP phase [31,32]. In the former instance, exhaustive silylation with a monofunctional silane should lead to a homogeneously covered surface for the RP phase. This is indicated as route I in Fig. 1. When such a material is subjected to ageing, probably a homogeneous situation will prevail after the process, albeit with changed loadings of silane chains (route IV). Theoretically, the process of ageing could also provoke local inhomogeneities during the initial stages, which would, in turn, cause the further desilanization to lead to an inhomogeneously covered, aged RP phase (route V).

An inhomogeneous silica gel will, in all probability, lead to an inhomogeneous RP phase, following route III. In that case, the aged phase will also be inhomogeneous (route VI). Only when silylation aptitudes for, e.g., two different sections of surface area are very similar would the resulting RP phase lost its inhomogeneity and again behave like a homogeneous material (route II). In the ageing procedure the resulting RP phase would behave like those described above (i.e., according to route IV or V). Note that inhomogeneities in aged phases do not necessarily imply inhomogeneities in the fresh RP phases.

Now the question arises of whether homogeneous and inhomogeneous RP phases, fresh or aged, can be distinguished by solid-state NMR. For simplicity's sake we describe an inhomogeneous phase as consisting of two types of surface (see Fig. 8). Following earlier descriptions of the silica gel surface [31], crystalline domains are embedded in a matrix of amorphous material (Fig. 8). The types of silane chains protruding from such a surface would be different with regard to packing densities and, hence, would probably possess different conformational equilibria and mobilities. In our view, we would expect a maximum of three different silane chains (see Fig. 8): attached to the crystalline domains (B), to the edges of the crystalline domains (C) and to the amorphous matrix (A).

Differences in conformational equilibria should be visible in the form of different chemical shifts in the ^{13}C NMR spectra. A difference of 20% in the *anti-gauche* equilibrium should lead to differences in shift order of the order of 1 ppm. As we do not observe such differences (spectra not shown), we conclude that the con-

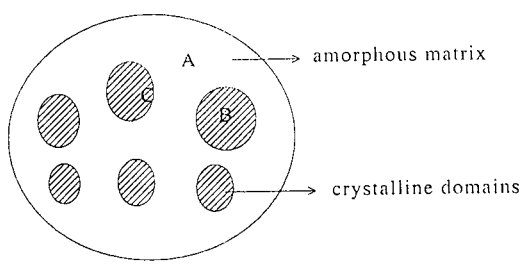

Fig. 8. The three different types of silane chains in a patched RP material: (A) silane chains in sparsely packed regions; (B) silane chains in densely packed regions; (C) see (B), near the edges of the patch.

formational equilibria of all chains in fresh and aged RP phases are equal to within 10%.

In all relaxation experiments, differences in mobilities should be carried over in different relaxation behaviour and hence be visible in multi-(bi-)exponential behaviour of the signal intensities versus interval times. Such behaviour was not detected in spite of extensive tests (see above). Iteration of the intensities with biexponential curves invariably led either to identical time constants of the two participating curves or to a vanishly small contribution for all but one time constant.

As described under Experimental, the NMR experiments were carried out on two sets (fresh and aged) of two special dimethyloctylsilane research phases, M1 and M2 and M-1A and M-2A, respectively. Both M1 and M2 represent maximum coverage of the respective silica gels.

From ^{29}Si CP-MAS-NMR measurements, chromatography and elemental analysis, it is known that substantial parts of the silane chains are removed on ageing under well defined experimental conditions [11]. When this removal of silane chains from the silica gel surface occurs in a random fashion, an aged phase should behave like a less than maximally covered phase. This means that the behaviour of an aged phase in the two solid-state NMR techniques used here should be comparable to that of the three less covered silica gels RX-1–RX-3 (see Section 3.1).

Table 3 summarizes the Lorentzian and $T_{1\rho}$ (^{13}C) time constants for two non-aged RP phases M-1 and M-2 (both maximally covered with silane chains) and the corresponding aged phases M-1A and M-2A. For all four samples correlation coefficients of 0.99 and higher were found for both measurements, except in the $T_{1\rho}$ (^{13}C) measurement on sample M-2A (correlation coefficient 0.97). From a comparison of the data in Table 3 and the data for the Zorbax materials in Table 2, the following conclusions can be drawn. The Lorentzian time constants for the RP phases M-1 and M-2 are almost identical. However, they differ from the corresponding values for the Zorbax phases (Table 2, RX-4). Minor differences are also seen for the $T_{1\rho}$ (^{13}C) time constants. This is ascribed to the different supporting silica gels for the M-1 and M-2 phases and Zorbax materials. However, when comparing both the Lorentzian and the $T_{1\rho}$ (^{13}C) time constants for M-1 and M-2 with those for the corresponding aged phases M-1A and M-2A (Table 3), no differences are found. Elemental analysis, however, shows that the aged materials M-1A and M-2A have lost at least 30% and 40% of carbon, respectively. These same values for the time constants, as already explained above, are certainly not expected intuitively as aged RP phases could very well behave like the less densely covered materials RX-1, RX-2 and RX-3. This finding can only be explained by assuming that the ageing process strips off silane chains not at random, but from specific locations, i.e., patching occurs on ageing. From Fig. 8, one can envisage that the type B silane chains should dephase quicker than the type C silane chains near the edges of the patch, because of the higher packing density and thus the more hampered mobility. Type A silane chains should have a slower dephasing behaviour than even type C silane chains. Therefore, both situations (resulting from routes V and VI) should lead to multi-exponential signal decays. However, only monoexponential behaviour was found, indicating large patches (where type C silane chains do not contribute much to the decay). Whether ageing in the two aged RP phases M-1A and M-2A occurs via route V or VI should in principle be distinguishable. In situation VI the RP-HPLC phase is already patched and during ageing the patches grow. Patching, however,

Table 3
Lorentzian and $T_{1\rho}$ (^{13}C) time constants for the non-aged (M-1 and M-2) and aged (M-1A and M-2A) RP phases

Notation	Lorentzian time constant[a] (ms) (±0.2)	$T_{1\rho}$ (^{13}C)[b] (ms) (±7)
M-1	2.3	146
M-1A	2.1	146
M-2	2.4	161
M-2A	2.5	150[c]

[a] For the silane groups (M^1).
[b] For the carbon atoms A (Fig. 2).
[c] Correlation coefficient 0.97.

could not be seen for the M-1 and M-2 samples (no multi-exponential behaviour), indicating that patching is probably formed via route V, i.e., patching develops on ageing from a non-patched RP material.

4. Conclusions

For the four Zorbax materials only differences in the NMR time constants were observed between the maximally covered material and the three less densely covered silica gels. This proves that steric interference between neighbouring silane chains in closely packed situations can be detected. For the two RP phases M-1 and M-2 no patching was found, i.e., the silane chains are probably homogeneously distributed over the silica gel surface. After ageing, no differences in mobilities were found between the original and the aged phases, now indicating, however, that patching developed on ageing.

Acknowledgement

The authors are greatly indebted to Dr. J.J. DeStefano of Rockland Technologies (Newport, DE, USA) for putting the materials RX-1, RX-2, RX-3 and RX-4 at their disposal.

References

[1] R.E. Majors, *LC*, 2 (1984) 660.
[2] L. Sander and S.A. Wise, *LC·GC Int.*, 6 (1990) 24.
[3] R.E. Majors, *J. Chromatogr. Sci.*, 18 (1980) 489.
[4] R.E. Majors, *LC·GC Int.*, 4 (1990) 12.
[5] L.R. Snyder, J.L. Glajch and J.J. Kirkland, *Practical HPLC Method Development*, Wiley-Interscience, New York, 1988.
[6] C.F. Poole and S.K. Poole, *Chromatography Today*, Elsevier, Amsterdam, 1991, Ch. 4.
[7] R.M. Smith, T.G. Hurdley, J.P. Westlake, R. Gill and M.P. Osselton, *J. Chromatogr.*, 455 (1988) 77.
[8] H.A. Claessens, L.J.M. van de Ven, J.W. de Haan and C.A. Cramers, *J. High Resolut. Chromatogr. Chromatogr. Commun.*, 6 (1983) 433.
[9] J.L. Glajch, J.J. Kirkland and J. Köhler, *J. Chromatogr.*, 384 (1987) 81.
[10] M.J.J. Hetem, J.W. de Haan, H.A. Claessens, L.J.M. van de Ven and C.A. Cramers, *Anal. Chem.*, 62 (1990) 2288.
[11] M.J.J. Hetem, *Ph.D. Thesis*, Eindhoven University of Technology, Eindhoven, 1990.
[12] J. Köhler, D.B. Chase, R.D. Farlee, A.J. Vega and J.J. Kirkland, *J. Chromatogr.*, 352 (1986) 275.
[13] F. Eisenbeiss, *Ber. Bunsenges. Phys. Chem.*, 93 (1989) 1019.
[14] K.K. Unger, K.D. Lork, B. Pfleiderer, K. Albert and E. Bayer, *J. Chromatogr.*, 556 (1991) 395.
[15] C.H. Lochmüller, A.S. Colborn, M.L. Hunnicut and J.M. Harris, *J. Am. Chem. Soc.*, 106 (1984) 4077.
[16] C.H. Lochmüller, A.S. Colborn, M.L. Hunnicut and J.M. Harris, *Anal. Chem.*, 55 (1983) 1344.
[17] W.V. Gerasimowicz, A.N. Garroway, J.B. Miller and L.C. Sander, *J. Phys. Chem.*, 96 (1992) 3658.
[18] I.S. Chuang, D.R. Kinney, C.E. Bronniman, R.C. Zeigler and G.E. Maciel, *J. Phys. Chem.*, 96 (1992) 4027.
[19] R.A. Komoroski, *High Resolution NMR Spectroscopy of Synthetic Polymers in Bulk*, VCH, Weimheim, 1986, Ch. 5.
[20] L.B. Alemany, D.M. Grant, T.D. Alger and R.J. Pugmire, *J. Am. Chem. Soc.*, 105 (1983) 6697.
[21] E.M. Menger, W.S. Veeman and E. de Boer, *Macromolecules*, 15 (1982) 1406.
[22] J. Schaefer, M.D. Sefcik, E.O. Stejskal and R.A. McKay, *Macromolecules*, 17 (1984) 1118.
[23] J. Schaefer, E.O. Stejskal and R. Buchdahl, *Macromolecules*, 2 (1977) 384.
[24] M. Alla and E. Lippmaa, *Chem. Phys. Lett.*, 37 (1976) 260.
[25] S.J. Opella and M.H. Frey, *J. Am. Chem. Soc.*, 101 (1979) 5854.
[26] S.J. Opella, M.H. Frey and T.A. Cross, *J. Am. Chem. Soc.*, 101 (1979) 5856.
[27] A.L. Cholli, W.M. Ritchey and J.L. Koenig, *Spectrosc. Lett.*, 16 (1983) 21.
[28] F.G. Riddell, S. Arumugam, K.D.M. Harris, M. Rogerson and J.H. Strange, *J. Am. Chem. Soc.*, 115 (1993) 188.
[29] G. Bodenhausen, R.E. Stark, R.J. Ruben and R.G. Griffin, *Chem. Phys. Lett.*, 67 (1979) 424.
[30] G.E. Maciel and D.W. Sindorf, *J. Am. Chem. Soc.*, 102 (1980) 7606.
[31] B. Pfleiderer, K. Albert, E. Bayer, L. van de Ven, J. de Haan and C. Cramers, *J. Phys. Chem.*, 94 (1990) 4189.
[32] K.D. Lork, *Ph.D. Thesis*, Johannes Gutenberg University, Mainz, 1988.

ELSEVIER

Journal of Chromatography A, 687 (1994) 223–232

JOURNAL OF CHROMATOGRAPHY A

Studies of ovomucoid-, avidin-, conalbumin- and flavoprotein-conjugated chiral stationary phases for separation of enantiomers by high-performance liquid chromatography

Nariyasu Mano[a,*], Yoshiya Oda[a], Naoki Asakawa[a], Yutaka Yoshida[a], Tadashi Sato[a], Toshinobu Miwa[b]

[a]*Department of Physical and Analytical Chemistry, Tsukuba Research Laboratories, Eisai Co., Ltd., 5-1-3 Tokodai, Tsukuba, Ibaraki 300-26, Japan*

[b]*Department of Pharmaceutical Research Laboratory, Eisai Co., Ltd., 2-1 Takehaya-machi, Kawashima-cho, Hashima-gun, Gifu 483, Japan*

First received 16 May 1994; revised manuscript received 15 August 1994

Abstract

The effects of organic modifiers, buffer salts and pH on the retention and chiral separation of four protein-immobilized chiral stationary phases (CSPs), an ovomucoid–CSP, an avidin–CSP, a conalbumin–CSP and a flavoprotein–CSP, were investigated. Both retention and enantioselectivity were affected by alteration of the mobile phase conditions, and it was elucidated that the hydrophobic and ionic interactions between enantiomers and chiral recognition moieties in immobilized protein molecules were important to the chiral separation of each CSP. The protein bindings of enantiomers for four native proteins were also examined with chiral separation chromatography using a commercial ovomucoid–CSP (Ultron ES-OVM). The racemate which showed significant differences in protein binding abilities among its enantiomers was excellently resolved by chromatography.

1. Introduction

Chiral separations of drug enantiomers by high-performance liquid chromatography (HPLC) have shown great progress in recent years [1–5], and the mechanisms of some of the chiral separation modes have been clarified step by step [6,7]. It is known that protein columns can be used for the separation of drug enantiomers within a broad range [8] and can be used under reversed-phase conditions [9]. However, the mechanism of chiral separation with protein-conjugated columns has not yet been clarified, because proteins are complex biopolymers consisting of a number of *l*-amino acids residues, and they are capable of many interactions with small molecules, such as hydrophobic and electrostatic interactions. It is known that many enzymes can recognize each drug enantiomer [10], which may be due to differences in affinities for the active sites in the enzymes [11]. Wainer and co-workers have described that a human serum albumin (HSA)-conjugated chiral stationary phase (CSP) undergoes an allosteric action in the retention of drug enantiomers [12] and reported that good correlations were obtained

* Corresponding author.

0021-9673/94/$07.00
SSDI 0021-9673(94)00782-9

between retention expressed as $k'/(k'+1)$ and the extent of albumin binding for benzodiazepines and coumarins [13]. We therefore considered that protein binding was essential for retention and chiral separation on protein–CSPs.

We have developed four protein-conjugated CSPs, namely an ovomucoid-conjugated CSP (OVM–CSP) [14], an avidin-conjugated CSP (AVI–CSP) [15], a conalbumin-conjugated CSP (CON–CSP) [16] and a flavoprotein-conjugated CSP (FLA–CSP) [17], and have described their usefulness for the analysis of drug enantiomers in biological samples [18–20].

In this study, we used four model compounds, (±)-ketoprofen (KP), (±)-propranolol (PP), (±)-chlormezanone (CM) and (±)-benzoin (BZ) (Fig. 1). We compared the retentions and chiral separation properties of four CSPs with alteration of the mobile phase properties, such as organic solvents, buffer concentration, buffer anion and pH. The hydrophobic interactions and the ionic interaction between enantiomers and chiral recognition moieties were important for chiral separation with each CSP. In addition, protein bindings of enantiomers for native proteins were examined, and the enantiomers which displayed a great protein binding ability showed strong retention in chromatography. Also, each CSP had a similar property in that the enantiomers which showed significant differences in protein binding abilities were excellently resolved by chromatography.

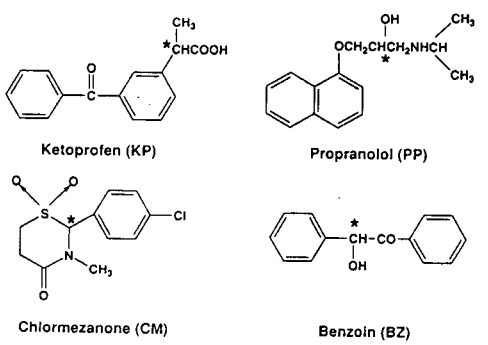

Fig. 1. Structures of model compounds. The chiral centres are indicated by asterisks.

2. Experimental

2.1. Materials

The solvents used were of HPLC grade. The four chicken egg white proteins were purified as described previously [21–24]. KP was purchased from Sigma (St. Louis, MO, USA), PP from Aldrich (Milwaukee, WI, USA), CM and BZ from Tokyo Kasei Kogyo (Tokyo, Japan), N,N-disuccinimidyl carbonate from Wako (Osaka, Japan) and N,N-disuccinimidyl suberate from Pierce (Rockford, IL, USA). The chiral column used in the protein binding study was an Ultron ES-OVM (5 μm, 150 mm × 4.6 mm I.D.), obtained from Shinwa Chemical Industries (Kyoto, Japan). The four protein CSP columns were prepared as described previously [14–17]. Nucleosil 5NH_2 was purchased from Macherey–Nagel (Düren, Germany). Centrifree micropartition systems (MPS-3) for ultrafiltration were obtained from Amicon (Beverly, MA, USA).

2.2. Chromatographic analysis with protein columns

Chromatographic analysis was performed using a Tosoh (Tokyo, Japan) CCPM pump, a WISP 712 autosampler (Waters, Milford, MA, USA), a Uvidec 100-VI UV spectrophotometer (Japan Spectroscopic, Tokyo, Japan) and a C-R4AX integrating recorder (Shimadzu, Kyoto, Japan). Known amounts of enantiomers were dissolved in water–methanol solutions, each solution was diluted with water to a concentration of 20 μg/ml and 10 μl of these solutions were injected into the HPLC column. All chromatographic experiments were carried out at a flow-rate of 1.0 ml/min and at room temperature.

2.3. Assay of protein binding of enantiomers for native proteins

The protein bindings of enantiomers were measured as follows. All solutions for incubation were prepared with 50 mM phosphate buffer. The final concentration of racemates was 100 μg/ml and that of proteins was 10 mg/ml. A

1-ml volume of sample solution was incubated for 1 h at about 25°C, and the free concentration of enantiomers in the filtrate was determined by HPLC with chiral separation using an Ultron ES-OVM column after filtration using MPS-3. All operations were performed at ambient temperature with the mobile phase at a flow-rate of 1.0 ml/min.

3. Results and discussion

The retention and the chiral resolution of enantiomers with protein-immobilized CSPs were influenced by mobile phase conditions such as buffer concentration, buffer anion, organic modifier and pH. Variations in these conditions may change the interaction of solutes with the solid phase caused by the conformation of the protein and/or the electrostatic situation and the hydrophobicity of solutes.

The variations in the capacity factor (k') and the separation factor (α) with alteration of methanol content are shown in Table 1. The k' values of all compounds on every CSP increased with decreasing methanol content. Hence these four CSPs clearly undergo a reversed-phase separation. In addition, the α values also increased with decreasing methanol content in almost all instances, although PP vs. OVM–CSP

Table 1
Effect of methanol content on retention and chiral separation of enantiomers on four CSPs

CSP	MeOH (%)	KP		PP		CM		BZ	
		k'_1	α	k'_1	α	k'_1	α	k'_1	α
OVM	15	2.48	1.11	–	–	1.40	2.91	3.72	2.15
	20	1.64	1.00	67.67	1.07	0.93	2.14	2.33	1.96
	25	1.16	1.00	33.89	1.09	0.67	1.63	1.24	1.67
	30	0.87	1.00	19.27	1.11	0.60	1.18	0.81	1.47
	35	0.69	1.00	11.63	1.13	0.55	1.00	0.59	1.29
	40	0.58	1.00	8.23	1.14	0.45	1.00	0.49	1.20
AVI	10	–	–	4.87	1.02	4.60	1.20	4.25	1.02
	15	22.24	1.75	4.10	1.04	3.03	1.32	3.07	1.06
	20	12.92	1.59	3.46	1.03	1.94	1.44	2.17	1.06
	25	8.06	1.47	3.12	1.00	1.38	1.49	1.62	1.05
	30	5.05	1.37	2.61	1.00	0.98	1.53	1.21	1.00
	35	3.23	1.30	2.33	1.00	0.75	1.57	0.93	1.00
	40	2.39	1.25	2.11	1.00	0.63	1.56	0.76	1.00
CON	2	5.60	1.00	7.71	1.00	1.35	1.19	2.96	1.06
	4	4.48	1.00	6.45	1.00	1.19	1.16	2.54	1.06
	6	3.77	1.00	5.63	1.00	1.10	1.13	2.20	1.05
	8	3.30	1.00	4.87	1.00	1.10	1.00	1.98	1.05
	10	2.96	1.00	4.30	1.00	1.03	1.00	1.87	1.00
FLA	2	8.83	1.19	–	–	1.48	1.72	6.38	1.48
	4	6.59	1.18	31.85	1.00	1.28	1.66	5.36	1.45
	6	4.69	1.16	23.88	1.00	1.07	1.58	3.90	1.36
	8	4.31	1.14	21.34	1.00	1.04	1.54	3.54	1.33
	10	3.03	1.12	16.00	1.00	0.84	1.44	2.61	1.25
	15	1.79	1.07	12.05	1.00	0.72	1.31	1.84	1.19
	20	1.36	1.00	9.65	1.00	0.64	1.23	1.47	1.14

Chromatographic conditions: mobile phase, 20 m*M* phosphate buffer (pH 6.0)–methanol; flow-rate, 1.0 ml/min; detection, UV at 230 nm; sample amount, 200 ng in 10 μl. k'_1 = Capacity factor of first-eluted enantiomer; α = separation factor.

and CM vs. AVI–CSP showed opposite results. This trend of α values was clearly observed when neutral compounds were used on the OVM–, CON– and FLA–CSPs.

The effects of organic modifiers of the mobile phase on the retention and separation of enantiomers on the four CSPs are shown in Table 2. This examination also showed that these four CSPs were involved in a reversed-phase separation mode. In the case of using straight-chain alcohols as organic modifiers such as methanol, ethanol and 1-propanol, an increase in the hydrophobicity of their alcohols induced a decrease in the α values. These results were the same as those obtained in the experiment with variation in methanol content mentioned above. On the other hand, using 2-propanol resulted in α values the same as or lower than those obtained using ethanol. Different results in chiral separation were sometimes induced by adding acetonitrile to the mobile phase. The α valve of PP using acetonitrile was larger than that using methanol, in spite of the significantly weaker retention on OVM–CSP, and FLA–CSP using acetonitrile also promoted better enantioselectivity for BZ than with 1-propanol with almost the same retention capacity.

From the results obtained in these studies, the increase in α values with decreasing hydrophobicity in the mobile phase suggests that the hydrophobic interaction in chiral recognition cavities significantly affected the difference in affinity for protein–CSPs. Addition of methanol as an organic modifier resulted in better resolution than that of other straight-chain alcoholic solvents on every CSP. Methanol is the most polarized and the smallest molecule among the organic solvents generally used in HPLC, hence it may be able to elute with minimum interference from hydrophobic interactions between the

Table 2
Effect of organic modifiers on retention and chiral separation of enantiomers on four CSPs

CSP	Solvent	KP		PP		CM		BZ	
		k'_1	α	k'_1	α	k'_1	α	k'_1	α
OVM	Methanol	1.64	1.00	67.67	1.07	0.93	2.14	2.33	1.96
	Ethanol	1.14	1.00	13.82	1.00	0.56	1.18	1.00	1.49
	1-Propanol	0.74	1.00	1.19	1.00	0.35	1.00	0.55	1.00
	2-Propanol	0.91	1.00	3.98	1.00	0.48	1.00	0.78	1.42
	Acetonitrile	0.71	1.00	4.01	1.15	0.37	1.00	0.58	1.00
AVI	Methanol	12.92	1.59	3.46	1.03	1.94	1.44	2.17	1.06
	Ethanol	4.52	1.31	2.44	1.00	1.14	1.11	1.50	1.00
	1-Propanol	1.97	1.00	1.66	1.00	0.66	1.00	1.05	1.00
	2-Propanol	2.92	1.11	2.31	1.00	0.89	1.00	1.38	1.00
	Acetonitrile	1.89	1.00	1.44	1.00	0.53	1.00	0.87	1.00
CON	Methanol	5.60	1.00	7.71	1.00	1.35	1.19	2.96	1.06
	Ethanol	4.15	1.00	5.49	1.00	1.18	1.12	2.43	1.06
	1-Propanol	3.51	1.00	4.31	1.00	1.12	1.00	2.18	1.00
	2-Propanol	4.60	1.00	4.03	1.00	1.22	1.00	2.46	1.00
	Acetonitrile	4.73	1.00	6.03	1.00	1.28	1.00	2.43	1.00
FLA	Methanol	3.03	1.12	16.00	1.00	0.84	1.44	2.61	1.25
	Ethanol	1.93	1.10	8.07	1.00	0.73	1.15	1.77	1.14
	1-Propanol	1.37	1.00	3.91	1.00	0.62	1.00	1.22	1.00
	2-Propanol	2.02	1.10	6.54	1.00	0.71	1.00	1.75	1.13
	Acetonitrile	1.26	1.00	4.50	1.00	0.56	1.00	1.21	1.09

Chromatographic conditions: mobile phase, 20 m*M* phosphate buffer (pH 6.0)–organic solvent (OVM, 80:20; AVI, 80:20; CON, 98:2; FLA, 90:10); flow-rate, 1.0 ml/min; detection, UV at 230 nm; sample amount, 200 ng in 10 μl. k'_1 = Capacity factor of first-eluted enantiomer; α = separation factor.

solutes and the chiral recognition cavities on proteins immobilized on a silica support. On the other hand, the results for PP vs. OVM–CSP and CM vs. AVI–CSP in Table 1 were exceptional cases and suggest that methanol as an organic modifier did not interfere much with the specific interactions in the chiral recognition cavities in those cases. Acetonitrile was sometimes a good organic modifier in the mobile phase. The reason for this seems to be that the interference mechanism with acetonitrile on the hydrophobic interaction between solutes and chiral recognition moieties in the solid phase differs from that with methanol, and the hydrophobic interaction in cavities having a specific affinity was influenced by the hydroxyl group in the alcohol.

The effects of buffer concentration in the mobile phase on k' and α values on every CSP are shown in Table 3. The k' and α values of CM and BZ were not substantially changed. The k' values of KP on the OVM–, AVI– and CON–CSPs decreased with increasing buffer concentration, whereas those on the FLA–CSP were not changed. Although the k' values of PP on FLA–CSP decreased with increasing buffer concentration, those on the other three CSPs did not vary, in contrast to the results with KP. On the other hand, with AVI–CSP, the α values of PP increased with increase in buffer concentration, whereas those of all the others were not substantially altered. These results suggest that the ionic interaction between protein–CSPs and ionic solutes contributed to the retention capacity.

Changes in the buffer anion in the mobile phase also affected the retention of ionic solutes on the four CSPs (Table 4). The k' of KP increased when borate buffer was employed in comparison with the use of phosphate buffer on

Table 3
Effect of buffer concentration on retention and chiral separation of enantiomers on four CSPs

CSP	Buffer concentration (m*M*)	KP		PP		CM		BZ	
		k'_1	α	k'_1	α	k'_1	α	k'_1	α
OVM	5	1.68	1.00	32.75	1.08	0.69	1.64	1.31	1.68
	10	1.52	1.00	30.04	1.07	0.71	1.63	1.33	1.68
	20	1.16	1.00	33.89	1.09	0.67	1.63	1.24	1.67
	50	1.05	1.00	30.00	1.08	0.69	1.67	1.36	1.68
	100	1.01	1.00	23.15	1.07	0.69	1.64	1.31	1.69
AVI	5	22.73	1.60	2.98	1.00	2.00	1.43	2.19	1.06
	10	17.78	1.59	3.06	1.00	2.01	1.45	2.20	1.06
	20	12.92	1.59	3.46	1.03	1.94	1.44	2.17	1.06
	50	10.05	1.57	3.13	1.06	2.00	1.49	2.17	1.06
	100	8.29	1.52	2.83	1.07	1.96	1.53	2.10	1.06
CON	5	8.12	1.00	8.43	1.00	1.50	1.30	3.18	1.11
	10	6.98	1.00	10.49	1.00	1.56	1.51	3.31	1.12
	20	5.60	1.00	7.71	1.00	1.35	1.19	2.96	1.06
	50	5.11	1.00	8.48	1.00	1.54	1.12	3.28	1.06
	100	4.45	1.00	7.50	1.00	1.43	1.15	3.15	1.05
FLA	5	2.85	1.15	22.96	1.00	0.91	1.41	2.70	1.26
	10	3.13	1.16	18.40	1.00	0.90	1.42	2.73	1.27
	20	3.03	1.12	16.00	1.00	0.84	1.44	2.61	1.25
	50	2.80	1.13	13.47	1.00	0.89	1.43	2.64	1.28
	100	3.22	1.13	10.94	1.00	0.91	1.44	2.77	1.30

Chromatographic conditions: mobile phase, phosphate buffer (pH 6.0)–methanol (OVM 75:25; AVI, 80:20; CON, 98:2; FLA, 90:10); flow-rate, 1.0 ml/min; detection, UV at 230 nm; sample amount, 200 ng in 10 μl. k'_1 = Capacity factor of first-eluted enantiomer; α = separation factor.

Table 4
Effect of buffer anions on retention and chiral separation of enantiomers on four CSPs

CSP	Buffer	KP		PP		CM		BZ	
		k'_1	α	k'_1	α	k'_1	α	k'_1	α
OVM	Phosphate	1.16	1.00	33.89	1.09	0.67	1.63	1.24	1.67
	Acetate	3.15	1.00	19.74	1.09	0.71	1.63	1.31	1.66
	Borate	9.46	1.00	15.91	1.11	0.66	1.68	1.22	1.66
	Tartrate	1.00	1.00	24.04	1.05	0.75	1.63	1.35	1.62
	Citrate	1.01	1.00	26.23	1.09	0.71	1.00	1.37	1.69
AVI	Phosphate	15.38	1.58	2.87	1.05	1.99	1.45	2.20	1.07
	Acetate	7.22	2.27	1.68	1.00	1.45	1.30	1.92	1.00
	Borate	–	–	1.15	1.00	1.93	1.30	2.17	1.00
	Tartrate	10.07	1.53	2.67	1.06	1.96	1.56	2.19	1.00
	Citrate	6.30	1.60	3.38	1.07	1.92	1.57	2.16	1.04
CON	Phosphate	7.24	1.00	5.80	1.00	1.37	1.12	3.24	1.00
	Acetate	10.26	1.00	5.18	1.00	1.40	1.19	3.13	1.00
	Borate	20.14	1.00	5.58	1.00	1.39	1.19	3.20	1.00
	Tartrate	6.49	1.00	7.05	1.00	1.52	1.14	3.51	1.00
	Citrate	4.42	1.00	8.78	1.00	1.36	1.00	3.33	1.00
FLA	Phosphate	3.03	1.12	16.00	1.00	0.84	1.44	2.61	1.25
	Acetate	5.14	1.11	13.84	1.00	0.94	1.41	2.96	1.22
	Borate	6.72	1.13	18.35	1.00	0.90	1.34	2.70	1.21
	Tartrate	3.43	1.13	11.69	1.00	0.90	1.40	2.70	1.27
	Citrate	2.61	1.15	14.38	1.00	0.78	1.72	2.89	1.30

Chromatographic conditions: mobile phase, 20 m*M* buffer (pH 6.0)–methanol (OVM, 75:25; AVI, 90:10; CON, 98:2; FLA, 90:10); flow-rate, 1.0 ml/min; detection, UV at 230 nm; sample amount, 200 ng in 10 μl. k'_1 = Capacity factor of first-eluted enantiomer; α = separation factor.

every CSP, and the order of the increase in k' was OVM > AVI > CON > FLA. The strengths of retention using the borate buffer were about nine times those using phosphate buffer on OVM–CSP, about four times on AVI–CSP, about three times on CON–CSP and about double on FLA–CSP. This order agrees with the amounts of mannose in the carbohydrate [25]. The carbohydrate moiety of glycoproteins is known to form a carbohydrate–borate complex with the borate anion, and this protein surface change may be related to the above phenomenon. On the other hand, in contrast to the result with KP, the k' value of PP on the OVM– and AVI–CSPs was the lowest when the borate buffer was employed, although on the CON– and FLA–CSPs it was not substantially changed compared with the result with the phosphate buffer. Regarding the α values, the OVM–, CON– and FLA–CSPs did not display much variation, whereas AVI–CSP showed different results attributable to the change in buffer anion.

Table 5 shows the results for k' and α values obtained on changing the pH of the mobile phase. The p*I* values of OVM, AVI, CON and FLA are 3.9–4.3, 9.5–10.0, 6.05–6.6 and 3.9–4.1, respectively [25]. However, KP was most strongly retained at pH 4 on every CSP. This may indicate that the same amino acid residue in the four proteins is related to the retention of KP. KP has a carboxylic acid group in its molecule, so that its p*K* value is about 4–5. Consequently, the retention of KP increased with pH change from 7 to 4 in the mobile phase because its hydrophobicity increased. However, at pH 3, the retention of KP became weak; we consider

Table 5
Effect of pH on retention and chiral separation of enantiomers on four CSPs

CSP	pH	KP		PP		CM		BZ	
		k'_1	α	k'_1	α	k'_1	α	k'_1	α
OVM	3.0	2.96	1.07	0.01	1.00	0.50	1.40	0.66	1.27
	4.0	4.04	1.00	1.61	1.00	0.55	1.35	0.88	1.53
	5.0	2.85	1.00	2.92	1.00	0.53	1.36	0.87	1.59
	6.0	0.91	1.00	16.25	1.10	0.53	1.36	0.82	1.49
	7.0	0.39	1.00	60.72	1.20	0.54	1.43	0.80	1.41
AVI	3.0	14.26	1.23	0.00	1.00	1.84	1.71	2.05	1.00
	4.0	34.69	1.38	0.70	1.00	1.81	1.59	2.04	1.05
	5.0	30.08	1.46	0.86	1.00	1.78	1.57	2.05	1.07
	6.0	15.38	1.58	2.87	1.05	1.99	1.45	2.20	1.07
	7.0	7.29	1.61	7.24	1.00	1.90	1.45	2.11	1.06
CON	3.0	22.65	1.00	0.15	1.00	1.71	1.00	3.26	1.00
	4.0	24.74	1.00	0.58	1.00	1.45	1.12	3.17	1.00
	5.0	19.16	1.00	2.06	1.00	1.45	1.23	3.11	1.08
	6.0	7.24	1.00	5.80	1.00	1.37	1.12	3.24	1.00
	7.0	2.66	1.00	2.66	1.00	1.42	1.18	3.27	1.00
FLA	3.0	11.58	1.12	0.00	1.00	0.95	1.05	2.10	1.13
	4.0	23.20	1.34	0.96	1.09	0.89	1.21	2.87	1.00
	5.0	12.39	1.27	4.83	1.07	0.87	1.36	2.86	1.19
	6.0	3.48	1.15	15.63	1.00	0.85	1.47	2.96	1.28
	7.0	1.42	1.00	–	–	0.94	1.53	3.01	1.29

Chromatographic conditions: mobile phase, 20 m*M* phosphate buffer–methanol (OVM, 70:30; AVI, 80:20; CON, 98:2; FLA, 90:10); flow-rate, 1.0 ml/min; detection, UV at 230 nm; sample amount, 200 ng in 10 μl. k'_1 = Capacity factor of first-eluted enantiomer; α = separation factor.

that alteration of the conformation of the protein itself based on the dissociation of an amino acid residue, which was attributed to the non-specific interaction, contributed to this phenomena. For PP, the k' values increased with increasing pH, although CON–CSP showed a different tendency. The pK of PP is 9.5; therefore, the hydrophobicity of the enantiomers themselves increases on approaching alkaline conditions. However, CON–CSP has a weaker hydrophobic interaction for retention in comparison with the other three CSPs; thus the change in the hydrophobicity of the protein itself seems to affect retention more than those of PP. On the other hand, the α values of KP on AVI–CSP changed with alteration of the buffer anion, although the other CSPs were not substantially affected except for CM vs. OVM– and FLA–CSPs. KP has a carboxylic acid group in the molecule, and the enantioselectivity of KP may decrease owing to inhibition due to the access of buffer anions containing a carboxylic acid to the chiral recognition cavity in AVI–CSP.

The k' values of non-ionic compounds were not greatly affected by pH changes, but the best pH conditions for chiral separation of CM and BZ were different among the four CSPs. These results seem to show that amino acid residues related to non-specific interactions were different from amino acid residues related to chiral recognition in many instances.

The recoveries in the protein binding assay procedure are shown in Table 6, and indicate that this assay procedure could determine the concentration of the four racemates in the filtrate without adsorption on an ultrafiltration mem-

Table 6
Recoveries of four racemates with native protein binding assay

Racemate	Recovery (%)	
	1	2
KP	100.3 ± 2.2	100.4 ± 2.1
PP	95.8 ± 2.2	96.2 ± 2.2
CM	99.2 ± 1.1	101.2 ± 1.0
BZ	101.4 ± 2.6	101.0 ± 2.6

Chromatographic conditions: column, Ultron ES-OVM (150 mm × 4.6 mm I.D.); mobile phase, (KP) acetonitrile–20 m*M* phosphate buffer (pH 3.0) (10:100), (PP) acetonitrile–20 m*M* phosphate buffer (pH 6.8) (30:100) and (CM, BZ) ethanol–20 m*M* phosphate buffer (pH 4.6) (10:100); flow-rate, 1.0 ml/min; detection, UV at 230 nm; $n = 4$. 1 = First-eluted enantiomer; 2 = second-eluted enantiomer.

brane. These results were sufficient for investigating the difference in protein binding between enantiomers. The results of protein binding of enantiomers for four native proteins are shown in Table 7. A tendency for the bindings of ionic compounds for native proteins to be stronger than those of non-ionic compounds was observed except for the cases of PP vs. CON and FLA. OVM showed good capacities for binding to each compound, whereas the binding capacity of CON was very weak except for KP. AVI did not show a binding capacity for PP. In addition, the binding ratios of KP for AVI were opposite those of the others. On the other hand, compounds which had greater differences in protein binding between enantiomers were better resolved on protein columns in each instance, as

Table 7
Protein binding (%) of enantiomers for native proteins

Protein	pH	KP			PP			CM			BZ		
		1	2	2/1	1	2	2/1	1	2	2/1	1	2	2/1
OVM	3.0	19.6	19.5	0.99	3.1	2.8	0.90	2.0	6.8	3.40	4.8	10.8	2.25
	4.0	4.4	6.7	1.52	17.6	17.3	0.98	5.0	15.6	3.12	4.0	11.5	2.88
	5.0	3.7	6.0	1.62	18.6	18.5	0.99	6.0	17.1	2.85	5.2	12.8	2.46
	6.0	3.1	5.8	1.87	20.4	20.5	1.00	4.2	16.4	3.90	6.0	13.5	2.25
	7.0	0.0	0.1	–	23.0	23.6	1.03	4.7	23.7	5.04	4.9	10.6	2.16
AVI	3.0	60.8	45.5	0.75	0.0	0.0	–	9.4	30.4	3.23	11.9	12.4	1.04
	4.0	70.5	52.6	0.75	0.0	0.0	–	18.2	30.7	1.69	12.2	12.7	1.04
	5.0	71.2	54.1	0.76	0.0	0.0	–	26.9	32.9	1.22	14.7	15.7	1.07
	6.0	76.3	57.8	0.76	0.0	0.0	–	27.9	32.8	1.18	16.6	17.7	1.07
	7.0	74.2	53.0	0.71	0.0	0.0	–	29.7	31.9	1.07	16.2	17.5	1.08
CON	3.0	42.0	39.8	0.95	0.0	0.0	–	2.8	1.2	0.43	0.0	0.0	–
	4.0	17.5	17.6	1.01	0.0	0.0	–	1.0	0.0	–	0.0	0.0	–
	5.0	16.2	16.2	1.00	0.0	0.0	–	0.1	0.0	–	0.0	0.0	–
	6.0	9.4	10.0	1.06	0.0	0.0	–	0.9	0.0	–	0.0	0.0	–
	7.0	0.0	0.0	–	6.8	5.8	0.85	0.9	0.0	–	0.0	0.0	–
FLA	3.0	32.4	34.0	1.05	0.0	0.0	–	1.9	0.5	0.26	4.8	4.9	1.02
	4.0	33.6	41.2	1.23	15.3	13.7	0.90	4.0	4.8	1.20	13.0	14.0	1.08
	5.0	28.5	38.1	1.34	13.7	11.6	0.85	2.3	3.3	1.43	15.6	17.9	1.15
	6.0	25.7	38.5	1.50	34.0	31.9	0.94	2.8	6.2	2.21	17.7	22.1	1.25
	7.0	8.4	11.6	1.38	55.2	55.3	1.00	0.9	10.9	12.11	18.4	29.7	1.61

1 = Protein binding (%) of first-eluted enantiomer of each compound on Ultron ES-OVM; 2 = protein binding (%) of second-eluted enantiomer of each compound on Ultron ES-OVM; 2/1 = protein binding ratio.

shown in Fig. 2. The opposite binding ratios of KP for AVI (Table 7) suggest that the elution order of KP on AVI–CSP may be opposite to that on the other CSPs. OVM–CSP showed the best chiral recognition ability among the four CSPs using four enantiomers. However, AVI–CSP could achieve the chiral resolution of KP much better than OVM–CSP. This is due to the difference in the contributions to non-specific interactions. That is, AVI shows a smaller change in non-specific interactions than OVM on immobilization on the silica support.

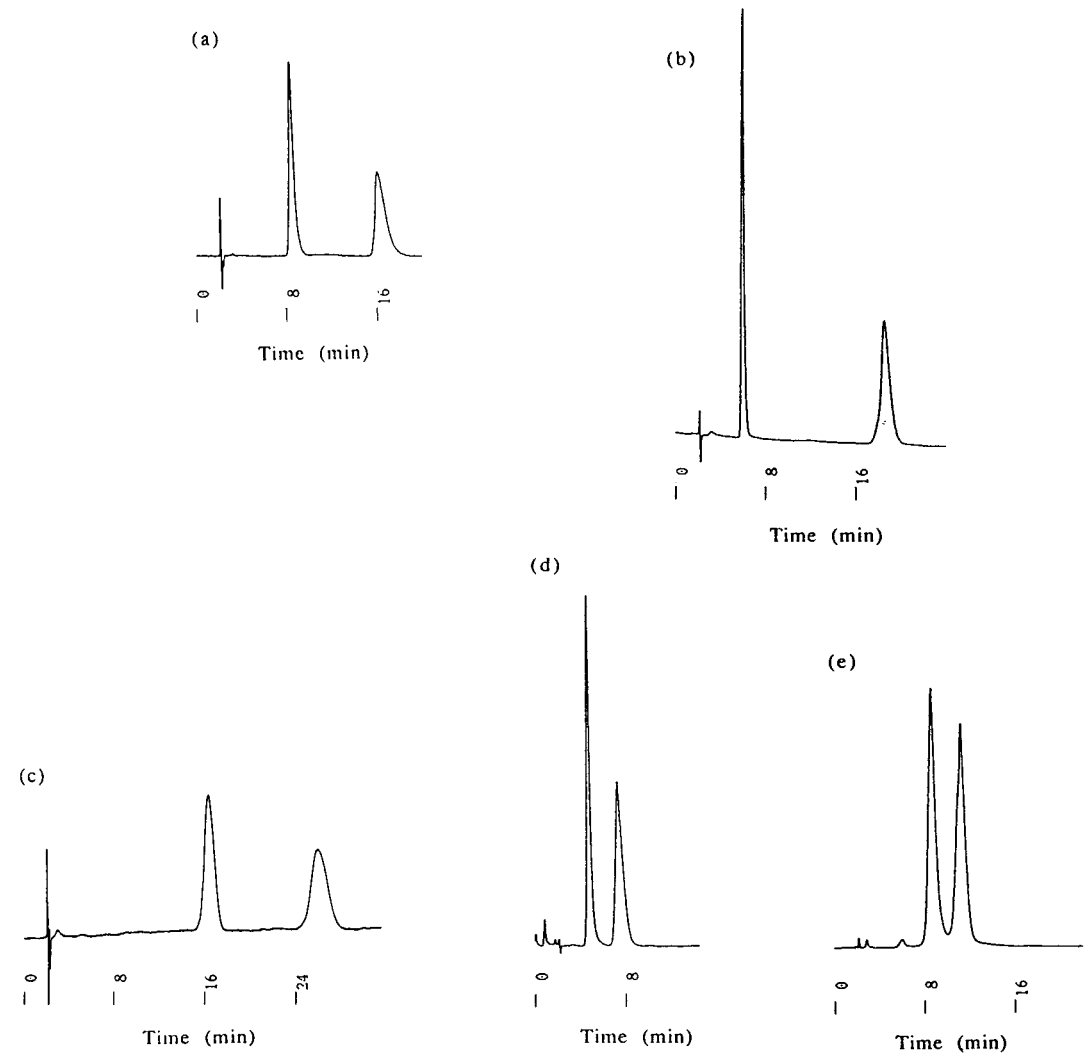

Fig. 2. Typical chromatograms obtained on protein-immobilized CSPs. Chromatographic conditions: column, (a, b) OVM–CSP (150 mm × 4.6 mm I.D.), (c) AVI–CSP (150 mm × 4.6 mm I.D.) and (d, e) FLA–CSP (150 mm × 4.6 mm I.D.); sample, (a, e) benzoin, (b, d) chlormezanone and (c) ketoprofen; mobile phase, (a) 20 m*M* phosphate buffer (pH 6.0)–methanol (85:15), (b) 20 m*M* phosphate buffer (pH 5.0)–methanol (90:10), (c) 20 m*M* phosphate buffer (pH 7.0)–methanol (80:20), (d) 20 m*M* phosphate buffer (pH 7.0)–methanol (98:2) and (e) 20 m*M* phosphate buffer (pH 6.0)–methanol (94:6); flow-rate, 1.0 ml/min; detection, UV at 230 nm; column temperature, room temperature; sample amount, 200 ng in 10 μl.

Protein CSPs act in the reversed-phase mode, so the retention times of solutes were controlled by the concentration of the organic solvents in the mobile phase. However, these organic solvents interfere with the interaction between solutes and chiral recognition moieties in proteins. It is preferable to choose mobile phase components that produce an appropriate retention for analysis with less interference for affinity binding in chiral recognition cavities for the resolution of enantiomers on protein CSPs.

4. Conclusions

The retention properties and chiral separations of enantiomers on four protein CSPs were investigated, and these four CSPs were found to have different properties. The retentions of the enantiomers on each CSP were influenced by both hydrophobic interactions and ionic interactions on all non-specific parts in the solid phase, and chiral separations might also be influenced by the hydrophobic interactions and the ionic interactions and changes in conformation of the protein molecule itself, such as ionization or non-ionization of amino acid residues in chiral recognition moieties. The protein binding properties contribute substantially to the retention and chiral separation on each protein CSP.

Acknowledgement

The authors thank Mr. Hiroshi Inoue (Kawashima Factory, Eisai) for the purification and supply of the four chicken egg white proteins.

References

[1] J.I. Seeman, H.V. Secor, D.W. Armstrong, K.D. Timmons and T.J. Ward, *Anal. Chem.*, 60 (1988) 2120.
[2] S. Allenmark and B. Bomgren, *J. Chromatogr.*, 264 (1983) 63.
[3] J. Hermansson, *J. Chromatogr.*, 269 (1983) 71.
[4] Y. Okamoto and K. Hatada, *J. Liq. Chromatogr.*, 9 (1986) 369.
[5] N. Oi and H. Kitahara, *J. Liq. Chromatogr.*, 9 (1986) 511.
[6] A. Dobashi, Y. Dobashi and S. Hara, *J. Liq. Chromatogr.*, 9 (1986) 243.
[7] Th.R.E. Hampe, J. Schlüter, K.H. Brandt, J. Nagel, E. Lamparter and G. Blaschke, *J. Chromatogr.*, 634 (1993) 205.
[8] K.M. Kirkland, K.L. Neilson and D.A. McCombs, *J. Chromatogr.*, 545 (1991) 43.
[9] J. Iredale, A.-F. Aubry and I. Wainer, *Chromatographia*, 31 (1991) 329.
[10] C.-S. Chen, T. Chen and W.-Ru Shieh, *Biochim. Biophys. Acta*, 1033 (1990) 1.
[11] R.D. Knihinicki, K.M. Williams and R.O. Day, *Biochem. Pharmacol.* 38 (1989) 4389.
[12] E. Domenici, C. Bertucci, P. Salvadori and I.W. Wainer, *J. Pharm.. Sci.*, 80 (1991) 164.
[13] T.A.G. Noctor, M.J. Diaz-Perez and I.W. Wainer, *J. Pharm. Sci.*, 82 (1993) 675.
[14] T. Miwa, M. Ichikawa, M. Tsuno, T. Hattori, T. Miyakawa, M. Kayano and Y. Miyake, *Chem. Pharm. Bull.*, 35 (1987) 682.
[15] Y. Oda, N. Asakawa, S. Abe, Y. Yoshida and T. Sato, *J. Chromatogr.*, 572 (1991) 133.
[16] N. Mano, Y. Oda, T. Miwa, N. Asakawa, Y. Yoshida and T. Sato, *J. Chromatogr.*, 603 (1992) 105.
[17] N. Mano, Y. Oda, N. Asakawa, Y. Yoshida, T. Sato and T. Miwa, *J. Chromatogr.*, 623 (1992) 221.
[18] Y. Oda, N. Asakawa, Y. Yoshida and T. Sato, *Pharm. Res.*, 8 (1991) 997.
[19] Y. Oda, H. Ohe, N. Asakawa, Y. Yoshida, T. Sato and T. Nakagawa, *J. Liq. Chromatogr.*, 15 (1992) 2997.
[20] N. Mano, Y. Oda, H. Ohe, N. Asakawa, Y. Yoshida and T. Sato, *J. Pharm. Biomed. Anal.*, 12 (1994) 557.
[21] E. Frederiq and H.F. Deutsch, *J. Biol. Chem.*, 181 (1949) 499.
[22] T. Miwa, T. Miyakawa and Y. Miyake, *J. Chromatogr.*, 457 (1988) 227.
[23] M.B. Rhodes, P.R. Azari and R.E. Feeney, *J. Biol. Chem.*, 230 (1958) 399.
[24] M.B. Rhodes, N. Bennet and R.E. Feeney, *J. Biol. Chem.*, 234 (1959) 2054.
[25] Y. Sato and K. Watanabe, *Proteins Nucleic Acids Enzymes*, 23 (1978) 54.

ELSEVIER

Journal of Chromatography A, 687 (1994) 233–239

JOURNAL OF CHROMATOGRAPHY A

Study of the k' or log k'–log P_{ow} correlation for a group of benzene derivatives and polycyclic aromatic hydrocarbons in micellar liquid chromatography with a C_8 column

M.A. García, M.L. Marina*

Departamento de Química Analítica, Facultad de Ciencias, Universidad de Alcalá de Henares, 28871 Alcalá de Henares (Madrid), Spain

First received 27 May 1994; revised manuscript received 29 August 1994

Abstract

The correlation between the capacity factor (k') or its logarithm (log k') and the logarithm of the octanol–water partition coefficient (log P_{ow}) for a group of 23 organic compounds (eleven benzene derivatives and twelve polycyclic aromatic hydrocarbons) was studied. The hydrophobicity range of the compounds chosen to study these correlations seems to be an important factor. In fact, the average r^2 values for 69 mobile phases of different composition and the 23-compound group is better for k'–log P_{ow} than for the log k'–log P_{ow} correlation. However, the average r^2 values for 84 different mobile phases proved to be better in the log k'–log P_{ow} correlation for the fifteen benzene and naphthalene derivatives group and similar in k'–log P_{ow} and log k'–log P_{ow} correlations for the ten monosubstituted benzene derivatives group.

1. Introduction

The hydrophobicity of an organic compound has been correlated with its biological activity or toxicity. The determination of the hydrophobicity has been used in various disciplines such as drug design and toxicology [1–3].

Traditionally, the logarithm of the octanol–water partition coefficient (log P_{ow}) has been used to measure the hydrophobicity of an organic compound. However, owing to the disadvantages of the standard "shake-flask" method for determining this partition coefficient [4], several attempts have been made in order to determine log P_{ow} by other techniques, some of them chromatographic. A relationship between the logarithm of the capacity factor of a non-congeneric series of non-ionized solutes and their log P_{ow} values was obtained in reversed-phase high performance liquid chromatography (RP-HPLC) with aqueous–organic mobile phases [5].

As micelles are known as simple chemical models for biomembranes [6], micellar liquid chromatography (MLC), in which a surfactant at a concentration above its critical micellar concentration is used in the mobile phase, seems to be an interesting possibility for evaluating log P_{ow}.

Several studies on the correlation between MLC retention and log P_{ow} have been published [6–12]. However, some contradictory results have been obtained concerning which of the two

* Corresponding author.

0021-9673/94/$07.00
SSDI 0021-9673(94)00825-6

parameters (k' or log k') best correlates with log P_{ow}.

In this work, the correlation between k' or log k' and log P_{ow} was studied for a group of 23 organic compounds (eleven benzene derivatives and twelve polycyclic aromatic hydrocarbons) in an MLC system. Sodium dodecyl sulphate (SDS) and hexadecyltrimethylammonium bromide (CTAB) were used as surfactants. These micellar phases were modified with methanol, *n*-propanol or *n*-butanol at different percentages.

2. Experimental

2.1. Apparatus

The chromatograph consisted of a Model 1050 pump, a Model 1050 automatic injector, a Model 1050 spectrophotometric detector of variable wavelength and an HP 3394 integrator (all from Hewlett–Packard).

Retention data for the fifteen benzene and naphthalene derivatives in the SDS and CTAB mobile phases in the absence and presence of *n*-propanol and *n*-butanol modifiers and for the 23 compounds in SDS–10% methanol were obtained with a Spherisorb C_8 column (15 cm × 4.0 mm I.D.) ($d_p = 5$ μm) (Teknokroma). In all mobile phases modified with alcohols, the concentration of the alcohol was 3, 5 or 10%.

Retention data for the eight polycyclic aromatic hydrocarbons in an MLC system (using SDS and CTAB mobile phases modified with *n*-propanol and *n*-butanol with a surfactant concentration ranging from 0.050 to 0.140 *M*) were also used in this study. Data on these mobile phases with a surfactant concentration ranging from 0.050 to 0.120 *M* were taken from Ref. [13].

A 0.45-μm filter and a filtration system (Millipore) were used.

2.2. Reagents

SDS, CTAB, methanol, *n*-propanol and *n*-butanol (all from Merck) were used as received. Water purified with a Milli-Q system (Millipore) was used.

Benzene derivatives and polycyclic aromatic hydrocarbons were **1** = benzene, **2** = benzylic alcohol, **3** = benzamide; **4** = toluene, **5** = benzonitrile, **6** = nitrobenzene, **7** = phenol, **8** = 2-phenylethanol, **9** = chlorobenzene, **10** = phenylacetonitrile, **11** = 3,5-dimethylphenol, **12** = naphthalene, **13** = 1-naphthol, **14** = 2-naphthol, **15** = 1-naphthylamine, **16** = pyrene, **17** = phenanthrene, **18** = 2,3-benzofluorene, **19** = fluorene, **20** = fluoranthene, **21** = acenaphthylene, **22** = acenaphthene and **23** = anthracene.

2.3. Procedure

Micellar mobile phases were prepared by dissolving the appropriate amount of surfactant and alcohol in water in an ultrasonic bath followed by filtration. Stock solutions of test solutes were prepared in the mobile phase itself and their concentrations were adjusted to permit their detection from the injection of a 20-μl volume of sample. The void volume of the column for SDS micelles was determined from the retention time of the peak originating from the injection of the nitrate anion into the chromatographic system. For CTAB mobile phases, the first deviation of the baseline was employed.

The column and the mobile phase were water jacketed and thermostated at 25 ± 1°C with a circulating water-bath.

3. Results and discussion

The capacity factors for the 23 compounds in an MLC system in which 69 different mobile phases of CTAB and SDS modified with methanol, *n*-propanol or *n*-butanol were used.

As the retention of the fifteen benzene and naphthalene derivatives (**1–15**) in the chromatographic system was less than that of the other polycyclic aromatic hydrocarbons (**16–23**), it was possible to determine the capacity factor for the fifteen referenced compounds in mobile phases not modified by alcohols. Therefore, capacity

factor data for these compounds were obtained for 84 different mobile phases.

With the retention data obtained, the correlation between k' or log k' with log P_{ow} was studied by using the log P_{ow} values grouped in Table 1.

The average r^2 values pertaining to each surfactant concentration in the mobile phase (five, six or seven different concentrations of surfactant for a given mobile phase) are given at Table 2. These r^2 values are given for both the k'–log P_{ow} and the log k'–log P_{ow} correlation and for the three groups of the compounds studied: all 23 compounds (**1–23**), the fifteen benzene and naphthalene derivatives (**1–15**) and the ten monosubstituted benzene derivatives (compounds **1–10**).

As can be seen at Table 2, k' always correlates better with log P_{ow} than log k' for the group of 23 compounds studied. In fact, for all mobile phases employed, the average r^2 values is greater in the k'–log P_{ow} correlation than in the log k'–log P_{ow} correlation irrespective of the nature of the surfactant in the mobile phase. In general terms, the best results are obtained with a low percentage of alcohol in the mobile phase (3 or 5%). The worst value for r^2 corresponding to the k'–log P_{ow} correlation is obtained for the SDS–10% methanol mobile phases.

Concerning the influence of the surfactant concentration on the k'–log P_{ow} correlation, the r^2 values obtained for each surfactant concentration (values not shown) indicated that, in many cases, the k'–log P_{ow} correlation improves when the surfactant concentration in the mobile phase decreases, especially in the case of CTAB.

Table 2 also shows that for the fifteen benzene and naphthalene derivatives, k' correlates better with log P_{ow} than log k' only in the case of CTAB mobile phases. A better correlation is obtained for log k'–log P_{ow} when SDS is employed as a surfactant. However, for all mobile phases used except SDS–10% methanol, although the average r^2 value is greater in the log k'–log P_{ow} correlation (0.8854), it is not significantly different from that corresponding to k'–log P_{ow} correlation (0.8655). For this group of compounds, the addition of *n*-propanol and *n*-butanol at low percentages (3 or 5%) to CTAB mobile phases seems to improve the k'–log P_{ow} and log k'–log P_{ow} correlations. However, with SDS mobile phases, the best correlations are obtained in the absence of alcohols.

With the ten monosubstituted benzene derivatives, a similar result to that with the fifteen benzene and naphthalene derivatives is obtained. The k'–log P_{ow} correlation is better than the log k'–log P_{ow} correlation only when CTAB is employed as a surfactant. However, for SDS mobile phases, the average r^2 values are very similar for both correlations (k'–log P_{ow} and log k'–log P_{ow}) and this also occurs for the average r^2 values corresponding to all mobile phases. The group of ten benzene derivatives is characterized by a general increase in the average r^2 values, especially for log k'–log P_{ow} correlation. With regard to the presence of alcohols in mobile phase, the addition of these organic

Table 1
Log P_{ow} values for the 23 compounds studied

No.	Compounds	Log P_{ow}
1	Benzene	2.13[a]
2	Benzyl alcohol	1.10[a]
3	Benzamide	0.64[a]
4	Toluene	2.69[a]
5	Benzonitrile	1.56[a]
6	Nitrobenzene	1.85[a]
7	Phenol	1.46[a]
8	2-Phenylethanol	1.36[a]
9	Chlorobenzene	2.84[a]
10	Phenylacetonitrile	1.56[a]
11	3,5-Dimethylphenol	2.35[a]
12	Naphthalene	3.37[a]
13	1-Naphthol	2.98[a]
14	2-Naphthol	2.84[a]
15	Naphthylamine	2.22[a]
16	Pyrene	4.88[a]
17	Phenanthrene	4.46[a]
18	2,3-Benzofluorene	5.03[b]
19	Flourene	4.18[a]
20	Flouranthene	4.50[b]
21	Acenaphtylene	3.48[b]
22	Acenaphthene	3.82[b]
23	Anthracene	4.45[a]

[a] Values taken from Ref. [6].
[b] Values taken from Ref. [14].

Table 2
Average of r^2 values corresponding to five, six or seven concentrations of surfactant in each mobile phase

Mobile phase	k' (23)	Log k' (23)	k' (15)	Log k' (15)	k' (10)	Log k' (10)
CTAB[a]	–	–	0.9082	0.8779	0.9255	0.8802
CTAB–3% PrOH[a]	0.9571	0.8534	0.9598	0.9076	0.9692	0.9284
CTAB–5% PrOH[a]	0.9518	0.8453	0.9609	0.9072	0.9773	0.9406
CTAB–10% PrOH[a]	0.9275	0.8365	0.9038	0.8876	0.9786	0.9573
CTAB–3% BuOH[a]	0.9566	0.8600	0.9757	0.9237	0.9610	0.9528
CTAB–5% BuOH[a]	0.9286	0.8400	0.9299	0.9097	0.9765	0.9642
CTAB–10% BuOH[a]	0.9015	0.8189	0.8355	0.8458	0.9689	0.9450
$r^{2\,d}$	0.9372	0.8423	0.9248	0.8942	0.9653	0.9383
SDS[b]	–	–	0.8547	0.900	0.9160	0.9271
SDS–10% MeOH[b]	0.8750	0.8644	0.5770	0.7765	0.9183	0.9260
SDS–3% PrOH[b]	0.9410	0.9305	0.8283	0.8775	0.9337	0.9274
SDS–5% PrOH[b]	0.9393	0.9156	0.7824	0.8689	0.9278	0.9506
SDS–10% PrOH[c]	0.9292	0.9197	0.7798	0.8726	0.9083	0.9422
SDS–3% BuOH[b]	0.9485	0.9091	0.8075	0.9067	0.9363	0.9430
SDS–5% BuOH[b]	0.9417	0.8899	0.7936	0.8691	0.9403	0.9494
SDS–10% BuOH[b]	0.9245	0.8423	0.7981	0.8421	0.9517	0.9392
$\bar{r}^{2\,e}$	0.9374	0.9012	0.8063	0.8767	0.9256	0.9398
$\bar{r}^{2\,f}$	0.9373	0.8717	0.8655	0.8854	0.9454	0.9390
$\bar{r}^{2\,g}$	0.9061	0.8680	0.7212	0.8309	0.9318	0.9325

Mobile phase components: MeOH = methanol; PrOH = *n*-propanol; BuOH = *n*-butanol.
[a] Average of r^2 values corresponding to five concentrations of surfactant in each mobile phase.
[b] As above for six concentrations.
[c] As above for seven concentrations.
[d] Average of r^2 values corresponding to all CTAB mobile phases.
[e] Average of r^2 values corresponding to all SDS mobile phases except SDS–10% methanol.
[f] Average of r^2 values corresponding to all CTAB and SDS mobile phases studied except SDS–10% methanol.
[g] Average of r^2 values corresponding to all SDS and CTAB mobile phases studied.

modifiers to CTAB and SDS mobile phases generally improves the k'–log P_{ow} and log k'–log P_{ow} correlations.

The results obtained demonstrate the importance of the hydrophobicity range of compounds on the k' or log k'–log P_{ow} correlation. In fact, for all 23 compounds studied (hydrophobicity ranged from 0.64 to 5.03) k' correlated better with log P_{ow} than log k'. For the group of fifteen benzene and naphthalene derivatives (log P_{ow} ranged from 0.64 to 3.37) or the group of ten monosubstituted benzene derivatives (log P_{ow} ranged from 0.64 to 2.84) k' and log k' correlated similarly with log P_{ow} or even log k' correlated better with log P_{ow} than k', especially if SDS mobile phases were employed. These results are grouped in Fig. 1, showing the Box plot for average of r^2 values for the three groups of compounds studied and for k'–log P_{ow} and log

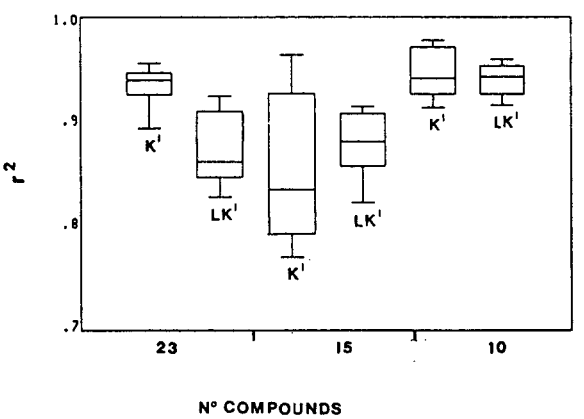

Fig. 1. Box plots for the average of r^2 values for three groups of compounds and for k'–log P_{ow} and log k'–log P_{ow} correlations. All mobile phases except SDS–10% methanol have been considered.

k'–log P_{ow} correlations. All mobile phases except SDS–10% methanol have been included in Fig. 1.

Figs. 2 and 3 show the variation of k' and log k' with log P_{ow} for CTAB and SDS mobile phases modified with 3% n-propanol and for concentrations of both surfactants of 0.05 and 0.120 M. The curvature observed for log k'–log P_{ow} plots can be explained by the solubility limit theory developed by Hinze and Weber [15]. For compounds with low log P_{ow} values, the solutes are as water soluble as they can be, so the water–stationary phase partitioning plays its largest role for these solutes. Highly hydrophobic solutes become insoluble in water, and then the micelle-stationary phase equilibrium becomes predominant. In this equilibrium the two phases are chemically similar and the partition coefficient approaches unity and becomes independent of hydrophobicity. The log k'–log P_{ow} curve flattens.

The point on the curve where the "break" occurs is a value of log P_{ow} limit which can depend on the nature of the surfactant and/or the effect of alcohols. This explains why log k'–log P_{ow} correlation improves when the most hydrophobic compounds are eliminated on the curve (see Fig. 1).

Figs. 2 and 3 also show that a higher dispersion of experimental points occurs when SDS

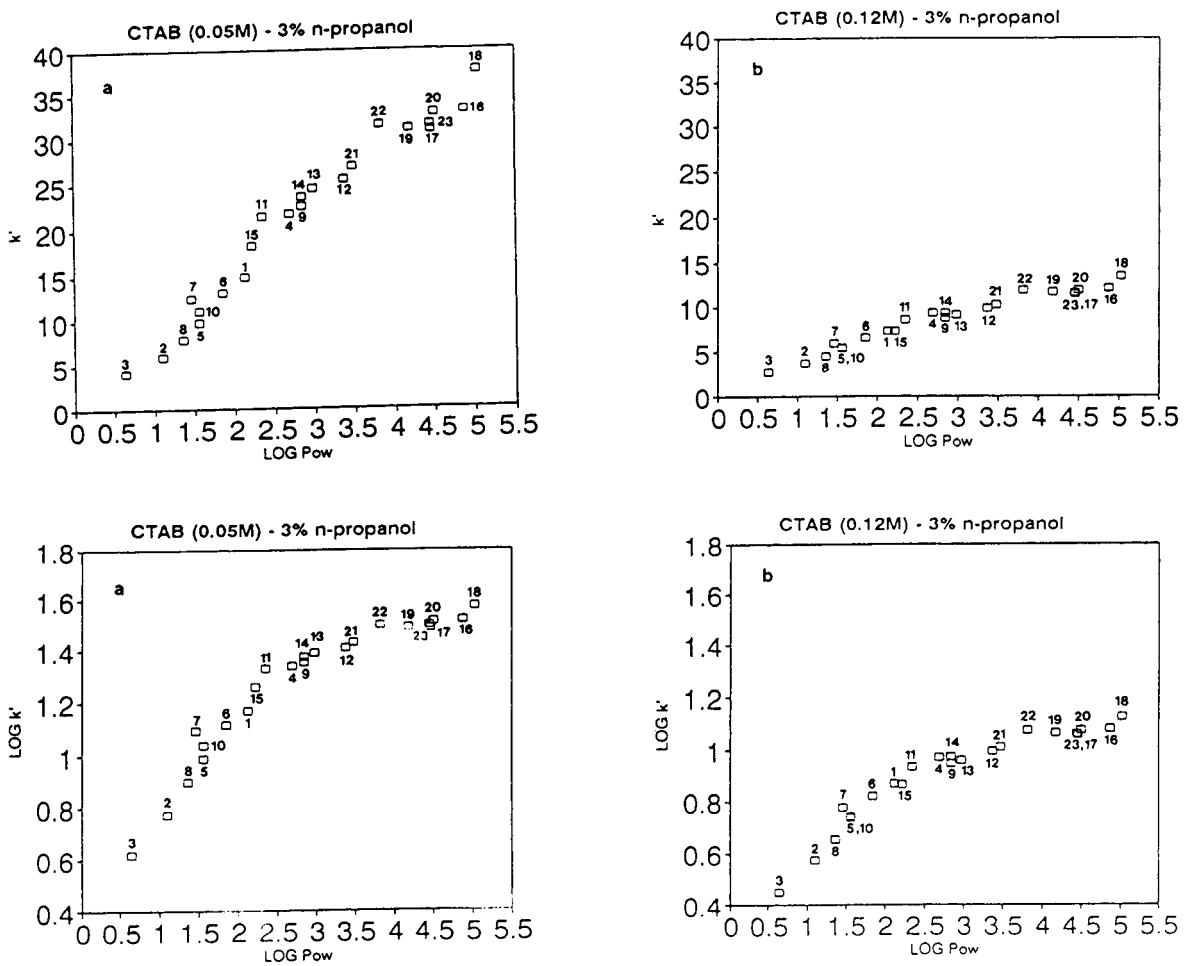

Fig. 2. Variation of k' and log k' with log P_{ow} for a CTAB–3% n-propanol mobile phase: (a) 0.05 M CTAB; (b) 0.12 M CTAB.

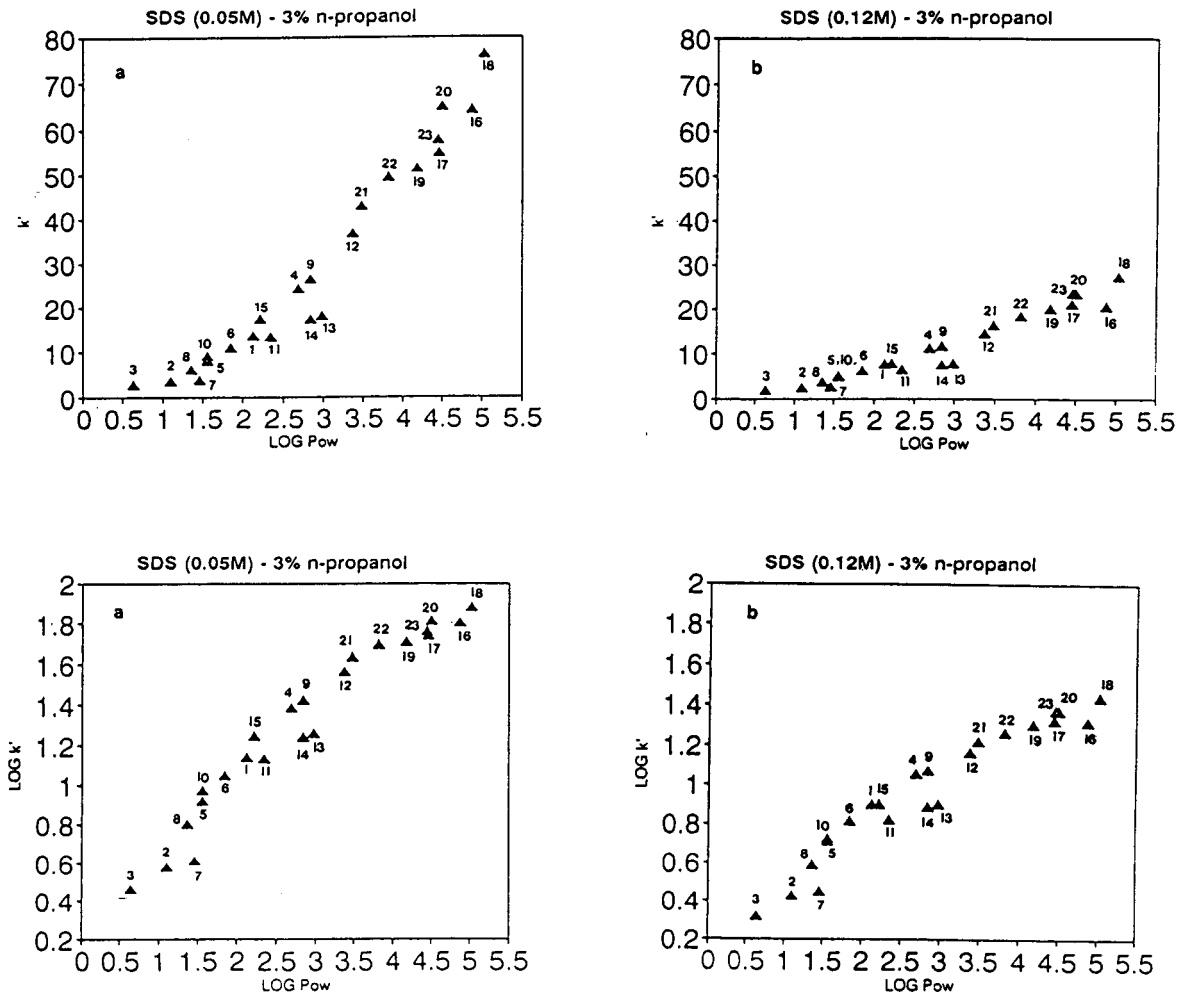

Fig. 3. Variation of k' and log k' with log P_{ow} for a SDS–3% *n*-propanol mobile phase: (a) 0.05 *M* SDS; (b) 0.12 *M* SDS.

mobile phases are used versus CTAB mobile phases.

A 0.050 *M* CTAB mobile phase modified with 3% *n*-propanol was chosen to calculate log P_{ow} from the experimental capacity factor data and the equation of the straight line. These calculated log P_{ow} values are plotted versus the experimental values in Fig. 4. The equation used to obtain these calculated log P_{ow} values was

$$k' = 0.2852 + 7.3770 \log P_{ow}$$

$$r^2 = 0.9615$$

and the average of the relative error obtained between the calculated and experimental values was 9.56%.

4. Conclusions

From the results presented in this work and for the group of benzene derivatives and polycyclic aromatic hydrocarbons studied, the following conclusions can be drawn. For the 23 benzene derivatives and polycyclic aromatic hydrocarbons, k' always correlates better with log P_{ow} than log k', irrespective of the nature of the surfactant present in mobile phase and the na-

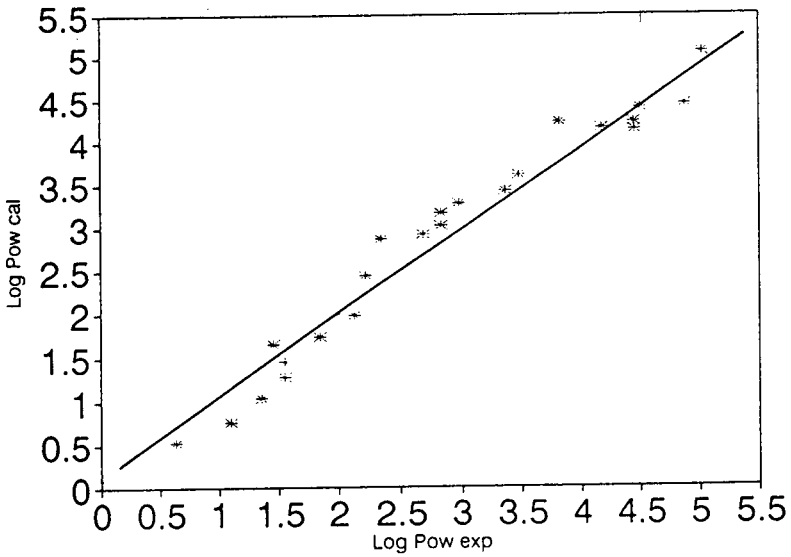

Fig. 4. Calculated versus experimental log P_{ow} values. The calculated values were obtained by means of the equation of the straight line corresponding to the variation of k' with log P_{ow} for a 0.05 M CTAB–3% n-propanol mobile phase.

ture and percentage of the alcohol used as modifier. However, for the fifteen benzene and naphthalene derivatives and the ten monosubstituted benzenes, k' correlates better with log P_{ow} than log k' only when CTAB mobile phases are used, the log k'–log P_{ow} correlation being similar to or even better than the k'–log P_{ow} correlation if SDS mobile phases are used. These results show that the hydrophobicity range of the compounds chosen is an important factor to be taken into account in this kind of study. Then, depending on the situation, either k' or log k' might better fit the data and one must therefore try both and use the one with the best correlation.

Acknowledgements

The authors thank the Comunidad Autónoma de Madrid (Spain) for project C102/91. They also thank C. Marina for linguistic assistance.

References

[1] C. Hansch, in E.J. Ariens (Editor), *Drug Design*, Vol. 1, Academic Press, New York, 1971, p. 271.
[2] L. Goldberg (Editor), *Structure–Activity Correlation as a Predictive Tool in Toxicology*, Hemisphere, Washington, DC, 1983.
[3] C. Hansch and A. Leo, *Substituent Constants for Correlation Analysis in Chemistry and Biology*, Wiley–Interscience, New York, 1979.
[4] R. Kaliszan, *Quantitative Structure–Chromatographic Retention Relationships*, Wiley, New York, 1987, p. 1.
[5] R. Kaliszan, *Anal. Chem.*, 64 (1992) 619A.
[6] M.G. Khaledi and E.D. Breyer, *Anal. Chem.*, 61 (1989) 1040.
[7] F. Gago, J. Alvarez-Builla, J. Elguero and J.C. Díez-Masa, *Anal. Chem.*, 59 (1987) 921.
[8] B.K. Lavine, A.J. White and J.H. Han, *J. Chromatogr.*, 542 (1991) 29.
[9] V. González, M.A. Rodríguez-Delgado, M.J. Sánchez and F. García-Montelongo, *Chromatographia*, 34 (1992) 627.
[10] E.D. Breyer, J.K. Strasters and M.G. Khaledi, *Anal. Chem.*, 63 (1991) 828.
[11] M.G. Khaledi, E. Peuler and J. Ngeh-Ngwainbi, *Anal. Chem.*, 59 (1987) 2738.
[12] M.F. Borgerding, F.H. Quina, W.L. Hinze, J. Bowermaster and H.M. McNair, *Anal. Chem.*, 60 (1988) 2520.
[13] M.A. García, O. Jiménez and M.L. Marina, *J. Chromatogr. A*, 675 (1994) 1.
[14] K. Jinno and K. Kawasaki, *Chromatographia*, 17 (1983) 445.
[15] W.L. Hinze and S.G. Weber, *Anal. Chem.*, 63 (1991) 1808.

ELSEVIER

Journal of Chromatography A, 687 (1994) 241–248

JOURNAL OF CHROMATOGRAPHY A

High-performance liquid chromatographic separation of β-amino alcohols I. Separation of (*R*,*S*)-1-(dialkylamino)-2-alkanols on an amylose-based chiral stationary phase

L.W. Nicholson[a,*], C.D. Pfeiffer[a], C.T. Goralski[b], B. Singaram[c], G.B. Fisher[c]

[a]*Analytical Sciences, The Dow Chemical Company, Midland, MI 48667, USA*

[b]*Pharmaceuticals Process Research, The Dow Chemical Company, Midland, MI 48674, USA*

[c]*Department of Chemistry and Biochemistry, University of California at Santa Cruz, Santa Cruz, CA 95064, USA*

First received 12 April 1994; revised manuscript received 12 August 1994

Abstract

Direct enantiomeric separations of racemic mixtures of (*R*,*S*)-1-(dialkylamino)-2-alkanols were achieved with a variety of alcohol-modified pentane mobile phases and a Chiralpak AD chiral stationary phase. The effects of the aliphatic component and the alcohol modifier in the mobile phase were studied independently. The best separations were obtained with pentane based mobile phases. A variety of alcohol modifiers were investigated that introduced steric factors or affected hydrogen bonding. Ring size and hetero atom effects of the substituents were noted. Some differences in enantioselectivity between columns were observed.

1. Introduction

Enantiomerically pure β-amino alcohols are important pharmacological agents in medicinal chemistry [1,2]. Therapeutic activity of these molecules can be divided into three categories based on their pharmacological action: vaso constrictors, antihypertensive agents and β-blockers [3]. Many of the β-blockers are marketed as racemic mixtures, but their mode of action is enantioselective [4,5]. The (*S*)-enantiomers are often 50–500-fold more active than their antipode [6]. The binding affinity to the β-receptor has been reported to range from 10 to 1000, for atenolol and pindolol, respectively [1].

The preparation [7–9] and use of β-amino alcohols in organic syntheses has been increasing [9]. Many important transformations of prochiral substrates into chiral compounds of high enantiomeric purity have been achieved using a catalytic amount of an enantiomerically pure β-amino alcohol as a chiral auxiliary [9,10].

There are several methods available for the synthesis of racemic β-amino alcohols [11]. Enantiomerically pure β-amino alcohols are usually obtained either from amino acids or by resolution procedures [12]. The only general asymmetric syntheses of β-amino alcohols currently available are the homogeneous asymmetric hydrogenation of α-amino ketones, using

* Corresponding author.

0021-9673/94/$07.00
SSDI 0021-9673(94)00795-O

(*R*)-(+)- and (*S*)-(−)-2,2′-bis(diphenylphosphine)-1,1′-binaphthyl–ruthenium (BINAP–Ru) complexes with hydrogen pressures of 50–100 atm (1 atm = 101 325 Pa) [13], and the asymmetric reduction of α-amino ketones with the chiral borohydride, K Glucoride [7].

A general synthesis for the preparation of racemic β-amino alcohols via the hydroboration/oxidation of enamines has been developed [11]. This procedure was extended to the preparation of enantiomerically pure β-amino alcohols via the asymmetric hydroboration of enamines using diisopinocampheylborane at 0°C in tetrahydrofuran (THF) generating enantiomeric excesses ranging from 50 to 86% [14].

Accurate determination of the enantiomeric purity of β-amino alcohols is essential to assess their effectiveness as both therapeutic agents and chiral auxiliaries. Many chromatographic techniques [1,15–33] have been employed for the analysis of derivatized and underivatized β-amino alcohols, but the use of HPLC procedures predominate [18]. Pirkle and Burke [34] recently described a N-3,5-dinitrobenzoyl-α-amino phosphonate chiral stationary phase (CSP) that was developed specifically for the separation of β-blockers. Many direct separations of amino alcohols have also been achieved on modified cellulose and amylose CSPs [35–40].

Papers describing enantiomeric separations using cellulose or amylose based CSPs frequently include discussions of the solute-CSP interactions and recognition mechanisms. Hydrogen bonding, dipole and π–π interactions have been identified [35–43] as important interactive forces that may be used to form the diastereomeric solute–CSP complexes which yield the separations. Enantiomeric discrimination may also be influenced by steric fit in the "chiral cavity" of the CSP [43,44]. The composition of the mobile phase is an important factor in these separations. Most of the separations have been obtained using normal-phase conditions with an aliphatic carrier and alcohol modifier in the mobile phase. The type and concentration of the alcohol in the mobile phase has a significant effect on some separations [35,39–44]. Water has been added to a few of the mobile phases to improve resolution [35,45,46].

This article describes the synthesis and direct enantiomeric separation of β-dialkylamino alcohols using a 3,5-dimethylphenyl carbamate modified amylose CSP (Chiralpak AD, Chiral Technologies).

2. Experimental

2.1. Synthesis

The following reagents were purchased from Aldrich and used without further purification: 1,2-epoxyhexane, 1,2-epoxyoctane, 1,2-epoxydecane, styrene oxide, (*R*)-(+)-styrene oxide, pyrrolidine and morpholine. (*R*)-1,2-Epoxyoctane was obtained as a gift from Nippon Mining. All new compounds gave satisfactory C,H,N analyses, and their structures were further confirmed by ^{1}H and ^{13}C NMR spectrometry and Fourier transform (FT) IR spectroscopy.

2.2. Preparation of the amino alcohols

The compounds were prepared by the neat reaction of the appropriate secondary amine and 1,2-epoxyalkane or styrene oxide at reflux. Synthetic procedures will be reported elsewhere [47].

2.3. Materials

HPLC-grade pentane, hexane, *n*-heptane, methanol (MeOH) and 2-propanol (IPA) were purchased from Fisher Scientific. Absolute ethanol (EtOH) was obtained from Quantum Chemical Corp. USI Division and HPLC-grade water from a Barnstead brand NANOpure II water-purification system. Cyclohexanol, 1-octanol, *tert.*-amyl alcohol, 2,2,2-trifluoroethanol and 1,1,1,3,3,3-hexafluoro-2-propanol were purchased from Aldrich and were ≥99% pure. Mobile phases were prepared by blending appropriate volumes of liquids in a 1-l graduated cylinder and mixing with a stirring bar. The

mobile phases were neither vacuum degassed nor sparged with helium before or during their use.

2.4. Instrumentation

Chromatographic separations were achieved using a liquid chromatograph constructed from the following components: a Milton Roy reciprocating piston pump operating at 1–2 ml/min, a Rheodyne Model 7125 injector, a 250 × 4.6 mm I.D. Chiralpak AD column from Chiral Technologies and a Kratos 773 UV absorbance detector. The detector output was stored and reprocessed using a Perkin-Elmer Nelson ACCESS*CHROM data system.

2.5. Chromatography

A series of structurally similar amino alcohols and various mobile phases were used to investigate solute–CSP interactions affecting the separation of amino alcohols on an amylose-based CSP. Racemic mixtures of each compound were analyzed individually and then combined with the other compounds of the series and reanalyzed each time the composition of the mobile phase was changed.

The elution order of selected enantiomers was established by analyzing material of known absolute configuration. Capacity factors and resolutions were computed from the retention times and peak widths. The capacity factors for the first peak of each pair of enantiomers (k'_1) and R_s values are provided in the appropriate tables. Mobile phase, substituent and CSP effects are described below.

3. Results and discussion

3.1. Mobile phase effects

Hydrocarbon component

The effect of the aliphatic component in the mobile phase has received little attention. Three hydrocarbons, pentane, hexane and heptane, were selected for evaluation. Pentane was selected to permit the use of a variety of alcohols in the mobile phase. MeOH has limited solubility in hexane and higher alkanes but is miscible in all proportions with pentane. Pentane is also a convenient co-solvent for EtOH and IPA.

Mobile phases containing 5% EtOH and 95% of either *n*-pentane, hexane or heptane were prepared and used to determine the effect of the aliphatic component of the mobile phase. Although slight differences in retention time and resolution were noted for some compounds, elution order, apparent peak shapes and the stereoselectivities were unaffected when only the aliphatic component was varied. However, the results shown in Table 1 for 1-(4-morpholino)-2-octanol and 2-(4-morpholino)-1-phenylethanol, compounds B and D of Table 2, revealed that improvements in resolution were achieved when pentane was used as the aliphatic component of the mobile phase. The poorest resolution was obtained with heptane.

Alcohol component

The effect of the alcohol modifier in the mobile phase on retention and resolution was complex (Fig. 1 and Table 2), yet the (*R*)-enantiomers always eluted first. The results pre-

Table 1
Effect of the aliphatic component in the mobile phase on resolution

Solvent	Compound B			Compound D		
	k'_1	α	R_s	k'_1	α	R_s
Pentane	1.58	1.31	3.48	5.38	1.48	5.02
Hexane	1.52	1.30	2.97	4.78	1.49	4.56
Heptane	1.76	1.31	2.54	5.38	1.49	4.41

Table 2
Chromatographic parameters for β-dialkylamino alcohols

	R1	R2	MeOH			EtOH			IPA		
			k_1'	α	R_s	k_1'	α	R_s	k_1'	α	R_s
A	$CH_3(CH_2)_5$	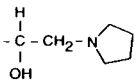	1.07	1.32	1.57	0.56	1.36	1.79	0.86	1.00	0.00
B	$CH_3(CH_2)_5$	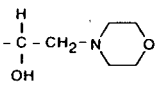	1.92	1.29	1.96	1.34 (1.51)	1.36 (1.63)	4.26 (1.47)	1.33	1.00	0.00
C	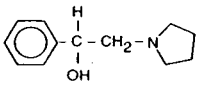		2.02	1.61	6.07	1.68	1.75	4.20	2.18	1.27	0.69
D	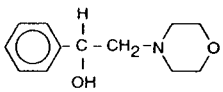		5.02	1.23	3.50	4.54	1.44	6.26	3.37	1.45	5.64
E	$CH_3(CH_2)_3$	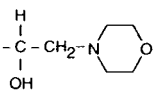	(1.32)	(1.13)	(1.07)	(1.28)	(1.20)	(1.55)	(1.58)	(1.00)	(0.00)
F	$CH_3(CH_2)_7$	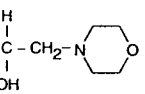	(1.11)	(1.15)	(1.23)	(1.06)	(1.18)	(1.34)	(1.17)	(1.00)	(0.00)

Results in parenthesis were obtained with a Chiralpak AD column manufactured in January 1992, all other results were obtained with a column manufactured in December 1990.

sented in Table 2 contain no obvious trends in retention, stereoselectivity or resolution when R_1 was held constant and R_2 was varied. However both retention and resolution increased when R_2 (A vs. C and B vs. D) was constant and R_1 was a phenyl group rather than an aliphatic group. Stereoselectivity was generally better when MeOH or EtOH was used as the alcohol component of the mobile phase.

The enantiomers of compounds A and B contained an aliphatic substituent at R_1 while compounds C and D contained an phenyl substituent in this position. The enantiomers of compounds A and B generally eluted before the enantiomers of compounds C and D, regardless of the other substituents at R_1 and R_2 or the composition of the mobile phase (Fig. 1). The resolution increased significantly in all mobile phases when the R_1 substituent was a phenyl group rather than the aliphatic substituent (A vs. C and B vs. D).

Peak tailing for the pyrrolidino compounds, A and C, increased as the polarity of the alcohol modifier in the mobile phase decreased (Fig. 1). The pyrrolidino group is the smallest of the amine substituents and is also more basic than the morpholino group. Consequently, ring size and the polarity of the mobile phase may play a role in peak shape. All interactions that affect peak shape are moderated by the strength of the alcohol modifier. Mobile phases containing MeOH gave the best peak shape and those containing IPA gave the worst peak shape.

Some differences in column performance and peak shape were noted when the same mixture was injected onto two columns prepared from different lots of packing material. The resolution and peak shapes obtained from the separation of

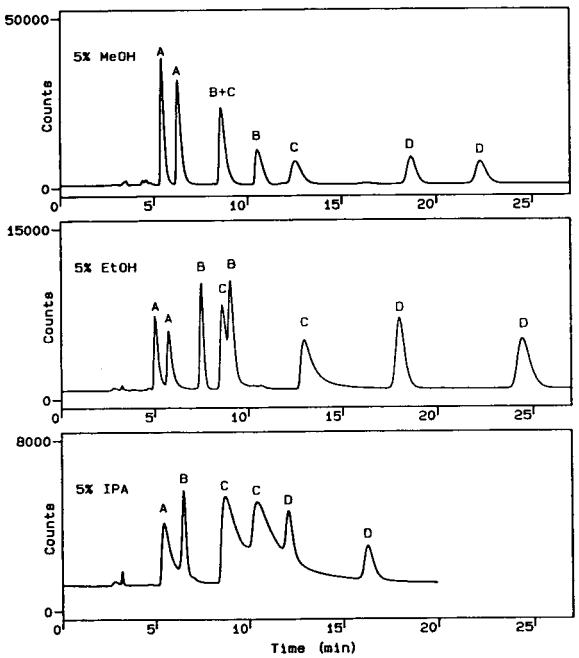

Fig. 1. Effect of MeOH, EtOH and IPA in a pentane-based mobile phase on the direct enantiomeric separation of some β-dialkylamino alcohols. Chromatographic conditions: mobile phase, 95% pentane and 5% MeOH (A), EtOH (B) or IPA (C); flow-rate 1 ml/min; injection volume, 10 μl; analytical column Chiralpak AD; UV detection at 210 nm.

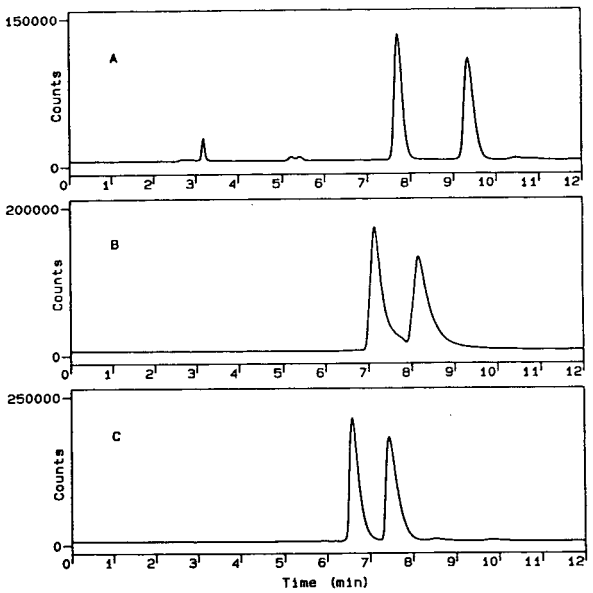

Fig. 2. Representative example of the difference in the separation of 1-(4-morpholino)-2-octanol (compound B) obtained with two different Chiralpak AD columns. Chromatographic conditions: mobile phase, ethanol–pentane (5:95); flow-rate 2 ml/min; injection volume, 10 μl; analytical column Chiralpak AD; UV detection at 210 nm. (A) Column A, manufactured in December 1990 and never exposed to diethylamine; (B) column B, manufactured in January 1992 and never exposed to diethylamine; column B after exposure to 0.1% diethylamine in the mobile phase and reequilibration with a mobile phase of ethanol–pentane (5:95).

1-(4-morpholino)-2-octanol (compound B, Table 2) were significantly different (Fig. 2).

Aboul-Enein and Serignese [39] used diethylamine in hexane-based mobile phases to improve the peak shape of a series of β-blockers that they resolved on a cellulose 3,5-dimethylphenyl carbamate CSP. Adding 0.1–0.4% diethylamine to the mobile phase slightly decreased retention times, led to sharper and more symmetrical peaks, and improved resolution.

We attempted to improve peak shape of 1-(4-morpholino)-2-octanol (Fig. 2B) by conditioning column B for several hours after adding 0.1% diethylamine to the mobile phase. The column was reequilibrated with a mobile phase containing EtOH–pentane (5:95) and the separation repeated (Fig. 2C). Retention was reduced slightly, resolution increased, and the peak tailing was decreased. The cellulose- and amylose-based stationary phases may have an affinity for some additives or compounds. The chromatograms may, therefore, reflect the history of the column or the lot of silica gel used in its manufacturing.

Specific type of alcohol

The alcohol component of the mobile phase affects enantiomeric separations obtained with cellulosic and amylosic CSPs [35,39–44]. We investigated the effect of the alcohol on the separation of 1-(4-morpholino)-2-octanol and 2-(4-morpholino)-1-phenylethanol (compounds B and D of Table 2) by using six different alcohol-modified pentane mobile phases. The modifiers included two aliphatic alcohols, EtOH and 1-octanol, two unusual modifiers, cyclohexanol and *tert.*-amyl alcohol, chosen for their steric

bulk, and two fluorinated alcohols chosen for their potential ability to influence hydrogen bonding interactions. The composition of the mobile phases was based on volume and not molarity as reported by Wainer et al. [44]. Therefore, the number of alcohol molecules available for solvation or competing for active sites was not constant in all mobile phases and may have influenced some of the results.

The effect of the alcohol modifiers is shown in Fig. 3. The following conclusions regarding changes in retention or resolution were drawn from comparisons to the separation obtained with the mobile phase EtOH–pentane (5:95). Retention was shorter when fluorinated alcohols or cyclohexanol were used and longer when *tert.*-amyl alcohol or 1-octanol were used. The best resolution was obtained with EtOH–pentane; the worst when *tert.*-amyl alcohol or cyclohexanol was used. *tert.*-Amyl alcohol and cyclohexanol are the most bulky alcohol modifiers and may interfere with the binding sites near the chiral cavity. Peak shape was affected the most when aliphatic alcohol modifiers were used. Peak tailing was pronounced with *tert.*-amyl alcohol and 1-octanol.

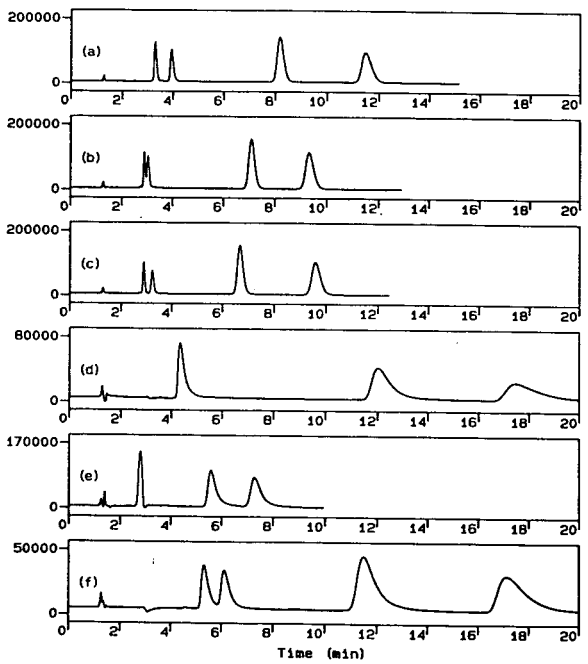

Fig. 3. Effect of alcohol modifiers in a pentane-based mobile phase on the direct enantiomeric separation of 1-(4-morpholino)-2-octanol (compound B) and 2-(4-morpholino)-1-phenylethanol (compound D). Chromatographic conditions: mobile phase 95% pentane and (a) 5% EtOH, (b) 1.5% 2,2,2-trifluoroethanol and 3.5% EtOH, (c) 1.5% 1,1,1,3,3,3-hexafluoropropanol and 3.5% EtOH, (d) 5% *tert.*-amyl alcohol, (e) 5% cyclohexanol, (f) 5% 1-octanol; flow-rate 2 ml/min; injection volume, 10 μl; analytical column Chiralpak AD; UV detection at 210 nm.

The effect of the alcohol modifiers was significantly different when R_1 was a phenyl group, for example, 2-(4-morpholino)-1-phenylethanol (compound D of Table 2). Retention was longer when *tert.*-amyl alcohol or 1-octanol were used and shorter when cyclohexanol was used. The best resolution was obtained in EtOH–pentane. The effect on peak shape was more dramatic for 2-(4-morpholino)-1-phenylethanol than 1-(4-morpholino)-2-octanol. Peak tailing was the most pronounced in *tert.*-amyl alcohol.

The use of 1.5% (v/v) of the fluorinated alcohols reduced retention and resolution regardless of the type of substituent at R_1. Peak shapes were unaffected. The fluorinated alcohols increased the eluotropic strength of the mobile phase without eliminating the hydrogen bonding essential for chiral recognition.

Effect of water

Water has been used as a mobile phase modifier in supercritical fluid chromatography [16,17] and in conventional HPLC [35,45,46] separations of enantiomers. Balmér et al. [45] initially reported that the water content of their mobile phase, 4% IPA and 0.1% diethylamine in hexane, was very important in the enantiomeric separation of metoprolol and its α-hydroxy metabolite. The addition of water did not significantly effect the retention of the (*R*)-enantiomer, but the retention of the (*S*)-isomer was nearly halved. However, the water effect may not be universal. When Balmér et al. [46] used water in the mobile phase to separate the enantiomers of almokalant on Chiracel OD and Chiralpak AD CSPs, they found that the stereoselectivity was affected. The retention of the (*R*)-isomer was decreased on both CSPs. When Balmér et al. [35] studied the effect of water on the separation

of amino alcohols they again found that it had a significant affect and caused a reversal in elution order of one of the solutes. The retention of the (*R*)-enantiomer was almost unaffected while the retention of the (*S*)-enantiomer decreased when the alcohol concentration was held constant and the water increased from 0.1 to about 1.6 g/l.

The effect of water was evaluated in our studies by comparing separations of the enantiomers of 2-(4-morpholino)-1-phenylethanol (compound D of Table 2) with and without water in the mobile phase. The separations were obtained by using mobile phases that contained known amounts of water added to IPA–pentane (5:95). Addition of up to 2000 mg/l of water generally increased retention and resolution. The addition of water significantly decreased peak tailing while increasing both retention and resolution (Fig. 4). These results indicate that it may be beneficial to add water to an IPA–pentane (5:95) mobile phase to improve separations for compounds structurally similar to 2-(4-morpholino)-1-phenylethanol.

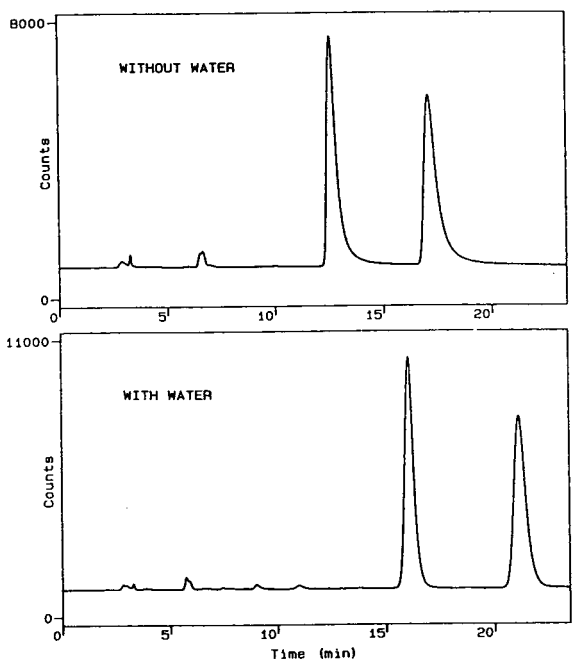

Fig. 4. Effect of adding water to an IPA–pentane mobile phase on the separation of 2-(4-morpholino)-1-phenylethanol (compound D). Chromatographic conditions: mobile phase, 0.15% water in IPA–pentane (5:95); flow-rate 1 ml/min; injection volume, 10 μl; analytical column Chiralpak AD; UV detection at 210 nm.

3.2. Substituent effects

Ring size and heteroatom effects associated with the substituent at R_2 were noted in the various mobile phases (Table 2). Retention increased when the pyrrolidino group was replaced with a morpholino group (compare A vs. B and C vs. D). Resolution also increased in all of the comparisons except for A vs. B in an IPA-modified mobile phase and C vs. D in the MeOH-modified mobile phase. The size of the R_2 group may be important from steric considerations, and the hydrogen bonding capacity of the cyclic amine appears to be enhanced by the presence of an additional heteroatom in the ring system.

Acknowledgements

The authors wish to thank Mr. Joe Raab of the Michigan Division Purchasing Department and Mr. Hiroyoshi Shimizu of Dow Chemical Japan for their assistance in obtaining (*R*)-1,2-epoxyoctane.

References

[1] C.L. Davies, *J. Chromatogr.*, 531 (1990) 131.
[2] D.T. Witak and M.N. Inbasekaran, in M. Grayson (Editor), *Kirk-Othmer Encyclopedia of Chemical Technology*, Vol. 17, Wiley, New York, 1982, pp. 311–345.
[3] Q. Yang, Z.-P. Sun and D.-K. Ling, *J. Chromatogr.*, 447 (1988) 208.
[4] E.J. Ariëns, in A.M. Krstulovic (Editor), *Chiral Separations by HPLC: Applications to Pharmaceutical Compounds*, Wiley/Ellis Horwood, Chichester, 1989, pp. 31–68.
[5] B. Waldeck, *Chirality*, 5 (1993) 350.
[6] W. Nelson and T. Burke, *J. Org. Chem.*, 43 (1978) 3641; and references cited therein.
[7] B.T. Cho and Y.S. Chun, *Tetrahedron Asymmetry*, 3 (1992) 341.
[8] K. Soai, S. Yokoyama and T. Hayasaka, *J. Org. Chem.*, 56 (1991) 4264.

[9] K. Soai, M. Okudo and M. Okamoto, *Tetrahedron Lett.*, 32 (1991) 95.
[10] K. Soai, S. Yokoyama, T. Hayasaka and K. Ebihara, *J. Org. Chem.*, 53 (1988) 4148.
[11] C.T. Goralski, B. Singaram and H.C. Brown, *J. Org. Chem.*, 52 (1987) 4014; and references cited therein.
[12] G.M. Coppola and H.F. Schuster, *Asymmetric Synthesis: Construction of Chiral Molecules Using Amino Acids*, Wiley-Interscience, New York, 1987, pp. 53, 85, 115, 133, 159, 188.
[13] M. Kitamura, T. Ohkuma, S. Inoue, N. Sayo, H. Kumobayashi, S. Akutagawa, T. Ohta, H. Takaya and R. Noyori, *J. Am. Chem. Soc.*, 110 (1988) 629.
[14] G.B. Fisher, C.T. Goralski, L.W. Nicholson and B. Singaram, *Tetrahedron Lett.*, 34 (1993) 7693.
[15] W.-Y. Li, H.L. Jin and D.W. Armstrong, *J. Chromatogr.*, 509 (1990) 303.
[16] L. Siert, N. Bargmann, A. Tambuté and M. Caude, *Chirality*, 4 (1992) 252.
[17] P. Biermanns, C. Miller, V. Lyon and W. Wilson, *LC·GC*, 11 (1993) 744.
[18] G. Egginger, W. Lindner, C. Vandenbosch and D.L. Massarat, *Biomed. Chromatogr.*, 7 (1993) 277.
[19] B. Gallinella, F. La Torre, R. Cirilli and C. Villani, *J. Chromatogr.*, 639 (1993) 193.
[20] L. Olsen, K. Brønnum-Hansen, P. Helboe, G.H. Jørgensen and S. Kryger, *J. Chromatogr.* 636 (1993) 231.
[21] Y. Dobashi and S. Hara, *J. Org Chem.*, 52 (1987) 2490.
[22] I.W. Wainer, T.D. Doyle, F.S. Fry, Jr. and Z. Hamidzadeh, *J. Chromatogr.*, 355 (1986) 149.
[23] E. Delée, L. Le Garrec, I. Jullien, S. Béranger, J.C. Pascal and H. Pinhas, *Chromatographia*, 24 (1987) 357.
[24] K. Iwaki, S. Yoshida, N. Nimura, T. Kinoshita, K. Takeda and H. Ogura, *Chromatographia*, 23 (1987) 899.
[25] S. Yamazaki, T. Takeuchi and T. Tanimura, *J. Chromatogr.*, 540 (1991) 169.
[26] J. Gal, *J. Liq. Chromatogr.*, 9 (1986) 673.
[27] C. Pettersson, E. Heldin and H.W. Stuurman, *J. Chromatogr. Sci.*, 28 (1990) 413.
[28] C. Pettersson and M. Josefsson, *Chromatographia*, 21 (1986) 321.
[29] E. Heldin, K.-J. Lindner, C. Pettersson, W. Lindner and R. Rao, *Chromatographia*, 32 (1991) 407.
[30] F. Gasparrini, D. Misiti, C. Villani and F. La Torre, *J. Chromatogr.*, 539 (1991) 25.
[31] M. Ohwa, M. Akiyoshi and S. Mitamura, *J. Chromatogr.*, 521 (1990) 122.
[32] K.M. Kirkland, K.L. Neilson and D.A. McCombs, *J. Chromatogr.*, 545 (1991) 43.
[33] G. Gübitz, B. Pierer and W. Wendelin, *Chirality*, 4 (1992) 333.
[34] W.H. Pirkle and J.A. Burke, III, *J. Chromatogr.*, 557 (1991) 173.
[35] K. Balmér, P.-O. Lagerström, B.-A. Persson and G. Schill, *J. Chromatogr.*, 592 (1992) 331.
[36] C.B. Ching, B.G. Lim, E.J.D. Lee and S.C. Ng, *Chirality*, 4 (1992) 174.
[37] Y. Okamoto, M. Kawashima, R. Aburatani, K. Hatada, T. Nishiyama and M. Masuda, *Chem. Lett.*, (1986) 1237.
[38] H.Y. Aboul-Enein and M.R. Isalm, *J. Chromatogr.*, 511 (1990) 109.
[39] H.Y. Aboul-Enein and V. Serignese, *J. Liq. Chromatogr.*, 16 (1993) 197.
[40] Th. Hollenhorst and G. Blaschke, *J. Chromatogr.*, 585 (1991) 329.
[41] Y. Okamoto, M. Kawashima and K. Hatada, *J. Chromatogr.*, 363 (1986) 173.
[42] H.Y. Aboul-Enein and R. Islam, *J. Liq. Chromatogr.*, 13 (1990) 485.
[43] I.W. Wainer, M.C. Alembik and E. Smith, *J. Chromatogr.*, 388 (1987) 65.
[44] I.W. Wainer, R.M. Stiffen and T. Shibata, *J. Chromatogr.*, 411 (1987) 139.
[45] K. Balmér, A. Persson, P.-O. Lagerström, B.-A. Persson and G. Schill, *J. Chromatogr.*, 553 (1991) 391.
[46] K. Balmér, P.-O. Lagerström, S. Larsson and B.-A. Persson, *J. Chromatogr.*, 631 (1993) 191.
[47] G.B. Fisher, C.T. Goralski, L.W. Nicholson and B. Singaram, *J. Org Chem.*, submitted for publication.

ELSEVIER

Journal of Chromatography A, 687 (1994) 249–258

JOURNAL OF CHROMATOGRAPHY A

On-line coupling of flow field-flow fractionation and multi-angle laser light scattering

Dierk Roessner, Werner-Michael Kulicke*

Institut für Technische und Makromolekulare Chemie, Universität Hamburg, Bundesstrasse 45, 20146 Hamburg, Germany

First received 6 June 1994; revised manuscript received 16 August 1994

Abstract

This paper describes the first successful coupling of a flow field-flow fractionator with a multi-angle laser light-scattering photometer in order to carry out absolute measurements of even high molar mass and radius of gyration distributions. Two standards with broad molar mass distributions, polystyrene particles and coil-shaped dissolved dextrans were investigated in order to establish the efficiency of this experimental apparatus. The distribution functions of molar mass and radius of gyration were determined for the samples. The results calculated for the dextran sample from the distribution functions were a weight-average molar mass of 2 730 000 g/mol and a z-average radius of gyration of 47 nm. Comparison with results obtained from a conventional apparatus, consisting of size-exclusion chromatography and a light-scattering photometer, showed that field-flow fractionation is able to separate molecules in the range where size-exclusion chromatography fails owing to the existence of an exclusion boundary. The polystyrene latex sample gave results of 13 400 000 g/mol for the weight-average molar mass and 15 nm for the z-average radius of gyration. In addition, a structure–property relationship in the form of an $\langle R_G^2 \rangle^{1/2}$ versus M relationship was calculated for each substance. For the polystyrene latex standard in water an exponent of 0.33 ± 0.02 was found. The corresponding value for the dextran in 0.1 M sodium nitrate solution was 0.50 ± 0.01.

1. Introduction

In view of the increasing interest in water-soluble polymers, which results from their numerous applications, there is a great demand for information on the steric structure of these substances, which holds for both non-ionic [1,2] and ionic [1,3–5] polymers. The steric structure may be described by distributions or average values of the molar masses and radii. One example of an application where a knowledge of these parameters is important is the clinical use of polymeric substances as plasma expanders for restoring the volume and improving the flow behaviour of blood. Solutions of hydroxyethyl starch or dextran in electrolytic solutions isotonic with the blood are used for this purpose. These polymers, the structures of which affect the pharmacokinetics and pharmacology of the preparation, can be fractionated by means of size-exclusion chromatography (SEC) and thus be characterized in more detail [6,7].

However, this established method of fractionation is subject to certain restrictions that prevent the characterization of polymer molecules strongly adsorbed by the packing material in the column. In addition, large polymer molecules can be excluded from fractionation or degraded

* Corresponding author.

0021-9673/94/$07.00
SSDI 0021-9673(94)00818-3

even at low flow-rates [8]. These problems occur for a large number of high-molar-mass, water-soluble polymers with interesting technical applications. Examples of these are the synthetic high-molar-mass polyelectrolytes used in industrial chemistry as flocculating agents for clarifying sludges [9], or cellulose derivatives [10] used in building materials, foodstuffs, paper, cosmetics and pharmaceuticals. Such polymers can exceed a radius of gyration of more than 200 nm [3] and consequently they are excluded because of their hydrodynamic volume, and therefore cannot be fractionated by size-exclusion chromatography.

Field-flow fractionation (FFF) was developed in order to fractionate substances for which size-exclusion chromatography is not effective. As demonstrated by Giddings and co-workers, it is a method for rapidly and efficiently fractionating high-molar-mass macromolecules and particles. Three different methods of field-flow fractionation have proved to be successful: sedimentation field-flow fractionation [11–13], thermal field-flow fractionation [14–16] and flow field-flow fractionation [17–19] (FFFF). The advantages of these fractionation techniques lie in their lack of sensitivity to adsorption [20] and in their extremely high upper working limit of particle diameters of ca. 50 μm [21].

The aim of our investigations was to establish whether the FFFF method could be coupled with a multi-angle laser light-scattering photometer for absolute measurement of masses and radii, thus obviating the need for any calibration with polymer standards or a universal elution curve. Successful coupling of FFFF with multi-angle laser light scattering (MALLS) would have the advantage of permitting the analytical fractionation of even problematic, high-molar-mass polymers and the on-line determination of molar masses and radii of gyration. In addition, the concentration of each of the species to be eluted can be measured by means of a differential refractometer. In this way, from a single experiment, it should be possible to carry out determinations of the distributions of molar mass and radius of gyration together with their mean values and to establish a structure–property relationship [22].

2. Theory

2.1. Multi-angle laser light scattering

Light scattering is one of a few methods available for the absolute determination of molar mass and structure and is certainly applicable over the broadest range of molar mass of any method. Early developments of the theory of light scattering from macromolecular solutions and suspensions were made by Einstein [23], Raman [24], Debye [25] and Zimm [26].

Values for the molar mass M and radius of gyration $\langle R_G^2 \rangle^{1/2}$ at each slice across the distribution were calculated using the usual light scattering equations:

$$\frac{Kc}{R_\vartheta} = \frac{1}{M_W P_{(\vartheta)}} + 2A_2 c \tag{1}$$

where

$$K = \frac{4\pi^2 n_0^2}{N_A \lambda_0^4} \left(\frac{dn}{dc}\right)^2 \tag{2}$$

$$R_\vartheta = \frac{r^2 I_\vartheta}{I_0 V} \tag{3}$$

$$P_{(\vartheta)}^{-1} = 1 + \frac{\langle R_G^2 \rangle_z q^2}{3} \tag{4}$$

$$q = \frac{4\pi n_0}{\lambda_0} \cdot \sin\left(\frac{\vartheta}{2}\right) \tag{5}$$

This equation incorporates the light-scattering constant for vertically polarized incident light, K, which contains the refractive index increment dn/dc, the concentration, c, the Rayleigh ratio, R_ϑ, at the scattering angle ϑ, the weight-average molar mass, M_w, and the second virial coefficient A_2. The Rayleigh ratio, R_ϑ, is used to obtain a parameter for the scattered light intensity that is independent of the measuring conditions. The function $P_{(\vartheta)}$ describes the angular dependence of the scattered light intensity. For small angles it is only dependent on the radius of gyration and not on factors such as molecular conformation or branching.

Irrespective of the fractionation method, one must assume that in a fractionation experiment on polymers with a unique relationship between molar mass and radius of gyration and elution

volume, the distribution within a given element of the elution volume is so negligibly small that the weight-average molar mass and the z-average radius of gyration become equivalent to the values for a monodisperse sample.

2.2. Flow field-flow fractionation

The essential component of a field-flow fractionator is the so-called channel. In the case of FFFF, it consists of two Perspex blocks fitted with ceramic frits and a semi-permeable membrane. Between these blocks there is a spacer with the cut-out channel. Two currents are generated in the channel: the channel flow, $\dot{V}$, along the block and the cross flow, $\dot{V}_x$, perpendicular to the channel flow using the frits installed in the channel. The perpendicular or external field forces the various species of the sample into different flow layers of the laminar channel flow, where they are transported at different velocities and thus only separated according to their diffusion coefficients.

The mathematical formulation of the elution behaviour of polymers and particles during field-flow fractionation and especially during flow field-flow fractionation has been discussed in detail in a number of publications [27–29]. For flow field-flow fractionation in the normal mode the following equation applies to the retention time of a species, t_R:

$$t_R = \frac{w^2}{6D} \cdot \frac{\dot{V}_x}{\dot{V}} \tag{6}$$

From Eq. 6 it can be seen that the retention time, t_R, of a species is directly proportional to the square of the channel thickness, w, and inversely proportional to the diffusion coefficient, D, of the species. There is also a direct proportionality with the quotient of cross flow, $\dot{V}_x$, and channel flow, $\dot{V}$. This indicates that the retention time of a species can be varied by altering the channel flow or cross flow. The diffusion coefficient can be used for calculating the molecular dimensions in the form of the Stokes diameter, d_S. The mathematical basis for this is provided by the Stokes–Einstein equation shown in Eq. 7.

$$D = \frac{kT}{3\pi\eta d_S} \tag{7}$$

$$t_R = \frac{\pi\eta w^2}{2kT} \cdot \frac{\dot{V}_x}{\dot{V}} \cdot d_S \tag{8}$$

Eq. 8, which can be formed by linking Eqs. 6 and 7, gives the dependence of the retention time, t_R, on the material and experimental parameters. FFF enables diffusion coefficients and particle dimensions to be measured absolutely. In the case of homogeneous, spherical particles, the molar mass can also be determined absolutely in this way. For coil-shaped polymers in solution, FFFF yields relatively determined molar masses [30]. For this reason, the absolute method of light scattering was employed to determine molar mass, thus obviating the need for calibration with polymer standards.

3. Experimental

The FFFF experiments were carried out with a Model F-1000 Universal Fractionator, manufactured by FFFractionation (Salt Lake City, UT, USA). A schematic representation of the experimental apparatus is given in Fig. 1. The dimensions of the channel were 28.5 cm long, 2.0

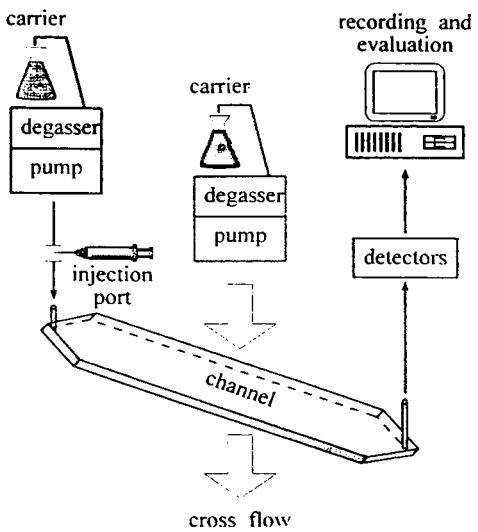

Fig. 1. Schematic representation of FFFF–MALLS apparatus.

cm wide and 0.025 cm thick. Two HPLC pumps were employed to generate the current of the carrier liquid. The volume flows were monitored gravimetrically. The polystyrene sample was specially provided for the experiments by FFFractionation. FFFF experiments with this sample used doubly distilled water containing 0.02% (w/w) sodium azide and 0.05% (w/w) sodium dodecyl sulphate as the carrier liquid. The FFFF experiments on the polysaccharide dextran (Pfeifer and Langen Pharma) were carried out in a 0.1 *M* sodium nitrate solution containing 0.02% (w/w) of sodium azide.

Size-exclusion chromatography employed TSK 60/50/40/30 PW XL columns (Toyo Soda), arranged in order of decreasing pore size. The columns were conditioned in a column heater at 295 K. The flow-rate was 1 ml min^{-1}. The solvent used was doubly distilled water containing 0.1 *M* sodium nitrate and 0.02% (w/w) sodium azide. A 100-μl injection loop and a $1 \cdot 10^{-3}$ g ml^{-1} solution of dextran were used.

Concentration detection was performed with a Shodex RI SE-51 differential refractometer manufactured by Showa Denko (Tokyo, Japan). Detection of scattered light was carried out with a Watt Technologies (Santa Barbara, CA, USA) Dawn-F multi-angle laser light-scattering photometer. The instrument was operated with vertically polarized light of wavelength 632.8 nm at a temperature of 295 K. The light-scattering photometer was calibrated with toluene. The normalization coefficients were measured with gold dispersion. The spider-plot method with narrowly distributed standards was used to measure the interdetector volume [31]. The signal from the differential refractometer was routed to the Dawn-F, which was interfaced to an AT computer. Software from Wyatt Technologies was used to analyse the data.

4. Results and discussion

4.1. Fractionation of a particle dispersion

Lattices are dispersions of spherical polymer particles manufactured by emulsion polymerization. They are characterized by a low viscosity, even at high concentrations, and are used on a large commercial scale for the manufacture of paints, impregnating agents and adhesive pastes.

The results of the FFFF–MALLS experiments on the polystyrene latex standard B1 are summarized in Figs. 2–5 and Tables 1 and 2. In Fig. 2 the radii of gyration calculated from the initial curves of the scattering functions are plotted as a function of the elution volume.

The fluctuation of the data points at small elution volumes is the result of the fact that the particle dimensions in this area are approximately $<\lambda/20$. For such small particles the angular dependence of $P(\vartheta)$ becomes unimportant since the scattering is essentially isotropic, and one is therefore unable to determine the radius of gyration. According to the equation

$$d_{LS} = \sqrt{\frac{20}{3}} \cdot \langle R_G^2 \rangle^{1/2} \quad (9)$$

which relates spherical particle dimensions to the radius of gyration, the lowest radius that can be measured is about 9 nm. In the range of higher elution volumes there is a fluctuation of data points because of the weak signals of the photodiodes.

By including the concentration, which was measured on-line with the differential refractometer for each of the eluates investigated, it is possible to calculate the radius of gyration distribution shown in Fig. 3. The range that could not be measured because of the limitation in

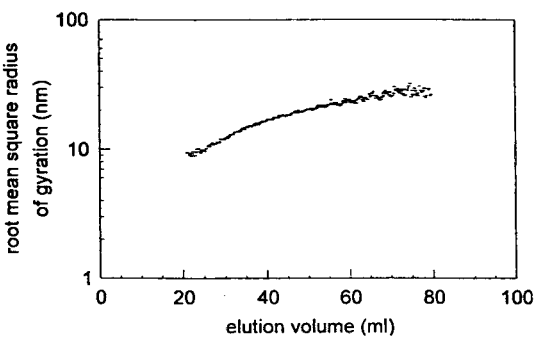

Fig. 2. Radii of gyration of the polystyrene latex sample B1 as a function of the elution volume. The channel flow was 1.0 ml min^{-1} and the cross-flow 2.0 ml min^{-1}.

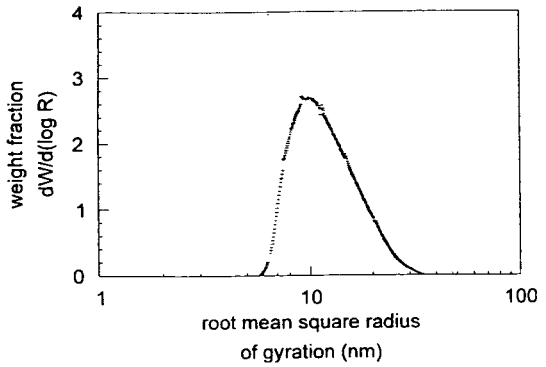

Fig. 3. Differential distribution of the radius of gyration for the polystyrene latex sample B1.

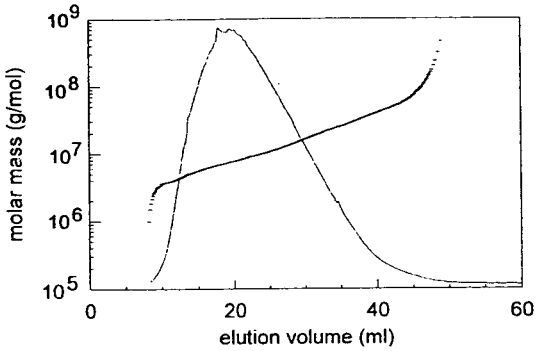

Fig. 4. Refractive index chromatogram and plot of molar masses of the polystyrene latex sample B1 determined by means of light-scattering measurements as a function of the elution volume.

light scattering was calculated by using a linear extrapolation in the radius versus mass plot. The data were used to determine the characteristic average values $\langle R_G^2 \rangle_n^{1/2}$, $\langle R_G^2 \rangle_w^{1/2}$ and $\langle R_G^2 \rangle_z^{1/2}$ by means of their definition relationships [22].The error values are the percentage standard deviations resulting from four measurements. The distribution function was used to determine the minimum, maximum and most frequent diameter, d_{LS}.

These values are compiled in Table 1 under the heading FFFF–MALLS. To verify these values, they are compared with Stokes diameters, d_S, from an FFFF–UV experiment on this sample. The FFFF–UV experiment was carried out by FFFractionation [32], who used FFFF to separate the sample and a UV detector to monitor the eluate. In addition, Table 1 also includes the measured diffusion coefficients, D. Good agreement between the independently determined dimensions can be seen.

In Fig. 4 the refractive index chromatogram and the molar masses of the polystyrene latex sample determined by means of light scattering are represented as a function of the elution volume. With small elution volumes and correspondingly small particles the molar masses deviate to lower values. This behaviour must be a direct measure of the secondary instrument broadening that occurs in the system. Such instrumental broadening would be expected to

Table 1
Compilation of the dimensions of the polystyrene latex standard B1

Variable	FFFF–MALLS	FFFF–UV (254 nm)
$\langle R_G^2 \rangle_n^{1/2}$ (nm)	10 ± 10%	–
$\langle R_G^2 \rangle_w^{1/2}$ (nm)	12 ± 8%	–
$\langle R_G^2 \rangle_z^{1/2}$ (nm)	15 ± 7%	–
Maximum D ($cm^2\ s^{-1}$)	$2.9 \cdot 10^{-7}$	$2.9 \cdot 10^{-7}$
Most frequent D ($cm^2\ s^{-1}$)	$2.0 \cdot 10^{-7}$	$1.5 \cdot 10^{-7}$
Minimum D ($cm^2\ s^{-1}$)	$0.6 \cdot 10^{-7}$	$0.5 \cdot 10^{-7}$
Minimum diameter (nm)	$d_{LS} = 16$	$d_S = 16$
Most frequent diameter (nm)	$d_{LS} = 26$	$d_S = 28$
Maximum diameter (nm)	$d_{LS} = 85$	$d_S = 83$

The radii of gyration of the FFFF–MALLS experiments result from evaluation of the scattered light intensities, and the diameters d_{LS} were calculated from the radii of gyration. The FFFF–UV experiment was carried out by FFFractionation and yielded the Stokes diameters, d_S. The errors indicated correspond to the percentage standard deviation of the results from four experiments.

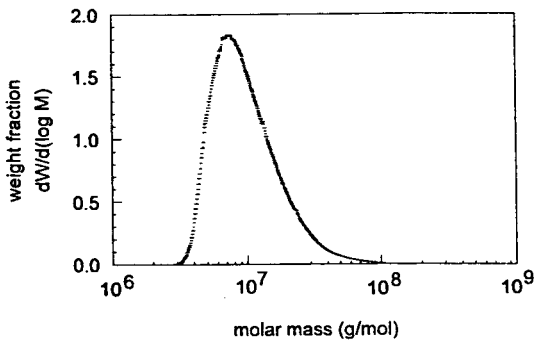

Fig. 5. Differential distribution of the molar mass for the polystyrene latex sample B1.

lower the molar mass by causing excessively high concentration values [31,33]. In the range of higher elution volumes and correspondingly large particles the molar masses deviate to higher values. This behaviour seems to be the result of the different sensitivities of the two detectors. In this range of low concentrations and large particles the light-scattering photometer, sensitive to molar mass, yields high signals whereas the differential refractometer yields no significant signal because of the very low concentration of the scattering particles.

The molar mass distribution represented in Fig. 5 was calculated by including the concentration of each respective species. From this distribution it was possible to determine the number-average, weight-average and z-average molar masses, and also other characteristic values. These results and molar mass values from an FFFF–UV experiment are compiled in Table 2.

The measurements of the polystyrene latex standard show that the multi-angle laser light-scattering photometer is suitable for monitoring the eluate from the flow field-flow fractionator. The angular-dependent scattered light readings yield the absolutely determined radius of gyration and molar mass and, by including the respective concentrations, they also yield the distributions for these two variables. For lattices FFF provides absolute values for diffusion coefficients and hence, by employing the Stokes–Einstein relationship, also the absolute values for Stokes diameter and molar mass. In this way it is possible to determine the structural parameters of lattices independently of one another in a single experiment. Correlation of the results obtained by these two methods may be regarded as sufficiently accurate. However, it must be remembered that the procedure applied in the evaluation of the scattered light measurements contains two assumptions that are not fulfilled in the case of measurements on particles. The first assumption is that the wave front is not altered

Table 2
Compilation of the molar mass values for the polystyrene latex standard B1

Variable	FFFF–MALLS	FFFF–UV (254 nm)
M_n (g mol^{-1})	$7.3 \cdot 10^6 \pm 12\%$	–
M_w (g mol^{-1})	$13.4 \cdot 10^6 \pm 13\%$	–
M_z (g mol^{-1})	$32.1 \cdot 10^6 \pm 15\%$	–
M_w/M_n	1.8	–
M_z/M_n	4.4	–
Minimum M (g mol^{-1})	$2.9 \cdot 10^6$	$1.3 \cdot 10^6$
Most frequent M (g mol^{-1})	$7.1 \cdot 10^6$	$7.3 \cdot 10^6$
Maximum M (g mol^{-1})	$180 \cdot 10^6$	$190 \cdot 10^6$

The data from the FFFF–MALLS measurements result from scattered light measurements. The molar masses of the FFFF–UV experiment carried out by FFFractionation were calculated from the Stokes diameters.

on its passage through the sample and the second is that the difference in refractive index between sample and solvent is small.

4.2. Fractionation of a coil-shaped dissolved polymer

Dextrans are neutral, branched exopolysaccharides that are made enzymatically from sucrose. They are used as the base for manufacturing plasma expanders. In a three-dimensionally cross-linked form they serve as a separating medium in size-exclusion chromatography under the name Sephadex gel. This polymer was used for conducting trials on FFFF–MALLS as a means of characterizing coil-shaped dissolved polymers. In order to verify the results, the polymer was also characterized by means of SEC–MALLS.

The differential distribution of radius of gyration is represented in Fig. 6 and the differential distribution of molar mass in Fig. 7. The distributions were determined by means of FFFF/MALLS. It can be seen that this sample consists of a low-molar-mass fraction with a radius of gyration of ca. 20 nm and a molar mass of ca. $3.5 \cdot 10^5$ g mol^{-1}, and a high molar mass fraction with a radius of gyration of ca. 45 nm and a molar mass of ca. $3 \cdot 10^6$ g mol^{-1}.

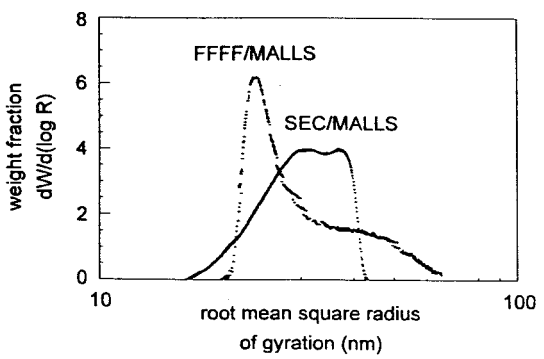

Fig. 6. Differential distribution of the radius of gyration for dextran, fractionation and detection were performed with FFFF–MALLS and SEC–MALLS. The channel flow was 1.0 ml min^{-1} and the cross-flow 0.7 ml min^{-1}.

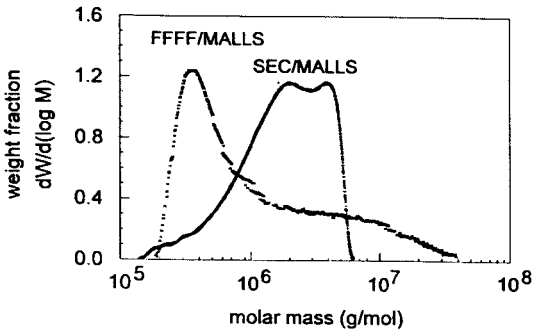

Fig. 7. Comparative representation of the differential distribution of molar mass from SEC–MALLS and FFF–MALLS experiments on the polysaccharide standard dextran.

Fig. 6 shows also the radius of gyration distribution and Fig. 7 the molar mass distribution of the dextran sample obtained by means of SEC–MALLS. The steep high-molar-mass flank can clearly be seen on the right-hand side in this distribution function. It is caused by the exclusion boundary of the chromatographic system. Comparison of the results for the two methods of fractionation shows that the low-molar-mass flank of the distribution function determined by SEC with the selected column combination has a better resolution. On the other hand, the resolution of FFFF in the middle and high molar mass range is better. This is to be expected because the mass selectivity and upper working limit of FFFF are much higher [34]. However, the fractionation of high-molar-mass substances is the most important aspect of this experiment. Proof of good separation by FFFF is given by the correct slope in the graph of $\langle R_G^2 \rangle^{1/2}$ versus M in Fig. 9. There is no loss of substance or degradation during the measurements, as the weight-average molar masses, M_w, for both experiments determined by light scattering are the same, within the limit of error.

Table 3 gives a compilation of the data from SEC–MALLS and FFFF–MALLS experiments for comparative purposes. The respective mean values calculated for the radii and molar masses show a significantly weaker degree of separation

Table 3
Compilation of the mean values of molar mass and radius of gyration for the dextran standard determined by FFFF–MALLS and SEC–MALLS

Variable	FFFF/MALLS	SEC/MALLS
M_n (g mol^{-1})	625 000 ± 14%	1 500 000 ± 8%
M_w (g mol^{-1})	2 730 000 ± 6%	2 680 000 ± 4%
M_z (g mol^{-1})	6 620 000 ± 9%	4 650 000 ± 6%
$\langle R_G^2 \rangle_n^{1/2}$ (nm)	29 ± 14%	40 ± 6%
$\langle R_G^2 \rangle_w^{1/2}$ (nm)	36 ± 6%	42 ± 5%
$\langle R_G^2 \rangle_z^{1/2}$ (nm)	47 ± 2%	44 ± 4%
M_w/M_n	4.4	1.8
M_z/M_n	10.6	3.1

The errors indicated correspond to the percentage standard deviation of the results from 10 experiments.

when compared with the results of FFFF–MALLS experiments. This results in the polydispersity being smaller by a factor of ca. 2.5. Within the limits of error for the two fractionation methods, the values of the weight-average molar mass, M_w, and the z-average radius of gyration, $\langle R_G^2 \rangle_z^{1/2}$, are the same. This is to be expected since light scattering yields precisely these moments of molar mass and radius of gyration for non-fractionated, and hence polydisperse, samples.

The investigations confirmed that this experimental set-up is able to determine distribution functions of the molar mass and the radius of gyration for dissolved polymers. The advantages of this set-up seems to lie in the applicability of FFFF, which is able to fractionate even problematic molecules of masses up to several 10^9 g mol^{-1} [34] combined with the high performance of the on-line MALLS photometer, which enables molar masses and radii of gyration to be measured absolutely.

4.3. Determination of the solution state

Performing an FFFF–MALLS experiment yields important data for polymer analysis in the form of distribution functions and means for the molar masses and radii of gyration. During the separation process, quasi-monodisperse fractions

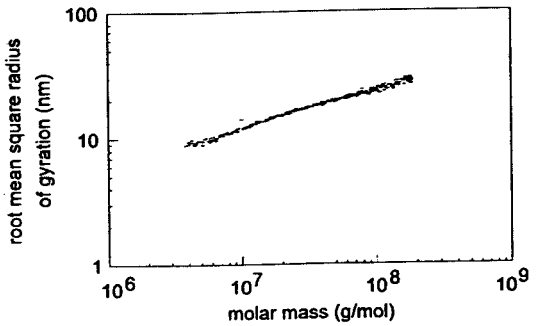

Fig. 8. Representation of the radii of gyration as a function of the molar mass for the polystyrene sample B1 in 0.05% (w/w) sodium dodecyl sulphate solution at 295 K, $\nu = 0.33$.

are characterized in terms of their molar mass and radius of gyration. These data can be used to establish a relationship between these two variables. The general form of such a relationship is given by

$$\langle R_G^2 \rangle^{1/2} = K_R M^{\nu} \tag{10}$$

Like the radius of gyration, the Staudinger index is a measure of the volume of a dissolved polymer molecule with respect to its mass. This quantitative relationship given by the Kuhn–Mark–Houwink–Sakurada relationship, represented by the equation

$$[\eta] = K_\eta M^a \tag{11}$$

Transformation from the form of Eq. 10 to that of Eq. 11 by means of the Flory–Fox theory [35] enables a comparison to be carried out of the experimental readings for the dextran with published Kuhn–Mark–Houwink–Sakurada relationships.

Table 4
Experimentally and theoretically derived $\langle R_G^2 \rangle^{1/2}$ versus M relationships for the polystyrene latex sample in 0.05% (w/w) sodium dodecyl sulphate solution

Source	Structure–property relationship
Experimental	$\langle R_G^2 \rangle^{1/2} = 0.055 M^{0.33}$ (nm)
Theoretical	$\langle R_G^2 \rangle^{1/2} = 0.056 M^{0.33}$ (nm)

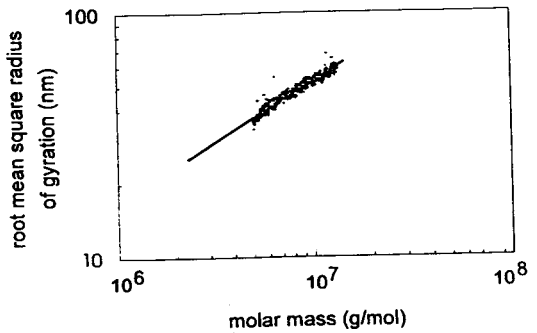

Fig. 9. Graph of the radius of gyration of the polysaccharide dextran as a function of the molar mass in 0.1 *M* sodium nitrate solution at a temperature of 295 K, determined by SEC–MALLS and FFFF–MALLS.

In Fig. 8 the radii of gyration for the polystyrene latex sample are plotted against the molar masses in accordance with Eq. 10. The exponent ν was determined from the double-logarithmic plot. The pre-exponential factor K_R was determined by calculating the density of particles from the values of the measured radii and molar masses of the slices along the distribution. Table 4 provides a compilation of the experimental and a theoretical $\langle R_G^2 \rangle^{1/2}$ versus M relationship for rigid spheres. Good agreement can be seen.

Fig. 9 is a double-logarithmic plot of the $\langle R_G^2 \rangle^{0.5}$ versus M relationship for dextran. The solvent used was 0.1 *M* sodium nitrate solution containing 200 ppm of sodium azide. Measurements were carried out at a temperature of 295 K. The constant $K_R = 0.03$ and the exponent $\nu = 0.50 \pm 0.01$ were determined by linear extrapolation. Application of Flory–Fox–theory enabled the Kuhn–Mark–Houwink–Sakurada relationship to be calculated. For comparison this result is listed along with the corresponding literature data in Table 5 [36–41]. Good agreement can be seen between the experimentally determined values and the published data. These studies confirm that FFFF coupled with MALLS can also yield information about the solution state of the polymer.

Table 5
Measured $\langle R_G^2 \rangle^{1/2}$ versus M and calculated $[\eta]$ versus M relationship and published data for dextrans

Source	Solvent	Structure–property relationship
This work	0.1 *M* $NaNO_3$	$\langle R_G^2 \rangle^{1/2} = 0.03M^{0.50}$
		$[\eta] = 0.10M^{0.50}$ [a]
[36]	0.1 *M* $NaNO_3$	$\langle R_G^2 \rangle^{1/2} \approx M^{0.48}$
[37]	0.1 *M* $NaNO_3$	$[\eta] = 0.37M^{0.40}$
[38]	H_2O	$[\eta] = 0.12M^{0.499}$
[39]	H_2O	$[\eta] = 0.17M^{0.452}$
[40]	H_2O	$[\eta] = 0.10M^{0.50}$
[41]	H_2O	$[\eta] = 0.05M^{0.60}$

[a] Application of Flory–Fox theory.

Symbols

A_2	second virial coefficient
a	exponent of the $[\eta]$ versus M relationship
c	concentration
D	diffusion coefficient
d_{LS}	diameter calculated from the radius of gyration
dn/dc	refractive index increment
d_S	Stokes diameter
I	intensity of light
k	constant for light scattering with vertically polarized incident light
K_R	pre-exponential factor of the $\langle R_G^2 \rangle^{1/2}$ versus M relationship
K_η	pre-exponential factor of the $[\eta]$ versus M relationship
k	Boltzmann constant
M	molar mass
N_A	Avogadro's number
n	refractive index
$P_{(\vartheta)}$	scattering function
q	scattering vector
r	radius
R_ϑ	reduced scattered light intensity, Rayleigh ratio
$\langle R_G^2 \rangle^{1/2}$	root mean square radius of gyration
T	absolute temperature
t_R	retention time
V	scattering volume
$\dot{V}$	channel flow
$\dot{V}_x$	cross-flow

Greek letters

η	viscosity
$[\eta]$	Staudinger index
ϑ	scattering angle
λ	wavelength of light
ν	Exponent of the $\langle R_G^2 \rangle^{1/2}$ versus M relationship

Acknowledgement

This work was kindly supported by the Deutsche Forschungsgemeinschaft (DFG).

References

[1] W.-M. Kulicke (Editor), *Analysis of Polymers (Macromolecular Symposium Series)*, Hüthig and Wepf, Heidelberg, 1992.
[2] W.-M. Kulicke, J. Klein and R. Kniewske, *Prog. Polym. Sci.*, 8 (1982) 373.
[3] T. Griebel and W.-M. Kulicke, *Makromol. Chem.*, 193 (1992) 811.
[4] T. Griebel, W.-M. Kulicke and A. Hashemzadeh, *Colloid Polym. Sci.*, 269 (1991) 113.
[5] W.-M. Kulicke and H.-H. Hörl, *Colloid Polym. Sci.*, 263 (1985) 530.
[6] H.A. Adams and G. Hempelmann, *Anästhesiol. Intensivmed.*, 10 (1991) 277.
[7] W.-M. Kulicke, D. Roessner and W. Kull, *Starch/Stärke*, 45 (1993) 445.
[8] W.-M. Kulicke and N. Böse, *Colloid Polym. Sci.*, 262 (1984) 197.
[9] W.-M. Kulicke, S. Lenk, H.-D. Detzner and T. Weiss, *Chem.-Ing.-Tech.*, 5 (1993) 541.
[10] T. Griebel, W.-M. Kulicke and R. Kniewske, *J. Getreide Mehl Brot*, 5 (1992) 154.
[11] J.C. Giddings and M.H. Moon, *Anal. Chem.*, 64 (1992) 3029.
[12] W.W. Yau and J.J. Kirkland, *J. Chromatogr.*, 218 (1981) 217.
[13] J.C. Giddings, F.J.F. Yang and M.N. Myers, *Anal. Chem.*, 46 (1974) 1917.
[14] G. Liu and J.C. Giddings, *Chromatographia*, 34 (1992) 483.
[15] J.J. Kirkland and S.W. Rementer, *Anal. Chem.*, 64 (1992) 904.
[16] J.C. Giddings, L.K. Smith and M.N. Myers, *Anal. Chem.*, 48 (1976) 1587.
[17] J.J. Kirkland, C.H. Dilks and S.W. Rementer, *Anal. Chem.*, 64 (1992) 1295.
[18] M.A. Benincasa and J.C. Giddings, *Anal. Chem.*, 64 (1992) 790.
[19] J.J. Kirkland and C.H. Dilks, *Anal. Chem.*, 64 (1992) 2836.
[20] J.C. Giddings, M.A. Benincasa, M.K. Liu and P. Li, *Polym. Mater. Sci. Eng.*, 65 (1991) 21.
[21] S.K. Ratanathanawongs and J.C. Giddings, *Polym. Mater. Sci. Eng.*, 62 (1990) 181.
[22] P.J. Wyatt, *Anal. Chim. Acta*, 272 (1993) 1.
[23] A. Einstein, *Ann. Phys.*, 33 (1910) 1275.
[24] C.V. Raman, *Indian J. Phys.*, 2 (1927) 1.
[25] P. Debye, *J. Appl. Phys.*, 15 (1944) 338.
[26] B.H. Zimm, *J. Chem. Phys.*, 13 (1945) 141.
[27] J.J. Kirkland, C.H. Dilks, S.W. Rementer and W.W. Yau, *J. Chromatogr.*, 593 (1992) 339.
[28] M.-K. Liu, P.S. Williams, M.N. Myers and J.C. Giddings, *Anal. Chem.*, 63 (1991) 2115.
[29] K.G. Wahlund, H.S. Winegarner, K.D. Caldwall and J.C. Giddings, *Anal. Chem.*, 58 (1986) 573.
[30] M.T. Nguyen and R. Beckett, *Polym. Int.*, 30 (1993) 337.
[31] P.J. Wyatt and L.A. Papazian, *LC·GC*, 11 (1993) 862.
[32] *Instrument Manual for Model F-1000 Universal Fractionator*, FFFractionation, Salt Lake City, UT.
[33] P.J. Wyatt, *J. Chromatogr.*, 648 (1993) 27.
[34] K.D. Caldwell, *Anal. Chem.*, 60 (1988) 959A.
[35] P.J. Flory and T.G. Fox, *J. Am. Chem. Soc.*, 73 (1951) 1904.
[36] J.A.M. Smit, J.A.P.P. van Dijk, M.G. Mennen and M. Daoud, *Macromolecules*, 25 (1992) 3585.
[37] B. Tinland, J. Mazet and M. Rinaudo, *Makromol. Chem. Rapid Commun.*, 9 (1988) 69.
[38] A.M. Basedow, K.H. Ebert, H. Ederer and H. Hunger, *Makromol. Chem.*, 177 (1976) 1501.
[39] *Pharmacosmos Dextran Standards*, Pharmacosmos, Viby, 1988.
[40] F.R. Senti, N.N. Hellman, N.H. Ludwig, G.E. Babcock, R. Tobin and C.A. Class, *J. Polym. Sci.*, 17 (1955) 527.
[41] K. Gekko and H. Noguchi, *Biopolymers*, 10 (1971) 1513.

ELSEVIER

Journal of Chromatography A, 687 (1994) 259–281

JOURNAL OF CHROMATOGRAPHY A

Noise, filters and detection limits☆

Xun-Yun Sun[1], Hameraj Singh, Brian Millier, Charles H. Warren, Walter A. Aue*

Department of Chemistry, Dalhousie University, Halifax, Nova Scotia B3H 4J3, Canada

First received 22 March 1994; revised manuscript received 19 August 1994

Abstract

The "noise" of chromatographic baselines has been investigated in regard to the detector, the nature and extent of filtering or smoothing, and the methodologies of qualitative and quantitative assessment: all in order to clarify the role such factors play in the determination and interconversion of some common types of detection limits. This study scrutinizes baselines from the flame photometric detector in single-channel continuous and ten-channel multiplexing versions; it also examines baselines from flame ionization and electron-capture detectors. It makes use of finite impulse response and non-weighted moving-average digital smoothing, as well as three-pole analog filtering.

Baseline fluctuations are quantified by the standard deviation derived from the common root-mean-square (RMS) calculation, or from the less common least-squares Gaussian fit; peak-to-peak noise ($N_{p\text{-}p}$) is estimated by procedures including or excluding presumed outliers. Individual results are expressed as the ratio of $N_{p\text{-}p}$ measurement and RMS calculation performed on the *same* data set. A wide variety of such ratios are then assembled from different detectors, filters, and smoothing conditions. They prove conclusively that —contrary to common belief— the conversion factor between the two types of measurements *does* vary: usually between 4 and 10, but occasionally even farther. Consequently, the conversion factor between the corresponding two types of detection limits varies as well.

The $N_{p\text{-}p}$/RMS ratio depends largely on the detector-of-origin, its condition, and the extent to which noise has been filtered. In contrast, the nature and sophistication of the filter hardly matters: either for the $N_{p\text{-}p}$/RMS ratio or for the practical detection limit. This is because the slow undulations characteristic of heavily filtered baselines represent —at least in the detectors we used— dampened fast noise rather than aboriginally slow noise. Corresponding computer simulations, based on amplitudinally random noise smoothed by stationary boxcar or non-weighted moving-average filters, produce results strikingly similar to actual baselines. *Simulated* fast RMS noise correlates, as expected, with the square root (log–log slope = 1/2) of the filter's time constant. The corresponding slopes for *experimental* noise are usually close to 1/2 as well. Most importantly, though, the *simulated* $N_{p\text{-}p}$/RMS ratio varies strongly with the extent of smoothing —thus mimicking and thereby explaining the behavior of the *experimental* ratio.

1. Introduction

Detection limits —in the widest sense of the term— are ubiquitous in the analytical and chromatographic literature, despite the fact that no single technique for their determination has

* Corresponding author.

☆ Part of doctoral thesis of H.S.

[1] Present address: Environmental Trace Substances Center, 5450 South Sinclair Road, Columbia, MO 65203, USA.

0021-9673/94/$07.00
SSDI 0021-9673(94)00805-1

yet managed to achieve universal acceptance. Indeed, it is not unusual to encounter numbers whose ambiguous derivation or lacking definition make interlaboratory comparison difficult: a situation frequently deplored (e.g. [1]). Even literature from the 1990s often describes detection limits merely as "$S/N = 2$" or "$S/N = 3$", while failing to mention whether N was measured peak-to-peak or root-mean-square (two measurements that differ from one another by far more than 2 differs from 3 —and in the opposite direction to boot). This manuscript is unlikely to change the situation; if anything, it will further complicate it.

There are three general approaches to documenting detection limits in chromatography and beyond. The first is pictorial (and by now rare in the literature, though still our own preference): it displays the recorder trace of a signal small enough, a baseline long enough and noise large enough, to allow evaluation by the analyst. The second and third are numerical: they list the amounts or concentrations or flows at which the signal/noise ratio (S/N) assumes certain quality values, e.g. 2, 3, 10, etc.. Aside from the latter, level-of-confidence parameter, the only difference between the two numerical assessments is the quantification of noise: whether it is measured peak-to-peak ($N_{p\text{-}p}$) or calculated root-mean-square (RMS). Though often poorly defined in practice, so far the matter is well understood.

What is less well understood is the precise relationship of these two numerical assessments. Yet their relationship is of great *practical* value. It holds theoretical interest as well; and it has even affected the promotional efforts of instrument companies. Hence: do these two assessments correlate; can one set of measurements accurately predict the other? If so, what is the *numerical* value of the conversion factor?

Under ideal circumstances of short-term noise and normal (Gaussian) distribution, a reasonable correlation can be established between the theoretically time-dependent $N_{p\text{-}p}$ and the theoretically time-independent standard deviation σ of baseline fluctuations in chromatography [2]. In spectroscopy, a widely quoted rule-of-thumb neglects the effects of sampling time and equates $N_{p\text{-}p}$ with five times the RMS noise, where RMS is considered to equal the standard deviation of a Gaussian distribution (e.g. [3,4]). But is chromatographic noise always Gaussian?

One could argue that it really should not matter: all numerical detection limits are single significant digits by definition. A recent book, devoted almost exclusively to detection limits and their meaning, expresses it thus: "One finds, for example, that at least 13 replicates are necessary to obtain s within 50% of the true σ (90% confidence interval)" [5]. If so, the conversion factor between the two detection limits may by its very nature be thought of as similarly vague, i.e. inherently incapable of sharper definition.

But what particular number then to use? The conversion factor of *one*-digit detection limits can legitimately be a *two*-digit number —if justified by its obtainment, of course. The replicates of conversion factors (each from a single set of noise data) are of considerably greater precision than the replicates of noise itself (from several data sets). For instance, one of our earlier studies used 27 noisy baselines, i.e. 27 values of the conversion factor (ratio), in order to determine the latter as the two-digit number $N_{p\text{-}p}/\sigma = 5.5 \pm 0.4$; though it did so expressedly "only for our particular measurement techniques and circumstances" [6].

Recently we measured that ratio again on the same detector. However, the detector was now monitored by a radically different (discontinuous, multiplexing) detection system [7], and the new ratio turned out to be significantly smaller than the old one. That was disconcerting. Furthermore, the ratio clearly varied with the extent of data filtering or smoothing.

Note on terms: the verbs "filter" and "smooth" may appear synonymous in this manuscript. However, these terms are not treated as synonyms in the specialized literature [8–12]. There, to "filter" implies an —irreversible and of necessity fast— reduction of noise on data during the acquisition phase; to "smooth" suggests an —often much slower and algorithmically more complex— reduction of noise on already ac-

quired and safely stored data. The same algorithm, if fast enough, can serve as either a "filter" or a "smoother" [8]. In this work, the common three-pole analog filter (resistor–capacitor, RC) is used primarily as a filter but can be employed as a smoother as well; the faster non-weighted moving-average filter (AVG) is designed to function as either a filter or a smoother; and the slower conventional finite-impulse-response filter (FIR) is available as a smoother only.

Back to the main question: why does the $N_{p\text{-}p}$/RMS ratio vary with conditions? Why should filtering or smoothing change it? Can its change be explained and predicted? To answer these questions, the "nature" of chromatographic noise will have to be further scrutinized. But that brings up a host of new questions. What is the *initial* character (the "unfiltered" distribution) of such noise? Can truly unfiltered noise even be measured? Would it be *source*-dependent, i.e. would it for instance differ among the flame ionization detector (FID), the electron-capture detector (ECD) and the flame photometric detector (FPD)? Would it differ between continuously ("two-dimensional", 2D) and discontinuously ("three-dimensional", 3D) sampled FPD versions? And would all that affect the different approaches used to define detection limits?

Trying to define the barely detectable may literally amount to much ado about (almost) nothing. Yet, in the literature, detection limits are quite frequently discussed and defined [1,2,13–17], even to the extent of a whole book [17]; and they are, by necessity, even more frequently used (and abused).

3. Experimental

All data sets were obtained from chromatographs carrying well-tested and well-proven (though perhaps slightly worn) detectors. The early FPD data came from a Shimadzu GC-4BMP (2D-FPD) model connected to a laboratory-made computer interface; the more recent ones came from the same unit equipped with a 600-rpm wheel carrying a semicircular variable-interference filter, supported by hardware and software for operation as a ten-channel FPD with wavelength as the third dimension (3D-FPD) [7]. The wheel spun at 600 rpm, i.e. at an acquisition time of 5 ms for each 100 ms data point. The FID and the Ni-63 ECD were conventional units (Shimadzu and Tracor, respectively). Detector conditions remained typical of routine operation; they had no obvious bearing on the results of this study.

All raw data flows were routed through a conventional electrometer of RC time constant 0.22 s, with the exception of those coming from the 3D-FPD. The photomultiplier output of the latter was processed by a high-speed amplifier and split into ten 5-ms segments per revolution of the wheel; the data were then assigned to one of three ranges of decadic sensitivity, summed by a gated integrator, converted into digital form, and forwarded to a computer for storage and display [7]. In (our own) "WHEEL" software, two types of low-pass digital filters were available for smoothing operations on the ten-channel data: a non-weighted moving average (hereafter referred to as AVG) with operator-defined window width; and a weighted moving average (a conventional finite-impulse-response filter hereafter referred to as FIR) with operator-defined, fully variable cut-off frequency and the choice of 32, 64 or 128 taps [7]. Half the symmetric table of its weighting coefficients, which follow the Hamming window function, was calculated [18] by

$$\text{coefficient}(m) = \frac{\sin\left[(\text{cut-off frequency}/\text{sampling rate})m\pi\right]}{m\pi} \cdot \{0.54 + 0.46\cos\left[m\pi/(\text{filter taps}/2)\right]\}$$

where $1 < m < (\text{filter taps}/2)$.

The conventional (2D) FPD, the ECD and the FID (the latter via a laboratory-built preamplifier) were monitored on the same Shimadzu GC-4BMPF electrometer, which fed an interface and thence one of our own, two-channel computer programs named "CHROM-8" [19]. This program contains, inter alia, the FIR filter algorithm. It also provides a routine that sorts

baseline fluctuations according to the magnitude of their deviation from the mean (a form of software-based multichannel analyzer), and feeds the resulting array of (raw or smoothed) baseline data to a Dalhousie University undergraduate network program offering least-squares fitting of Gaussian and other types of curves. The enforced Gaussian fit then yields the nominal standard deviation σ_{fit}. (Note that data files can be imported, a pair at a time, from the newer ten-channel WHEEL program into the older two-channel CHROM-8 program —but not the other way around.)

In addition to the smoothing and evaluating functions that are confined to the computer, the raw or treated data flow can be returned from the CHROM-8 program (or from the WHEEL program through the CHROM-8 program) to the analog domain; and it can, via a simple, laboratory-made three-pole filter with a set of time constants, be recorded on a chart (that filter will hereafter be referred to as RC). Raw or smoothed data can also be forwarded directly to a laser printer. And, obviously, the electrometer output can remain completely in the analog domain, i.e. it can provide in the conventional manner (usually via the RC filter) confirmatory baselines or chromatograms on the strip-chart recorder.

The older and newer versions of the laboratory-developed detection limit program[2] differ somewhat in their analytical objective, algorithmic approach, operational convenience, and range of application (though they did not differ, whenever checked, in their results).

The older CHROM-8's "SIGMA" routine [6] employs very heavy digital filtering of the baseline noise (with an operator-adjustable time constant) in order to establish a smooth "zero line" (slightly offset by computational inaccuracies), from which the real baseline fluctuations are measured. The algorithm then uses the conventional formula for calculating the RMS deviation:

$$\mathrm{RMS} = \sqrt{\frac{\sum (x_i - \bar{x}_i)^2}{n}} = \sigma$$

[Note: The definitions use the value, not the ± range of the standard deviation. To use the latter, adjust any derivative equation by an appropriately placed factor of two.]

The newer WHEEL's "DL" program [7] uses a second-order least-squares fit of the baseline (from 50 points selected by the computer at equal intervals on those stretches of the chromatogram that the operator designates as "baseline"). The deviations x_i are then measured from this smooth line. They are used directly (recourse to the mean $\bar{x}_i$ having become superfluous):

$$\mathrm{RMS} = \sqrt{\frac{\sum x_i^2}{n}}$$

For this study, n equals 10^3 to 10^4 data points (very roughly 2 to 20 min worth of chromatographic acquisition time).

The DL program proceeds to compute numerical values for the most popular types of detection limits. [Note that these may be associated in the literature with different names —e.g. "detectability", "limit of detection (LOD)", etc. [1,2,13–17]— depending on the analytical circumstance and purpose, the algorithmic formula and the desired level of confidence]. Alluding to disciplinary preferences —but used here solely for ease of reference— we shall denote the algorithmic detection limits based on $S/\mathrm{RMS} = 3$ as DL_{spec}, and those based on $S/N_{p\text{-}p} = 2$ as DL_{chrom}. Thus,

$$\mathrm{DL}_{spec} = 3 \cdot \frac{\mathrm{RMS}}{S} \cdot A \text{ (g or mol)}$$

where S is the signal (peak height) and A is the amount injected (presumed to be equal to the amount reaching the detector).

In terms of minimum detectable flow at peak apex (which, for a Gaussian peak of standard

[2] Researchers interested in these and other programs for non-commercial purposes are invited to contact B.M. for executable copies. For information on the Gaussian fit program, please contact C.H.W.; for information on the noise simulations, H.S.

deviation σ_p, is equal to $A/2\sigma_p$), the computer calculates

$$DL_{spec} = 3 \cdot \frac{RMS}{S} \cdot \frac{A}{2\sigma_p} \text{ (g/s or mol/s)}$$

(Note: the computer measures $2\sigma_p$ as the width of the peak, in s, at 60.7% of its height —regardless of its occasionally asymmetric shape.)

To determine the "chromatographic" $S/N_{p\text{-}p}$ = 2 detection limit on the screen, the operator uses cursors to define the signal S (the peak height) and the peak-to-peak baseline noise $N_{p\text{-}p}$. The latter is available in two versions, depending on whether or not the operator's pattern recognition and judgement is taken into account.

To wit: the first version is "objective" and "inclusive" (i.e. it is independent of the operator and representative of *all* signal excursions, thus including the sharp and strong fluctuations that appear to extend beyond the normal distribution of noise and are hence called "spikes" or "outliers"). We shall name $N_{p\text{-}p}$ noise thus measured N_{all}. The second version is "subjective" and "exclusive" (i.e. it allows the operator to define the *core* of the noise, thereby excluding what appear to be spikes). We shall name $N_{p\text{-}p}$ noise thus measured N_{core}. Obviously, $N_{all} > N_{core}$ in spiky experimental situations; in simulations (which start with perfect Gaussian distributions), $N_{p\text{-}p} = N_{all}$.

The DL calculation, similar to the one above, is then

$$DL_{chrom} = 2 \cdot \frac{N_{p\text{-}p}}{S} \cdot A \text{ (g or mol)}$$

and

$$DL_{chrom} = 2 \cdot \frac{N_{p\text{-}p}}{S} \cdot \frac{A}{2\sigma_p} \text{ (g/s or mol/s)}$$

(Note: The first number in each equation, i.e. p = 2, 3, etc., is the level-of-confidence or probability-related parameter that —for purposes *other* than of this study— can be adjusted to suit analytical objectives or literature definitions.)

Obviously, each of the equations above simply relates the detection limit to the commonly used signal/noise ratio (S/N); with noise being whatever the analyst wants it to be:

$$DL = p \cdot \frac{A}{S/N} \text{ (g or mol)}$$

or

$$DL = \frac{p}{2\sigma_p} \cdot \frac{A}{S/N} \text{ (g/s or mol/s)}$$

(This is both trivial and well-known, as indeed are most of the preceding definitions and relationships. Yet, they needed to be given here again: on one hand to provide a clear record of procedures used; on the other to establish unequivocal terms for discussions to follow. The *new* designations —e.g. N_{all}, N_{core}, σ_{fit}, etc.— are intended for *this* study only. They are not proposed for wider usage: too heavily already is this subject fraught with terms and definitions.)

3. Results and discussion

The prime objective of this study is to address the connection between detection limits that rely on baseline noise as defined by, on one hand, the peak-to-peak (p-p) measurement and by, on the other hand, the root-mean-square (RMS) calculation. This study represents a bottom-up approach (i.e., what does real-life noise look like before and after smoothing?) rather than a top-down enquiry (i.e., what happens mathematically to a temporal array of normal or exponentially modified distributions when exposed to algorithmic filters of different types and varying time constants?) The essential objective of this study thus concerns not the statistics or electronics of the two basic measurements of noise, but the measurements themselves: how does the experienced chromatographer reasonably perform and interconvert them?

This question emphasises the practical. Consequently, a selection of frequently used detectors, filters and evaluation methods is recruited to provide the experimental data. The detectors include the FID, ECD and FPD, plus a variation of the FPD that happened to be available in our

laboratory. The filters include a plain AVG and a sophisticated FIR, as well as a simple three-pole analog RC filter. The evaluation methods include the $N_{p\text{-}p}$-based approach with outliers included (N_{all}) or excluded (N_{core}), and the standard-deviation approach based on the usual calculation (RMS) or the graphical evaluation from an enforced Gaussian fit (σ_{fit}). Not all their possible combinations are explored here; nor would it be reasonable to do so in view of the large number of different detectors and filters that litter the analytical battlefield. However, enough combinations will be investigated to allow general trends to be recognized. The difficulty of recognizing trends will generally increase from comparisons done on a single data file; to comparisons done on several data files from a single set of experiments; to comparisons done on data files from several sets of experiments.

The most important question of this study is whether $N_{p\text{-}p}$ and σ-based measurements of baseline noise are linked in any fundamental way. An easy and significant answer to this question can be found in the area of conventional data smoothing.

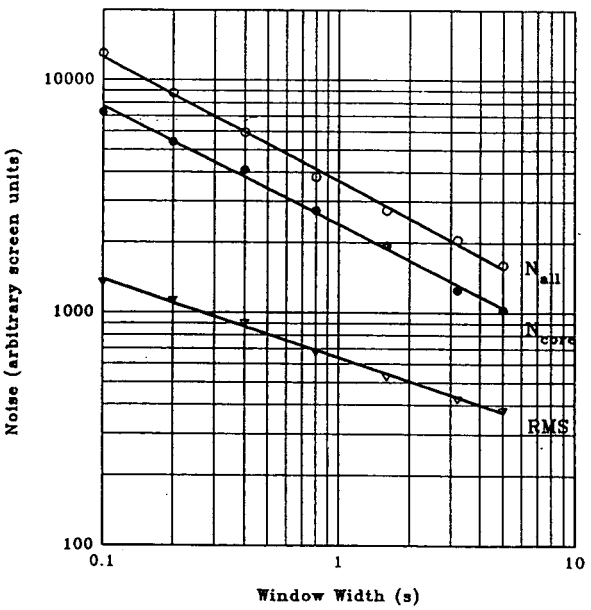

Fig. 1. Variation of three measurements of noise with increasing window width of the AVG filter. Noise: 15 min baseline from segment 2 (ca. 430 to 460 nm) of 3D-FPD [7], H_2 50 ml/min, air 40 ml/min, R-374 photomultiplier tube at −950 V.

3.1. Effect of filters on the $N_{p\text{-}p}$/RMS ratio

Fig. 1 provides the answer in one of its simplest and clearest experimental versions. It shows 3D-FPD baseline noise, measured as N_{all}, N_{core} and RMS, as it decreases with the increasing window width of the AVG filter. Clearly, the two types of noise measurement do depend to *different* degrees on the extent of filtering. Their ratio must therefore depend on the extent of filtering as well: the value of N_{all}/RMS changes from approximately 9 at 0.1 s, to 5.7 at 1 s, to (extrapolated) 3.6 at 10 s. And the conversion factor for the two types of detection limits, DL_{chrom} and DL_{spec}, varies accordingly. This may come as a surprise. It is not, however, an experimental singularity: Although Fig. 1 happens to be particularly clear (to the point of being slightly deceptive), it does exemplify a trend evident in almost all of the tested detector–filter combinations.

That the N_{all}/RMS ratio should change with the filter time constant did not seem obvious to us at the beginning of this study. We will therefore attempt to make the case for it in general —and deliberately simplistic— terms. In such terms, "noise" can be perceived as deviations of the signal from an imagined smooth ("true") baseline. So, incidentally, can a peak. The analyst's pattern recognition can easily tell the difference between the two. More than just an evaluation of peak width and noise magnitude seems to be involved here: the analyst instantly recognizes the "shapes" of chromatographic peaks. In fact, their characteristically different shapes are still under active investigation [10], mostly by physical chemists. But can chromatographic noise also assume recognizably different shapes?

3.2. Noise "shape"

This question is not quite as silly as it sounds. Recognition of peaks should be easier —mean-

ing the detection limit could be lower— if peaks had shape but noise did not [10,11]. That brings up the question what causes noise, and what modifies it on its way to a determination of the detection limit. Characterization of noise as to its origin, power spectrum, and influence on S/N is particularly well developed in spectrochemical analysis (e.g. [4,20]), and that literature underlies much of the following discussion.

If the noise of, say, an FPD is due to the quantum nature of light ("photon shot noise"), it is random and there should be no shape to it (beyond the shape of the extremely rapid electron avalanches in the photomultiplier tube, of course). If the FPD noise is due to changes in the flame (flicker, fluctuations in column bleed and flow, dust particles, drafts, etc.) it will show these events by their different signatures in different frequency ranges. Such noise will not be random in amplitude; it will be shaped. A similar random/non-random assessment can be made of the complex and still not completely understood processes that translate the random emission of β-rays inside the ECD into the interrelated fluctuations of ion-pair generation and distribution, ion–molecule chemistry, and pulsed charged-particle collection on one hand [21–25]; and the various physical and chemical disturbances known to occur in the ECD on the other. Ditto the chemiionization reaction(s) and sundry associated processes; and the bleeds, leaks, drafts and spikes that produce and/or influence the current of an FID [26].

Thus, ample opportunity exists for initial detector noise to contain recognizable shapes. However, chromatographic detection systems are far too sluggish to display the profiles of the fast "primary" events (FPD photon detection, ECD and FID ion generation and collection). In a typical case, the time constant of the electrometer may be 0.1 s and the full-scale response of the strip-chart recorder 1 s. In addition, analog or digital filters with selectable time constants in the 1–10-s range are often used. Detection limits, in particular, are determined by smoothing the chromatogram as heavily as the concentration profile of the analyte and the conscience of the analyst will allow. The question of "shape" concerns therefore not only the original but also —and more so— the *filtered* noise.

Different types of filters and smoothing algorithms [9–12,27–29] are often surprisingly similar in the job they do on the noise. This is perhaps best appreciated by considering the job they do on the (much more frequently investigated) analyte peak. The tip of the peak, say its uppermost ten percent, is its most vulnerable part; not surprisingly so since the signal might undergo there a, say, 170° change of direction. Different filters —at least the ones commonly found in chromatographic laboratories— all do adequate noise jobs, but they do clip peaks to different extents.

Let us now imagine that the signal excursions above and below the baseline, which we normally call noise, were a succession of small, sharp peaks. An increase in the severity of data smoothing then means that the sharp tips of these peaks will become round tops, i.e. that they will change their shape from protrusive to pouchy. As this occurs, the peak-to-peak noise will decrease rapidly, the root-mean-square noise will decrease slowly. The ratio of the two noise measurements, $N_{p\text{-}p}$/RMS, will therefore change to lower values.

The argument that a shape shift affects the $N_{p\text{-}p}$/RMS ratio is further advanced, albeit intuitively, by the geometric metaphor presented in Fig. 2. Its triangular, sinusoidal and hemispherical waveforms are, for simplicity's sake, restricted here to the same single frequency and

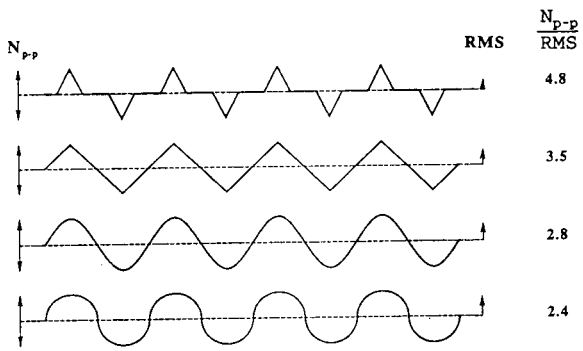

Fig. 2. Geometric figures treated as noise. See text for explanation.

amplitude. {Random distributions of frequency and amplitude could no doubt be called upon to make the resulting waveforms conform more closely to noisy baselines. Even at a single frequency and amplitude, however, the traces already resemble to a remarkable degree what, for instance, IUPAC considers to be noise ([30]; cf. Ref. [31])}

The $N_{p\text{-}p}$ values of Fig. 2 are all the same; the RMS values, however, and hence the $N_{p\text{-}p}$/RMS ratios, vary by a factor of two. (They could, of course, vary by much more if the top triangular trace were made a bit spikier). Now imagine analyte peaks of identical height superimposed on these waveforms for purpose of determining their detection limits: all limits based on $N_{p\text{-}p}$ would then be the same, while the limits based on RMS would vary by a factor of two. (This raises the question which of the two noise definitions the conscientious analyst could reasonably choose for determining a chromatographic detection limit.)

What Fig. 2 suggests is, in general terms, this: The spikier the excursions of original noise from the "true" baseline (i.e. the larger their ratios of height to width) and the less they are filtered, the higher will be the $N_{p\text{-}p}$/RMS ratio of the noise. Conversely, the rounder the original noise features, and the more they are filtered, the lower will be the $N_{p\text{-}p}$/RMS ratio. Furthermore, the more severely a particular type of filter crops the tops of baseline excursions, the more it will depress their $N_{p\text{-}p}$/RMS ratio.

3.3. Noise "distribution"

If noise were always normally distributed, there would exist a clear (though sampling-time dependent) statistical correlation between N_{all} and RMS [2]. Conversely, since experiments often show this not to be the case, the distribution cannot always be normal. Consequently we are including σ_{fit} in this study. Fig. 3 shows the particularly poignant example of an FID baseline unsmoothed (though, of course, filtered by the 0.22-s RC time constant of the electrometer). Its spikes suggest that the detector needs cleaning (or perhaps someone came into the room or touched the instrument?). Two spikes appear prominent on the chart-recorded baseline (see insert); these episodes last long enough to enter the distribution as *several* data points. Spikes or not spikes, they exemplify and illustrate a common phenomenon. The standard

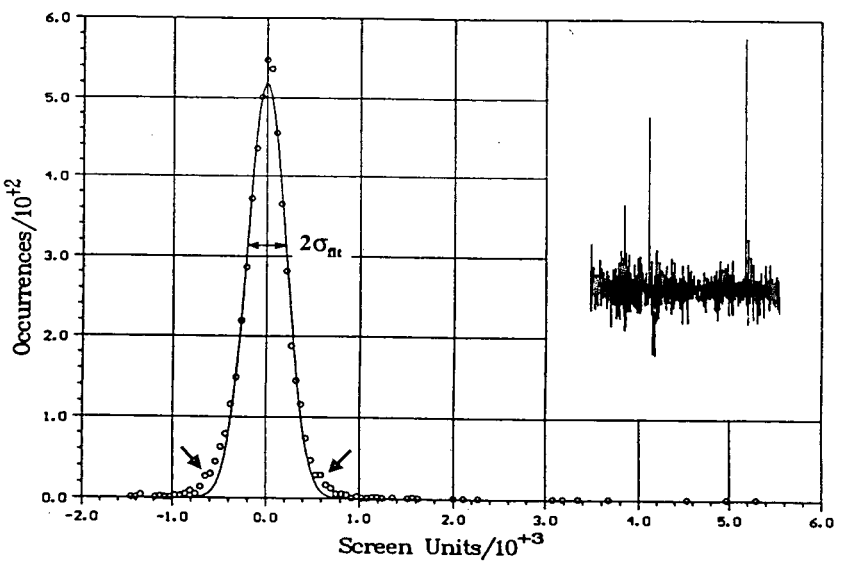

Fig. 3. Example of a baseline with spikes: unfiltered FID noise. Insert: conventional recorder trace.

deviation as measured by RMS is larger here than that measured by σ_{fit}: Even spikes aside, the wings of the distribution (see arrows) are more intense than Gauss allows. Which measurement should then be considered, RMS or σ_{fit} ? Which should be considered in other cases of non-Gaussian or superimposed multiple Gaussian distributions?

But these problems are minor —at least in terms of their numerical implications— when compared to the problem of how to measure peak-to-peak noise: N_{all} is about four times as large as N_{core} in Fig. 3, and N_{all}/σ_{fit} is at the ridiculously high value of 30. A strong case could be made here for using the subjective N_{core} rather than the objective N_{all} assessment. (And a strong case could be made for cleaning the detector and smoothing the noise.)

Most detectors are better behaved than the FID of Fig. 3. Normal distributions are often approached. As an example, the top graph of Fig. 4 shows the noise from 22 min of regular FPD operation. Surrounding the solid line of the enforced Gaussian fit are two dashed lines, drawn to demarcate the square-root band at $\pm$[(number of occurrences)$^{1/2}$]. Asymmetric distributions *not* attributable to spikes can also be encountered. The bottom graph of Fig. 4 shows an example; the solid line again representing the enforced fit, the dashed line indicating what the corresponding author of this manuscript —blissfully unaware of shape and cause— imagined the "true" distribution to look like.

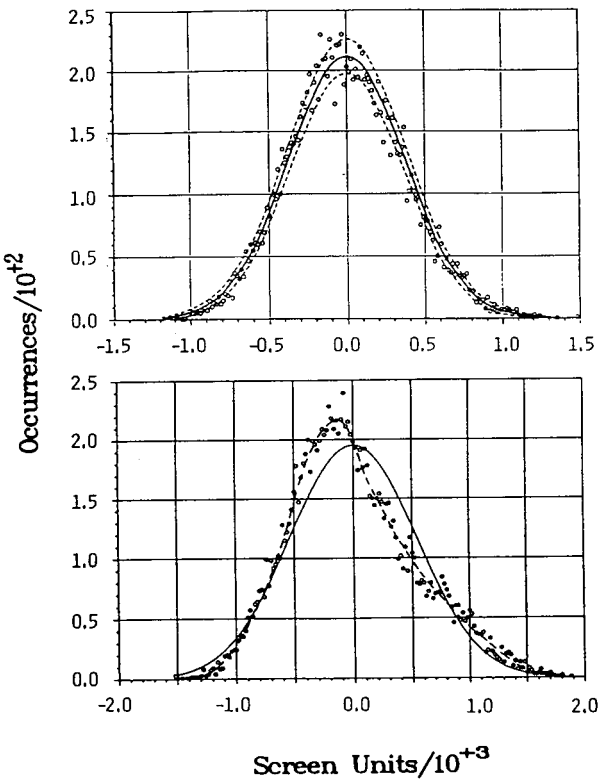

Fig. 4. Examples of noise distributions. Upper graph: Gaussian, unfiltered 2D-FPD noise. Solid line: enforced Gaussian; dashed lines: $\pm$ [(number of occurrences)$^{1/2}$]. Lower graph: asymmetric, heavily filtered 3D-FPD noise. Solid line: enforced Gaussian; dashed line: corresponding author's presumption.

3.4. Noise "speed"

It could be argued that deviations from the Gaussian shape may be due to noise processes of different duration and distribution, which would come sequentially to the fore as smoothing became increasingly effective. That would suggest the presence of weaker and slower (initial) noise components —with time constants within and perhaps beyond the filter range— which became visible only as the stronger and faster components were progressively quelled by the filter.

However, such does not seem to be the case here, at least not to any significant extent. If it were, then components slower than the 5-ms segment acquisition time of the 3D-FPD system should appear in two or more wavelength segments (provided they would do so optically) —and they could therefore be annulled or at least significantly decreased by the subtraction of two suitably chosen and scaled segments from one another. (Both our CHROM-8 and WHEEL programs provide the option of subtracting spectrally diverse detector backgrounds or sample matrices [7,19]).

Yet, such an attempt at noise subtraction failed. The noise did not decrease as expected, but instead increased by a factor of ca. $2^{1/2}$ [7]. Furthermore, a similar attempt using continuous,

i.e. electrometer-acquired two-channel data from a conventional FPD, had failed earlier in similar fashion. Thus, at least for these FPD cases, it appears that the relatively slow noise undulations (which figure prominently in heavily filtered baselines) do *not* originate as slow noise in the detector (e.g. as flame or flow flicker). Rather, they must owe their existence to fast noise being converted into slow.

3.5. Sundry detectors, sundry filters

We return to evaluating further combinations of detectors and filters. Table 1 presents a selection of four typical noise sources, all treated by the *same* filter. This selection includes conventional electron-capture and flame ionization detectors, the FPD in the intermittently sampled 3D version, and a conventional photomultiplier tube's dark current. Other systems behave similar. Note that the results of Table 1, representing noise or noise-ratio measurements by various definitions, may be compared only with due caution. They carry, at best, two significant digits —as, indeed, one expects them to. The important data —in terms of addressing various definitions of detection limits— are, of course, the ratios as given in the last four columns. (The

Table 1
FIR smoothing of noise from different sources

FIR cut-off[a]	N_{all}	N_{core}	RMS	σ_{fit}	N_{all}/RMS	N_{all}/σ_{fit}	N_{core}/RMS	N_{core}/σ_{fit}
^{63}Ni-ECD, d.c. mode, 5 min								
None	3 280	2 700	533	557	6.2	5.9	5.1	4.8
2	3 060	2 500	514	520	6.0	5.9	4.9	4.8
1	2 630	2 200	464	472	5.7	5.6	4.7	4.7
0.5	2 090	1 760	367	358	5.7	5.8	4.8	4.9
0.2	1 060	837	210	238	5.0	4.5	4.0	3.5
0.1	556	500	116	133	4.8	4.2	4.3	3.8
FID, 10 min								
None	14 300	7 130	1 100	875	13.0	16.3	6.5	8.1
2	12 800	5 730	984	792	13.0	16.2	5.8	7.2
1	7 720	4 400	758	628	10.2	12.3	5.8	7.0
0.5	4 630	2 800	482	426	9.6	10.9	5.8	6.6
0.2	1 550	1 100	224	216	6.9	7.2	4.9	5.1
0.1	711	617	122	122	5.8	5.8	5.1	5.1
3D-FPD, segment 4 (ca. 490–520 nm), 10 min								
None	16 900	10 100	2 580	2 490	6.6	6.8	3.9	4.1
2	7 860	4 330	1 160	1 150	6.8	6.8	3.7	3.8
1	5 060	2 710	780	774	6.5	6.5	3.5	3.5
0.5	3 310	1 800	522	530	6.3	6.2	3.4	3.4
0.2	1 660	930	276	253	6.0	6.6	3.4	3.7
0.1	899	520	159	142	5.7	6.3	3.3	3.7
Dark current, R-374 photomultiplier tube, −760 V, 5 min								
None	3 100	2 000	380	390	8.2	7.9	5.3	5.1
2	2 800	1 870	360	380	7.8	7.4	5.2	4.9
1	1 800	1 500	290	290	6.2	6.2	5.2	5.2
0.5	1 200	870	180	200	6.7	6.0	4.8	4.4
0.2	440	380	84	88	5.2	5.0	4.5	4.3
0.1	230	210	46	50	5.0	4.6	4.6	4.2

[a] In Hz, nominal.

first four columns of plain noise measurements have been included for purpose of complete documentation only. These data, coming as they do from different detectors, conditions, amplifiers, attenuations, etc., are of necessity given in arbitrary units and are hence comparable only within a particular set, not across the whole table.)

Table 1 suggests that different noise sources do produce *different* types of noise to start with. The highest and the lowest ratios in the "non-filtered" mode are about a factor of two apart. (The FID used here is somewhat cleaner than the one that produced Fig. 3.) The assumption of *different* types of noise is also supported by different distributions. In a perfectly Gaussian distribution, RMS and σ_{fit} are the same; and so are the ratios N_{all}/RMS and N_{all}/σ_{fit}. Examination of Table 1 shows, however, that the two measurements differ to a small but significant extent. Now, RMS is larger in the FID (as expected from Fig. 3) and the 3D-FPD; while σ_{fit} is larger in the ECD and the covered photomultiplier tube. These relationships hold (with minor exceptions) *throughout* the monitored smoothing ranges. Yet the differences between RMS and σ_{fit} are relatively small.

Perhaps the most striking trend apparent in Table 1 is that all the ratios decline (again with minor exceptions) as the extent of FIR smoothing increases. This parallels the relationships obtained with the AVG filter as portrayed in Fig. 1. Fig. 1 is, however, somewhat limited: the AVG filter is restricted to a window width of 50 data points, i.e. 5 s [7]. In contrast, the time constant of the FIR smoother is unrestricted. Fig. 5 presents therefore a close-up look at the ratios in two detectors —conventional FPD on top, FID on the bottom— over an FIR filter range that extends to longer time constants and includes more data points. The found dependence is illustrated by solid least-square linear regression lines. Note that, given the kind of subject and the type of plot, the data points are *expected* to show considerable scatter. Note also that these baselines —in contrast to those of Fig. 1— were obtained from an electrometer of RC time constant 0.22 s: consequently it would have made little sense to measure data points below that value.

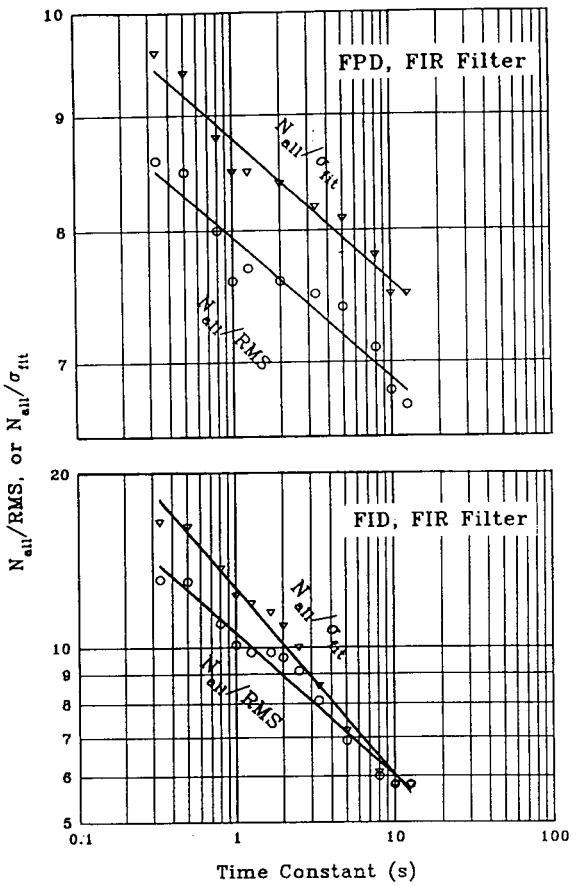

Fig. 5. Variation of N_{all}/RMS and N_{all}/σ_{fit} ratios with FIR smoothing of FPD and FID noise. The nominal time constant is the reciprocal FIR "cut-off frequency" (see Experimental). The solid lines are linear least-squares regression fits. Upper graph: 12 min of conventional FPD noise. Non-filtered ratios (straight from RC time constant 0.22 s electrometer): 9.7 and 8.8. Lower graph: 10 min conventional FID noise. Non-filtered ratios: 16 and 13.

Fig. 5 confirms that the N_{all}/RMS and N_{all}/σ_{fit} ratios decrease as the influence of the smoothing algorithm increases. The N_{core}/RMS and N_{core}/σ_{fit} ratios are not shown here; they display similar though somewhat less dramatic behaviour. So far the ratios behave as expected. However, so far we have considered only numerical, not visual behaviour —and the interrelated topics of noise, filters and detection limits

may contain significant perceptual components. Better expressed: "anyone who tries to analyse a time series without plotting it first is asking for trouble" [32].

3.6. Plotting experimental noise

One potential troublespot in this study is the N_{core} definition. We have no better way of defining what the first author perceived to be "core" noise than by displaying the results of his efforts on a 3D-FPD sample plot. In Fig. 6, the subjective N_{core} measurement is shown on the right, the objective N_{all} measurement on the left; for AVG window widths ranging from 0.1 (unfiltered) to 5 s.

(Note: It would have been easy for us to replace the analyst-assessed limits of N_{core} by a computer-calculated test for outliers —thereby changing N_{core} into a seemingly "objective" measurement. Indeed, such may be a reasonable action to propose *if* —and that is a psychologically insurmountable *if*— the scientific community were likely to agree on a binding set of rules for determining detection limits. But, in the context of this exploratory study, it would make little sense to introduce outlier tests for despiking baselines. Furthermore, we would not want to add to chromatographic practice yet another hidden algorithm whose precise effect on peak and noise is difficult to evaluate.

Beyond documenting the first author's holistic, subliminal perception (cf. [33]) in defining N_{core}, and beyond providing the visual record of a sample data file, Fig. 6 offers still further material for discussion. For instance: after about 1 min into the record, the top trace shows two strong, positive excursions. These persist in two more traces below, then subside. In contrast, the strongest positive excursion of the bottom trace occurs at about 4.25 min. Its presence can be followed up to the top trace, but just barely. So why do traces of different time constants emphasize different episodes?

The human eye is attracted to the highest amplitude of an individual excursion (the "record performance"); and so, of course, is the measurement of N_{all}. Filters, on the other hand,

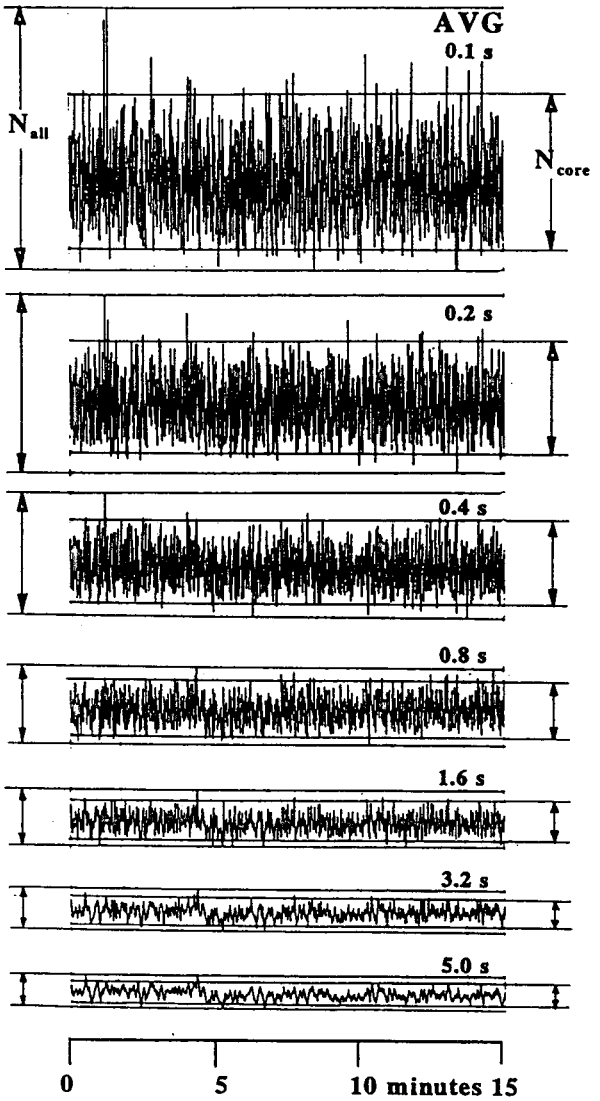

Fig. 6. Traces of AVG-smoothed 3D-FPD noise, comparing N_{all} measurements and N_{core} estimates. Laser printer.

take a broader view: they simply redistribute net total energy. A strong but lone excursion, dominant under light smoothing, might lose that dominance under heavy smoothing to a few weaker but closely positioned, equidirectional and hence mutually reinforcing excursions. (This effect can be observed in many human activities, including scientific evaluation. In a manner of speaking, even $N_{p\text{-}p}$ and RMS differ in the way they see noise as individual and collective phe-

nomena, respectively.) Different groups of noise excursions thus appear in time windows of different width; and recognizing particular noise episodes —whether original or derivative in nature— depends on choosing the correct time domain. For the present system such an interpretation implies that originally fast noise is being converted into visually slow noise by the filter. This conclusion is supported by our earlier-described failure to eliminate what appeared to be slow noise from 2D- and 3D-FPD chromatograms [7]; it will also be supported by later simulations resulting in square-root relationships.

To be sure, this only means that truly slow system noise did not exist to any significant extent in the baselines here considered; in many other chromatographic and spectroscopic systems it may well be present (e.g. as so-called "$1/f$" or "pink" noise [4]). If the latter is the case, then the filter may not just convert fast noise into seemingly slow noise, but it may also remove fast noise from genuinely slow noise. In Fig. 6, however, there is little or no evidence of that.

Fig. 6 can be analyzed by more than *visual* perception. Its raw data are the same as those of the earlier Fig. 1 —and combined these two figures raise several interesting and, more importantly, easily answered questions. In Fig. 1, the relationship of noise to window width (filter time constant) appears linear. Furthermore —although surprisingly and perhaps spuriously more so for N_{all} and N_{core} than for RMS— the slope is close to one half, suggesting a classical square-root dependence based on the randomness of noise. If *all* initial noise were indeed fast and normally distributed, would that translate into an amplitudinal square-root relationship of noise with the filter's time constant? Would *both* N_{all} and RMS obey it —i.e. would they perhaps become parallel and would the N_{all}/RMS ratio therefore become constant? The question is not trivial: such parallelism, if it were to occur, would provide support —of a theoretical if not of a practical nature— for proposing a *single* rule-of-thumb factor that could then be used, generally and legitimately, to interconvert the two types of measurements. For an answer to these questions, a purely Gaussian noise file is needed.

3.7. Plotting simulated noise

Random noise can be easily simulated. For expediency's sake we take a shortcut here and start from a preformed Gaussian distribution of noise *amplitudes* (despite the fact that most if not all of the random elements in initial noise are in the *time* domain). What is presumed random and dominant in initial noise are, of course, the *temporal intervals*: between photomultiplier tube electrons being ejected by photons in the FPD, between β's being emitted in the ECD, between charged particles being formed and collected in the FID. Seen through larger filter windows, short intervals between these primary events appear as positive, long intervals as negative amplitudinal excursions.

Note that, for purpose of noise calculations, the *initial* FID events can be assumed to have the same amplitude, i.e. that of a unit charge; and the photomultiplier tube electron avalanches can be assumed to be of similar strength (at least those avalanches set off by photons from the FPD flame). In contrast, the ECD's ion-pair yield of individual β-rays varies —in a predictable, inherent manner due to the comcomitant loss of neutrinos; in a much less predictable, condition-dependent manner due to the particulars of isotope plating, cell dimensions, foil contamination and β backscattering from nearby surfaces [34,35].

For the purpose at hand, Gaussian noise is generated either by a commercial program (Sigmaplot), or by blindly drawing marked paper squares (a tessellated Gaussian) out of a well-mixed bowl. (Within the expected variation, the results are the same. Later and longer simulations are therefore based on Sigmaplot inputs only.) Two types of averaging algorithms are used: a stationary boxcar and a non-weighted moving window [8—12]. The boxcar mimics the action of the gated integrator [7] in the 3D-FPD's fast acquisition circuit (although the length of the former is variable while that of the latter is fixed at 5 ms). The moving window

parallels the action of the AVG filter. The N_{all} and RMS values can be easily calculated, once the compromised start and end pieces (of half the boxcar length or window width) are removed.

The left side of Fig. 7 shows the visual effects of the AVG filter. (The boxcar traces look similar, but are computed only to a boxcar "length" —or "load"— of 64 initial data points.) Both types of simulated baseline look very much like the real one shown in Fig. 6; except that, there, some spikes are present and the window can open to only 50 data points. The earlier-discussed waxing and waning of particular experimental noise episodes across adjacent windows of different width can be observed in the simulated traces of Fig. 7 as well; thus adding weight to the adopted interpretation.

The numerical $N_{p\text{-}p}$ ($= N_{all}$) and RMS noise variation with window width and boxcar length is shown in Fig. 8. The points are averages of five replicates; from different random inputs, of course, and replete with standard-deviation error

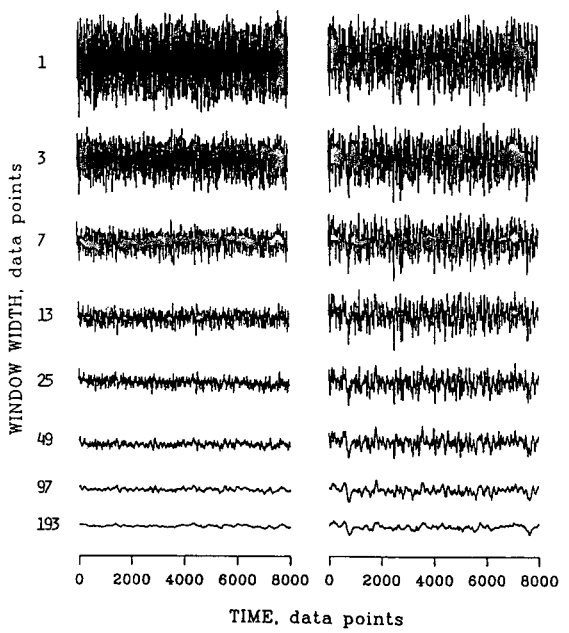

Fig. 7. Traces of AVG-smoothed, single-frequency and multi-frequency simulated Gaussian noise (one set out of five each). Left set: single frequency; right set: multiple frequencies. See text for explanation.

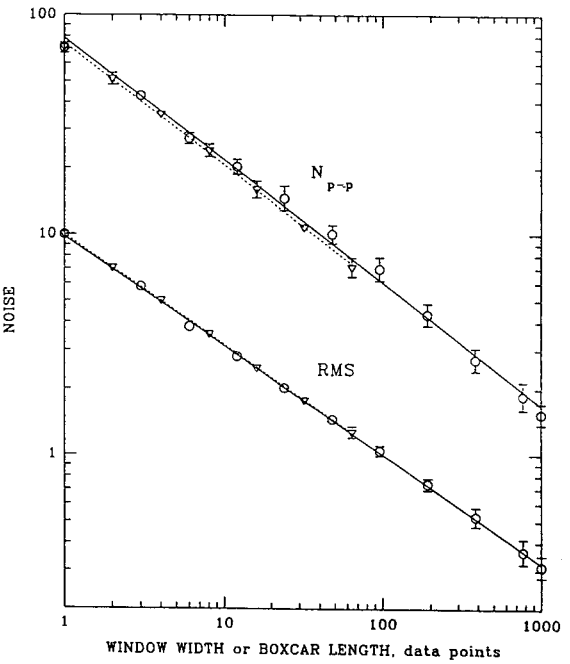

Fig. 8. Measurements on simulated single-frequency Gaussian noise, smoothed by boxcar (▽) and AVG (○) filters. Data points are averages of five independent sets (one AVG set is shown on the left side of Fig. 7).

bars on the least-squares linear regression lines. As expected, the two filters behave alike. Also as expected: it is the RMS line now that shows the square-root slope. The $N_{p\text{-}p}$/RMS ratio declines, over three orders of time variation, from roughly 8 to roughly 5. Compared to the experimental Fig. 1, this decline is somewhat less steep.

Far more important in the present context, however, is the fact that the "theoretical" $N_{p\text{-}p}$/RMS ratio of initially Gaussian noise is filter-width *dependent*, just as is the experimental ratio. In other words, in the absence of additional information about a particular system, the analyst can *not* correlate its two noise measurements $N_{p\text{-}p}$ and RMS —and, more importantly, its corresponding detection limits DL_{chrom} and DL_{spec}— by simply assuming the initial noise to be Gaussian. Even if that primary assumption were correct, it would not justify the use of a constant factor for the interconversion of $N_{p\text{-}p}$ and RMS. Note also that this particular simula-

tion assumes initial random noise of only a single frequency —there are no noise components of other speed present to complicate the picture. {The term "frequency" refers here to the imaginary *input* frequency, i.e. the reciprocal of the constant temporal interval between initial data points being introduced into the simulation. It should be recalled, though, that a random input can be considered equivalent to an infinite number of sine waves beating at an infinite number of frequencies (e.g. [20]).}

It is, of course, also possible to introduce random noise at several *different* frequencies, and then smooth the *compounded* initial noise. (For algorithmic convenience, noise of different frequencies is produced here from separate sets of random numbers treated by the AVG filter and multiplied by the square root of the latter's window width to equalize amplitudes. These constituent noise files, and their sum, are thus close to being amplitudinally random.) Although the results of filtering the summed noise are easy to predict, they are still instructive to view. For the right-side traces of Fig. 7, five different noise sources of different temporal input but equal amplitudinal deviation are combined, and the result divided by five. The comparison of the left and right sides of Fig. 7 shows noisy baselines of an obviously *different* character; although the nature of that difference may be hard to put into words.

It is, however, easy to put into numbers: the upper part of Fig. 9 shows the $N_{p\text{-}p}$ and RMS curves as derived from five independent replicates of the entire procedure. The procedure simulates —for the left side of the Fig. 9 plot— the response of aboriginal multi-frequency noise to filters of comparable window width; mimicking, for instance, the behaviour of a chromatographic baseline containing random source noise with initial frequencies in, say, the 10–0.3-Hz range, and being filtered with time constants in the 0.1–100-s range.

The results of filtering initial *multi*-frequency noise can be compared with the results of filtering initial *single*-frequency noise (for the latter, see Fig. 8). It is obvious why Fig. 9 displays a flatter section (very roughly of slope 1/4 in the

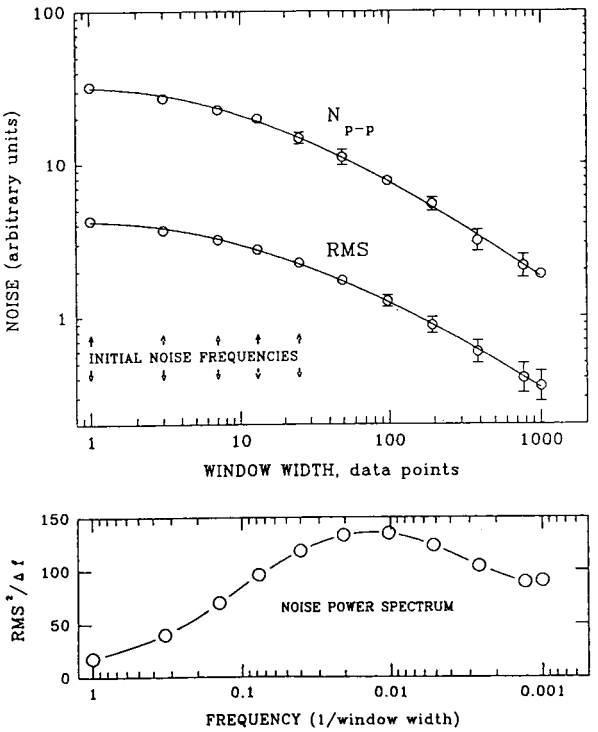

Fig. 9. Measurements on simulated multi-frequency, equal-amplitude noise, smoothed by AVG filter. Upper graph: $N_{p\text{-}p}$ ($= N_{all}$) and RMS; lower graph: conventional "noise power spectrum". Data points are averages of five independent sets (one set is shown on the right side of Fig. 7).

region where noise was introduced, as compared to the following, steeper region roughly of slope 1/2). The narrow window widths can reduce only the faster, not the slower noise components. Once the window width exceeds the time constants (the reciprocals of the introduction frequencies) of all five initial noise components, the curve resumes its familiar square-root slope. That, as in Fig. 8, is then merely the wake, i.e. the inherent residual, of the initial perturbations. Regardless of slope, however, the $N_{p\text{-}p}$/RMS ratio keeps *decreasing throughout* the whole time range. This is most important; and in this, single- and multi-frequency noise are alike. What this finding suggests is that the $N_{p\text{-}p}$/RMS ratio will decrease with the extent of filtering regardless of noise speed and composition.

Since the upper graph of Fig. 9 relies on an

unconventional choice of axes to suit the purpose of this study, we repeat for general interest —but refrain from discussing— its RMS result as a conventional "noise power spectrum" in the lower graph. (A similar graph for Fig. 8 would have simply shown the horizontal line considered characteristic of "white" noise [4,20,36]).

3.8. Again: sundry detectors, sundry filters

So far, the experimental curves used only FPD noise. What about FID and ECD noise? Fig. 10 shows these, plus a photomultiplier tube dark current noise —all as taken from the same, conventional electrometer and filtered by the same, common FIR filter. (The "unfiltered" noise levels are arbitrarily included in Fig. 10 at the RC time constant of the electrometer, i.e. at 0.22 s.)

Fig. 10 shows some expected and some unexpected features. The N_{all}/RMS ratios again decrease with the filter time constant as expected. Also as expected, differences show up between different detectors. What seems unexpected, however, is that all (least-squares second-order regression) curves are clearly nonlinear; and that their slopes vary from roughly zero to roughly one. Are the FID and the ECD, as well as the photomultiplier tube dark current, fundamentally different from the FPD that produced the close-to-square-root slope of Fig. 1?

The answer is no —and part of that answer can be given by a cogent experiment that uses the same FPD flame but samples it by two different acquisition systems. Its results are displayed in Fig. 11. The top part of Fig. 11 shows the "regular FPD" noise, i.e. noise that came through the same electrometer (and the same FIR filter) as the three noise records of Fig. 10: both figures are hence of the same bent. It does indeed make sense that the time constant of the electrometer —which is different in nature and

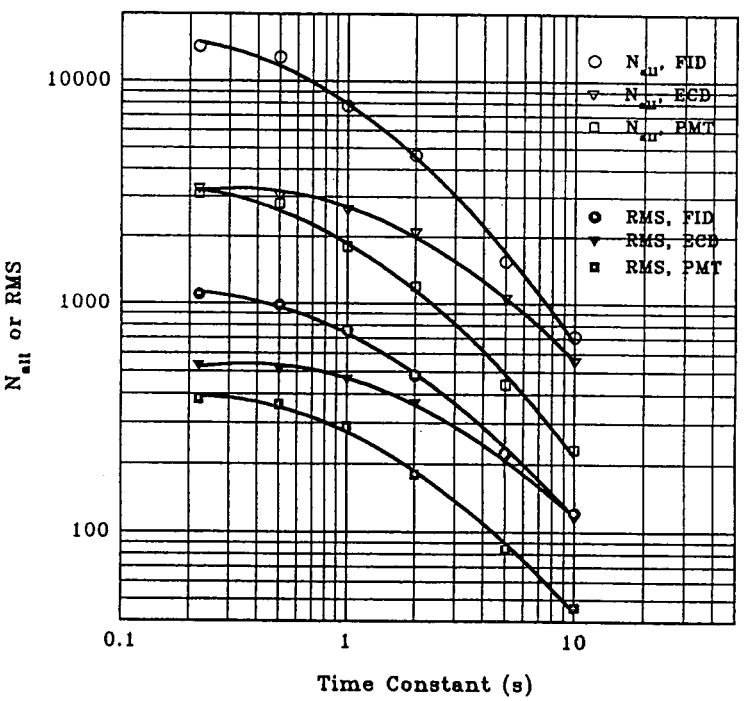

Fig. 10. Measurements on FID, ECD and photomultiplier tube (PMT) noise sources. Electrometer (RC time constant 0.22 s) and FIR filter. Second-order least-squares regression lines.

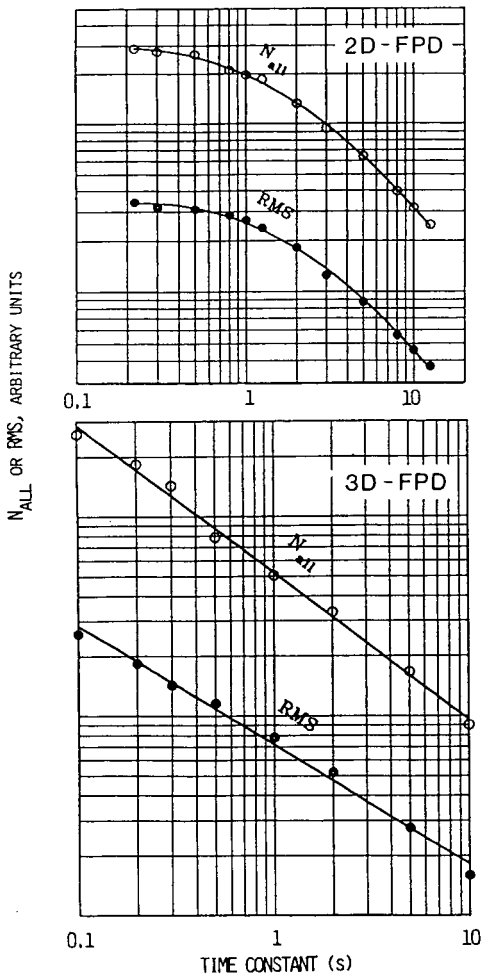

Fig. 11. Measurements on the same FPD noise source via slow and fast acquisition systems. Top: 2D-FPD, otherwise as in Fig. 10: bottom: 3D-FPD [7], first-order least-squares regression lines.

larger in value than the time constant of the fast 3D-FPD acquisition system [7]— should reduce the slope to essentially zero: in that region the noise is already filtered; and as a consequence the expected FIR filter action is largely pre-empted. In contrast, the bottom part of Fig. 11 shows the data for the much faster 3D-FPD system. This system is linear. As expected, the N_{all}/RMS ratio again varies —approximately from 10 to 5— and the (least-squares linear regression) RMS line shows a slope very close to 0.5.

3.9. General guidelines?

The central question of this study, i.e. the correlation between peak-to-peak and standard-deviation based measurements, can now be addressed for the present noise sources and their conditions. It is obvious that no single or single-series measurement can adequately establish such a correlation for *general* use. Nor can theoretical relationships be confidently employed as long as the distribution of noise has not been experimentally determined. The best that can be done under the circumstances is to estimate its range of behaviour over as many typical cases and conditions as possible.

This has been done in Fig. 12. Ten early experimental series are represented, comprising five types of noise sources, three types of filters, and three types of noise definitions (the fourth one available, σ_{fit}, was excluded: it would have made this particular representation less user-friendly without adding any significant new information). The overall variation of the $N_{p\text{-}p}$/RMS ratio covers the range from about 2 to 10 in this self-explanatory bar graph. The bars extend from the largest to the smallest ratio measured in each experimental set; in general, large ratios are derived from little-filtered, small ratios from much-filtered runs. The left ordinate shows the ratio itself; while the right ordinate shows the multiplication factor thereby implied for converting DL_{spec} at $S/RMS = 3$ to DL_{chrom} at $S/N_{p\text{-}p} = 2$.

Fig. 12 reinforces earlier conclusions: comparing the peak-to-peak and RMS based measurements of noise is like comparing apples and oranges tumbling out of chromatography's cornucopia. There is no simple and clear connection between the two, and what there is depends to a large extent on conditions. Thus, if the matter is deemed important enough to follow through —that is if *both* types of detection limits *must* be reported— it is up to the analyst to *measure both* under the prevailing laboratory conditions. Obviously, however, that process is time-consuming.

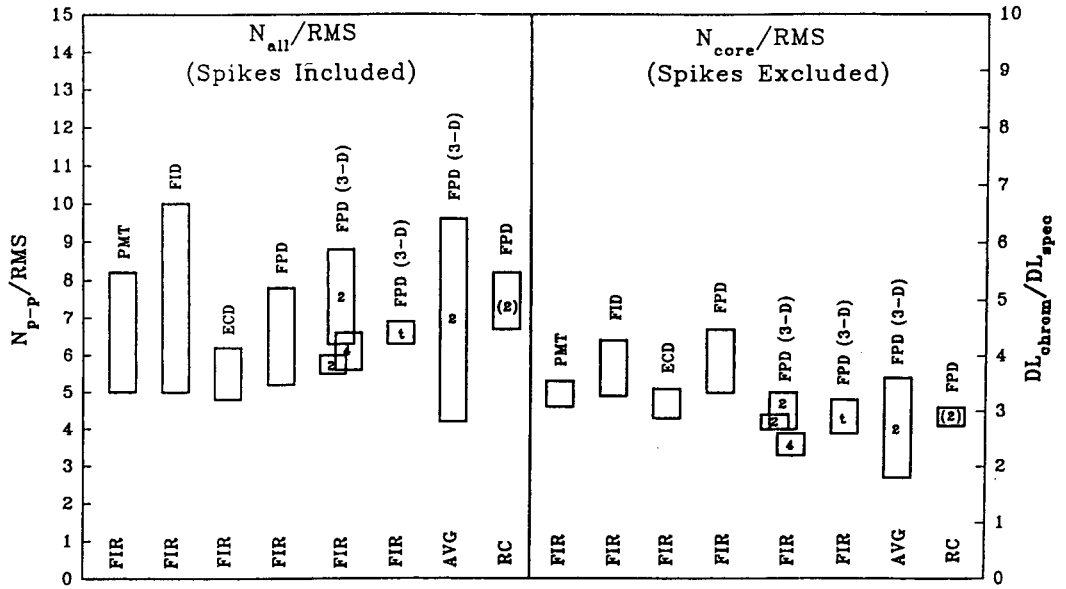

Fig. 12. Comparison of $N_{p\text{-}p}$/RMS and DL_{chrom}/DL_{spec} ranges for different detector and filter combinations. 2, 4 = Segment number in 3D-FPD; (2) = segment number 2, but monitored through stationary wheel via electrometer; t = total of 10 segments in 3D-FPD; PMT = dark current of a Hamamatsu R-374 photomultiplier tube.

Thus there is still some *practical* value in an attempt to narrow conditions and thereby tighten correlations, to the point where a however rough conversion factor may be made to serve less exacting demands. For chromatographic expediency (and only for that) we shall therefore try to come up with a few, very approximate guidelines.

The difference between the "spikes included" N_{all}/RMS and the "spikes excluded" N_{core}/RMS values in Fig. 12 is substantial; as expected it is mainly due to unsmoothed (really: lightly smoothed) noise specimen: their highest values are 10 and 6.8, respectively. With heavy smoothing, the two ratios move closer together (compare also Table 1). Thus the range of values is usually wider in the "spikes *included*" sets. These circumstances would suggest that, for a reasonably repeatable correlation of $N_{p\text{-}p}$ and RMS-based detection limits, the subjective "spikes excluded" measurement might prove the analyst's method of choice if true spikes are present and the smoothing is but light. If spikes are absent and the smoothing is heavy, the analyst may prefer the objective "spikes included" treatment. (The earlier mentioned statistical exclusion of outliers may ameliorate the dilemma this causes for some of the more discriminating software designers.)

On *heavily* smoothed data sets from the three conventional detectors FID, ECD and FPD, the N_{all}/RMS ratio usually falls between 5 and 6, remarkably close to the "$N_{p\text{-}p}$ = 5 RMS" spectroscopic rule-of-thumb (e.g. [3,4]). That implies a range of 3.3 to 4 for the DL_{chrom}/DL_{spec} ratio. The N_{core}/RMS ratios are smaller, but not by much. (These numbers depend, of course, on the permissible extent of smoothing, that is to say on the width of the analyte peak. As will be shown later, the longest time constants used for Fig. 12 would have not just smoothed but smothered a really fast chromatogram.)

3.10. Filters and signal/noise ratios: a practical example

The general "guidelines" suggested above for estimating noise, noise ratios and detection-limit

conversion factors do go at least as far as the data of Fig. 12 allow. Therefore, and for the purpose of illustration, we would like to examine the real-life example of a "detection-limit" file. (This is one of the easily characterized, manipulated, and displayed "noise-cum-analyte" files from our 3D-FPD repository. However, similar files from the 2D-FPD, the ECD and the FPD would, mutatis mutandis, have produced similar results.) The *same* data file is treated here with three *different* filters, to the extent reasonable or possible. A small part (5 min out of 12) of the original data file is displayed on the left side of Fig. 13. It calls to mind Ambrose Bierce's definition of noise as "the chief product and authenticating sign of civilization" (Ref. [37]; substitute "chromatography" for "civilization").

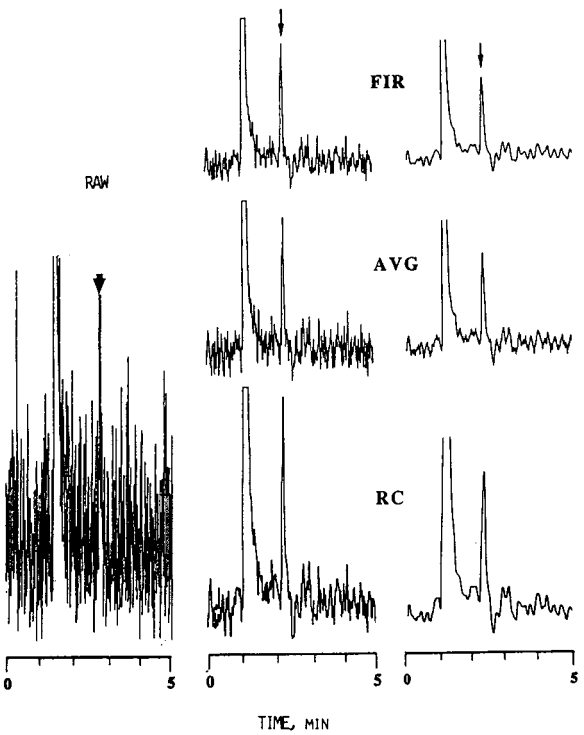

Fig. 13. Five minutes of 3D-FPD noise, with solvent and analyte peak, as smoothed by FIR, AVG and RC filters. Left: raw data file; laser printer; with added arrow marking the analyte peak. Middle: file smoothed to the $S/N_{10\%}$ level by FIR and AVG filter (laser printer) and RC filter (recorder); RC chromatogram adjusted for equal retention. Right: same as middle, but file smoothed to the S/N_{max} level by FIR, and to the strongest setting available by AVG and RC filters. See text for further explanations.

As the noise of the original Fig. 13 data file is being suppressed by the filters, and the analyte peak slowly emerges, the question arises to what level the process can or should be taken. At first thought, this level might be the *maximum* signal/noise ratio (S/N_{max}), at least for straightforward qualitative detection. If, however, the filtered data file is also to be used for quantitation, the argument could be made that the peak height should not be unduly truncated by the smoothing process. Therefore we add a detection-limit assessment at the particular level of filtering that reduces the peak height by an —arbitrary but still generally tolerable— 10% ($S/N_{10\%}$). As it turns out, all three filters are capable of reaching that level. Corresponding parts of the $S/N_{10\%}$ and S/N_{max} chromatograms are displayed in the middle and on the right side of Fig. 13, respectively. Fig. 14 translates these to numbers and plots them in a format conducive to putting forth some simple arguments.

In order to emphasize the controlling role of the analyte peak —whose width defines the extent of smoothing possible or permissible (e.g. [29])— the curves of Fig. 14 are normalized such that the 10% peak-height reduction appears at the same position; and that the three lines are superimposed on one another. This necessitates the use of three formally different abscissae. There is, however, no real contradiction between these three different scales. Time constants of different types of filters cannot be directly compared. Filter action depends on the nature as well as on the sophistication of the particular filter mechanism or algorithm; and the transfer functions of the three filters, operating here on not-quite-Gaussian noise, can at best be roughly estimated. The most glaring difference, i.e. the approximate factor of 1.7 between the time constants of the low-pass RC filter on one hand, and the AVG moving window on the other, is indeed expected [4,20].

All three curves in the top graph —a semilogarithmic plot of peak height reduction vs. filter time constant— appear to be linear. When the top graph is compared with the bottom

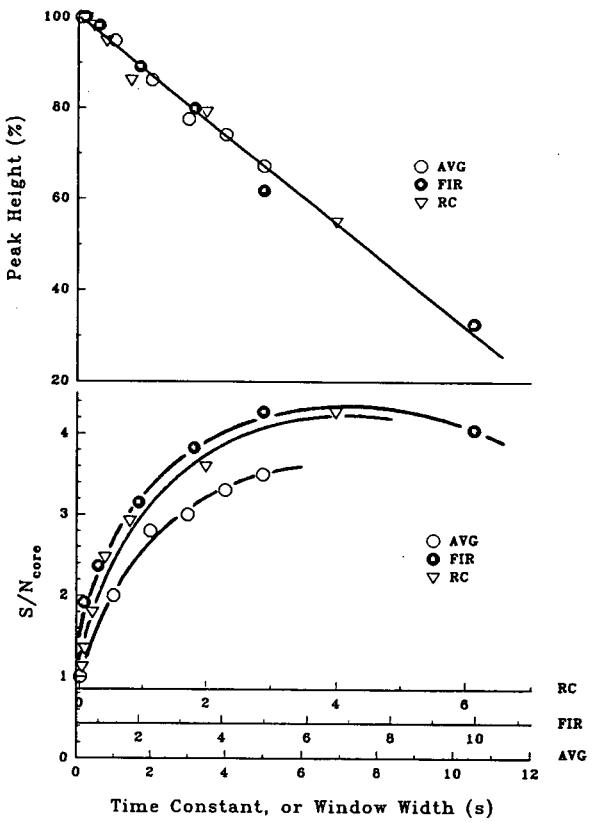

Fig. 14. Corresponding plots of reduction in peak height and S/N vs. nominal time constants of FIR (●), AVG (○) and RC (▽) filters.

graph, it turns out that the S/N increases until the peak height has been reduced by roughly one half! To filter that far may or may not endanger accuracy: how far the process can be driven obviously depends on the particular objectives of analysis and analyst (cf. [29]).

As expected, the fast but unweighted AVG filter performs less well than the slow but weighted FIR filter (running on its maximum of 128 taps). In terms of practical use, however, the difference is decidedly minor. The AVG and RC filters do not overtly reach the S/N_{max} level, but must be close to doing so. The three-pole RC filter is a very simple representative of its kind. Considerably sharper roll-offs can be achieved with units of higher order, say five- or six-pole filters. Again, however, the main advantage of the higher-order filters may only be that they can work a bit closer to the analyte peak without seriously cropping it —a small and usually negligible advantage if no initial noise components are present in that frequency region.

The reader may indeed be surprised at how little the three disparate filters differ in chromatographic performance. Filters, particularly complex and expensive ones, are designed to cut on and/or cut off within the smallest time-constant increment, i.e. they are expected to offer the sharpest roll-offs. Thus they are often judged by how well they can suppress *sine* waves of one frequency versus another [36]. Yet most of the slow noise seen in this paper appears to be just the square-root carry-over (transform) of fast noise: it represents an unavoidable, *minimum* contribution. Truly fast and random noise, in the Gestalt of a slow-moving transform, just can not be circumvented, subtracted or, for that matter, further suppressed by *any* algorithm. (In contrast, if the initial noise were to contain additional, sizeable amounts of *truly* slow components —components close but not equal to the chromatographic dispersion of the analyte peak— then the *higher*-order filters should, on a *relative* basis, provide larger improvements in the detection limit.)

It may be asked what typical improvement in noise —hence in detection limits— the chromatographer could expect from filtering a particular chromatogram; given that most of the initial noise was fast and random and that the filter did not unduly diminish the analyte peak. The fairly obvious answer is that the noise should be reduced by a factor of approximately $(t_F/t_A)^{1/2}$, where t_F and t_A are the (effective, comparable) time constants of filter and amplifier. As a typical order-of-magnitude example, the chromatographically permissible time constant of an RC filter may be 1 s, and the RC constant of the electrometer circuit that feeds it 0.1 s. The approximate decrease in noise the analyst can then expect from the filter is $10^{1/2}$, i.e. about threefold —and the approximate increase in S/N should be the same (provided the peak height has not been significantly compromised). This does, indeed, agree with our practi-

cal experience, in which we find that filters improve detection limits for conventional detector channels by factors of, typically, three to four.

On the other hand, fast acquisition systems, like that of the 3D-FPD, allow more noise to be transferred. Hence they will also allow more noise to be removed over the now wider frequency range of the smoothing process: such systems will appear to offer larger improvement factors. For instance, the maximum S/N improvement shown in Fig. 14 is close to sixfold. It is similarly obvious that excessively spiky baselines lead to apparently larger improvement factors (for the same time-constant ratio of filtered to unfiltered data), particularly if noise is measured as N_{all}.

The data of Fig. 14 do portray the situation correctly; however, they do not convey the full perceptional impact that the analyst may require for optimal pattern recognition and chromatographic diagnosis, or that the reader may desire for an appreciation of how far the smoothing process can actually be driven. This is one reason why we prefer to report our laboratory's (and assess other laboratories') detection limits in original graphic form, i.e. in the form of analyte peaks surrounded by noise, displayed above the chromatographic time scale (and perhaps supplemented in the caption by the effective filter constant) —rather than in the form of single and possibly equivocal numbers. Also, seeing is believing: the reader may have wondered whether it is really possible to derive relatively clean data —as those of Fig. 14— from a chromatogram as shown on the left side of Fig. 13; and whether the action of the three disparate filters is really that alike.

Accordingly, the results of the three filtering processes are presented first for $S/N_{10\%}$ in the middle, then for S/N_{max} (FIR) or the highest available filter setting (AVG and RC) on the right side of Fig. 13. FIR- and AVG-smoothed traces are reproduced on the laser printer, while the RC-smoothed trace is, of necessity, recorded on a chart and then amplified on a copier to obtain the same retention time scale for chromatographic line-up. (While that procedure does not change S/N, both peaks and noise appear a bit larger in comparison.)

To our eyes at least, noise at $S/N_{10\%}$ still appears faster than, hence qualitatively different from, the analyte peak. At S/N_{max}, this difference has essentially vanished: noise could now be perceived as a sequence of smaller peaks (particularly if this were a temperature-programmed run). In other words, the analyte peaks are distinguished by both size and width from the former type of noise, by size only from the latter type of noise. Obviously, *two* perceptional dimensions provide more acute discrimination —hence bestow higher confidence— than just one. It is for this reason that, despite the lower S/N, our group actually prefers to use filter settings close to those of $S/N_{10\%}$; even if merely qualitative evaluation is at stake. We realize, however, that such choice depends not only on the analytical objective, but also on the chromatographic experience and perceptional acuity of the individual analyst.

3.11. Adding perspective (some of it in revision)

To add the obvious: The experiments above —for sake of a clearer, preciser look at the subject— have evaluated the S/N of a *single* data file. Other data files will display the same relative behavior, though not the same absolute number. When a single-data-file S/N is changed into a conventional detection limit, the precision implied by, e.g., Fig. 14 may prove delusive. The detection limit must still remain a *one*-significant-digit number; and that it does can be ascertained by comparing different data files or different experimental series. While interesting in their own right, the differences between three types of filters, or between $S/N_{10\%}$ and S/N_{max}, or between N_{all} and N_{core} are —when measured from *one* data file— generally smaller than the corresponding differences between *two* data files treated by the *same* filter and evaluated according to the *same* definition.

In this context, we believe that a protocol for measuring detection limits would be helpful. Yet, we would also consider it presumptuous for us to

suggest one: this not only because we feel less qualified than others to do so, but also because a prematurely suggested protocol might hinder rather than help the advent of eventual consensus. Accordingly, we will be content to pose a few simple questions (sometimes parenthetically accompanied by our own biases) to make a few (im?)pertinent points.

Given its much better precision, is the analyst to choose and use but a *single* data file for determining the detection limit? Or should the analyst go for the best, or the worst, or the average (with or without standard deviation?) of *multiple* data files? (We are accustomed to using a "typical" one —whatever "typical" may mean in this context.) Furthermore, is the detector at its best, typical or worst performance during the measurement? And is the choice of test substances and chromatographic settings designed for general use, for a particular analysis, or for obtaining the lowest possible value of the detection limit? (We usually attempt to follow literature precedents —unless our own choice of standards and circumstances should yield better results.) *It is these choices* that often cause the largest discrepancies among reported DL values. It has been claimed, for instance, that commercial FIDs —most of which are of similar sensitivity— differ by an order of magnitude in their advertised detection limits.

Note that this does not deny noise analysis its proper place in the determination of detection limits —it just cautions that noise characteristics may be overwhelmed by extraneous circumstances of greater variance. Note also that we are concerned here only with *detector* noise —while the consideration of real-life samples must obviously involve not just detection but the *whole* analytical procedure including sampling. But that is, of course, another and far more complex problem.

However flawed, detection limits will continue to remain indispensable tools of the analytical trade. Nevertheless, chromatographers contemplating the use of a published method or the purchase of an advertised detector may well prefer to investigate —before they invest— a claimed "detection limit" with the help of their own standards and in accord with their own definitions.

Acknowledgement

This study was financially supported by NSERC Research Grant A-9604.

References

[1] J.P. Foley and J.G. Dorsey, *Chromatographia*, 18 (1984) 503.
[2] J.E. Knoll, *J. Chromatogr. Sci.*, 23 (1985) 422.
[3] T.C. O'Haver, in J.D. Winefordner (Editor), *Trace Analysis* (*Chemical Analysis*, Vol. 46), Wiley, New York, 1976, p. 28.
[4] J.D. Ingle, Jr. and S.R. Crouch, *Spectrochemical Analysis*, Prentice-Hall, Englewood Cliffs, NJ, 1988, mainly around pp. 136–140.
[5] L.A. Currie, in L.A. Currie (Editor), *Detection in Analytical Chemistry* (*ACS Symposium Series*, No. 361), American Chemical Society, Washington, DC, 1988, p. 33.
[6] X.-Y. Sun, B. Millier and W.A. Aue, *Can. J. Chem.*, 70 (1992) 1129.
[7] B. Millier, X.-Y. Sun and W.A. Aue, *J. Chromatogr. A*, 675 (1994) 155.
[8] S.D. Brown, in S.J. Haswell (Editor), *Practical Guide to Chemometrics*, Marcel Dekker, New York, 1992, p. 239.
[9] H.G. Hecht, *Mathematics in Chemistry*, Prentice-Hall, Englewoood Cliffs, NJ, 1990.
[10] N. Dyson, *Chromatographic Integration Methods* (*RSC Chromatography Monographs*), Royal Society of Chemistry, Cambridge, 1990.
[11] R.G. Brereton, *Chemometrics*, Ellis Horwood, New York, 1990.
[12] D.L. Massart, B.G.M. Vandeginste, S.N. Deming, Y. Michotte and L. Kaufman, *Chemometrics*, Elsevier, Amsterdam, 1988.
[13] J.D. Ingle, Jr. and S.R. Crouch, *Spectrochemical Analysis*, Prentice-Hall, Englewood Cliffs, NJ, 1988, pp. 172–176.
[14] G.L. Long and J.D. Winefordner, *Anal. Chem.*, 55 (1983) 713A.
[15] Analytical Methods Committee, *Analyst*, 112 (1987) 199.
[16] P.W.J.M. Boumans, *Spectrochim. Acta*, 46B (1991) 431, 917.
[17] L.A. Currie (Editor), *Detection in Analytical Chemistry* (*ACS Symposium Series*, No. 361), American Chemical Society, Washington, DC, 1988.
[18] R.W. Hamming, *Digital Filters*, Prentice Hall, Englewood Cliffs, NY, 2nd ed., 1983.

[19] W.A. Aue, B. Millier and X.-Y. Sun, *Can. J. Chem.*, 70 (1992) 1143.
[20] C.T.J. Alkemade, W. Snelleman, G.D. Boutilier, B.D. Pollard, J.D. Winefordner, T.L. Chester and N. Omenetto, *Spectrochim. Acta*, 33B (1978) 383.
[21] E.P. Grimsrud, in H.H. Hill, Jr. and D.G. McMinn (Editors), *Detectors for Capillary Chromatography* (*Chemical Analysis*, Vol. 121), Wiley-Interscience, New York, 1992, Ch. 5.
[22] A. Zlatkis and C.F. Poole (Editors), *Electron Capture* (*Journal of Chromatography Library*, Vol. 20), Elsevier, Amsterdam, 1981.
[23] J. Connor, *J. Chromatogr.*, 200 (1980) 15.
[24] W.A. Aue and S. Kapila, *J. Chromatogr.*, 188 (1980) 1.
[25] W.A. Aue, K.W.M. Siu, D. Beauchemin and S.S. Berman, *J. Chromatogr.*, 500 (1990) 95.
[26] D.G. McMinn and H.H. Hill, Jr., in H.H. Hill, Jr. and D.G. McMinn (Editors), *Detectors for Capillary Chromatography* (*Chemical Analysis*, Vol. 121), Wiley-Interscience, New York, 1992, Ch. 2.
[27] S.J. Haswell (Editor), *Practical Guide to Chemometrics*, Marcel Dekker, New York, 1992.
[28] H.C. Smit and H.L. Walg, *Chromatographia*, 8 (1975) 311.
[29] C.G. Enke and T.A. Nieman, *Anal. Chem.*, 48 (1976) 705A.
[30] *Nomenclature for Chromatography (IUPAC Recommendation 1993); Pure Appl. Chem.*, 65 (1993) 819 (p. 851).
[31] *ASTM E 685-79*, American Society for Testing and Materials, Philadelphia, PA, 1st ed., 1981; as shown by N. Dyson, *Chromatographic Integration Methods* (*RSC Chromatography Monographs*), Royal Society of Chemistry, Cambridge, 1990.
[32] C. Chatfield, *The Analysis of Time Series*, Chapman & Hall, London, 4th ed., 1989.
[33] P. Gray, *Psychology*, Worth Publishers, New York, 1991, Ch. 9.
[34] K.W.M. Siu and W.A. Aue, *Can. J. Chem.*, 65 (1987) 1012.
[35] A.W. McMahon and W.A. Aue, *Mikrochim. Acta*, II (1987) 91.
[36] K.W. Busch and M.A. Busch, *Multielement Detection Systems for Spectrochemical Analysis*, Wiley, New York, 1990, e.g. pp. 364–377.
[37] A. Bierce, *The Devil's Dictionary*, Sagamore Press, New York, 1957; as cited by W.R. Bennett, *Electrical Noise*, McGraw-Hill, New York, 1960.

ELSEVIER

Journal of Chromatography A, 687 (1994) 283–290

JOURNAL OF CHROMATOGRAPHY A

Fundamental noise in three chromatographic detectors☆

Walter A. Aue*, Hameraj Singh, Xun-Yun Sun[1]

Department of Chemistry, Dalhousie University, Halifax, Nova Scotia B3H 4J3, Canada

First received 27 April 1994; revised manuscript received 20 June 1994[2]

Abstract

Counting statistics are used to estimate the minimum theoretical noise of three chromatographic detectors, by assuming that the standard deviation of their baselines equals the square root of their primary chemical events. These primary events are taken to be the observed generation of photons in the flame photometric detector, the emission of β rays in the electron-capture detector, and the formation of ion pairs in the flame ionization detector. The theoretically estimated and the experimentally observed noise agree in every case. This suggests that baseline noise in the three particular detectors is due, predominantly if not exclusively, to random processes involving the atomic structure of matter: therefore, it cannot be further reduced.

1. Is there a minimal noise?

What causes chromatographic noise? The question has many answers; too many, in fact, to consider within a short manuscript. A more tractable question may be: What is the minimal detector noise? Or, differently put: What is the inherent, the unavoidable, the smallest possible part of the short-term baseline fluctuations we call noise? And: How does this fundamental noise compare with the experimentally measured one?

Good reasons exist for asking this question. Often, improvement in the signal-to-noise ratio (S/N) is achieved by decreasing noise rather than by increasing signal. However, if the actual noise is already close to the theoretical limit (and if it has already been smoothed to the maximum allowable extent), little is to be gained by attempting to suppress it further. Besides, knowing something about the nature of noise may turn out to be mechanistically interesting as well as analytically helpful.

In chromatographic detectors whose baselines derive from chemical reactions, these reactions must indeed contribute to noise —the question is only to what fraction of the total. The simplest unavoidable noise contribution is surely the one based on the atomic structure of matter. Detector reactions, as all chemical (or nuclear) events, are *random* at the molecular level. This implies that the standard deviation of their rate (and hence the noise of the baseline if no other source of variation is present) can be described as a square-root function of the time interval over which it is being observed. The generation of photons by chemiluminescence in the flame photometric detector (FPD), the emission of β

* Corresponding author.

☆ Part of doctoral thesis of H.S.

[1] Present address: Environmental Trace Substances Center, Room 207, 5450 South Sinclair Road, Columbia, MO 65203, USA.

[2] Publication delayed at the authors' request.

0021-9673/94/$07.00
SSDI 0021-9673(94)00582-T

particles by the radioactive foil in the electron-capture detector (ECD), and the formation of ion pairs by chemiionization in the flame ionization detector (FID) would certainly qualify as such primary, random events.

The three detectors mentioned (FPD, ECD and FID) all play prominent roles in chromatography. Much has been, and continues to be published on and about them (e.g. [1]). Since we happened to have at our disposal representative models of all three detectors, we thought it interesting to take a look at their noise characteristics. This the more because we had previously used these three detectors in a study of root-mean-square (RMS) and peak-to-peak noise ($N_{p\text{-}p}$) for possible interconversion of different types of detection limits [2].

In this study, we shall attempt to calculate the minimal noise levels of the FPD, ECD and FID as the square root of their (observed) fundamental events. If noise levels thus calculated should agree with experimentally measured ones, noise in the three detectors can be considered random and fundamental (i.e. non-reducible for a given measurement interval). Since various considerations, approximations and limitations are bound to become part and parcel of this attempt, we believe that the necessary equations are best developed and discussed with the help of actual cases and measurements. This will be done in a separate chapter for each detector. Following those chapters, an Appendix will condense the multi-step equation sets to single, compact and user-friendly (though perhaps not as easily appraised) formulae. These formulae can facilitate the evaluation of noise from particular FPDs, ECDs and FIDs —and perhaps other detectors— in the chromatographic laboratory.

2. Fundamental noise in the FPD?

We recently attempted to increase the S/N of a multi-channel FPD [3] by increasing its light throughput. The success or failure of such an attempt depends on the nature of noise [4–6]: in the case of prevalently colored or correlated noise (e.g. flame flicker or chromatographic flow fluctuations) the attempt is likely to fail; in the case of prevalently white or random noise (e.g. photon shot noise) the attempt is likely to succeed. In the latter case, the S/N should increase with the square root of the light throughput (or the time span, or the number of repetitions).

Consequently, one of the simplest experiments for characterizing FPD noise is to decrease the light throughput from a (constant) flame, while measuring both the photomultiplier tube (PMT) current and the corresponding noise level right down to the dark current. The experiment can be extended to the high-input side by increasing the emissivity of the flame, i.e. by making it larger and hotter. (This also tests whether the flame starts to produce flicker noise at particular flow conditions.)

Fig. 1 shows the result of this experiment.

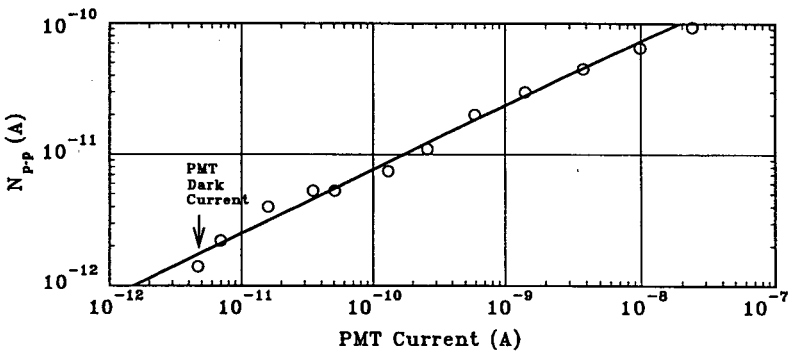

Fig. 1. Peak-to-peak noise vs. current in a Hamamatsu R-374 photomultiplier tube at −700 V; with different light input from a typical FPD flame (see text for details).

About half of the data points were obtained by intercepting different fractions of the constant FPD light beam (with the opaque edge of a variable interference filter wheel that happened to be mounted on one side of the detector [3]); the other half were obtained by observing the light beam through a conventional, filterless FPD channel (mounted on the other side) and adding larger and larger amounts of air to the flame. All data points still fall on *one* line in the log–log plot of Fig. 1; and, as determined by least-squares linear regression, the line has a slope very close to one half. This indicates, as expected, a random process.

It does not, however, identify photon shot noise (really: the temporal randomness in the sequence of observed luminescent flame events) as the main culprit. Other effects could have been responsible for the observed square-root relationship [4–6]. Fortunately, though, circumstantial evidence and a back-of-the-envelope estimate can help to illuminate the case.

From the current and gain of the PMT, it is easy to estimate the number of photons that eject an electron from the photocathode during a given time interval. The square root of this number, as is well known from counting statistics, represents the standard deviation of the random, minimal noise. It can be translated back to current and, after conversion from RMS to $N_{p\text{-}p}$, can be compared to the experimentally measured noise of Fig. 1. (Note: The $N_{p\text{-}p}$/RMS ratio changes with the detector, its condition, and the extent of data smoothing [2]. It is possible to measure RMS noise directly but, for ease of experiment and chromatographic relevance, we prefer to measure $N_{p\text{-}p}$.)

There are also a number of assumptions or approximations hidden in this estimate. While they should not call into question the validity of a result that has only one significant digit, they should at least be mentioned.

The easiest overlooked of these may be the time constant. It hides the transfer function of the filter (or of the electrometer). Given the noise-equivalent-bandpass characteristics of integrating vs. low-pass resistor–capacitor (RC) circuits [4], and given our own, practical experience in comparing non-weighted moving-window averaging with three-pole RC smoothing [2], we assume the effective integration time to equal roughly 1.7 times the RC constant of the filter. In the present case, the electrometer has a time constant of 0.22 s, hence the effective integration time is estimated to be 0.37 s.

The photon yield for the data points on the left side of Fig. 1 is about 20%, the typical value for the Hamamatsu R-374 PMT [7] receiving light from the leading edge of the variable interference filter (ca. 400 nm). The photon yield for the data points on the right side of Fig. 1 is an average that could, if necessary, be determined from the background spectrum and the sensitivity profile of the PMT; it drops strongly toward the red. The question is, however, whether the photon yield should be included in the noise calculation. While at least five photons strike the photocathode for each ejected electron, only photoelectrically effective ones count —and, therefore, only they need to be counted. *Non*-effective photons might as well have struck photoelectrically inert parts of the arrangement (as indeed the overwhelming majority of photons do). The noise-determining step in any multi-step process is obviously the one with the smallest rate of discrete events (here: the generation of electrons from the photocathode). The decision to exclude the photon yield from the calculation is further supported by the fact that Fig. 1 shows no discernable discontinuity in the mid-shift from mono- to polychromatic photons.

The gain of the R-374 PMT at −700 V (the voltage used in the experiment) is estimated as $2.0 \cdot 10^4$. This estimate is based on the specified gain at −1000 V ($= 5.3 \cdot 10^5$ [7]) and our own measurement of the gain ratio between −1000 and −700 V ($= 26$).

At, say, 1 nA of baseline current (which is a fairly typical value for our operation of the FPD, and allows us to neglect the much lower dark current)

$$1.0 \cdot 10^{-9}\ \mathrm{A} \cdot \frac{0.37\ \mathrm{s}}{1.6 \cdot 10^{-19}\ \mathrm{As/e^-}} \cdot \frac{1\ h\nu}{2 \cdot 10^4\ \mathrm{e^-}}$$

$$= 1.2 \cdot 10^5\ h\nu$$

hence the RMS noise of photoelectrically effective photons ($h\nu$) is $(1.2 \cdot 10^5)^{1/2} = 3.4 \cdot 10^2$ $h\nu$ (for an integration time of 0.37 s). Changing back into current and converting RMS to $N_{p\text{-}p}$ noise —with the conversion factor $(N_{p\text{-}p}/\mathrm{RMS})_{0.37\ s} = 8$ derived from our own measurements [2]— yields

$$3.4 \cdot 10^2\ h\nu \cdot \frac{2 \cdot 10^4\ e^-}{1\ h\nu} \cdot \frac{1.6 \cdot 10^{-19}\ \mathrm{As/e^-}}{0.37\ \mathrm{s}} \cdot 8 = N_{p\text{-}p} = 2 \cdot 10^{-11}\ \mathrm{A}$$

The result of the estimate is, of course, a one-significant-digit number, and it is deliberately written as one. This limitation being understood, the estimated noise compares well (almost too well) with the measured noise of about $2.4 \cdot 10^{-11}$ A. The accuracy and credibility of both experiment and estimate could obviously be improved, e.g. by using photon *counting*, boxcar averaging, monochromatic photons (just in case), direct RMS evaluation, etc. However, even the present comparison suggests very strongly that the randomness of luminescent events (computationally: the counting statistic of photoelectrons) is responsible for the overwhelming part of the noise. In other words, this presumably typical FPD produces noise that is random and close to the fundamental minimum.

3. Fundamental noise in the ECD?

The chemistry of the ECD has been the object of much study and the subject of much discussion (e.g. [1,8–11]); yet much of it remains poorly understood. What is not in doubt, however, is that the reactions leading to the ECD's response involve β decay and ion-pair generation, followed by the capture of electrons by analyte molecules. There is also little doubt that ion-pair distributions, space charges, and various ion–molecule reactions all influence the detector's behavior. Again, the noise-determining step is the step with the lowest rate of observed discrete events. Since one β ray forms many ion pairs on its travel through the gas phase —i.e., since many more electrons are collected than β rays emitted— the minimal noise characteristics should depend primarily on the number of (effective) radioactive decays.

There exists, however, a problem unique to β decay: β's are not monochromatic; they roughly conform to an exponential distribution in energy. A further complication is their backscattering from internal detector surfaces, particularly those of high atomic mass [12,13]. The exponential distribution of the ion pair yields from individual β's must distort and broaden the initially Gaussian distribution of their counts (the intervals between sequential decays that translate into noise amplitudes). Relatively short intervals between β's of relatively high energy must lead to the largest positive excursions of the baseline; relatively long intervals between β's of relatively low energy to the largest negative ones.

On the other hand, the ECD may have a built-in damping system in its chemistry (reactions) and physics (space charges): for instance, the second-order ion pair recombination is much faster in regions or during episodes of *high* ionic density. The ECD thus represents a system far more complex than that of the FPD, in which (effective) photons produce electron avalanches of approximately the *same* magnitude; or that of the FID, in which *unit* charges are produced and (nigh immediately and exhaustively) collected.

A cursory simulation suggests that the RMS value of Gaussian noise increases by a factor of somewhere around 1.6 if randomly chosen Gaussian distribution values are multiplied by randomly chosen exponential distribution values within limits reasonable for a real-life ^{63}Ni system [12]. Of the total specified foil activity (15 mCi), fewer than half of the β's will have the correct direction for reaching the gas phase (neglecting isotopic purity as well as coating thickness, contamination, and curvature of the foil). We therefore arbitrarily assume one half of all β's to be "effective" in generating gaseous ion pair trails. This is, admittedly, a very rough assumption.

One of our foils (in the Shimadzu ECD) is relatively new, but the other (in the Tracor

ECD) is beyond its teens —and its originally specified activity appears to have dropped from 15 to 11.9 mCi. (Of the drop, about 2 mCi is due to age, i.e. radioactive decay; the rest, we hope, is due to analytical contamination as opposed to annual clean-up. The apparent value of 11.9 mCi is derived from the ratio of maximal d.c. currents then vs. now, i.e. 3.0 vs. 2.37 nA). Not only is the Tracor ECD relatively old and the Shimadzu ECD relatively young, but the former is a two-chamber unit designed for d.c. and constant-frequency operation, the latter is a one-chamber unit designed for constant-current operation: the two thus provide ample opportunity for a wide-ranging comparison of duly representative measurements.

For the measurements, both ECDs are used in d.c. mode at their S/N-optimized potential; i.e. the way they would serve conventional d.c. ECD analysis. That means, however, that not all possible current is withdrawn (if it were, no electrons would be left for the analyte to capture, leaving the detector responseless). Yet, the electrons that are not withdrawn (34% in the Shimadzu, 38% in the Tracor) do kinetically and electrostatically influence the sampled system. Given our but rudimentary understanding of this system, such subtle and not-so-subtle effects are impossible to quantify.

It would have been interesting to produce for the ECD a graph similar to the one shown in Fig. 1 for the FPD. That would, however, have called for varying the random input itself, for instance by inserting a cylinder that would cover a variable fraction of the radioactive foil. For obvious reasons we did not want to do that. Although the following estimate of minimal noise must thus rely on a number only (as opposed to a number *and* a square-root relationship), it is at least based on mutually supportive data from two very differently constructed ECDs; ECDs that are, furthermore, monitored by different electrometers of different time constants.

The Shimadzu ECD has a 15 mCi ^{63}Ni cylindrical foil; it is operated at −0.20 V d.c., resulting in a 1.97 nA (of a maximum 3.0 nA) baseline current; and it makes use of a laboratory-made power supply and electrometer of RC time constant = 1.0 s (i.e. of an estimated 1.7 s integration time). Under these conditions, the $(N_{p\text{-}p}/\mathrm{RMS})_{1.7\ s}$ ratio is close to 5.5 [2].

The "effective" number of disintegrations (d) per second, i.e. the number of β's likely to reach the gas phase, are

$$15 \cdot 10^{-3}\ \mathrm{Ci} \cdot 3.7 \cdot 10^{10} \frac{d}{\mathrm{s \cdot Ci}} \cdot 0.5 = 2.8 \cdot 10^{8} \frac{d}{\mathrm{s}}$$

These β's can produce a maximum current of 3 nA, hence

$$\frac{3 \cdot 10^{-9}\ \mathrm{A}}{1.6 \cdot 10^{-19}\ \mathrm{As/e^-}} = 1.9 \cdot 10^{10}\ \mathrm{e^-/s}$$

suggesting that, on average, 68 electrons are generated per one β. For an integration time of 1.7 s, the RMS noise, adjusted for the exponential ion-pair yield of β's, is

$$N_{\mathrm{RMS}} = \left(2.8 \cdot 10^{8} \frac{d}{\mathrm{s}} \cdot 1.7\ \mathrm{s}\right)^{1/2} \cdot 1.6 = 3.5 \cdot 10^{4}\ d\ ,$$

which, when converted to current, pared to the baseline of 1.97 nA, and finally changed to $N_{p\text{-}p}$ noise, yields

$$\frac{3.5 \cdot 10^{4}\ d}{1.7\ s} \cdot \frac{68\ \mathrm{e^-}}{d} \cdot \frac{1.6 \cdot 10^{-19}\ \mathrm{As}}{\mathrm{e^-}} \cdot \frac{1.97}{3.0} \cdot 5.5 = N_{p\text{-}p} = 8 \cdot 10^{-13}\ \mathrm{A}$$

This compares well with the experimental result of 0.6 pA. (Note: here as elsewhere, the calculations are carried out with a larger number of digits; however, only *two* digits are normally shown and the result, for obvious reasons, is represented by a *single* significant digit. If desired, additional digits can be easily obtained by repeating the simple calculation.)

The analogous calculation for the Tracor ECD uses an estimated foil activity of 11.9 mCi and an estimated integration time of 0.17 s for the electrometer's 0.1 s RC time constant. The $(N_{p\text{-}p}/\mathrm{RMS})_{0.17\ s}$ conversion factor is about 6 [2]. The detector is operated at −18 V at a baseline current of 1.48 nA. Hence the RMS noise equals

$$\left(11.9\cdot10^{-3}\,\mathrm{Ci}\cdot3.7\cdot10^{10}\frac{d}{\mathrm{s}\cdot\mathrm{Ci}}\cdot0.5\cdot0.17\,\mathrm{s}\right)^{1/2}\cdot1.6 = N_{\mathrm{RMS}} = 9.8\cdot10^{3}\,d$$

and

$$\frac{9.8\cdot10^{3}\,d}{0.17\,\mathrm{s}}\cdot\frac{68\,\mathrm{e}^{-}}{d}\cdot\frac{1.6\cdot10^{-19}\,\mathrm{As}}{\mathrm{e}^{-}}\cdot\frac{1.48}{2.37}\cdot6.0 = N_{\mathrm{p\text{-}p}} = 2\cdot10^{-12}\,\mathrm{A}$$

This compares still reasonably well with the experimental result of 4.5 pA peak-to-peak noise.

No doubt experiments and estimates could both be improved, e.g. by measuring the foil count directly, by carrying out a more precise simulation of the roughly exponential β energy distribution, and by considering electron backscattering effects in their influence on the root-mean-square calculation of noise, etc. Yet the twin experiments suggest —in unison and, in our opinion, with sufficient congency— that (clean) ECD noise is predominantly caused by a fundamental process; and that this process is the decay of the radioisotope.

4. Fundamental FID noise?

A pure hydrogen–air flame contains very few ions; the FID baseline current is therefore very low. Jentzsch and Otte [14] mention a value of "$\leq 0.75\cdot10^{-11}$ A for an empty capillary replacing the column [and] obviously dependent on the cleanliness of the gases and the apparatus". For "spectroscopic" types of flames, Alkemade et al. [15] summarize: "The ionization found is often due to metallic or organic impurities. In pure H_2 flames some residual ionization close to thermal equilibrium may be found, involving NO^+ and H_3O^+ ions. The latter ion is formed by the recombination reaction $H + H + OH \rightarrow H_3O^+ + e^-$ (see Hayhurst and Telford 1972, 1975)".

In chromatographic practice, it is nigh impossible to exclude some contamination by carbon and silicon compounds (and occasionally by sodium or copper halides). However, the system may still behave in a fundamental, random manner. Consequently, rather than maintain our minimalist approach and attempt to design and test the *cleanest* FID possible, we decided to use a just reasonably clean FID (in our case part of a three-detector ECD–FPD–FID combination available from a thesis project), and deliberately dope it with small amounts of typical contaminants: either directly by adding different levels of methane, or indirectly by adding different levels of bleed from a heated Carbowax 20M column to the hydrogen stream (the latter arrangement bypasses and thereby spares the Shimadzu ECD a possibly detrimental exposure to reactive oxygenates from the decomposing column [16]). This may simulate a high baseline; or it may simulate a —*continuously* introduced— analyte. (Note that —typically though not exclusively— the noise of importance to chromatography is the noise of the baseline; the noise of importance to spectroscopy is the noise of the signal.)

Fig. 2 shows the interesting result of this experiment. Increasing the rate of ionization over a decade from that of the "pure" hydrogen–air flame results, indeed, in a *square-root* increase of noise, thereby suggesting a random process. At still higher background levels —i.e. higher than a tenfold increase and thus perhaps beyond acceptable operating conditions of the FID— the noise increases *proportionally* with the current.

If this were a spectroscopic system, one would

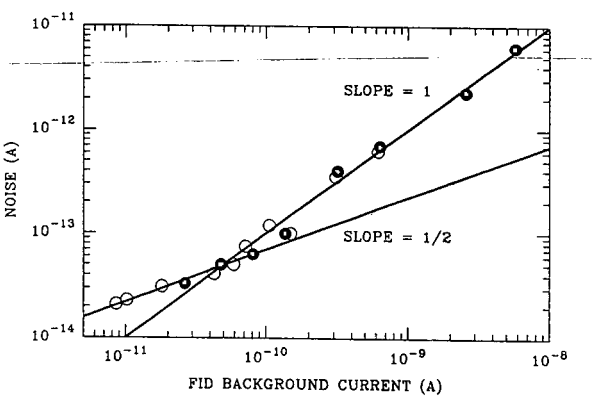

Fig. 2. Peak-to-peak noise vs. current in a flame ionization detector; with different levels of methane, or Carbowax 20M-derived bleed, added to the hydrogen flow. ● = Methane; ○ = Carbowax.

call the latter type of noise "multiplicative" and would typically attribute it to "analyte flicker" [17]. In spectroscopic systems it is indeed common to observe a change-over from additive to multiplicative noise (e.g. from photon shot noise to analyte fluctuation noise) as the signal level increases. A similar change-over appears to occur in the chemiionization system of the FID; a parallelism that could have been predicted.

It would be interesting, nevertheless, to find out what causes this excess noise —spatial or temporal heterogeneity in analyte concentration, perhaps, or influence of the analyte on the geometry or chemistry of the flame— and whether the square-root range can vary among different FID models and/or can be expanded for analytical ends by a change in conditions. However, in the particular context of this study (and, we presume, in the practical context of most chromatographic techniques), this question is of minor importance.

The experiment used the Tracor electrometer of RC = 0.10 s time constant, i.e. of an assumed 0.17 s integration time. The $(N_{p\text{-}p}/\mathrm{RMS})_{0.17\ s}$ ratio equals approximately 6 in this newly constructed FID (which, compared to older conventional FIDs in our possession, is still remarkably free of spikes). The baseline current in the absence of deliberately added column bleed or constantly bled-in analyte is $8.6 \cdot 10^{-12}$ A; the p-p noise at this point (the lowest data point of Fig. 2) is $2 \cdot 10^{-14}$ A. (This compares favorably with the noise level mentioned by Jentzsch and Otte, i.e., $\leq \pm 5 \cdot 10^{-14}$ A [14]; however, this comparison must remain highly approximate in the absence of any literature information on time constants.)

The number of ion pairs generated within the integration interval is then

$$8.6 \cdot 10^{-12}\ \mathrm{A} \cdot \frac{0.17\ \mathrm{s}}{1.6 \cdot 10^{-19}\ \mathrm{As/e^-}} = 9.1 \cdot 10^{6}\ \mathrm{e^-}$$

and $N_{p\text{-}p}$ equals

$$(9.1 \cdot 10^{6})^{1/2} \cdot \frac{1.6 \cdot 10^{-19}\ \mathrm{As/e^-}}{0.17\ \mathrm{s}} \cdot 6 = 2 \cdot 10^{-14}\ \mathrm{A}$$

The estimated magnitude of noise that originates from the randomness of ion-generating events is thus essentially identical with the value measured in a "clean" FID flame. Although —as in the ECD and FPD cases— experimental accuracy could no doubt be improved, the data are good enough to allow us to presume that most if not all of the FID's baseline noise is fundamental in character; i.e. that it is due to the atomic nature of matter and that, consequently, it is determined by, and cannot be reduced below, counting statistics.

The fact that this statement applies not only to the FID but also to the ECD and the FPD —i.e. to every one of the detectors tested— is welcome indeed. For one, it highlights a fundamental property that these three (and perhaps more) otherwise disparate chromatographic detectors have in common. Also, this fundamental property quantitatively defines the theoretical noise level. That can prove a practical advantage: it may help the analyst evaluate how well an actual detector is performing, or how clean it is, or how (or whether) the fluctuations of its baseline could be further reduced.

Acknowledgement

This study was supported by NSERC research grant A-9604.

Appendix

To facilitate such practical assessments, we have condensed the developed equation sets into single, simple and general formulas. The fundamental noise levels for the three detectors thus are

$$\mathrm{RMS_{FPD}} = \sqrt{\frac{I \cdot e \cdot g}{t}}$$

$$\mathrm{RMS_{ECD}} = I \cdot f_e \cdot \sqrt{\frac{1}{A_{\mathrm{eff.}} \cdot \mathrm{Ci} \cdot t}}$$

$$\mathrm{RMS_{FID}} = \sqrt{\frac{I \cdot e}{t}}$$

where, again, RMS is the root-mean-square (the

standard deviation σ in case of a Gaussian distribution) of the baseline fluctuations in A; I is the baseline current in A; e is the charge of the electron ($1.6 \cdot 10^{-19}$ As); t is the integration time of the measurement (the counting time or effective time constant of the acquisition/filter system); g is the PMT gain at the voltage of the experiment; A_{eff} is the effective activity of the ECD foil in Curies (for this study assumed to be roughly one half of the total remaining activity —a number in definite need of refinement); Ci is the number of disintegrations per second of one Curie ($3.7 \cdot 10^{10}$); and f_e is a factor that mainly describes the widening of the random-emission RMS noise band by the exponential β energy distribution. (Note: for this study, f_e is assumed to be roughly 1.6. This number has been confirmed —though only for the ideal mixing of Gaussian and exponential distributions— by a Dalhousie student project in chemometrics [18], which was carried out while this manuscript was under review.

References

[1] H.H. Hill and D.G. McMinn (Editors), *Detectors for Capillary Chromatography*, Wiley, New York, 1992.
[2] X.-Y. Sun, H. Singh, B. Millier, C.H. Warren and W.A. Aue, *J. Chromatogr. A*, 687 (1994) 259.
[3] B. Millier, X.-Y. Sun and W.A. Aue, *J. Chromatogr. A*, 675 (1994) 155.
[4] J.D. Ingle, Jr. and S.R. Crouch, *Spectrochemical Analysis*, Prentice Hall, Englewood Cliffs, NJ, 1988.
[5] K.W. Busch and M.A. Busch, *Multielement Detection Systems for Spectrochemical Analysis*, Wiley, New York, 1990.
[6] C.T. Alkemade, W. Snelleman, G.D. Boutilier, B.D. Pollard, J.D. Winefordner, T.L. Chester and N. Omenetto, *Spectrochim. Acta*, 33B (1978) 383.
[7] *Photomultiplier Tubes, 1992 Catalogue*, Hamamatsu Corp., 360 Foothill Road, Bridgewater, NJ 08807-0960, USA, 1992.
[8] A. Zlatkis and C.F. Poole (Editors), *Electron Capture (Journal of Chromatography Library*, Vol. 20), Elsevier, Amsterdam, 1981.
[9] J. Connor, *J. Chromatogr.*, 200 (1980) 15.
[10] W.A. Aue and S. Kapila, *J. Chromatogr.*, 188 (1980) 1.
[11] W.A. Aue, K.W.M. Siu, D. Beauchemin and S.S. Berman, *J. Chromatogr.*, 500 (1990) 95.
[12] K.W.M. Siu and W.A. Aue, *Can. J. Chem.*, 65 (1987) 1012.
[13] A.W. McMahon and W.A. Aue, *Mikrochim. Acta*, II (1987) 91.
[14] D. Jentzsch and E. Otte, *Detektoren in der Gas-Chromatographie (Methoden der Analyse in der Chemie*, Vol. 14), Akademische Verlagsgesellschaft, Frankfurt/Main, 1970, pp. 331–332.
[15] C.T.J. Alkemade, T. Hollander, W. Snelleman and P.J.T. Zeegers, *Metal Vapours in Flames*, Pergamon Press, Oxford, 1982, pp. 460–463.
[16] V. Paramasigamani and W.A. Aue, *J. Chromatogr.*, 168 (1979) 202.
[17] C.T.J. Alkemade, W. Snelleman, G.D. Boutilier and J.D. Winefordner, *Spectrochim. Acta*, 35B (1980) 261.
[18] Z.-P. Lin and P.D. Wentzell, unpublished results.

ELSEVIER

Journal of Chromatography A, 687 (1994) 291–301

JOURNAL OF CHROMATOGRAPHY A

Dual-channel response ratios from an integrative algorithm☆

Hameraj Singh, Brian Millier, Walter A. Aue*

Department of Chemistry, Dalhousie University, Halifax, Nova Scotia B3H 4J3, Canada

First received 27 April 1994; revised manuscript received 19 August 1994

Abstract

An integrative algorithm has been developed, and compared with existing differential algorithms, for automatically determining the response ratios of peaks from a dual-channel flame photometric detector. The comparison was carried out using high and low, and constant and variable concentrations of an organosulfur test compound; under different degrees of solvent quenching and at two sets of detector flow conditions; and with and without digital filtering. The new integral algorithm performed as well as —and, particularly in the presence of strong noise, significantly better than— the existing differential ones. Typically, the response ratios of good peaks varied by 2 to 3% R.S.D. for different, and by ca. 0.5% R.S.D. for similar concentrations; the former, larger variation owing to previously unnoticed spectral changes. Different algorithms, working on single, large and well-smoothed peaks, varied among themselves by typically less than 1% R.S.D. The integral response ratios were displayed on the screen in graphic form and simultaneously printed in numeric form. At the discretion of the operator, they could also be printed in the form of a scalable "response-ratio chromatogram", with or without the constituent signal traces.

1. Introduction

Response ratios (RRs) from dual- or multiple-channel detectors or sensors can serve as indicators of chemical or physical properties. RRs are commonly determined on chromatographically separated analytes. They can support such varied analytical tasks as the assessment of peak purity [1], the subtraction of matrix components [2] or interfering peaks [1], the production of element-specific chromatograms [3,4] and the determination of physicochemical constants [5]. RRs can be automatically determined and plotted as "response-ratio chromatograms" (RRCs) [1].

For studies involving the dual- or multi-channel [6] flame photometric detector (FPD), we determined RRs as *slope* ratios (i.e. by comparing the first differentials) of the twin luminescence outputs. The use of slopes served the purpose well [1,3,4,6]. Even then it was suggested, however, that determining RRs as *area* ratios (i.e. by comparing the integrals) might prove advantageous [1]. Integration is a common procedure in chromatography [7]; and it seemed likely that area ratios should be less vulnerable to shifts in phase, increases in noise, incongruities in peak shape, and —particularly in the case of sequential detection— discrepancies in retention time.

* Corresponding author.

☆ Part of doctoral thesis of H.S.

0021-9673/94/$07.00
SSDI 0021-9673(94)00804-3

For these reasons we decided to pursue an integrative approach to RR determination, and compare its results to those of the earlier developed differential approaches [1]. As a test system we used the dual-channel FPD that supported the prior study, and set its two channels to monitor two strong bands of the most common FPD analyte, sulfur. These two bands of the blue S_2 emission ($v = 0 \rightarrow 9$ at 394 and $0 \rightarrow 10$ at 405 nm of the system $B^3\Sigma_u^- \rightarrow X^3\Sigma_g^-$ [8]) are known to produce fairly constant RRs, even when peaks exceed the quadratic range or are quenched by co-eluting hydrocarbons [9]. To test the algorithms to their limits, the analyte was injected in variable and low, variable and high, constant and high, and constant and very high amounts; and the chromatograms, obtained from two different detector conditions, were used both with and without heavy digital filtering.

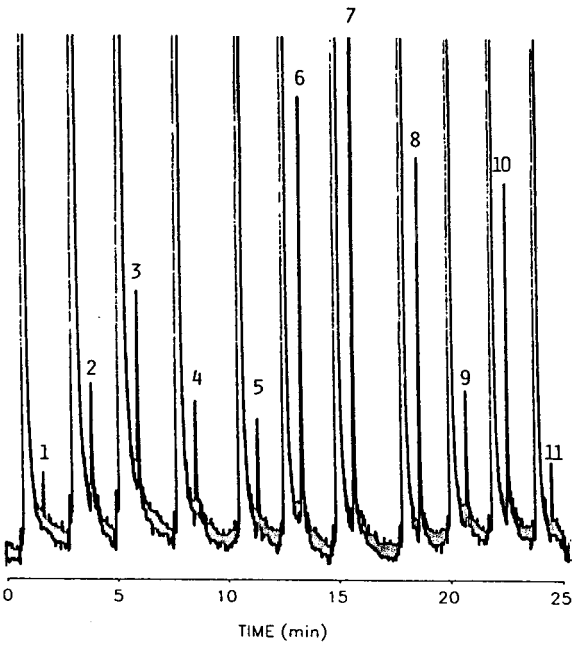

Fig. 1. Typical "unfiltered" chromatogram of "low and variable" analyte injections from ca. 0.5 to 2.0 ng of di(*tert.*-butyl) disulfide in acetone. The numbers marking the sulfur peaks are the same as those used in Tables 1 and 2. Channel 1 (405 nm); hydrogen 200 ml/min, air 50 ml/min.

2. Experimental

Several series of multiple di(*tert.*-butyl) disulfide injections into our ancient Shimadzu GC-4BMPF gas chromatograph with dual-channel FPD were stored in computer memory via a laboratory-developed interface and acquisition program [2]. The injections were done at variable and low (about 0.5 to 2 ng), at variable and high (about 5 to 20 ng) and, later, at constant high and very high (20 and 100 ng) levels of analyte. The variable injected amounts and volumes were selected such that the different sulfur peaks spanned the available screen range, and that the different volumes of solvent (acetone) produced tails of different prominence, i.e. of variable quenching ability. The low-analyte files deliberately included peaks that were close to the detection limit and hence encrusted by strong noise. Fig. 1 shows an example.

Both high-analyte and low-analyte files were examined "unfiltered" and "heavily filtered". The latter procedure used a finite-impulse-response (FIR) digital filter with Hamming window [10] and 32, 64 or 128 taps, whose cut-off frequency was adjusted to approach the maximum signal-to-noise ratio (an approach inevitably accompanied by a close to 50% reduction in peak height). Separate sets of individually "optimized" parameters (slope thresholds for start/stop commands, etc.) were used for differential and integral RR determinations.

The above variations were carried out at a set of general flow conditions that would typically be used for a larger number of FPD-active elements including sulfur. To guard against (only later noticed) concentration-dependent spectral changes, further data files were generated by using conditions whose gas flows were optimized for the S_2 luminescence, and by repeatedly injecting the *same* amounts of solvent and analyte.

Fig. 2 offers a simplified graphic comparison of the present integrative with the earlier differential approach: the latter averages the weighted absolute-slope ratios (the steeper the slope the heavier the weight) for the whole-peak mode; or

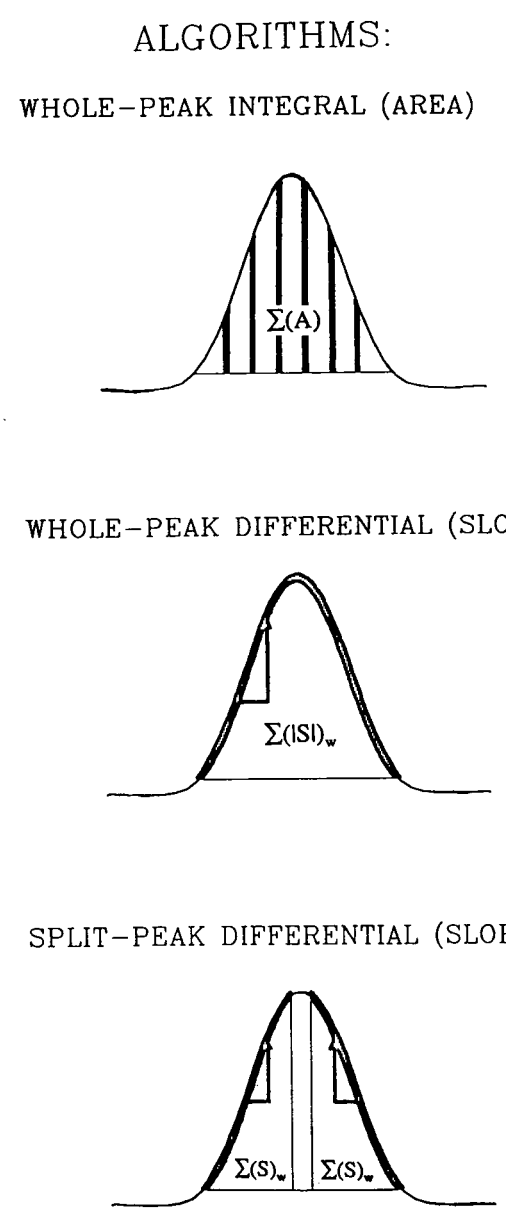

Fig. 2. Schematic representation of three different ways to evaluate chromatographic peaks (one peak only shown) for determining response ratios based on integral (area) or differential (slope) measurements. A = Amplitude; S = slope; w = weighted.

the weighted positive-slope ratios (up the peak, first "half") and negative-slope ratios (down the peak, second "half"), for the split-peak mode [1]. Note from Fig. 2 that the split-peak mode excludes a center slice containing the peak apex: slope ratios from the center, where both slopes go through zero, can under adverse conditions produce erroneously large or small numbers, particularly if the two peaks reach their maximum amplitude at a slightly different time. No such apex effect occurs in the integral mode; in fact, there the apex region represents the heaviest hence most important slice of the measurement.

Accordingly, the new integral RR algorithm[1] was written for the *whole*-peak mode only. Peak start and stop criteria were similar to those of the differential system [1]. Also as in the differential system, the objective was to cover not all but just the diagnostic parts of the peak. What mattered was not the most accurate determination of the peak areas themselves, but the most precise determination of their *ratio*. The often unreliable base of the peaks (the lowest 5–10% of peak height) was therefore routinely excluded by suitable cut-on/cut-off thresholds.

Briefly, the integrative algorithm searched for "valid" peaks (in a procedure similar to the one used by the differential algorithms), then integrated them and determined their ratio. To be accepted as "valid", a peak had to meet *all* of the following criteria:

(1) The peak had to be located within lower and upper "clipping" levels, as defined by the operator with the help of cursors superimposed on the chromatograms. The lower clipping level allowed the operator to exclude noise or solvent-caused baseline dips; the upper clipping level allowed him to exclude peaks that exceeded the range of the original data acquisition system (and were of concern only if one or both of the chromatograms had been previously reduced in amplitude). For the present study, clipping levels were *not* needed.

(2) For sole purpose of integration, the peak was assumed to "start" when its slope exceeded a "minimum slope" threshold, set by the operator in percent of full scale (= percent of

[1] Researchers interested in this program for non-commercial purposes are invited to contact B.M. for an executable copy.

screen height) per minute. The peak was assumed to "stop" when the slope —multiplied by −1 for the descent— dropped below the same slope threshold. (*Note:* The algorithm was designed to process roughly symmetric peaks. If strongly asymmetric ones should be encountered on a regular basis, the operator may prefer to define separate and different slope thresholds for ascent and descent.) The necessary threshold values could be easily estimated on the screen by imagining tangents drawn through the desired start and stop points of some conveniently located peak.

The slope was calculated from the amplitude difference between two data points, with the distance (i.e. the time) between the data points set by the operator. For instance, a setting of "1" meant carrying out the slope determination over two adjacent data points or 0.1 s, "5" meant 0.5 s, etc. This was done to reduce the effect of short-term noise (if present). Slope values were calculated for every data point. Obtaining meaningful slope values thus depended on choosing the appropriate width of the moving window in which the slope appeared. (*Note:* If the signal had already been smoothed before the slope threshold criterion was applied, this choice mattered but little.)

(3) In order to be accepted by the algorithm as a valid peak "start", a specified, uninterrupted number of slope values had to exceed the set "minimum slope" value. For instance, if the operator answered "10" to the prompt requesting the "number of consecutive data points", at least 10 slope values in a row (1 s worth of chromatographic time) *all* had to fall above the slope threshold. The setting thus defined how long a peak-commencing upward (or a peak-terminating downward) slope had to last in order to trigger peak start and stop commands. Again, which "number of consecutive data points" to set was easily estimated on the screen from the width of the most slender peak.

With all prompts answered, i.e. all thresholds defined, the program searched for "valid" slopes throughout the chromatogram. It declared PEAKSTART and PEAKEND times if, and only if, all of the above criteria had been met for a particular peak. The algorithm to achieve this was included in a collection of in-house chromatographic routines called "CHROM-8". It analyzed the first-channel signal to define PEAKSTART and PEAKEND, then imposed these times on the second channel. This worked well if the two channels, as in this study, were fairly similar.

(Note, however, that our prime interest is analytical: it transcends the current exploratory and mainly statistical topic. In envisioned analytical methodology, the two channels could for instance originate from FPD wavelength regions spaced far apart, or they could even originate from different detectors. In addition, the sample could contain several elements or functional groups with different response characteristics. If, consequently, the two channels were to yield peaks grossly different in amplitude and perhaps even symmetry, it would be reasonable to include *both* channels in the peak diagnostics. To achieve this with minimal effort, an alternative collection of algorithms was assembled and, for practical purposes, called "CHROM-9". At its heart was a routine that took the average of the two channels, performed the diagnostics on the *averaged* peaks, and then imposed the derived PEAKSTART and PEAKEND times back onto the two constituent (original) channels —there to serve the subsequent computation of area-based response ratios. In addition, a subroutine dubbed "TD" ("time-delay") allowed one chromatogram to be temporally shifted until it best matched its twin in elution behavior. The latter feature was developed with sequential (as opposed to synchronous) detector channels in mind. For the current simultaneous signals from adjacent S_2 bands, however, the integrative CHROM-9 algorithm was unnecessary, the TD option inappropriate. Also, whenever double-checked on the data files of this study, CHROM-9 produced the same results as CHROM-8.)

The signal (amplitude, chromatographic response) at PEAKSTART time was defined as the average inside a 0.3-s window (a third of the sum of three successive data points, with the PEAKSTART datum in the middle). A similar smoothing procedure was used for the signal at

PEAKEND time. A horizontal baseline (really: a truncation line) was then defined by calculating the arithmetic mean of the smoothed PEAKSTART and PEAKEND signals. The "peak area" (for purpose of calculating area ratios) was obtained by summing all 0.1-s data point amplitudes *above that line*, from PEAKSTART to PEAKEND.

The algorithm then calculated the area ratio of corresponding peaks in the two channels. (Any magnification factors previously applied to one or both chromatograms were automatically factored into this response-ratio calculation.) The numerical RRs, together with the PEAKSTART and PEAKEND times (down to a tenth of a second), were arranged in a table —similar to the one shown in Ref. [1]— and forwarded to a matrix printer.

Meanwhile, the RRs appeared on the screen in the form of a (logarithmic) RRC [1], superimposed on the two constituent chromatograms. With the help of an auxiliary program, all three could be individually magnified or reduced in amplitude. The screen images could also be vertically offset and, if so desired, forwarded singly or in combination to a printer. Fig. 3 shows the example of a coarse "screen dump", as routinely obtained from an inexpensive matrix printer and typically destined for a laboratory notebook.

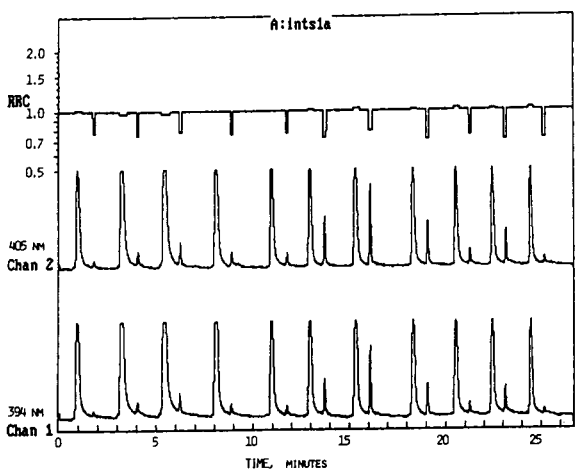

Fig. 3. Response-ratio chromatogram with its constituent (405 and 394 nm) chromatograms. Scaled for easier viewing; numbers and axis captions manually inserted. Screen-dumped on 8-point matrix printer (hence the stepped appearance). The caption shown on top, "A:intsla", is the automatically printed file title.

3. Results and discussion

There is little doubt that dual-channel RR algorithms perform well on strong peaks towering above straight and smooth baselines; just as conventional integrator algorithms [7] do. The obvious question, however, is how well they cope with the more difficult types of terrain in which smaller peaks —overlapping one another, perhaps— rise from an undulating baseline overgrown with noise. In such cases, conventional integrators have been shown to produce errors (in estimating single-peak areas) of up to 40% [11].

The test protocol offered therefore chromatograms of considerable challenge: by including non-filtered data {i.e. data filtered only by the resistor–capacitor (RC) time constant of the electrometer (cf. Ref. [12]) }; by approaching the detection limit; by letting peaks ride on strong or weak solvent tails (and thus be strongly or weakly quenched); and by injecting variable amounts of both analyte and solvent.

Table 1 shows an example of such a worst-case scenario: it lists the RRs for the sulfur peaks numbered in the Fig. 1 chromatogram. Table 1 lists in addition the means, together with the relative standard deviation (± R.S.D.) values, both for a *single peak* determined by all four algorithms (row), and for all peaks determined by a *single algorithm* (column). As expected for a worst-case scenario, the "precision" of the measurements is unacceptably large —with the important exception, however, of the 7.2% R.S.D. value for the *integral* (area-ratio) mode. In contrast, the differential (slope-ratio) mode produces not only very large relative deviations; it also produces highly inaccurate means.

This is as expected, since summed *differential* ratios should be much more susceptible to severe variations in slope, i.e. to noise obscuring the algorithmically important parts of the peak. The

Table 1
Response ratios from a non-filtered, low and variable level chromatogram

Peak	Area ratios	Slope ratios			Average (% R.S.D.)
		Whole peak	Split peak		
			First half[a]	Second half[a]	
1	0.851	2.305	1.319	2.984	1.865 (51.5)
2	0.716	1.639	1.141	2.096	1.398 (42.8)
3	0.786	1.689	1.129	2.910	1.629 (57.2)
4	0.731	1.416	1.350	1.425	1.231 (27.2)
5	0.762	1.448	1.095	1.413	1.180 (27.2)
6	0.734	1.344	1.260	1.833	1.293 (34.8)
7[b]	0.779	0.809	0.736	1.500	0.956 (38,1)
8	0.639	0.798	0.880	0.965	0.821 (16.9)
9	0.729	1.613	1.622	1.103	1.267 (34.2)
10	0.721	1.171	1.376	0.901	1.042 (27.8)
11	0.786	1.984	1.763	1.159	1.423 (38.6)
Average (% R.S.D.)	0.749 (7.21)	1.474 (30.8)	1.243 (23.9)	1.663 (43.8)	

Conditions: hydrogen 200 ml/min, air 50 ml/min. RC time constant of electrometer 0.22 s. Injections vary from 0.5 to 2.0 ng di(*tert.*-butyl) disulfide in acetone.
[a] The "half" is actually less than 50% since the center slice that contains the peak apex is excised by the split-peak algorithm (see Fig. 2).
[b] Off-scale peak.

Table 2
Response ratios from a filtered, low and variable level chromatogram

Peak	Area ratios	Slope ratios			Average (% R.S.D.)
		Whole peak	Split peak		
			First half	Second half	
1[a]	0.808	0.904	0.885	0.873	0.868 (4.8)
2	0.756	0.760	0.770	0.739	0.756 (1.7)
3	0.787	0.784	0.771	0.796	0.785 (1.3)
4	0.767	0.786	0.761	0.796	0.778 (2.1)
5	0.789	0.788	0.770	0.803	0.788 (1.7)
6	0.730	0.723	0.714	0.703	0.724 (1.0)
7[b]	0.799	0.837	0.831	0.833	0.825 (2.1)
8	0.712	0.715	0.708	0.720	0.714 (0.71)
9	0.748	0.776	0.770	0.760	0.764 (1.6)
10	0.716	0.722	0.722	0.721	0.720 (0.40)
11[a]	0.764	0.810	0.786	0.795	0.789 (2.4)
Average (% R.S.D.)	0.761 (4.3)	0.782 (7.1)	0.772 (6.7)	0.766 (6.8)	

Conditions as in Table 1, except FIR cut-off frequency of 0.2 Hz.
[a] Values obtained in zoom mode to avoid screen resolution problems.
[b] Off-scale peak in non-filtered chromatogram.

numbers in Table 1, measured under deliberately marginal conditions, clearly indicate that integral measurements (of truncated peaks) provide preciser —and as we shall see later, also more accurate— data than differential measurements.

Again as expected, the situation is much improved by heavily filtering the chromatograms before measuring the RRs. Table 2 shows the results. All R.S.D. values are now acceptable. (On a poor data file such as this, we consider an R.S.D. of less than ± 10% to represent a reasonable criterion of acceptability). The means are very close to one another, and are essentially identical to the "integral" mean of Table 1. It is interesting to note that the four algorithms now differ less among each other when evaluating the *same peak* (most values are in the 1–2% R.S.D. range, with the median at 1.7%), than peaks differ among each other when evaluated by the *same algorithm* (these values all fall into the 4–7% R.S.D. range).

The precision improves, as expected, when larger amounts of analyte are used. Fig. 4 shows the "non-filtered" first-channel chromatogram of this series. It should be mentioned that the better RRs are not due to a diminution of quenching: the sulfur peaks are still quenched by the same percentage as in Fig. 1. This is not immediately obvious from the picture —the solvent appears to tail very little at the higher attenuation— but percent quenching depends only on the concentration of the quencher, not on the concentration of the analyte [13]. The quencher, i.e. the solvent and/or its fragmentation products, has not reached the limit of its quenching power —it has reached the limit of its own luminescence. The fact that the linear range of (probably CH and CC) luminescence has indeed been exceeded, can be appreciated from the very similar peak heights resulting from very different volumes of solvent.

Table 3 contains the RRs for the chromatographic data file shown in Fig. 4, i.e. for the typical example of a "non-filtered", high-analyte level run. The individual integral and differential algorithms now produce essentially the same R.S.D. (close to 3%) for *all* peaks combined. When the action of the four algorithms is compared for the *same* peak, the R.S.D. values are generally lower (mostly between 0.5 and 3%, median 1.1% R.S.D.).

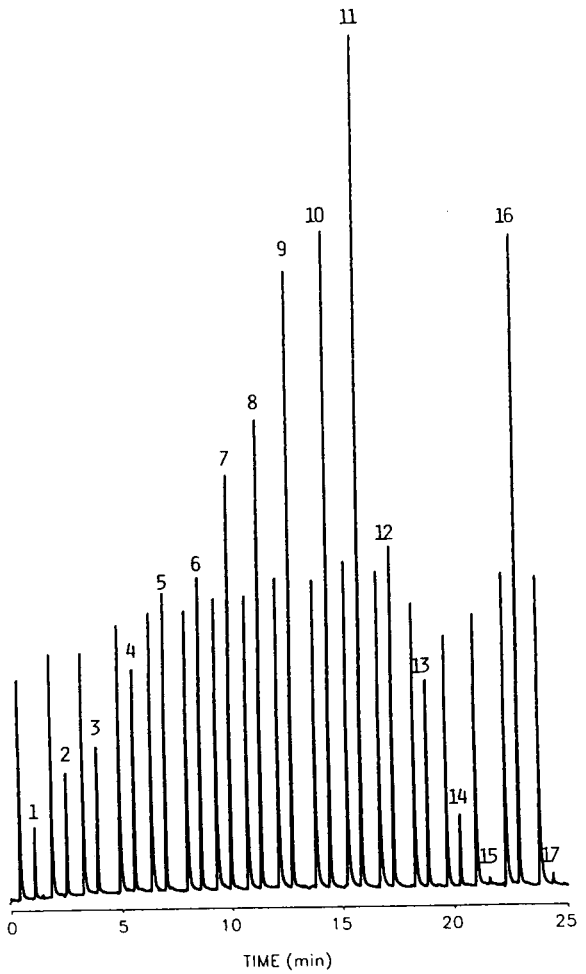

Fig. 4. Typical "unfiltered" chromatogram of "high and variable" analyte injections from ca. 5 to 20 ng of di(*tert.*-butyl) disulfide in acetone. The numbers marking the sulfur peaks are the same as those in Table 3. Channel 1 (405 nm); hydrogen 200 ml/min, air 50 ml/min.

The same chromatogram as given in Fig. 4, but now heavily filtered, produces data hardly different from those of Table 3, at least as far as the mean response ratios are concerned. Also, the R.S.D. values for each of the four algorithms, working separately on *all* peaks, are again similar (close to 2.7%). However, the

Table 3
Response ratios from a non-filtered, high and variable level chromatogram

Peak	Area ratios	Slope ratios			Average (% R.S.D.)
		Whole peak	Split peak		
			First half	Second half	
1	0.795	0.801	0.801	0.828	0.806 (1.8)
2	0.795	0.819	0.809	0.806	0.807 (1.2)
3	0.801	0.797	0.809	0.797	0.801 (0.71)
4	0.803	0.805	0.811	0.816	0.809 (0.73)
5	0.811	0.806	0.808	0.825	0.813 (1.1)
6	0.816	0.819	0.826	0.823	0.821 (0.54)
7	0.822	0.825	0.827	0.836	0.828 (0.73)
8	0.821	0.821	0.821	0.837	0.825 (0.97)
9	0.835	0.833	0.830	0.851	0.837 (1.1)
10	0.834	0.856	0.874	0.851	0.854 (1.9)
11[a]	0.888	0.855	0.833	0.894	0.868 (3.3)
12	0.839	0.834	0.833	0.852	0.840 (1.0)
13	0.834	0.832	0.838	0.841	0.836 (0.48)
14	0.828	0.851	0.836	0.840	0.839 (1.1)
15[b]	0.779	0.880	0.890	0.844	0.848 (5.9)
16	0.843	0.846	0.847	0.862	0.850 (1.0)
17[b]	0.843	0.872	0.870	0.872	0.864 (1.6)
Average (% R.S.D.)	0.823 (3.1)	0.832 (3.0)	0.833 (3.0)	0.840 (2.8)	

Conditions as in Table 1 except injections from 5 to 20 ng di(*tert.*-butyl) disulfide in acetone.
[a] Off-scale peak.
[b] Values obtained in zoom mode to avoid screen resolution problems.

R.S.D. values for the four algorithms working on the *same* peak now fall mostly into the 0.1 to 0.3% range (median 0.23%): a significant improvement when compared to the "non-filtered" data. (The full data set is not shown here to save space.)

It thus appears that all tested integral and differential algorithms concur within relatively narrow margins of error (certainly below 1% R.S.D.) when measuring the same, good-quality peak. As supported by this concurrence —and the low probability of all four algorithms having the same bias— we consider all four algorithms to be essentially accurate. The variability of the RRs themselves thus seems to be due not to algorithmic but to chromatographic, i.e. spectral differences. This should come as no surprise in light of the differently sized and differently quenched peaks. Although the S_2 bands predominate, smaller contributions of other excited sulfur species [9,14] may still be present —not to mention carbon-based emissions and/or background luminescences. Chromatographic response ratios, in addition to their many other roles in analysis, can thus serve as exquisitely sensitive probes of spectrochemical change.

Although we originally did not plan to do so, the relatively strong RR variation of differently sized and quenched peaks demanded that we either confirm or deny the algorithms' potential involvement in the comparatively large ± 3% R.S.D. spread. To obtain data files that excluded, as far as convenient, any spectral variation, the detector conditions were optimized for the S_2 emission (earlier conditions had been those that afforded good overall response to a rather wide variety of elements, including sulfur). Also, the same analyte amount and the

same injection volume were used throughout each experimental run.

Table 4 shows the results from one set of heavily filtered chromatograms, as obtained from very high, constant levels of analyte (just bordering the upper end of the linear range, in fact). The obvious difference to the earlier, variable-analyte runs is the much lower R.S.D. value for the *same* algorithm working on *all* 16 peaks: it is of similar magnitude as the R.S.D. value for all four algorithms working on the same peak. Somewhat lower (but still constant) analyte levels gave the same result, i.e. the R.S.D. values for heavily filtered chromatograms were close to 0.5% for the integral and the two split-peak differential modes.

The values for the *whole*-peak differential mode were, however, clearly worse (in the 1–1.5% range). Speculatively we believe this to be a consequence of working close to the upper linear-range limit. The likely relevant effect to consider here is the behavior of the peak apex. It is the peak apex that approaches or breaches the linear range; and it is the peak apex where, as argued earlier on grounds of principle, *slope* ratio measurements are likely to show the greatest error. Accordingly, the apex-free *split*-peak values of the differential approach agree well with the (*whole*-peak) values of the algorithmically quite different integral approach; but they disagree with the values of the otherwise similar *whole*-peak differential approach —both in mean and in % R.S.D. (0.734, 0.736 and 0.737 vs. 0.746; and 0.42, 0.41 and 0.38 vs. 1.2; respectively). Since the apex-burdened whole-peak differential mode is here the odd algorithm out, its forced inclusion in the group of four brings about an R.S.D. value higher than expected.

In other words: if the spectral conditions are fairly constant, three algorithms will produce essentially the same response ratio —with both

Table 4
Response ratios from a filtered, very high and constant level chromatogram

Peak	Area ratios	Slope ratios			Average (% R.S.D.)
		Whole peak	Split peak		
			First half	Second half	
1	0.739	0.745	0.736	0.737	0.739 (0.546)
2	0.733	0.739	0.733	0.734	0.735 (0.391)
3	0.733	0.753	0.733	0.734	0.738 (1.334)
4	0.733	0.746	0.734	0.736	0.737 (0.809)
5	0.731	0.739	0.731	0.732	0.733 (0.527)
6	0.731	0.745	0.732	0.736	0.736 (0.866)
7	0.733	0.744	0.734	0.737	0.737 (0.674)
8	0.741	0.748	0.743	0.742	0.744 (0.418)
9	0.738	0.749	0.739	0.742	0.742 (0.669)
10	0.737	0.743	0.738	0.739	0.739 (0.356)
11	0.737	0.777	0.738	0.740	0.748 (2.590)
12	0.735	0.743	0.736	0.737	0.738 (0.487)
13	0.733	0.740	0.736	0.738	0.737 (0.405)
14	0.731	0.742	0.734	0.737	0.736 (0.637)
15	0.735	0.746	0.736	0.739	0.739 (0.672)
16	0.732	0.741	0.736	0.735	0.736 (0.508)
Average (% R.S.D.)	0.734 (0.419)	0.746 (1.209)	0.736 (0.406)	0.737 (0.377)	

Conditions: hydrogen 50 ml/min, air 40 ml/min. FIR cut-off frequency 0.2 Hz. Injections of 100 ng di(*tert.*-butyl) disulfide in acetone.

types of R.S.D. values hovering around 0.5%. In contrast, the fourth (the whole-peak differential mode) is a bit off and its R.S.D. a bit worse (in the 1–1.5% range, typically). To keep matters in perspective, however, even this poorer precision should still amply satisfy most analytical requirements.

4. Conclusions

To summarize —and at the same time to include summaries of some directly comparable data sets not reproduced in full here for reasons of space— Table 5 lists the R.S.D. roster for three typical chromatographic files being exposed to all four algorithmic treatments. (Other files run for this study follow the same trends.) A variety of conclusions and expectations can be drawn from these files:

(1) The algorithms do perform satisfactorily over the whole concentration range —even peaks close to the detection limit (see Fig. 1) can be successfully evaluated.

(2) In the particular case of S_2 —and likely of some other FPD emitters as well (cf. Ref. [9])— care has to be taken that the spectral characteristics of the emitter do indeed remain constant throughout the concentration/quenching ranges of analysis. Under reasonable circumstances, the algorithms are sensitive enough to pick up changes in spectrum smaller than 1% —a change that would, for example, not be normally recognized in conventional single-channel spectrophotometry. (Hence, such algorithms might find use in spectrochemically motivated work.)

(3) In this study, heavy filtering invariably improved the precision of RR data. Although the dependence of R.S.D. values on the time constant of the filter has not been investigated in any detail, it is obvious that dual-channel chromatograms should be routinely filtered before the response ratios of their peaks are determined.

(4) In general, the *split*-peak values —although having less than half of the peak to operate on— are as precise, or preciser than, the whole-peak values in the *differential* mode. We speculatively attribute this to the —slope-ratio-wise— less precise apex section being excised by the split-peak algorithm.

(5) On noisy chromatograms, the *integral*

Table 5
Summary of relative standard deviations (%) of dual-channel FPD response ratios as determined by different algorithms on chromatograms varying in detector conditions, analyte levels and time-constant settings

No. of peaks	Analyte injection level[a]	Chromatogram filtered?[b]	Area ratios	Slope ratios			Median of Single peak R.S.D.s[c]
				Whole peak	Split peak		
					First half	Second half	
11	Low, variable	No	7.2	31	24	44	35
		Yes	4.3	7.1	6.7	6.8	1.7
17	High, variable	No	3.1	3.0	3.0	2.8	1.1
		Yes	2.6	2.7	2.6	2.7	0.23
16	Very high, constant	No	0.42	3.0	1.3	1.1	2.4
		Yes	0.42	1.2	0.41	0.38	0.59

[a] Typical levels of di(*tert.*-butyl) disulfide in acetone: low and variable: 0.5 to 2.0 ng; high and variable: 5 to 20 ng, both at hydrogen 200 and air 50 ml/min; very high and constant: 100 ng, hydrogen 50, air 40 ml/min.
[b] "No" represents an RC time constant of 0.22 s; "Yes" represents an FIR filter with filter taps and cut-off frequency set to give peak height reduction in the 50 to 60% range (close to maximum S/N).
[c] Median of same-peak R.S.D. values as determined by the four algorithms (see utmost right columns in Tables 1–4).

(area ratio) approach performed better than the *differential* (slope ratio) approach.

(6) The *integral* algorithm is at present available in *whole*-peak mode only. However, the addition of a split-peak integral mode —if desired for checks of peak purity, peak overlap, etc.— should require only the minor software adjustment of bisecting the peak at the apex. Similarly, operator-selected (i.e. cursor-defined) peak slices could be evaluated by the integrative (as opposed to the already existing differential) approach as well.

(7) General principles suggest that —in comparison with RRs determined by the differential (slope) method— RRs determined by the integral (area) method should be less susceptible to those detrimental effects of shifts in retention time and/or concentration profile that arise from monitoring two *sequential* detectors. They should also be less susceptible to the insidious effects of electronic phase shifts that can occur even when two channels of the *same* detector are monitored.

Acknowledgement

Financial support for this study was provided by NSERC operating grant A-9604.

References

[1] B. Millier, X.-Y. Sun and W.A. Aue, *Anal. Chem.*, 65 (1993) 104.
[2] W.A. Aue, B. Millier and X.-Y. Sun, *Can. J. Chem.*, 70 (1992) 1143.
[3] W.A. Aue, B. Millier and X.-Y. Sun, *Anal. Chem.*, 63 (1991) 2951.
[4] W.A. Aue, X.-Y. Sun and B. Millier, *J. Chromatogr.*, 606 (1992) 73.
[5] I. Berglund and P.K. Dasgupta, *Anal. Chem.*, 63 (1991) 2175 and 64 (1992) 3007.
[6] B. Millier, X.-Y. Sun and W.A. Aue, *J. Chromatogr. A*, 675 (1994) 155.
[7] N. Dyson, *Chromatographic Integration Methods*, Royal Society of Chemistry, Cambridge, UK, 1990.
[8] R.W.B. Pearse and A.G. Gaydon, *The Identification of Molecular Spectra*, Chapman & Hall, London, 4th ed., 1976.
[9] X.-Y. Sun and W.A. Aue, *J. Chromatogr. A*, 667 (1994) 191.
[10] C. Chatfield, *The Analysis of Time Series*, Chapman & Hall, London, 4th ed., 1989, p. 116.
[11] A.N. Papas and M.F. Delaney, *Anal. Chem.*, 59 (1987) 54A.
[12] X.-Y. Sun, H. Singh, B. Millier, C.H. Warren and W.A. Aue, *J. Chromatogr. A*, 687 (1994) 259.
[13] W.A. Aue and X.-Y. Sun, *J. Chromatogr.*, 641 (1993) 291.
[14] W.A. Aue and X.-Y. Sun, *J. Chromatogr.*, 633 (1993) 151.

ELSEVIER

Journal of Chromatography A, 687 (1994) 303–313

JOURNAL OF CHROMATOGRAPHY A

Confirmational analysis of polycyclic aromatic hydrocarbons in soil extracts by cryotrapping gas chromatography–Fourier transform infrared spectrometry

T. Visser*, M.J. Vredenbregt, A.P.J.M. de Jong

Laboratory for Organic Analytical Chemistry, National Institute for Public Health and Environmental Protection, P.O. Box 1, 3720 BA Bilthoven, Netherlands

First received 27 June 1994; revised manuscript received 30 August 1994

Abstract

The utility of cryotrapping gas chromatography–Fourier transform infrared spectrometry for isomer differentiation and identification of polycyclic aromatic hydrocarbons (PAHs) in soil samples was investigated. Extracts of sediment, soil and river clay were examined and compared with the results from previous analysis by high-performance liquid chromatography with fluorescence detection. The presence of most of the detected PAHs could be confirmed at a level of 1–4 ng per component injected. In addition, previously undetermined PAHs were identified and valuable structural information was obtained on the identity of two co-eluting isomers. Most of the cryotrapping spectra of PAHs appeared to be similar to spectra recorded with the KBr pelleting technique. Small intensity differences were observed but absorption frequencies were found within the data point resolution of the recorded spectra.

1. Introduction

Polycyclic aromatic hydrocarbons (PAHs) are important environmental pollutants because of the suspected biological activity of most of these compounds and their widespread occurrence. Over the years, a variety of techniques have been developed to determine PAHs both qualitatively and quantitatively. At present, gas chromatography (GC) with flame ionization detection is usually the method of choice. Next, GC combined with mass spectrometry and high-performance liquid chromatography (HPLC) with UV or fluorescence detection are applied when more specific detection of PAH congeners is required. Discrimination of structural isomers however, remains difficult. Unambiguous identification is important as the mutagenity and carcinogenity among the isomers may differ considerably [1]. Additional, complementary information is therefore frequently required.

Infrared spectrometry is known to be very suitable for the discrimination and identification of molecules and for that reason GC combined with Fourier transform infrared spectrometry (GC–FT-IR) can be a helpful tool for the assignment of PAH isomers [2–8] and related compounds such as nitrated PAHs [9], chlorinated biphenyls [10,11] and dibenzodioxins and furans [12–15]. GC–FT-IR analysis of PAHs in real

* Corresponding author.

0021-9673/94/$07.00
SSDI 0021-9673(94)00851-5

samples is only rarely reported, mainly because of the limited sensitivity of systems equipped with light-pipe interfacing [2,3,5,7]. Improved detection limits in the (sub)nanogram range are achieved with matrix isolation [4] and cryotrapping or direct-deposition GC–FT-IR [8,16]. These techniques utilize low-temperature storage of the GC eluate to extend the time available for FT–IR analysis, yielding considerably higher sensitivity than is possible with conventional light-pipe interfaces.

The object of this study was to explore the usefulness of cryotrapping GC–FT-IR for the identification of PAHs in complex environmental samples and in particular to confirm the qualitative results from a standard HPLC–fluorescence method, currently used in our laboratory, to determine sixteen so-called "EPA" PAHs. For this purpose, extracts of sediment, soil and river clay were examined in parallel by both techniques.

2. Experimental

2.1. Samples

The sediment, soil and river clay samples were prepared by extraction of 20 g of material with 2×75 mL of light petroleum–acetone (3:1). Clean-up of the extract was performed with a column filled with deactivated aluminium oxide. Sodium sulphate was used as drying agent. The purified extracts were gently dried at room temperature with a flow of nitrogen. The residues were subsequently dissolved in 1 ml of acetonitrile for HPLC analysis. The river clay extract was additionally concentrated to 300 μl for GC–FT-IR measurement.

2.2. HPLC

Reversed-phase HPLC was carried out according to a procedure routinely used in the laboratory. The standard mixture used in this procedure was Standard Reference Material (SRM) 1647b from the National Institute of Standards and Technology (NIST), obtained from C.N. Schmidt (Amsterdam, Netherlands), consisting of sixteen PAHs in acetonitrile solution. The certified concentrations are in the range 3–20 ng/μL.

Separation was performed on an LC 250 pump (Perkin–Elmer) equipped with an automatic WISP injector (Waters). The column, 100×3 mm I.D. (Chrompack), was packed with 5-μm Chromspher PAH. The column temperature was maintained at 30°C. Gradient elution was executed with acetonitrile–water (40:60)(A) and acetonitrile (B). The gradient programme was 0–2 min, 90% A–10% B; 2–27 min, linear change to 0% A–100% B; 27–32 min, 0% A–100% B; 32–34 min, linear change to 90% A–10% B and 34–39 min, 90% A–10% B. The flow-rate was 1 ml/min and the volume injected was 10 μl.

2.3. Fluorescence detection

A Waters FLU$_3$470 spectrometer was used for fluorescence detection. The excitation/emission wavelengths were as follows: 0–11.5 min, 253/333 nm; 11.5–14.2 min, 253/373 nm; 14.2–17.5 min, 263/420 nm; 17.5–22.5 min, 270/382 nm; and 22.5–39 min, 280/460 nm. The internal standard was 6 methylchrysene. Peak heights were used for quantification.

2.4. Gas chromatography

GC separations were performed on a Carlo Erba MEGA 5160 gas chromatograph using a split–splitless injector. The gas chromatograph was equipped with a DB-17 capillary column (J&W Scientific) (15 m $\times$ 0.25 mm I.D., film thickness 0.15 μm). This column was chosen because it gave a good separation between the isomers of fluoranthene and between benzo[*a*]pyrene and benzo[*e*] pyrene. In addition, thin-film stationary phases are preferred for cryotrapping GC–FT-IR because of the lower column bleeding compared with thick-film columns. According to Smyrl et al. [8], column bleeding may cause severe deterioration of the GC–FT-IR performance.

The injector temperature was 250°C and the

injection volume was 1 μl. The carrier gas was helium with a calculated flow-rate of 0.8 ml/min. After optimization the following temperature programme was chosen for the analysis of the extracts: 60°C, for 3 min, followed by an increase of 20°C/min to 140°C and then 5°C/min to 290°C, which was held isothermal for 10 min.

SRM 2260 (obtained from C.N. Schmidt) NIST, consisting of 24 PAHs in toluene solution, was used for chromatographic optimization and to establish retention times and detection limits. The nominal concentration of the PAHs in the standard solution was 60 ng/μl. Aliquots of 200 μl were diluted to concentrations of 30, 2, 1, 0.5 and 0.25 ng/μl. Standard solutions of 60 and 30 ng/μl were injected with splitting ratios of 1 : 10 and 1 : 30. Standards with concentrations of 2, 1, 0.5 and 0.25 ng/μl and all extracts were analysed with splitless injection.

2.5. FT-IR spectrometry

Infrared spectrometric detection was carried out with a Digilab (Biorad) (FTS-40 Fourier transform instrument equipped with a Digilab Tracer cryotrapping GC interface and an SPC 3200 computer for data acquisition and processing. A detailed description of the interface is given in Ref. [8]. Connection between the GC column and the FT-IR interface was accomplished with a 1-m deactivated fused-silica transfer line of 150 μm I.D. by means of a silver ferrule connector (Bio-rad). A fused-silica deposition tip of 150 μm I.D. was fixed at the end of the transfer line, acting as a restricting element to reduce the operating flow-rate to ca. 1 ml/min. The transfer line and deposition tip were heated to 290°C. The tip was located 30 μm above the surface of a moving ZnSe window, which was cooled with liquid nitrogen to 77 K. Stepwise shifting of the window was accomplished with an X–Y stepper motor. The standard software programme TRTP was used to reduce the number of steps per second at proceeding retention time in order to compensate for GC peak broadening. The high-vacuum interface housing was held at 10^{-5} Torr to prevent condensation of atmospheric substances.

Spectra of the trapped GC eluate were recorded "on-the-fly", i.e., a few seconds after deposition, by averaging four scans every 2 s with an optical resolution of 8 cm^{-1}. Incidentally, post-run scanning of trapped components was performed after completion of the GC run by repositioning the corresponding window coordinates (i.e. retention times) into the IR beam. Post-run spectra were recorded with 512 scans co-added and an optical resolution of 2 or 8 cm^{-1}.

GC–FT-IR traces of integrated IR absorption as a function of time were constructed by standard Gram–Schmidt vector orthogonalization. A so-called functional group (Fg) chromatogram of the preselected wavenumber region 700–950 cm^{-1} was used for monitoring the elution of PAHs as the strongest absorptions of these compounds are found in this region. In addition, interference of eluting non-aromatics is relatively small in this wavenumber interval.

3. Results and discussion

The functional group GC–FT-IR trace at 700–950 cm^{-1} of a standard solution of SRM 2260 is shown in Fig. 1. The identity of all 24 PAH components was established from the elution sequence combined with the similarity between the obtained cryotrapping spectra and the KBr reference spectra from the literature [17,18] or

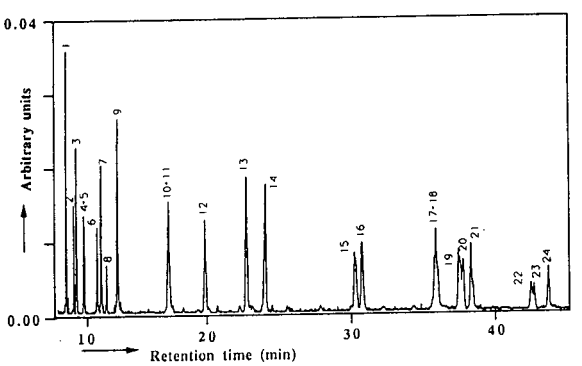

Fig. 1. Functional group GC–FT-IR (700–950 cm^{-1}) of the standard solution of SRM 2260. Concentration 60 ng/μl per component; splitting ratio 1 : 10.

from an in-house recorded collection. The corresponding retention times (t_R) and concentrations are summarized in Table 1. The reproducibility of t_R was established from three subsequent injections to be within 0.03 min.

Under the chromatographic conditions used, not all compounds were uniquely separated. However, interference-free spectra of all components were obtained either straightforwardly from individual chromatographic peaks or from spectra on the wings of a GC peak in case of co-elution.

All 24 cryotrapping FT-IR spectra were found to differ, evidently endorsing the discriminative properties of FT-IR. Typical examples are the spectra of the isomers benzo[*a*]pyrene and benzo[*e*]pyrene as shown in Fig. 2. In addition to the relatively strong absorption bands of the =C–H out-of-plane bending vibrations in the region 700–950 cm^{-1}, the bands in the in-plane =C–H and skeletal region 1600–1000 cm^{-1} appeared to be useful for distinguishing between the different compounds and isomers.

Differences between the cryotrapping IR spectra of the 24 PAHs and the spectra recorded with the conventional KBr pelleting technique appeared to be small. The intensities of the absorption bands may differ slightly, but the band maxima are within the data point resolution (4 cm^{-1}) of the on-the-fly spectra. This is in agreement with earlier findings [8,16] and it endorses that reference collections of conventionally recorded spectra can be helpful for identification purposes. Band narrowing as an effect of the low temperature (77 K) as reported by Smyrl et al. [8] occurred only to a negligible extent in the

Table 1
Identity, retention times (t_R) and concentrations of PAHs in SRM 2260

Peak No.[a]	Component	t_R (min)	Concentration (ng/μl)
1	Naphthalene	7.51	66.0
2	2-Methylnaphthalene	8.51	65.5
3	1-Methylnaphthalene	8.91	65.5
4	Biphenyl	9.67	65.8
5	2,6-Dimethylnaphthalene	9.77	65.6
6	Acenaphthylene	11.20	63.2
7	Acenaphthene	11.57	68.2
8	2,3,5-Trimethylnaphthalene	12.12	58.4
9	Fluorene	13.12	65.4
10	Phenanthrene	17.29	65.7
11	Anthracene	17.31	49.7
12	1-Methylphenanthrene	20.01	65.0
13	Fluoranthene	22.88	66.0
14	Pyrene	24.15	66.0
15	Benz[*a*]anthracene	30.04	57.1
16	Chrysene	30.43	66.2
17	Benzo[*b*]fluoranthene	35.18	65.7
18	Benzo[*k*]fluoranthene	35.35	65.4
19	Benzo[*e*]pyrene	36.85	65.7
20	Benzo[*a*]pyrene	37.10	59.3
21	Perylene	37.71	49.7
22	Indeno[1,2,3-cd]pyrene	42.67	58.3
23	Dibenz[*a,h*]anthracene	42.98	49.3
24	Benzo[*ghi*]perylene	44.91	58.7

[a] Peak numbers refer to Fig. 1.

Table 2
Comparison of HPLC–fluorescence and GC–FT-IR analysis of PAHs in a sediment sample

Peak No.[a]	Component	HPLC detected[b]	GC–FT-IR identified[b]
9	Fluorene	+	−
10	Phenanthrene	+	+
11	Anthracene	+	+
13	Fluoranthene	+	+
14	Pyrene	+	+
15	Benz[*a*]anthracene	+	+
16	Chrysene	+	+
17	Benzo[*b*]fluoranthene	+	+
18	Benzo[*k*]fluoranthene	+	−
19	Benzo[*e*]pyrene	−	+
20	Benzo[*a*]pyrene	+	+
21	Perylene	−	+
22	Indeno[1, 2,3-*cd*]pyrene	+	+
23	Dibenz[*a*,*h*]anthracene	+	−
24	Benzo[*ghi*]perylene	+	+

[a] Peak numbers refer to Fig. 3.
[b] + Positively detected or confirmed; − not detected or confirmed.

Table 3
Comparison of HPLC–fluorescence and GC–FT-IR analysis of PAHs in a soil sample

Peak No.[a]	Component	HPLC detected[b]	GC–FT-IR identified[b]
9	Fluorene	+	−
10	Phenanthrene	+	+
11	Anthracene	+	−
12	1-Methylphenanthene	−	+
13	Fluoranthene	+	+
14	Pyrene	+	+
15	Benz[*a*]anthracene	+	−
16	Chrysene	+	−
17	Benzo[*b*]fluoranthene	+	+
◆	Benzo[*j*]fluoranthene	−	+
18	Benzo[*k*]fluoranthene	+	−
19	Benzo[*e*]pyrene	−	+
20	Benzo[*a*]pyrene	+	−
22	Indeno[1,2,3-*cd*]pyrene	+	+
23	Dibenz[*a*,*h*]anthracene	+	−
24	Benzo[*ghi*]perylene	+	−

[a] Peak numbers refer to Fig. 4.
[b] + Positively detected or confirmed; − not detected or confirmed.

Table 4
Comparison of HPLC–fluorescence and GC–FT-IR analysis of PAHs in a river clay sample

Peak No.[a]	Component	HPLC detected[b]	GC–FT-IR identified[b]
10	Phenanthrene	+	+
11	Anthracene	+	–
13	Fluoranthene	+	+
14	Pyrene	+	+
15	Benz[*a*]anthracene	+	+
16	Chrysene	+	+
17	Benzo[*b*]fluoranthene	+	+
18	Benzo[*k*]fluoranthene	+	+
19	Benzo[*e*]pyrene	–	+
20	Benzo[*a*]pyrene	+	–
22	Indeno[1,2,3-*cd*]pyrene	+	–
23	Dibenz[*a*,*h*]anthracene	+	–
24	Benzo[*ghi*]perylene	+	–

[a] Peak numbers refer to Fig. 5.
[b] + Positively detected or confirmed; – not detected or confirmed.

postrun spectra of the volatile naphthalenes and biphenyl, recorded with a data point resolution of 1 cm^{-1}.

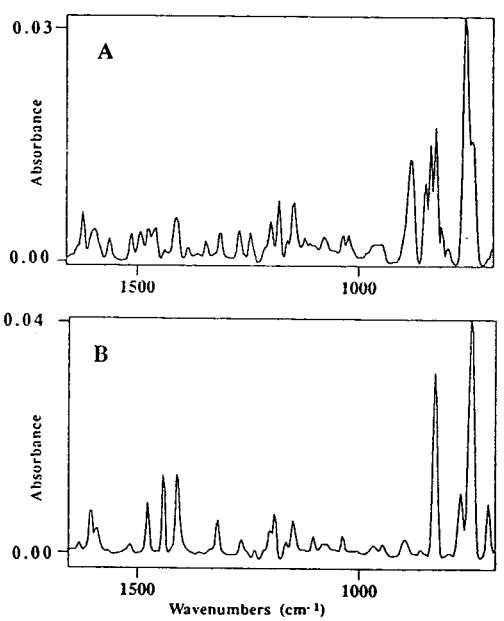

Fig. 2. Cryotrapping GC–FT-IR spectra of the isomers (A) benzo[*a*]pyrene and (B) benzo[*e*]pyrene taken from the chromatogram in Fig. 1.

3.1. Detection limits

Although the aim of this study was to confirm results of HPLC–fluorescence analysis qualitatively, experiments with dilute standard solutions were carried out to obtain an insight into the sensitivity of GC–FT-IR for PAH analysis. Elution of all components of the dilute standards was seen in the Fg chromatogram at 950–700 cm^{-1} to a smallest amount of 1 ng injected. Amounts of 0.5 ng were no longer visible in the chromatograms but identifiable spectra were obtained by carrying out postrun measurements at the previously established retention time window (see Table 1). Postrun measurement of the 0.25-ng injections only provided spectra of naphthalene, fluorene, fluoranthene and pyrene.

3.2. Samples

GC–FT-IR analysis of soil extracts in acetonitrile was hampered by a limitation in the deposition mechanism of the GC–FT-IR interface. When using splitless injection, the large amount of solvent causes a vapour cloud at the end of the deposition tip which is partly spread over the deposition window. Despite the high vacuum in the GC–FT-IR interface, solvent crystallization

on the window occurs, usually in an area that covers the point where immobilization of the chromatogram begins. As result of this effect, the first 10–15 min of the GC trace of samples in acetonitrile were found to be IR opaque and no information could be obtained in this region. Therefore, PAHs with $t_R \leq 15$ min were not taken into account.

Results of the comparative GC–FT-IR and HPLC–fluorescence determinations of PAHs in sediment, soil and river clay extracts are summarized in Tables 2, 3 and 4, respectively. The corresponding chromatograms are shown in Figs. 3, 4 and 5. As can be seen, the signal-to-noise ratio of the GC–FT-IR traces is much lower than that of the HPLC–fluorescence traces, owing to the lower sensitivity of FT-IR. In addition, the chemical background is higher as fluorescence detection is transparent to most of the non-PAH compounds, whereas, inherent to the FT-IR principle, the FT-IR chromatogram comprises full-spectrum data of all eluting substances. As a

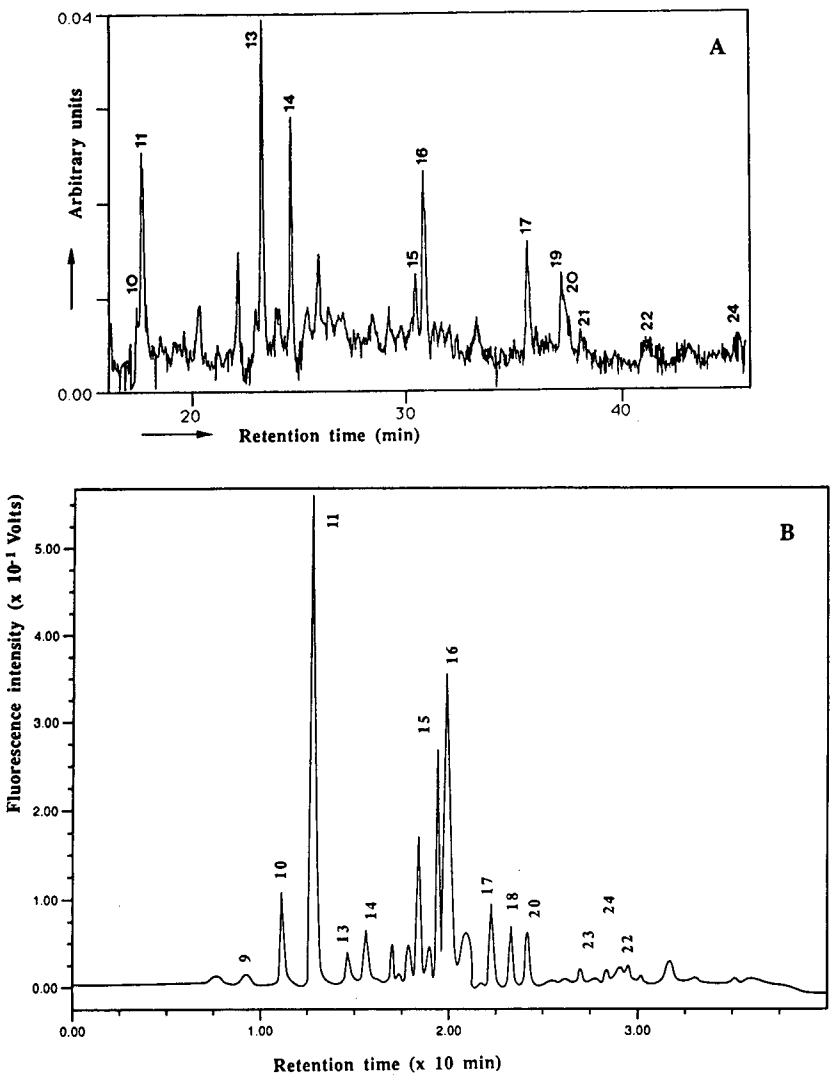

Fig. 3. (A) Functional group GC–FT-IR (A) and (B) HPLC–fluorescence analysis of a sediment extract.

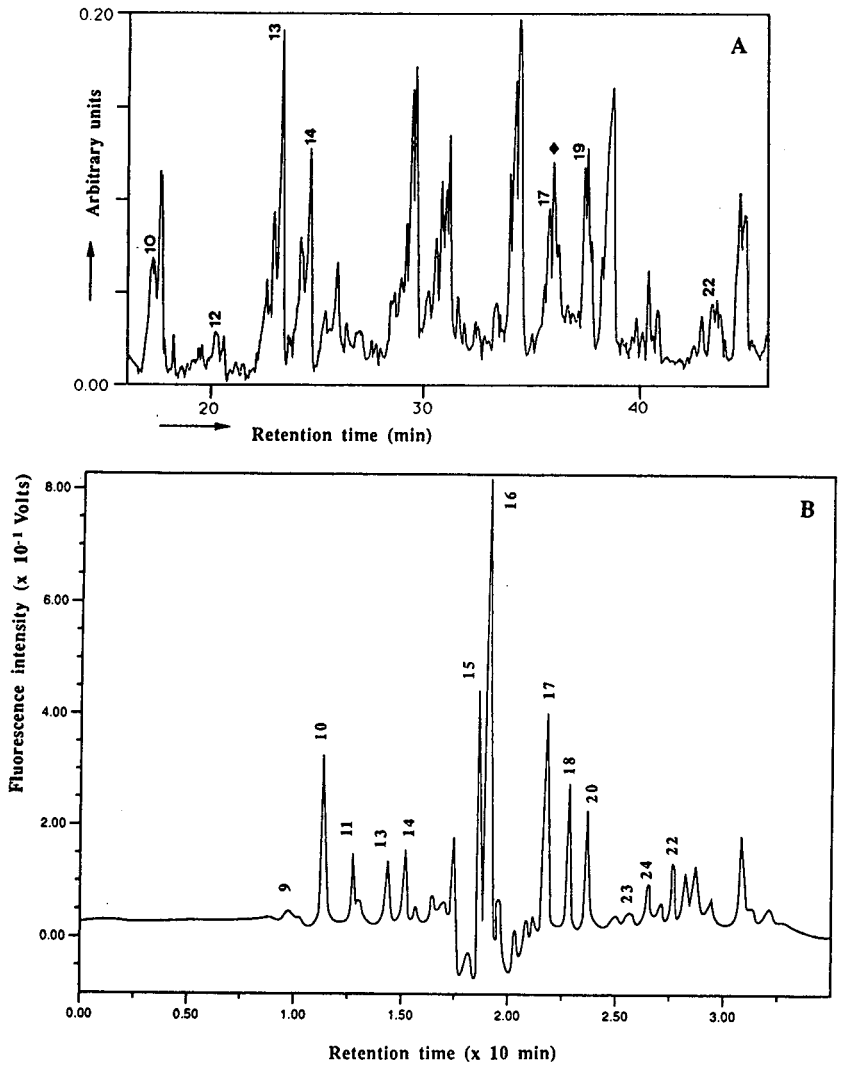

Fig. 4. (A) Functional group GC–FT-IR (A) and (B) HPLC–fluorescence analysis of a soil extract.

consequence, IR spectra may contain interfering absorption bands of co-eluting compounds. Incidentally, this phenomenon was observed. In the sediment extract for instance, the spectrum shown in Fig. 6 was obtained at a retention time matching with that of the benzo[*e*]pyrene standard. The molecular fingerprint region clearly shows all significant bands present in the reference spectrum of this compound (Fig. 2B) and therefore it has been identified positively, despite the presence of absorptions at 1450 and 1020 cm^{-1}. Matching of retention times and agreement in IR absorption frequencies of at least five characteristic bands in the sample and reference spectra turned out to be a useful criterion for the positive identification of this type of compound and, following this procedure, the occurrence of twelve PAH was confirmed in the sediment sample.

Compared with the results of the HPLC analysis, the presence of benzo[*k*]fluoranthene and dibenz[*a*,*h*]anthracene could not be confirmed in

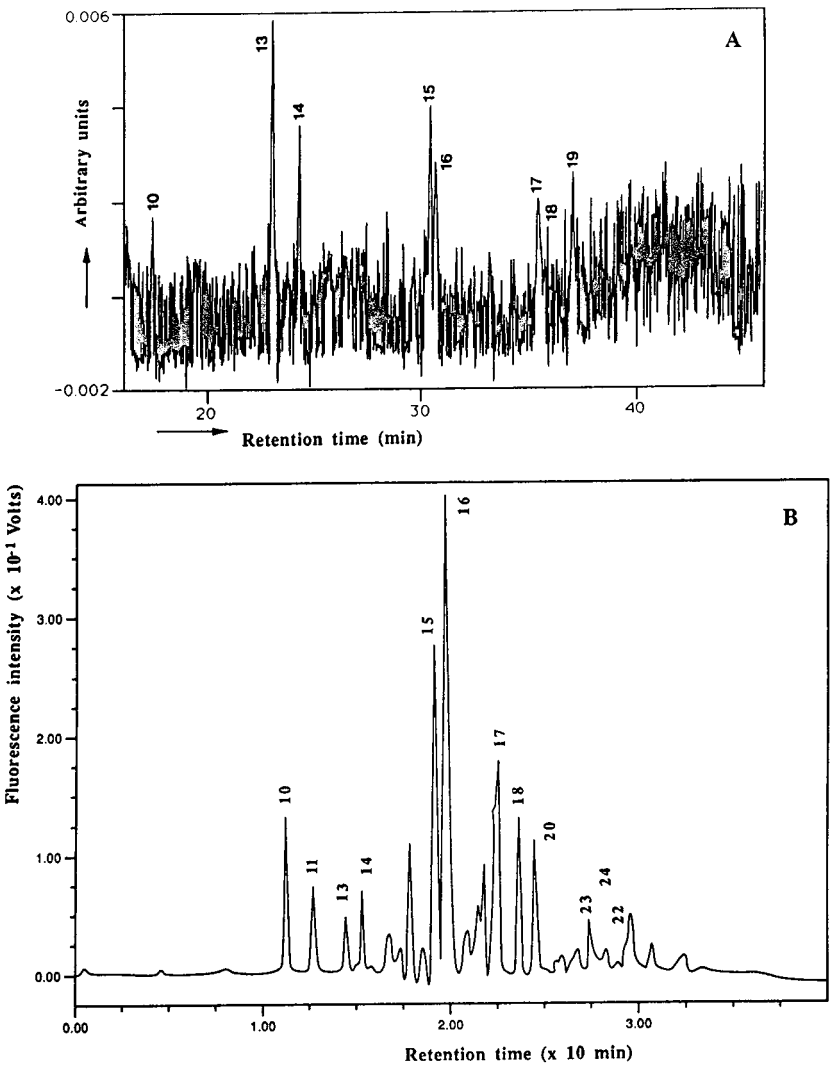

Fig. 5. (A) Functional group GC–FT-IR and (B) HPLC–fluorescence analysis of a river clay extract.

the sediment extract because of insufficient sensitivity of the GC–FT-IR system. In contrast, perylene, benzo[*e*]pyrene and related (poly) aromatic compounds such as anthraquinone have been identified. Indeed, these compounds were not determined by HPLC–fluorescence analysis, but it should be noted that these components were absent in the HPLC reference standard.

The high chemical background in the GC–FT-IR trace of the soil extract (Fig. 4A) hampered identification of several PAHs, determined by HPLC–fluorescence. Eight compounds could be identified by precise selection of background spectra in the close vicinity of the chromatographic peak of interest. Seven of these were determined directly with the help of the IR spectra obtained from the SRM 2260 solution. Benzo[*j*]fluoranthene was not identified straightforwardly as it was absent in the standards. However, a library search in a reference collection of KBr spectra revealed a high similarity index for the spectrum of this molecule. The

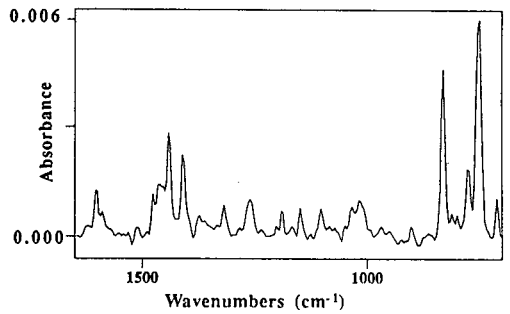

Fig. 6. Cryotrapping spectrum of benzo[*e*]pyrene with interfering bands at 1450 and 1020 cm^{-1}, obtained from peak 19 in the chromatogram in Fig. 3A.

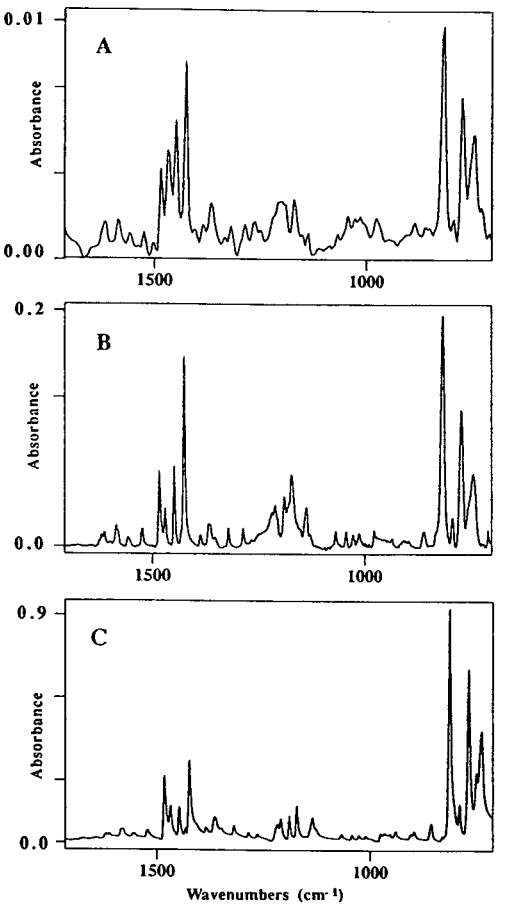

Fig. 7. IR spectra of benzo[*j*]fluoranthene: (A) cryotrapping spectrum obtained from peak ◆ in the chromatogram in Fig. 4A; (B) cryotrapping spectrum obtained from a standard solution; (C) KBr reference spectrum.

identity was checked by separate recording of the cryotrapping spectrum of the standard. All three spectra are shown in Fig. 7.

The signal-to-noise ratio of the GC–FT-IR trace of the river clay extract (Fig. 5A) was very poor as a result of the low concentration of the components (estimated as 0.5–2 ng/μl in the concentrated extract). For that reason, the presence of only eight PAHs could be confirmed.

The discriminative value of FT-IR detection was demonstrated by the identification of benzo[*e*]pyrene in all three extracts. Initially, HPLC analysis indicated the presence of the [*a*] isomer only, but this could not be confirmed with GC–FT-IR. In contrast, the IR spectrum of the [*e*] congener was identified in the sediment, soil and river clay extracts. Closer examination of the HPLC analysis, however, indicated that, under the chosen experimental conditions, co-elution of the [*a*] and [*e*] isomers may occur. Combined with insufficient detector specificity, this probably caused incorrect conclusions.

4. Conclusions

It is concluded that cryotrapping GC–FT-IR can be a helpful tool for the qualitative analysis of PAHs in environmental samples. The results of HPLC–fluorescence analysis of three soil extracts have been largely confirmed. In addition, the presence of other (poly)aromatic compounds was established. The technique appears to be specifically suited to distinguishing between structural isomers, which is particularly valuable in case co-elution in the HPLC analysis occurs.

The detection limit is in the range 0.25–1 ng injected for standard solutions and 1–4 ng for soil extracts. As such, cryotrapping GC–FT-IR can be a valuable confirmational technique for PAHs in addition to GC–FID, GC–MS and HPLC–UV/fluorescence.

It was endorsed that cryotrapping IR spectra of PAHs largely resemble spectra recorded with the KBr pelleting technique at room temperature. Consequently, existing spectrum libraries can be used for the interpretation and identification of cryotrapping spectra of unknowns.

Acknowledgements

Ms. C.J. Berkhoff, Ms. W.C. Hijman and Mr. J.Y. Wammes are grateful acknowledged for the preparation of the extracts and for carrying out the HPLC analyses.

References

[1] W. Slooff, J.A. Janus, A.J.C.M. Matthysen, G.K. Montizaan and J.P.M. Ros (Editors), *Integrated Criteria Document PAHs, Report No. 58474011*, National Institute of Public Health and Environmental Protection, Bilthoven, 1989.
[2] K.S. Chiu, K. Biemann, K. Krishnan and S.L. Hill, *Anal. Chem.*, 56 (1984) 1610.
[3] V.N. Garg, B.D. Bhatt, V.K. Kaushik and K.R. Murthy, *J. Chromatogr. Sci.* 25 (1987) 237.
[4] J.W. Childers, N.K. Wilson and R.K. Barbour, *Appl. Spectrosc.*, 43 (1989) 1344.
[5] M. Guiliano, P. Doumenq, A. Jawad and G. Mille, *Appl. Spectrosc.*, 43 (1989) 571.
[6] D.F. Gurka, S.M. Pyle, I. Farnham and R. Titus, *J. Chromatogr. Sci.* 29 (1991) 339.
[7] J. Semmler, P.W. Yang and G.E. Crawford, *Vibr. Spectrosc.*, 2 (1991) 189.
[8] N.R. Smyrl, D.M. Hembree, W.E. Davis, D.M. Williams and J.C. Vance, *Appl. Spectrosc.*, 46 (1992) 277.
[9] V.F. Kalasinsky, C. Saiwan and K.G. Whitehead, *J. Chromatogr. Sci.*, 26 (1988) 584.
[10] J.F. Schneider, G.T. Reedy and D.G. Ettinger, *J. Chromatogr. Sci.*, 23 (1985) 49.
[11] D.M. Hembree, N.R. Smyrl, W.E. Davis and D.M. Williams, *Analyst*, 118 (1993), 249.
[12] C.J. Wurrey, B.J. Fairless and H.E. Kimball, *App. Spectrosc.*, 43 (1989) 1317.
[13] J. Grainger and L.T. Gelbaum, *Appl. Spectrosc.*, 41 (1987) 809.
[14] J. Grainger, V.V. Reddy and D.G. Patterson, *Appl. Spectrosc.*, 44 (1990) 41.
[15] J.W. Childer, N.K. Wilson, R.L. Harless and R.K. Barbour, *Chemosphere*, 25 (1992) 1285.
[16] T. Visser and M.J. Vredenbregt, *Vibr. Spectrosc.*, 1 (1990) 205.
[17] W. Karcher, R.J. Fordham, J.J. Dubois, P.G.J.M. Glaude and J.A.M. Ligthart (Editors) *Spectral Atlas of Polycyclic Aromatic Compounds*, Reidel, Dordrecht, 1985.
[18] *Documentation of Molecular Spectroscopy*, Verlag Chemie, Weinheim, and Butterworths, London, 1967.

ELSEVIER

Journal of Chromatography A, 687 (1994) 315–321

JOURNAL OF CHROMATOGRAPHY A

Identification of 4-oxoheptanedioic acid in the marine atmosphere by capillary gas chromatography–mass spectrometry

Futoshi Sakaguchi[1], Kimitaka Kawamura*

Department of Chemistry, Faculty of Science, Tokyo Metropolitan University, 1-1 Minami-Ohsawa, Hachioji, Tokyo 192-03, Japan

First received 26 May 1994; revised manuscript received 16 August 1994

Abstract

A capillary gas chromatographic (GC) analysis of the water-soluble fraction isolated from marine aerosols after BF_3–*n*-butanol derivatization showed the presence of several unknown carboxylic acids. Based on the characteristic mass fragment ions and molecular ion, and also the chemical composition calculated from accurate mass measurements, it is hypothesized that one of the unknown compounds is 4-oxoheptanedioic acid dibutyl ester. A comparison of its GC retention time and mass spectra with those of the dibutyl ester of an authentic standard confirmed that 4-oxoheptanedioic acid is present in the marine aerosols. This paper reports, for the first time, the identification of 4-oxoheptanedioic acid (4-ketopimelic acid) in marine atmospheric samples.

1. Introduction

Previous studies of water-soluble organic compounds including dicarboxylic acids in aerosol samples have provided important information for the photochemical oxidation mechanisms of organic matter in atmospheric environments [1–3]. Photochemical chamber experiments have also indicated the production of low-molecular-mass polar organic compounds from unsaturated hydrocarbons [4,5]. During the course of a capillary gas chromatographic (GC) study on short-chain α,ω-dicarboxylic acids, we detected many unknown peaks in the diacid fraction isolated from remote marine aerosols. Some of them were identified as ω-oxocarboxylic acids [6]. Identification of these unknown compounds is generally important because their chemical structures sometimes provide information on the origin, transformation mechanisms and fate of organic aerosols in the atmosphere. We have successfully identified one of the unknown compounds as an α,ω-dicarboxylic acid (C_7) containing an additional keto group at the C-4 position (4-oxoheptanedioic acid).

In this paper we present electron impact mass spectra for 4-oxoheptanedioic acid dibutyl ester, identified in the BF_3–*n*-butanol derivatives of the water-soluble fraction isolated from remote marine aerosols using GC combined with low- and high-resolution mass spectrometry. Mass

* Corresponding author.

[1] Present address: Petroleum Laboratory, Research and Development Division, Japan Energy Corporation, 3-17-35 Niizo-Minami, Toda, Saitama 335, Japan.

0021-9673/94/$07.00
SSDI 0021-9673(94)00925-2

fragmentation mechanisms are described, based on the chemical compositions obtained from accurate mass measurements of the molecular ion and of characteristic mass fragment ions.

2. Experimental

2.1. Reagents and chemicals

All organic solvents were purchased from Wako. They were redistilled in the laboratory and checked for purity by GC prior to use. Organic-free pure water was prepared in the laboratory as follows. Water obtained from a Milli-Q system (Millipore) was boiled with potassium permanganate and then redistilled in all-glass apparatus. The redistilled organic solvents and pure water were stored in brown glass bottles with a Teflon-lined screw-cap. A solution of 14% boron trifluoride in *n*-butanol was purchased from Alltech/Applied Science. Authentic 4-oxoheptanedioic acid (4-ketopimelic acid) was purchased from Aldrich. The standard was derivatized to the dibutyl ester by the procedure described above.

2.2. Aerosol samples

Remote marine aerosol samples were collected on pre-combusted (450°C) quartz-fibre filters (Pallflex, 20 × 25 cm) using a high-volume air sampler (Shibata, HVC-1000), in the western equatorial and western North Pacific Ocean during a cruise of R/V Hakuho Maru (KH 90-2 and 90-3). The air sampler was operated with a wind speed and wind sector system to avoid potential contamination from the ship engine exhausts [7]. Thirty-three marine aerosol samples were collected in 13°S–34°N, 140°E–150°W during the period 3 September to 13 December 1990. Blank filters were set in the sampler cartridge, exposed to the air for a few seconds and then recovered. Filter samples and blank filters were placed in precleaned glass bottles (150 ml) with a Teflon-lined screw-cap and stored at −20°C until analysis.

2.3. Isolation

Water-soluble fractions were isolated and analysed by the methods reported previously [7]. Briefly, one eighth of each filter sample, which was cut into pieces of ca. 1 cm^2, was extracted with organic-free water under ultrasonication. The water extracts, containing short-chain α, ω-dicarboxylic acids and related compounds, were concentrated to ca. 1 ml by rotary evaporation under vacuum. To remove suspended particles, the concentrates were passed through a glass column (Pasteur pipette) packed with quartz-fibre wool and transferred to a 10-ml test-tube with a ground-glass stopper. The extracts were concentrated using a rotary evaporator under vacuum and then dried in a nitrogen stream. A 0.2-ml aliquot of 14% boron trifluoride in *n*-butanol was immediately added to the test-tube and the carboxyl groups were derivatized to dibutyl esters at 100°C for 30 min. To the test-tube were added *n*-hexane (5 ml), pure water (3 ml) and acetonitrile (0.2 ml), and the esters were extracted into the *n*-hexane layer. The hexane extracts were washed twice with pure water (3 ml). The extract containing the diacid dibutyl esters and unknown compounds was concentrated using a rotary evaporator and a nitrogen stream. The esters were dissolved in 50 μl of hexane and then analysed by GC and GC–mass spectrometry (GC–MS).

The water-bath temperature during rotary evaporation was maintained at less than 50°C for water extracts and less than 30°C for esters. Recoveries of oxalic acid and succinic acid were 70% and 90%, respectively [7].

2.4. GC, GC–MS and GC–high resolution (HR) MS analysis

Dibutyl esters of carboxylic acids were determined using a capillary gas chromatograph (Hewlett-Packard HP-5890) equipped with a split–splitless injector, a Hewlett-Packard fused-silica capillary column (HP-5, 25 m × 0.32 mm I.D., 0.52-μm film thickness) and a flame ioniza-

tion detector. Helium was used as the carrier gas. The column oven temperature was programmed from 50°C (held for 2 min) to 120°C at 30°C/min, and then to 310°C (held for 10 min) at 8°C/min. The temperatures of the injection port and the detector were maintained at 300 and 320°C, respectively. The data were processed using a Hewlett-Packard 3396A integrator or a Shimadzu C-R7A Chromatopac integrator. Conventional GC–MS analysis was conducted using an ion-trap mass spectrometer (Finnigan MAT ITS-40) interfaced to a capillary gas chromatograph (Varian GC 3400). The GC–MS data were processed using the ITS 40 data system with a NIST library. High-resolution mass spectra were obtained using a double-focusing mass spectrometer (JEOL SX-102) interfaced to a capillary gas chromatograph (HP 5890 Series II). The SX-102 mass spectrometer was operated at a resolution of 10 000. The GC column conditions for the GC–MS measurements were similar to those described above.

3. Results and discussion

Fig. 1 shows a reconstructed ion chromatogram of the butyl esters of a fraction isolated from the equatorial Pacific aerosol sample. Homologous series of straight-chain saturated α,ω-dicarboxylic acids and of ω-oxocarboxylic acids were detected in the range C_2–C_9 in the marine aerosol samples studied [6,7]. In the samples studied, oxalic (C_2^{di}), malonic (C_3^{di}), succinic (C_4^{di}), glyoxylic (ω-oxocarboxylic acid, C_2^{ω}) and malic acid (hydroxysuccinic acid, C_4^{di}) were detected as major species. These low-molecular-mass dicarboxylic acids and related compounds have been reported in continental [8–10] and marine [1,2,7] aerosols, and are considered for the most part to be derived from the photochemical oxidation of anthropogenic unsaturated hydrocarbons [10] and biogenic unsaturated fatty acids [1,3,8].

In addition to the small diacids and ω-oxo acids identified in the aerosol samples, many

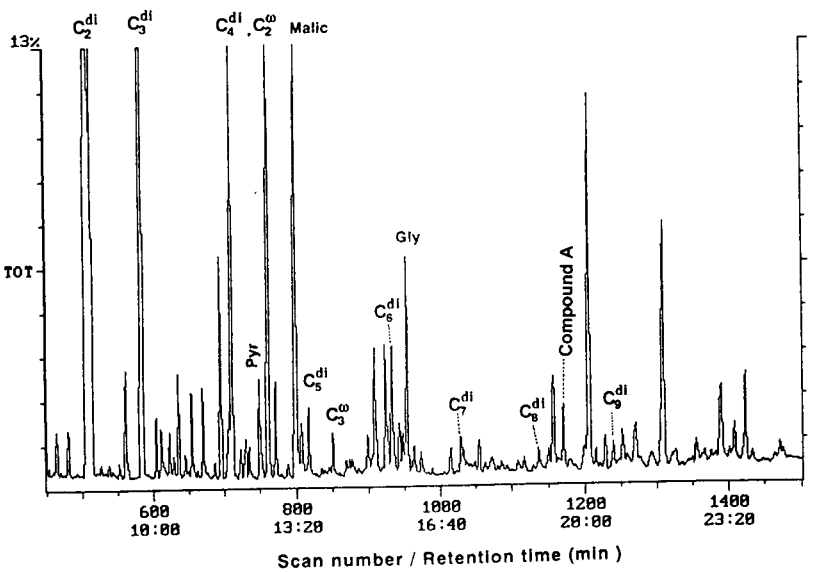

Fig. 1. Reconstructed ion chromatogram of the dicarboxylic acid dibutyl ester fraction isolated from the remote marine aerosol sample (QFF 276) collected from the western equatorial Pacific (2.39°N, 154.81°E). C_n^{di} and C_n^{ω} denote α,ω-dicarboxylic acid and ω-oxocarboxylic acid with n carbon atoms, respectively. Pyr, Malic and Gly denote pyruvic acid, malic acid and glyoxal, respectively.

unknown peaks were detected in the gas chromatogram of the BF_3–*n*-butanol derivatized ester fraction. Among them, we have successfully identified one peak (hereafter refered to as compound A; see Fig. 1) as a ketodicarboxylic acid dibutyl ester. Compound A elutes between suberic acid (C_8) dibutyl ester ($M_r = 286$) and azelaic acid (C_9) dibutyl ester ($M_r = 300$), suggesting that it molecular mass is close to those of C_8 or C_9 dicarboxylic acid dibutyl esters. The results showed that compound A was not detected in the blanks, indicating that it was not the result of contamination during either sample collection, transportation, storage or analytical procedures in the laboratory.

Fig. 2 shows an electron impact mass spectrum (low resolution) for compound A, together with its possible structure. The mass spectrum gives a base peak at *m/z* 101 and other characteristic fragments at *m/z* 41, 55, 73, 111, 129, 157, 185, 213 and 286. Unfortunately, the NIST library search did not provide any matching spectrum. The *m/z* 286 ion was interpreted as the molecular ion (M^+). The *m/z* 213 (M − 73) ion suggested the presence of a butyl ester group in the structure of compound A. It probably arises by elimination of a butoxy group (C_4H_9O) from a butyl ester moiety, and further decomposes by loss of C_4H_8 [8,11] to result in the *m/z* 157 ion. The M^+ ion probably decomposes via α-cleavage at the carbonyl group of a butyl ester to give the base peak at *m/z* 101 ($COOC_4H_9$) and the complementary M − 101 ion (*m/z* 185). The latter further decomposes to give the *m/z* 111 ion by loss of butanol. Because of an absence of an even-mass number fragment ion, the structure of compound A is suggested to have no γ-hydrogen that can produce such a fragment ion through a McLafferty rearrangement. These considerations suggested that compound A contains an additional functional group in the carboxylic acid skeleton.

According to the above mass spectral information and interpretation, we considered compound A to be a dibutyl ester of a straight chain α,ω-dicarboxylic acid containing an additional keto group at a γ-position. We hypothesized, from the molecular mass ($M_r = 286$), that compound A is the dibutyl ester of 4-oxoheptanedioic acid ($C_{15}H_{26}O_5$) (see Fig. 2). By assuming this structure, the *m/z* 157 and 129 ions can be explained as being formed by a cleavage of a C–C bond adjacent to the keto group. The *m/z* 129 ion may also occur by loss of CO from

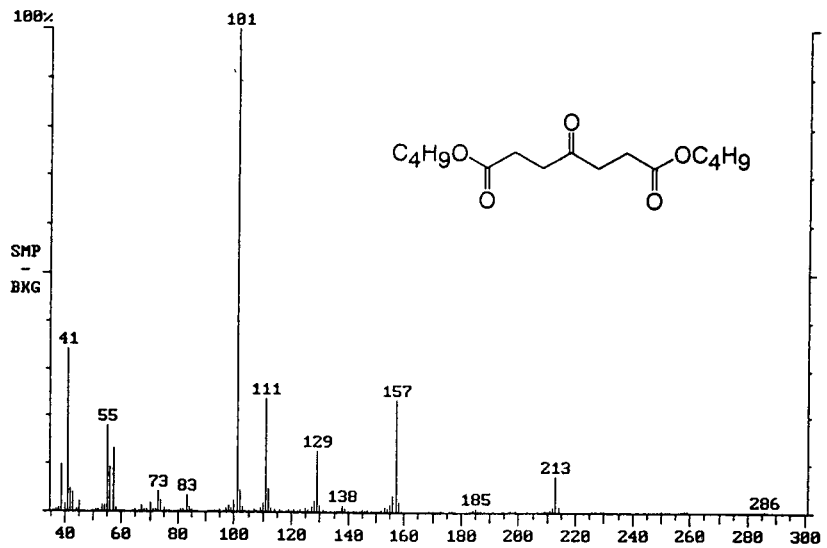

Fig. 2. Electron impact mass spectrum obtained for the unknown compound A and its hypothesized structure.

Table 1
Accurate mass measurements by HRMS for the molecular ion and major fragment ions of the compound A and their calculated chemical composition

Mass (m/z)	Error (mu)	Unsaturation	Composition
286.1746	−3.4	3.0	$C_{15}H_{26}O_5$
213.1134	0.7	3.5	$C_{11}H_{17}O_4$
157.0872	0.7	2.5	$C_8H_{13}O_3$
157.0501	0.0	3.5	$C_7H_9O_4$
129.0580	2.8	2.5	$C_6H_9O_3$
111.0436	−1.0	3.5	$C_6H_7O_2$
101.0230	−0.8	2.5	$C_4H_5O_3$
73.0285	−0.5	1.5	$C_3H_5O_2$

the m/z 157 ion, and decomposes to the m/z 55 ion (CH_2CHCO) by loss of butanol. These considerations are consistent with the hypothesized structure of compound A (4-oxoheptanedioic acid).

To confirm the structure, the mass spectrum of compound A was measured with a high-resolution mass spectrometer interfaced to a capillary gas chromatograph. Table 1 summarizes the measured accurate masses for the molecular ion ($M_r = 286$) and major mass fragment ions and their postulated elemental compositions. Differences between the measured and calculated masses are within ±5 mu as seen in Table 1. The accurate mass measurement of the molecular ion (M^+; m/z 286.1746) indicates that the elemental composition of compound A is $C_{15}H_{26}O_6$, consistent with the structure of 4-oxoheptanedioic acid dibutyl ester as hypothesized above. The fragment ion of m/z 213.1134 corresponds to $C_{11}H_{17}O_4$, a fragment ion $(M - 73)^+$ derived by a loss of a butoxy group (C_4H_9O). These considerations indicate that the hypothesized structure of 4-oxoheptanedioic acid dibutyl ester is correct. Based on the HRMS results, this structure was further examined by considering mass fragmentation mechanisms, as shown in Fig. 3.

The HRMS measurements indicate that the m/z 157 ion obtained by the low-resolution mass spectrometer (Fig. 2) is composed of two different ions, of m/z 157.0501 and 157.0872 (see Table 1). As seen in Fig. 4, a high-resolution mass spectrum clearly shows two fragment ions in the mass range 156.8–157.3. The elemental composition of the m/z 157.0872 ion is calculated as $C_8H_{13}O_3$. This formula is consistent with the mass fragment ($C_8H_{13}O_3$) predicted from α-cleavage at the C–C bond adjacent to the keto group as shown in Fig. 3. In contrast, the elemental composition of the m/z 157.0501 ion is calculated as $C_7H_9O_4$. This fragment should be produced from the m/z 213 ion ($C_{11}H_{17}O_4$) by loss of C_4H_8 ($M_r = 56$) (see Fig. 3). The elemental composition of the m/z 129.0580 ion is calculated to be $C_6H_9O_3$, which is probably produced by loss of CO from the m/z 157.0501 ion ($C_7H_9O_4$). The composition for m/z 111.0436 is calculated as $C_6H_7O_2$, which is produced by an elimination of H_2O from the

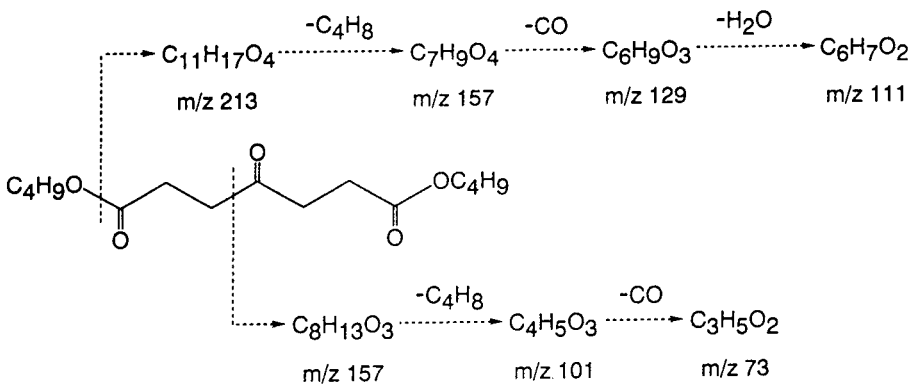

Fig. 3. Proposed schemes for mass fragmentation mechanisms of 4-oxoheptanedioic acid dibutyl ester.

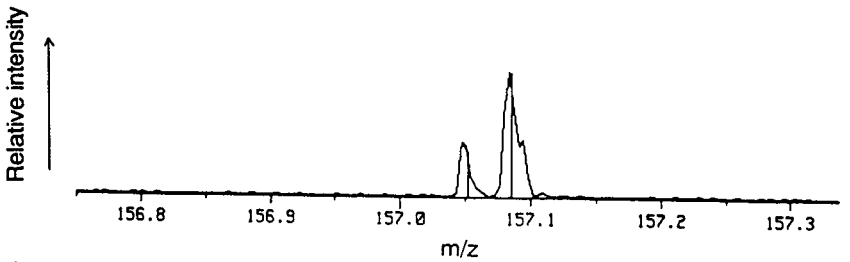

Fig. 4. High-resolution mass spectrum obtained for the unknown compound A in the mass range from m/z 156.75 to 157.35.

m/z 129.0580 ion ($C_6H_9O_3$). Elimination of C_4H_8 from the m/z 157.0872 ion ($C_8H_{13}O_3$) produces the base peak at m/z 101.0230 ($C_4H_5O_3$).

Initially, we considered that the m/z 185 ion was derived by loss of the butyl ester portion ($COOC_4H_9$), and the m/z 111 ion was produced by a subsequent loss of butanol from the m/z 185 ion. However, the calculated composition ($C_4H_5O_3$) for the m/z 101.0230 ion does not support α-cleavage at the butyl ester portion, but rather suggests the production of the m/z 101 ion by elimination of C_4H_8 from $C_8H_{13}O_3$ (m/z 157.0872, Table 1). These considerations led to the conclusion that the m/z 101.0230 ($C_4H_5O_3$) fragment ion is not $COOC_4H_9$ but occurs by loss of C_4H_8 from the m/z 157.0872 ion ($C_8H_{13}O_3$). The elemental composition of the m/z 73.0285 ion is calculated as $C_3H_5O_2$, which probably arises from the m/z 101.0230 ion ($C_4H_5O_3$) by loss of CO. The lack of detection of the m/z 73 ion derived from butyl ester moiety (OC_4H_9) suggests that elimination of the butoxy group is insignificant. All the results and interpretations based on the high-resolution mass spectra support the hypothesis that compound A is 4-oxoheptanedioic acid dibutyl ester.

Authentic 4-oxoheptanedioc acid (4-oxopimelic acid) was purchased and esterified with 14% BF_3–n-butanol to the corresponding dibutyl ester, using the procedure described above for the samples. The ester was analysed by GC and GC–MS. The GC retention time of the esterified authentic compound showed excellent agreement with that of compound A. Further, the low-resolution mass spectrum of the esterified authentic standard was confirmed to be identical with that of compound A (Fig. 2). The GC–HRMS analysis further supported the chemical composition for the molecular ion and mass fragment ions, as listed in Table 1. The data provide unequivocal evidence for identification of 4-oxoheptanedioic acid and indicate that the presumed mass fragmentation mechanism for the ester (Fig. 3) is reasonable. In the final stage of this study, we realized that this compound had been reported in continental aerosols as the dimethyl ester with no mass spectral information [8].

The concentrations of 4-oxoheptanedioic acid were found to be 0.03–2.5 ng/m^3 in the marine aerosol samples studied. Its concentrations were lower than those of dicarboxylic acids such as oxalic and malonic acid. However, this compound was detected in relatively high abundance in the marine aerosols collected over western equatorial Pacific. Although the source has not yet been identified, 4-oxoheptanedioic acid may be produced in the atmosphere by the photochemical oxidation of precursor compounds such as monocarboxylic acids having an additional keto group at the C-4 position. Interestingly, 4-ketocarboxylic acids (C_7–C_{13}) have been detected in the marine atmosphere [2,12]. They are probably produced by oxidation of monocarboxylic acids which are counterparts of the photochemical oxidation reactions of biogenic unsaturated fatty acids [1,2]. 4-Oxoheptanedioic acid may be further oxidized in the atmosphere to result in malonic and/or succinic acid, which have been abundantly detected in marine and continental aerosols [7,10].

4. Conclusions

A dicarboxylic acid with an additional keto group (4-oxoheptanedioic acid) has been identified for the first time in marine aerosol samples, collected from the western Pacific, by using capillary GC–MS and GC–HRMS. The molecular structure was hypothesized based on the molecular ion and fragment ions obtained from low- and high-resolution mass spectra. The hypothesized structure was confirmed by comparing the GC retention time and mass spectra with those of the authentic standard. Based on the elemental compositions of the fragment ions obtained from high-resolution mass measurements, the formation mechanisms of the characteristic mass fragments of 4-oxoheptanedioc acid butyl ester were interpreted. 4-Oxoheptanedioic acid may be an intermediate in the formation of dicarboxylic acids such as succinic acid. This study demonstrated that capillary GC–HRMS is a powerful technique for identifying highly oxygenated organic compounds in atmospheric samples, which often retain information on the photochemical transformation of organic matter in the atmosphere.

Acknowledgement

This study was supported in part by the Ministry of Education, Science and Culture through Grant-in-Aid 03248104.

References

[1] K. Kawamura and R.B. Gagosian, *Nature*, 325 (1987) 330–332.
[2] K. Kawamura and R.B. Gagosian, *J. Atmos. Chem.*, 11 (1990) 107–122.
[3] E.G. Stephanou and N. Stratigakis, *Environ. Sci. Technol.*, 27 (1993) 1403–1407.
[4] H. Bandow, N. Washida and H. Akimoto, *Bull. Chem. Soc., Jpn.*, 58 (1985) 2531–2540.
[5] S. Hatakeyama, M. Ohno, J. Weng, H. Takagi and H. Akimoto, *Environ. Sci. Technol.*, 21 (1987) 52–57.
[6] K. Kawamura, *Anal. Chem.*, 65 (1993) 3505–3511.
[7] K. Kawamura and K. Usukura, *J. Oceanogr.*, 49 (1993) 271–283.
[8] Y. Yokouchi and Y. Ambe, *Atmos. Environ.*, 20 (1986) 1727–1734.
[9] H. Satsumabayashi, H. Kurita, Y. Yokouchi and H. Ueda, *Tellus*, 41B (1989) 219–229.
[10] K. Kawamura and K. Ikushima, *Environ. Sci. Technol.*, 27 (1993) 2227–2235.
[11] H. Budzinkiewicz, C. Djerassi and D.H. Williams, *Mass Spectrometry of Organic Compounds*, Holden-Day, San Francisco, 1967, p. 690.
[12] K. Kawamura and R.B. Gagosian, *J. Chromatogr.*, 438 (1988) 299–307.

ELSEVIER

Journal of Chromatography A, 687 (1994) 323–332

JOURNAL OF CHROMATOGRAPHY A

Comparative study of the determination of tebufenozide in formulated products by gas chromatographic and liquid chromatographic methods

K.M.S. Sundaram[a,*], R. Nott[a], E.E. Lewin[b]

[a]*Forest Pest Management Institute, Natural Resources Canada–Canadian Forest Service, 1219 Queen Street East, P.O. Box 490, Sault Ste. Marie, Ontario, P6A 5M7, Canada*

[b]*Research Laboratories, Rohm & Haas Company, 727 Norristown Road, Spring House, PA 19477, USA*

First received 1 March 1994; revised manuscript received 22 July 1994

Abstract

Thirteen formulated products (formulation concentrates and spray mixes) containing tebufenozide [N′-*tert.*-butyl-N′-(3,5-dimethylbenzoyl)-N-(4-ethylbenzoyl) hydrazine, also known as RH-5992; trade name MIMIC], were analyzed, after solvent dissolution by agitation, using direct gas chromatography (GC) and reversed-phase high-performance liquid chromatography (HPLC). The responses of the analyte to three GC detection methods (flame ionization detection, FID; nitrogen–phosphorus detection, NPD and electron-capture detection, ECD) using three fused-silica capillary columns of varying internal diameters were compared. The mini-bore (0.25 mm I.D.) DB-5 [(5% phenyl)-methylpolysiloxane] column, attached to the ECD system was better suited to quantify the analyte in formulated products than the mega-bore DB-1 (dimethylpolysiloxane) and DB-17 [(50% phenyl)-methylpolysiloxane] columns linked to the FID, NPD or ECD systems. Analysis by GC–FID and a reversed-phase HPLC method using an RP-8 column (10 μm particle size) with a mobile phase containing acetonitrile–dioxane–water and a diode-array UV detector set at 236 nm also gave values similar to the GC–ECD method. However, due to the rapidity and sensitivity of sample analysis, GC–ECD is the technique of choice for the quantification of MIMIC in formulated products.

1. Introduction

The hydrazine derivative tebufenozide (trade name: MIMIC), also known as RH-5992 [N′-*tert.*-butyl-N′-(3,5-dimethylbenzoyl)-N-(4-ethylbenzoyl) hydrazine] (Rohm & Haas, USA [1]) is a novel type of insect growth regulator interfering with the moulting process of lepidopteran insects. It acts as an agonist or mimic of insect moulting hormone, 20-hydroxyecdysone, by inducing premature, incomplete ecdysis resulting in death of the exposed insects. The material is lepidopteran specific and has no effect on crustacea, arachnida, or most other insect orders (beetles, aphids, flies etc.) and mites. It is essentially non-toxic to bees [2]. These desirable properties make the material a choice insecticide to suppress the lepidopteran insect populations in forests.

Aerial field trials conducted recently by the Forest Pest Management Institute, Natural Resources Canada–Canadian Forest Service, have

* Corresponding author.

0021-9673/94/$07.00
SSDI 0021-9673(94)00698-9

shown that MIMIC is effective in controlling the spruce budworm, *Choristoneura fumiferana* (Clem.), a destructive pest that causes considerable damage to the spruce-fir forests of eastern North America and is threatening the wood supply from large areas of forest in eastern Canada [3]. In aerial spray trials, the technical MIMIC is formulated by adding different adjuvants (commonly referred to as formulants or inerts) such as solvents, wetting agents, stickers, spreaders, penetrants and emulsifying agents to produce a "formulation concentrate". The formulation concentrate is then diluted with water in the field to form the "spray mix" or end-use product which is then applied by aircraft.

No method has been reported in the open literature, until now, to quantify the MIMIC present in either formulation concentrates or spray mixes. A high-performance liquid chromatographic (HPLC) method with diode-array UV detection (DAD) to analyze the residues of MIMIC in various forestry matrices, after extraction and sample cleanup, has been published recently [4]. Also, confidential gas chromatographic (GC) methods developed by the manufacturer, to quantify the analyte after necessary extraction, cleanup and derivatization from some agricultural commodities and without derivatization for some formulated products are on record and will be made available, presumably, as and when the registration protocol of the material is completed [5]. Unfortunately none of these methods specifically address the analysis of MIMIC from formulation concentrates and spray mixes because of the assumption that some of the additives in them with similar chromatographic characteristics could cause interference resulting in irreproducibility of results.

We have developed a reliable and sensitive GC method to quantify MIMIC present in the formulation concentrates and spray mixes without any derivatization step for the analyte. We also examined the applicability of our HPLC method reported earlier [3] for this purpose and made a comparison of the two instrumental techniques. The response of MIMIC to three different GC detection methods, viz., flame ionization detection (FID), nitrogen–phosphorus detection (NPD) and electron-capture detection (ECD) using three different GC fused-silica capillary columns (DB-1, DB-5 and DB-17) with varying internal diameters was also examined and compared to the response of the analyte in HPLC–DAD. Our findings are reported in this paper.

2. Experimental

2.1. Chemical standards

Analytical grade MIMIC (99.6% purity, lot No. AMB 9-40B, m.p. 186–188°C) was supplied courtesy of Rohm & Haas (Philadelphia, PA, USA). A stock solution containing 25 mg/25 ml of the analyte was prepared in an amber-coloured volumetric flask using methanol as solvent and stored at 0°C in darkness to prevent potential photodegradation. The stock solution was stable for 10 weeks at these conditions and fresh samples were prepared afterwards if necessary. Working solutions were prepared by serial dilution of the stock solution in ethyl acetate for GC analysis using NPD and in acetonitrile for HPLC and GC analyses using FID and ECD. All samples were diluted to levels within the predetermined linear range of the detectors.

2.2. Formulation concentrates and spray mixes

Four formulation concentrates and nine spray mixes were used in the present study. Three of the formulation concentrates were supplied courtesy of Rohm & Haas and the fourth one was received from the scientist in charge of the Formulation Project at the Institute. The nine spray mixes used in the laboratory and field microcosm studies during 1992/93 were prepared in the laboratory using the formulation concentrates. Table 1 lists all the formulation concentrates and spray mixes studied along with the active ingredient present in each.

2.3. Reagents

Acetonitrile, dioxane, methanol and ethyl acetate were HPLC grade (Optima, Fisher Sci-

Table 1
List of formulations used in the study

Sample	Description	Formulation type	AI (%, w/v)
FC-1	RH-5992 2F (concentrate); lot No. L-0914	Emulsion	24.0
FC-2	RH-5992 2F (XF-87024); lot No. AL-1534-1	Emulsion	24.0
FC-3	RH-5992 2F (XF-93011); lot No. CDP-1293-C	Oil	24.0
FC-4	RH-5992 flowable concentrate (in the laboratory)	Emulsion	25.0
SM-1	Spray mix; 35 g AI/2 l (prepared from FC-1)	Emulsion	1.75
SM-2	Spray mix; 70 g AI/2 l (prepared from FC-1)	Emulsion	3.5
SM-3	Spray mix; 140 g AI/2 l (prepared from FC-1)	Emulsion	7.0
SM-4	Spray mix; 35 g AI/2 l (prepared from FC-2)	Emulsion	1.75
SM-5	Spray mix; 70 g AI/2 l (prepared from FC-2)	Emulsion	3.5
SM-6	Spray mix; 140 g AI/2 l (prepared from FC-2)	Emulsion	7.0
SM-7	Spray mix; 35 g AI/2 l (prepared from FC-3)	Emulsion–suspension	1.75
SM-8	Spray mix; 70 g AI/2 l (prepared from FC-3)	Emulsion–suspension	3.5
SM-9	Spray mix; 140 g AI/2 l (prepared from FC-3)	Emulsion–suspension	7.0

AI = Active ingredient.

entific) filtered through a Nylaflo nylon membrane filter, 0.2 μm pore size (No. 66602, Gelman Sciences). Water was deionized, glass-distilled by a Mega-Pure System (Model No. MP-6A, Corning) and filtered as above.

2.4. Apparatus

The HPLC system used in the study was a Hewlett-Packard (HP) (Analytical Division, Palo Alto, CA, USA) Model 1090M incorporating an HP diode-array detector (λ range 190 to 600 nm); an HP 9000 Series 300 (Model 310) computer work station (HP 79995R Series M operating software, Rev. 3.21); an automatic sampler; and a variable-volume auto-injector fitted with a 250-μl syringe. The instrument also had a binary solvent-delivery system with a helium-purge degassing system and two dual-syringe metering pumps that gave stable and reproducible flows. The instrument parameters used for the analysis of environmental substrates [3] were nearly the same for this study. The analytical column was a LiChrosorb RP-8, 10 μm, 200 × 4.6 mm I.D. (No. 79915MO-174, HP) which was preceded by a MOS-Hypersil (C_8), 5 μm, 20 × 4.0 mm I.D. guard column (No. 79916KT-121, HP). The mobile phase composition consisted of 50% water and 50% acetonitrile–dioxane (4:1, v/v) with a flow-rate of 0.8 ml/min maintained at an oven temperature of 40°C. The sample DAD wavelength was 236 ± 4 nm with a reference λ of 430 ± 50 nm. The auto-injector volume was set at 40 μl.

Two HP Model 5890A gas chromatographs, one fitted with FID and NPD systems, and the other fitted with an ECD system, were used in the study. Both gas chromatographs accommodated an HP 7673A autosampler and an HP 3392A computerized integrator for area and height measurements of the peaks. The fused-silica capillary columns tested in this study were (1) DB-1 (dimethylpolysiloxane), 15 m × 0.53 mm I.D. with 1.5 μm film thickness (d_f) (No. J1251012); (2) DB-5 [(5% phenyl)-methylpolysiloxane], 15 m × 0.25 mm I.D. with d_f 0.25 μm (No. J1225012); and (3) DB-17 [(50% phenyl)-methylpolysiloxane], 15 m × 0.53 mm I.D. with d_f 1.0 μm (No. J1251712), all from Chromatographic Specialties. A 1 m × 0.53 mm I.D. deactivated guard column (No. J1602535, Chromatographic Specialties) was joined to each column with a glass capillary column connector. Helium was used as the carrier gas throughout the study. Air and hydrogen were used as the detector gases, with helium make-up in the FID and NPD systems. We used 5% methane in argon as the make-up gas in the ECD system. The injection volume was 2 μl in the splitless mode of operation. The different gas flow-rates

and temperatures used form part of the discussion and are therefore listed in the Results and discussion section.

2.5. Sample preparation

To evaluate the analytical method using HPLC and GC, the formulation concentrates and spray mixes were agitated in a Magni Whirl mechanical shaker (Blue M Electric Company) at room temperature for 2 h at 200 excitations/min. From each sample, 100 μl, in triplicate, were pipetted into 100-ml volumetric flasks and diluted to the mark using acetonitrile (HPLC grade). After thorough mixing, 1.0 ml of each spray mix dilution and 100 μl of each formulation concentrate solution were further diluted to 10 ml in separate volumetric flasks. Depending on the concentration, some of the additives present in the formulation concentrates and spray mixes coagulated and precipitated when diluted with acetonitrile. This did not adversely affect either the solubility or the content of the active ingredient. A 1-ml volume of the diluted sample was then passed through an Acrodisc 3CR PTFE 0.45-μm filter (No. 4472, Gelman Sciences) and directly analyzed by HPLC or GC without any solvent partition or column cleanup. The injection volumes varied according to the technique and detector used. At least three replicate injections were made of each analyzed sample.

2.6. Calculations

The percentage (w/v) of MIMIC in a formulation concentrate or spray mix was determined by the expression

$$\text{MIMIC}\,(\%) = (A_{\text{sam.}}/A_{\text{std.}}) \cdot (C_{\text{std.}}/V_{\text{sam.}}) \cdot F \over 100\%$$

where $A_{\text{sam.}}$ is the mean peak area of three successive injections of the sample, $A_{\text{std.}}$ is the mean peak area of the standard injected immediately prior to and after the sample injections, $C_{\text{std.}}$ is the concentration of the standard in μg/ml, $V_{\text{sam.}}$ is the volume (μl) of formulation concentrate or spray mix taken for analysis and F is the dilution factor (μl · ml/μg) ($F = 10$ for formulation concentrates; $F = 1$ for spray mixes).

3. Results and discussion

3.1. HPLC–DAD

The chromatography performance (repeatability and linearity) for the insecticide on the RP-8 column (10 μm, 200 × 4.6 mm I.D.) was optimized by multiple injections of the standard solutions at varying concentrations. Under the optimum HPLC parameters listed earlier under Apparatus, the DAD response to MIMIC was linear over the concentration range of 2 to > 1000 ng in the 40-μl injection volume with a retention time (t_R) of 18.2 min. A linear regression of the data points (amounts injected and corresponding area counts) throughout the range gave a correlation coefficient of 1.000. The regression equation data are presented in Table 2.

Quantification of the formulation concentrates and spray mixes was based upon the peak areas obtained from triplicate injections of each sample and comparing them with the peak areas obtained for the appropriate external standards injected immediately prior to and after the sample. The results of the analysis for MIMIC content in thirteen samples by HPLC are given in Table 3. The values of active ingredient obtained by measurement agreed with the expected value for each sample (absolute error ranged from 0.6 to 6.4%) and the deviation was minimal [relative standard deviation (R.S.D.) ranged from 0.1 to 4.1%]. A typical HPLC chromatogram is illustrated in Fig. 1a. Although the resolution of the analyte was satisfactory, the retention time was longer than noted with GC methods discussed below. The method detection limit (MDL) for a 99% confidence level was determined as thrice the standard deviation (σ) using repeated measurements of low-level standards [6]. Usually, the MDL is determined from the variability of repeated blank measurements but since no response was observed for any

Table 2
Linear regression analysis of MIMIC calibration standards for different detectors using the regression equation: $y = b + mx$ [where y is the detector response, b is the intercept, m is the slope and x is the amount (ng) of MIMIC injected]

Detector	Intercept (V s)	Slope	r^2	Linear range (ng)		MDL (ng)
				Lower limit	Upper limit[a]	
HPLC–DAD	0.611[b]	2.02322	1.000	2	>1000	0.8
GC–FID	−0.00090	0.00582	0.999	0.10	>50	0.04
GC–NPD	−0.00115	0.00506	0.999	0.50	>50	0.10
GC–ECD[c]	0.02264	0.39035	1.000	0.05	40	0.02
GC–ECD[d]	0.01759	0.29211	1.000	0.05	40	0.02

[a] The upper limit was only tested to the reported values and may be much higher where indicated.
[b] The units for the DAD response are mAU s.
[c] GC conditions were similar to those used for FID and NPD (see text).
[d] Performed under final optimized GC conditions (see text).

blank injection, a low-level standard (less than 10 times the MDL) was used. The MDL for the analyte at the lower limit of concentration was found to be 0.8 ng for the detector.

3.2. GC–FID

The GC part of the study was initiated first by using FID. A 1 m × 0.53 mm I.D. deactivated

Table 3
Comparison of results obtained by HPLC–DAD, GC–FID and GC–ECD analysis

Sample	Active ingredient (%, w/v)									
	Theoretical	HPLC–DAD			GC–FID			GC–ECD		
		Mean ± S.D.	R.S.D. (%)	Error[a] (%)	Mean ± S.D.	R.S.D. (%)	Error (%)	Mean ± S.D.	R.S.D. (%)	Error (%)
FC-1	24.0	24.3 ± 1.0	4.1	1.2	24.1 ± 0.3	1.2	0.4	23.3 ± 0.1	0.4	2.9
FC-2	24.0	22.9 ± 0.1	0.4	4.6	21.2 ± 0.2	0.9	11.7	21.6 ± 0.4	1.9	10.0
FC-3	24.0	23.8 ± 0.1	0.4	0.8	23.3 ± 0.3	1.3	2.9	24.3 ± 0.1	0.4	1.2
FC-4	25.0	23.8 ± 0.9	3.8	4.8	22.6 ± 0.5	2.2	9.6	23.1 ± 0.4	1.7	7.6
SM-1	1.75	1.81 ± 0.01	0.6	3.4	1.67 ± 0.04	2.4	4.6	1.71 ± 0.02	1.2	2.3
SM-2	3.50	3.43 ± 0.01	0.3	2.0	3.42 ± 0.05	1.5	2.3	3.42 ± 0.04	1.2	2.3
SM-3	7.00	6.77 ± 0.01	0.1	3.3	6.94 ± 0.04	0.6	0.9	6.82 ± 0.07	1.0	2.6
SM-4	1.75	1.65 ± 0.01	0.6	5.7	1.63 ± 0.01	0.6	6.9	1.53 ± 0.08	5.2	12.6
SM-5	3.50	3.30 ± 0.02	0.6	5.7	3.23 ± 0.11	3.4	7.7	3.26 ± 0.10	3.1	6.9
SM-6	7.00	6.55 ± 0.04	0.6	6.4	6.85 ± 0.13	1.9	2.1	6.71 ± 0.14	2.1	4.1
SM-7	1.75	1.72 ± 0.01	0.6	1.7	1.70 ± 0.05	2.9	2.9	1.62 ± 0.03	1.9	7.4
SM-8	3.50	3.52 ± 0.01	0.3	0.6	3.48 ± 0.08	2.3	0.6	3.46 ± 0.05	1.4	1.1
SM-9	7.00	7.10 ± 0.03	0.4	1.4	7.23 ± 0.31	4.3	3.3	7.20 ± 0.18	2.5	2.9
Average			1.0	3.2		2.0	4.3		1.8	4.9

[a] This value represents the absolute error which can be defined as the deviation of the calculated result from the theoretical value in absolute terms of percentage.

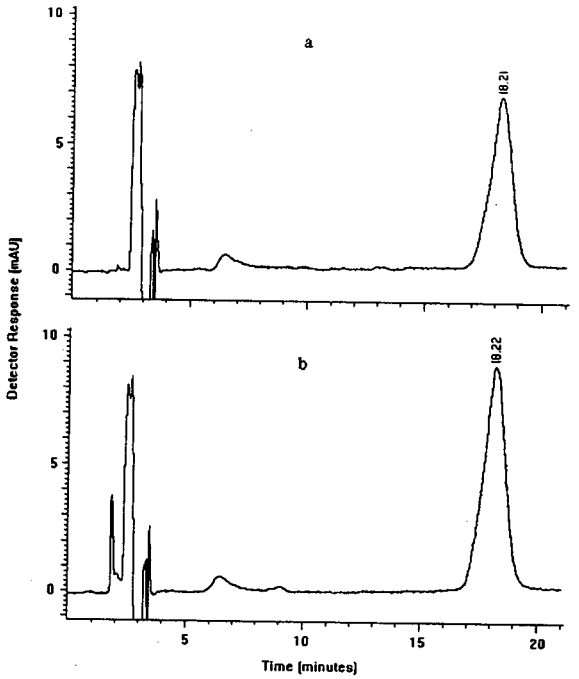

Fig. 1. Typical HPLC chromatograms of MIMIC (see text for HPLC parameters used). (a) DAD response to 5.0 μg/ml standard. (b) DAD response to representative MIMIC formulation.

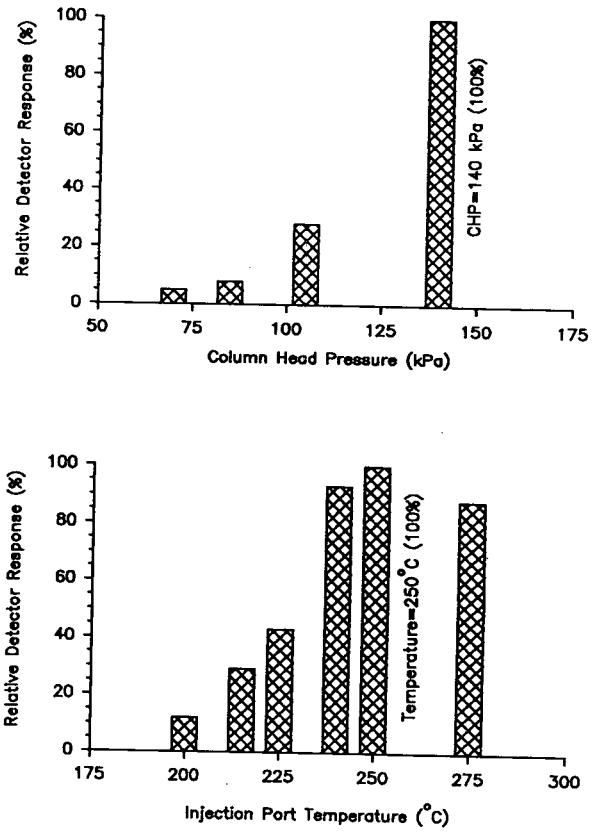

Fig. 2. Effects of (a) column head pressure and (b) injection port temperature on GC–FID response to MIMIC.

guard column was connected to the DB-5, 15 m × 0.25 mm I.D. fused-silica capillary column with a glass capillary column connector, installed and conditioned prior to attachment to the FID system. Subsequently, trials were carried out to get good detector response to the injected analyte by methodically selecting the appropriate GC parameters. Repeated injections of the standard significantly enhanced and stabilized the detector response producing a distinctive peak with area proportional to the concentration of the analyte. In addition to flow-rates of gases (detector), the column head pressure (CHP) and injection port temperature were optimized because they had significant effect on the sensitivity of FID to MIMIC. Fig. 2 shows the enormous variability in detector response to CHP and injection port temperatures.

The chromatographic performance for the detection of MIMIC was fine tuned and the suitable parameters established were: *Gases*: carrier (helium) CHP, 140 kPa (linear velocity, 55 cm/s); inlet purge flow, 60 ml/min (purge on at 0.5 min); septum purge flow, 3 ml/min; hydrogen (detector), 35 ml/min; air, 270 ml/min; make-up (helium), 30 ml/min. *Temperatures*: splitless injection port, 250°C; detector, 260°C. *Oven programme*: initial 60°C at 0.75 min; ramp rate A 40°/min; final A 210°C at 5 min; ramp rate B 10°/min; final B 240°C at 3.5 min. Using these operating conditions, peak area variations with similar concentrations of the analyte or the test sample was found to be less than 1%.

Under the above operating parameters, the t_R for the analyte was 12.5 min. The peak was sharp and well resolved with no chromatographic interference in the vicinity of the t_R of MIMIC. A typical chromatogram for MIMIC by FID is

presented in Fig. 3a. The detector response to MIMIC was found to be linear in the range 0.10 to >50 ng ($r^2 = 0.999$) in the 2-μl injection volume as shown in Table 2 and Fig. 4. The MDL of MIMIC using the FID was determined as 0.04 ng in the 2-μl injection volume. The analyte concentrations in the formulation concentrates and spray mixes obtained by the GC–FID using the DB-5 column are given in Table 3. The R.S.D. by this method ranged from 0.6 to 4.3% while the absolute error of the measurements varied from 0.4 to 11.7%. Fig. 3b illustrates a typical chromatogram obtained from the analysis of a MIMIC formulation.

Two chromatographic mega-bore columns, namely DB-1 and DB-17 were also tried to quantify the analyte in the formulation concentrates and spray mixes under similar operating parameters used for DB-5. Detector response and peak shape were inferior on these columns in comparison to the mini-bore DB-5 column.

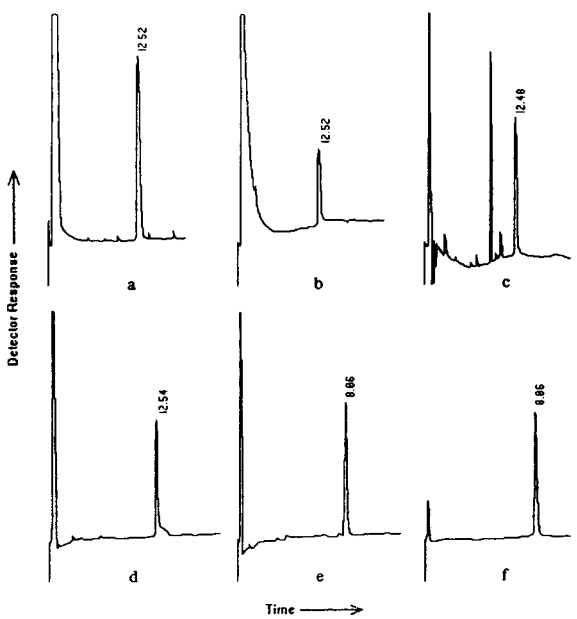

Fig. 3. Typical GC chromatograms of MIMIC (see text for various GC conditions used). (a) FID response to 25 μg/ml standard (integrator attenuation 2^5). (b) FID response to representative MIMIC formulation (attenuation 2^3). (c) NPD response to 25 μg/ml standard (attenuation 2^5). (d) ECD response to 1.0 μg/ml standard at GC conditions similar to FID and NPD (attenuation 2^7). (e) ECD response to 1.0 μg/ml standard at optimized conditions (attenuation 2^8). (f) ECD response to representative MIMIC formulation (attenuation 2^{11}). Numbers at peaks indicate retention times in min.

3.3. GC–NPD

To investigate the response of NPD to MIMIC, the DB-5 column used above was reconditioned and attached to the detector. After achieving required stabilization, the detector response was optimized (as discussed for FID) using the following parameters: *Gases*: carrier (helium) CHP, 140 kPa (linear velocity 55 cm/s); inlet purge flow, 60 ml/min (purge on at 0.5 min); septum purge flow, 3 ml/min; hydrogen (detector), 4 ml/min; air, 100 ml/min; make-up (helium), 35 ml/min. *Temperatures*: splitless injection port, 250°C; detector, 260°C. *Oven programme*: same as for GC–FID.

The NPD sensitivity was slightly lower than the FID one. Usually, the NPD provides greater sensitivity for nitrogen-containing compounds, however this was not observed in this particular study: further investigation is necessary. The NPD response was linear over the range of 0.50 to >50 ng ($r^2 = 0.999$) injected (Table 2, Fig. 4) versus 0.10 to >50 ng in FID with a MDL of 0.10 ng compared to the value of 0.04 ng in the FID. One major drawback of NPD was that column temperature had a significant effect on the sensitivity of the detector. Due to the temperature gradient, the baseline rose dramatically, therefore column compensation was done by subtracting the signal from a blank run from the signal of the sample run. However, even with column compensation, considerable baseline instability was observed at lower concentration levels especially when the attenuation was decreased. This hampered quantification of the analyte at low concentration levels compared to FID (see Table 2). A typical chromatogram for the NPD response of MIMIC is shown in Fig. 3c. The impurity peaks in the vicinity of the analyte peak did not in any way influence its resolution. These extraneous peaks, on further investigation, were due to the contaminations found in the septa of the injection vials. Replacement of

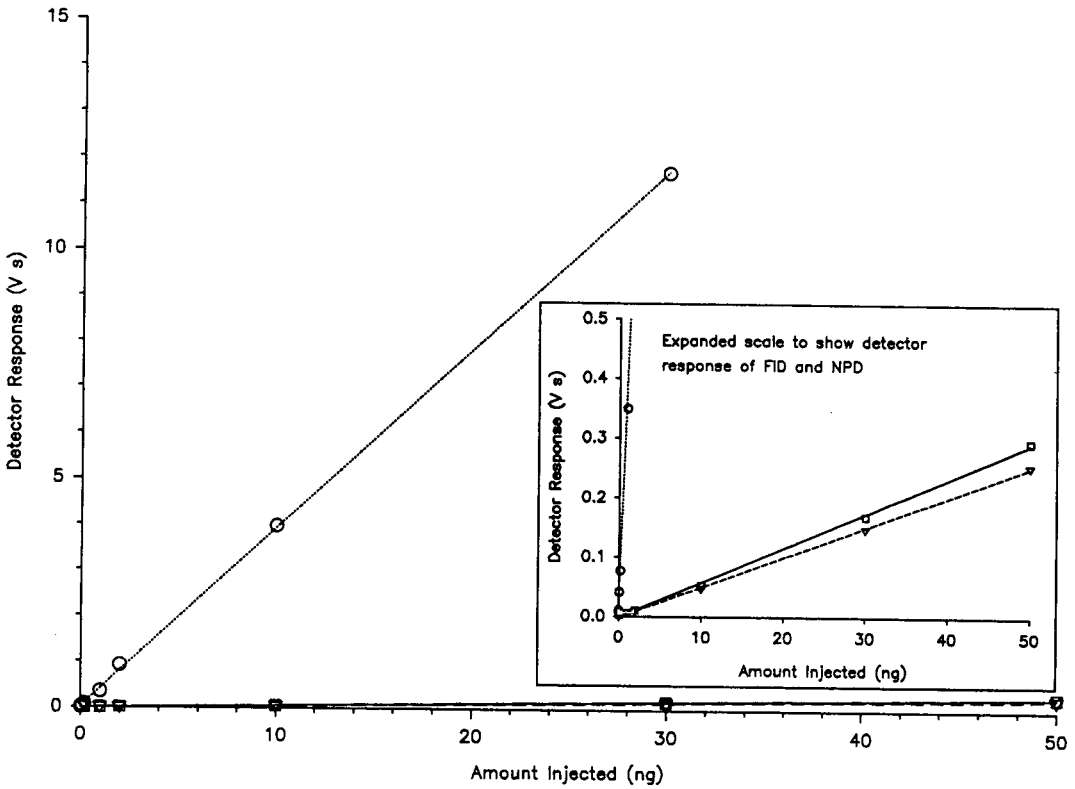

Fig. 4. A comparison of FID, NPD and ECD responses to MIMIC under identical GC conditions. ○ = ECD (V s = 0.02264 + 0.39035 ng, $r^2 = 1.000$); □ = FID (V s = − 0.00090 + 0.00582 ng, $r^2 = 0.999$); ▽ = NPD (V s = − 0.00115 + 0.00506 ng, $r^2 = 0.999$).

the septa, HP part 5181-1210, used to seal the injection vials with PTFE-lined (both sides) silicone septa (HP part 5181-1211), eliminated the appearance of these ghost peaks. A higher MDL (0.10 ng) coupled with a narrower linear range (0.5 to > 50 ng) compared to FID, made NPD a less favourable choice for quantification of MIMIC. Because of these inherent problems, further attempts to quantify the analyte from formulation concentrates and spray mixes were not attempted. However, if other GC conditions are studied, evaluated and eventually optimized, NPD could very likely be useful to analyze the MIMIC present in these materials.

Attempts to chromatograph MIMIC using the DB-1 and DB-17 mega-bore columns were unsatisfactory due to massive baseline instability in addition to poor resolution (broad, tailing peaks) and non-reproducible retention times. Compared to FID, the performance of NPD was less than satisfactory in the analysis of MIMIC.

3.4. GC–ECD

To study the response of GC–ECD to MIMIC using the DB-5 column, the temperature conditions of the oven were initially set the same as in GC–FID and the other operating parameters were optimized as follows: *Gases*: carrier (helium) CHP, 140 kPa (linear velocity 55 cm/s); inlet purge flow, 60 ml/min (purge on at 0.5 min); septum purge flow, 3 ml/min; detector make-up (5% methane in argon), 80 ml/min. *Temperatures*: splitless injection port, 250°C; detector, 310°C. *Oven programme*: as for GC–FID.

Generally, the ECD response to MIMIC was nearly 60 to 70 times higher than that observed for FID and NPD. The linear range of ECD was found to be 0.05 to 40 ng ($r^2 = 1.000$) of MIMIC injected (Table 2, Fig. 4) with a MDL of 0.02 ng. ECD gave a narrower linearity range due to the marked increase in sensitivity, and the MDL observed (0.02 ng) was lower than with FID (0.04 ng) and NPD (0.10 ng). Due to the increase in sensitivity at these conditions, some peak tailing was observed for MIMIC which was not present in chromatograms obtained by FID and NPD (Fig. 3a and c). Fig. 3d illustrates the tailing effects of the above conditions on the peak shape of MIMIC at the increased sensitivity by ECD. The cause of the peak tailing, symptomatic of asymmetric elution, was probably due to the final column temperature being too low since MIMIC is relatively non-volatile. An alternative oven temperature program introduced as follows: initial 60°C at 0.75 min; ramp rate 30°/min; final 280°C at 2 min.; eliminated the distortion resulting in a more symmetrical peak shape for the analyte. The retention time of MIMIC using these improved parameters was 8.0 min while the linear range, r^2 and MDL were not noticeably affected (Table 2). Fig. 3e shows the sharp, symmetrical peak obtained for the analyte using ECD. In Table 3 are shown the results of analysis of formulation concentrates and spray mixes of MIMIC. The R.S.D. values ranged from 0.4 to 5.2% and the absolute error of the measurements varied from 1.2 to 12.6% illustrating the smallest variance between the HPLC–DAD, GC–FID and GC–ECD methods.

The DB-1 mega-bore column (15 × 0.53 mm I.D.) was tested with ECD under the same GC conditions except that the carrier flow (helium) was maintained at 15 ml/min and the make-up gas flow was reduced to 65 ml/min. The results obtained from injections of the MIMIC standard were very comparable to those of the mini-bore DB-5 column under similar GC conditions. At a flow-rate of 15 ml/min, the retention time and peak areas obtained were nearly identical to the earlier observations. One major drawback to this mega-bore column was that the increase in carrier flow through the ECD system caused a rising baseline during temperature programming as observed with NPD.

The DB-17 mega-bore column (15 × 0.53 mm I.D.) was similarly tested but did not yield satisfactory results due to baseline drift and tailing peaks. Under identical conditions as for the DB-1 mega-bore column, the retention time of the analyte increased to 19.0 min giving a broad peak with appreciable reduction in sensitivity.

3.5. GC formulation analysis

Typical chromatograms obtained from injections of the formulations by HPLC–DAD, GC–FID and GC–ECD using the DB-5 column are shown in Figs. 1b, 3b and 3f, respectively. No interfering peaks were observed by either HPLC or GC analysis. The results obtained by these methods, as mentioned earlier, are quite similar and are given in Table 3. The results indicate that any method is equally suitable for the analysis of MIMIC in various types of formulations, whether they are oil or aqueous based. Overall, the HPLC method gave the lowest R.S.D. and absolute error values as compared to the GC methods. However, this difference was not at all significant. The methods provide a direct, time- and laboratory-saving approach to the analysis of MIMIC formulation concentrates and spray mixes. However, GC analysis using ECD with the mini-bore DB-5 column may be preferred because of its higher sensitivity than the other methods and the lower retention time for the analyte and less solvent consumption as compared to HPLC.

4. Conclusions

The results of this study show that the active ingredient MIMIC in various formulation concentrates and spray mixes can be easily analyzed by HPLC–DAD, GC–FID or GC–ECD techniques. The extraction requires no cleanup and the chromatograms are free from any extraneous peaks. The methods are rapid, precise and sensitive with excellent chromatographic resolu-

tion. The total chromatographic analysis and the total analysis time on average for the HPLC and GC methods were respectively 30 and 15 min and 4 and 2.5 h/sample. The mini-bore DB-5 fused-silica capillary column gave good separation and acceptable analysis time compared to the mega-bore columns. Current studies also show that GC–ECD methods have considerable potential to analyze the residues of MIMIC in forestry substrates such as conifer foliage, forest soils, natural water etc. at sub-μg to pg levels.

Acknowledgements

The authors acknowledge with thanks Dr. A. Sundaram and Mr. J. Leung of the Forest Pest Management Institute for providing the spray mixes and Dr. C. Patel and Dr. D.R. Hawkins of Rohm & Haas Company for supplying respectively the formulation concentrates and analytical-grade MIMIC used in this study.

References

[1] Rohm & Haas, *US Pat.*, 4 985 461 (1991).
[2] S.S. Hurt, *Bulletin on RH-5992 Toxicology*, Rohm & Haas, Philadelphia, PA, 1990, p. 2.
[3] B.L. Cadogan, A. Retnakaran, N. Payne, J. Meating, R. Scharbach, R. Wilson and W. Tomkins, *Forest Pest Control Forum Report*, Natural Resources Canada–Canadian Forest Service, Ottawa, ON, 1993, p. 322.
[4] K.M.S. Sundaram, J. Zhu and R. Nott, *J. AOAC Int.*, 76 (1993) 668.
[5] Personal communication, Rohm & Haas, Spring House, PA, 1993.
[6] L.H. Keith, *Environmental Sampling and Analysis: A Practical Guide*. Lewis Publ., Chelsea, MI, 1991, Ch. 10, p. 93.

ELSEVIER

Journal of Chromatography A, 687 (1994) 333–341

JOURNAL OF CHROMATOGRAPHY A

Combined liquid–liquid electroextraction and isotachophoresis as a fast on-line focusing step in capillary electrophoresis

E. van der Vlis, M. Mazereeuw, U.R. Tjaden*, H. Irth, J. van der Greef

Division of Analytical Chemistry, Center for Bio-Pharmaceutical Sciences, Leiden/Amsterdam Center for Drug Research, Leiden University, P.O. Box 9502, 2300 RA Leiden, Netherlands

First received 28 June 1994; revised manuscript received 22 July 1994

Abstract

Combined liquid–liquid electroextraction and isotachophoresis as a fast on-line focusing step in capillary electrophoresis is described. Owing to the limited conductivity of the organic phase, high electric field strengths can be applied, resulting in high migration rates. Liquid–liquid electroextraction is used to focus the analyte ions from a large organic sample into a small volume in the terminating buffer zone, just above the liquid–liquid interface. Simultaneously, isotachophoresis is used to focus the analyte ions between the terminating buffer and the leading buffer. A steady state is reached within a few minutes, as isotachophoresis starts with a small sample volume. On-line capillary zone electrophoresis is used for the separation of the analytes. Propantheline, neostigmine, salbutamol and terbutaline were used as model compounds, and crystal violet was used to visualize the process for tuning the system. Concentration detection limits of pure solutions down to 10^{-9}–10^{-10} mol/l for the model compounds were obtained using simple UV absorbance detection.

1. Introduction

Capillary zone electrophoresis (CZE) is a strong separation technique owing to its high efficiency, short analysis times and ease of operation. However, injection volumes in the low nanolitre range combined with a short optical path length (10–100 μm) make CZE a challenging field to be explored. Different attempts have been made to enhance the sensitivity in CZE by improving detection techniques and employing sample pretreatment prior to the CZE separation [1].

A favourable technique for on-line sample enrichment is isotachophoresis (ITP) [2–10]. The focusing time in ITP depends mainly on the concentration of constituents and related the electric field strength, the mobility of the analyte and the migration path length. Focusing times of more than 1 h are reported for very large sample volumes [11,12]. In such cases, the sample throughput is determined by the time required for sample handling, rather than the CZE run time. Therefore, long focusing times for large sample volumes still limit the applicability of ITP in bioanalysis.

Since the beginning of this century it has been known that by applying an electric field over the two phases in a liquid–liquid extraction system, the extraction rate of ionic analytes is increased [13]. Primarily this principle was used as a tool in chemical engineering for the enhancement of

* Corresponding author.

0021-9673/94/$07.00
SSDI 0021-9673(94)00776-4

mass transfer through the liquid–liquid interface [14–19]. This so-called electroextraction (EE) permits the rapid extraction of charged compounds from large volumes of organic solvents (up to several millilitres) owing to the extremely high local electric field strength. Further, high recoveries are obtained when exhaustive EE is considered. As the whole procedure is performed in a single capillary, the method can easily be automated.

EE is a sample enrichment technique that permits the rapid extraction of analytes from a large volume of organic solvent into a small buffer volume, just above the interface. On-line ITP is used to focus the analyte ions between the terminating buffer and the leading buffer. As EE yields a very small buffer volume containing the analyte ions, only a few minutes of ITP are needed to reach a steady state. Finally, on-line CZE is used for the separation of the analytes. In this paper, qualitative and quantitative aspects of the EE–ITP–CZE method are presented and discussed.

2. Experimental

2.1. Chemicals

All chemicals used were of analytical-reagent grade. All aqueous solutions were prepared using water purified with a Milli-Q system (Millipore, Bedford, MA, USA). Triethylamine, ethyl acetate (EtAc), potassium hydroxide and acetic acid were obtained from Merck (Darmstadt, Germany), methanol from Biosolve (Barneveld, Netherlands), β-alanine from Aldrich (Steinheim, Germany), crystal violet (CV) from Janssen Chimica (Beerse, Belgium), and terbutaline, neostigmine (N) and propantheline (P) from Sigma (St. Louis, MO, USA). Salbutamol was kindly donated by TNO Zeist (Netherlands).

The leading buffer consisted of 50 mmol/l triethylamine solution adjusted to pH 5 with acetic acid–methanol (20:80, v/v). The terminating buffer consisted of 10 mmol/l β-alanine solution adjusted to pH 5 with acetic acid–methanol (95:5, v/v). Standard solutions of the cationic species were made in so-called saturated EtAc. For this purpose, 10 mmol/l β-alanine solution, adjusted to pH 5 with acetic acid, was extracted with EtAc. Standard solutions of the model compounds at a concentration of 10^{-2} mol/l were prepared in methanol–water (50:50, v/v). Methanol was used for further dilution of the standard solutions to a concentration of 10^{-4} mol/l. Finally, saturated EtAc was used for further dilution of the methanol solutions obtained.

2.2. Apparatus

Fig. 1 is a schematic representation of the experimental set-up described hereafter. A programmable injection system for CE (PRINCE; Lauerlabs, Emmen, Netherlands) with the possibility of pressurized and/or electrokinetic injection was used for injection and control of the procedure. The current was registered in the low-μA range. EE–ITP–CZE took place in an untreated 100-μm fused-silica capillary (SGE, Ringwood, Victoria, Australia) with a total length of 90 cm. At 70 cm from the capillary inlet a detection window was obtained by burning off the polyimide coating. On-capillary UV absorbance detection was performed at 200 nm, using a Spectra 100 UV–Vis absorbance detector (Spectra-Physics, Mount View, CA, USA). The signal was digitized using a laboratory-made 12-bit A/D converter operating at a sampling frequency of 20 Hz. The A/D converter was connected to a computer (Mega ST4; Atari,

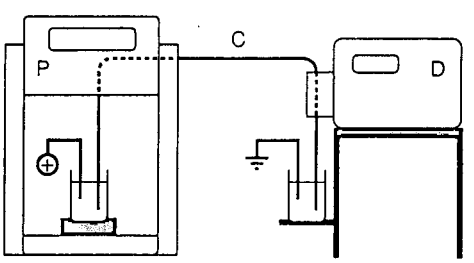

Fig. 1. Schematic representation of the EE–ITP–CZE set-up, consisting of a programmable injector (P), a 100-μm I.D. untreated fused-silica capillary (C) and a UV–Vis absorbance detector (D).

Sunnyvale, CA, USA) controlling the sampling frequency, collecting the data and handling the data using laboratory-written software.

2.3. EE–ITP–CZE procedure

Fig. 2 shows the different stages of the procedure and the positioning of the capillary and the electrode. The capillary is conditioned for 10 min daily with water, aqueous potassium hydroxide (0.25 mol/l), water and leading buffer. The 300-μl sample vials were made of glass. Platinum rod electrodes were used for both the anode and the cathode.

Step 1

A terminating buffer zone of approximately 15 mm is introduced hydrodynamically at 30 mbar for 18 s.

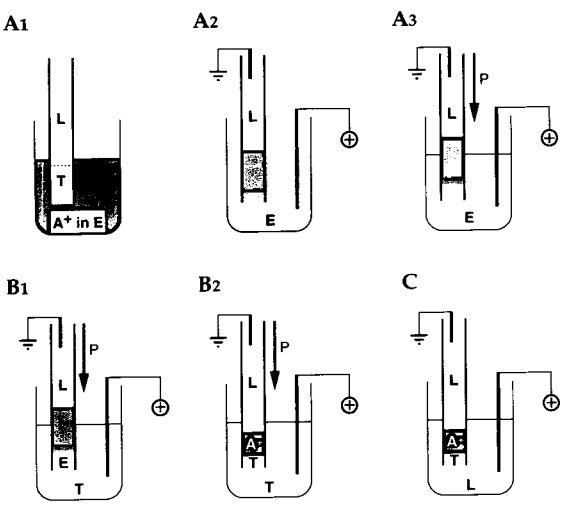

Fig. 2. Stepwise representation of the EE–ITP–CZE procedure. (A_1) The capillary, filled with leading buffer (L) and terminating buffer (T), is placed in the ethyl acetate (E) sample solution containing the cationic analyte molecules (A^+); (A_2) electroextraction (EE) is performed by applying a voltage; (A_3) during EE, using a pressure-induced counterflow (P) in the direction of the arrow, the sample solution is exhausted; (B_1) the analytes are focused by means of pressure-induced counterflow ITP, after the capillary is placed in the terminating buffer vial; (B_2) during ITP the remaining EtAc plug is pushed out of the capillary, while reaching the steady-state; (C) the capillary is placed in the leading buffer vial and CZE starts.

Step 2

The capillary inlet is placed in the sample vial containing the EtAc sample solution (A1). EE is started by applying a voltage of +10 kV for 1 min (A2), followed by an additional 9 min at +10 kV in combination with a 30-mbar pressure-induced counterflow to prevent more EtAc from entering the capillary (A3). The analyte molecules start to migrate through the interface between the organic phase and the buffer system and continue to migrate through the terminating buffer zone. Simultaneously, the analytes are focused between the terminating buffer and leading buffer.

Step 3

Next, the capillary inlet is placed in the terminating buffer vial. By applying a voltage of +15 kV for 1 min without applying a counterflow, the analytes that are still present in the terminating buffer zone are accelerated in the direction of the leading buffer, away from the interface between EtAc and the buffer system.

Step 4

ITP continues at +10 kV for 6 s. A 60-mbar pressure-induced counterflow is used to push the EtAc plug still present in the capillary towards the capillary outlet (B1).

Step 5

Until the current reaches 1.1 μA, ITP proceeds at +4 kV combined with a 40-mbar pressure-induced counterflow. This step usually takes less than 1 min (B2).

Step 6

CZE is started and performed in leading buffer [20] by applying a voltage of +30 kV (C).

3. Results and discussion

The anodic end of the separation capillary filled with leading buffer and a small plug of terminating buffer is placed in the organic sample solution (Fig. 2). By applying an electric field over the organic solvent and the buffer system a

mass transfer is induced. Analyte molecules of the same charge sign migrate from the organic solvent into the terminating buffer, in the direction of the oppositely charged electrode. On arrival in the terminating buffer zone, the analyte molecules continue to migrate towards the leading buffer. Thus, ITP is performed simultaneously and in conjunction with EE. Finally, the analyte molecules are focused between the terminating buffer and the leading buffer. While maintaining the steady state, the organic solvent that entered the capillary during EE is removed by using a pressure-induced counterflow. CZE is performed subsequently.

3.1. Theoretical aspects and optimization of electroextraction

Pure EtAc cannot conduct electric current and can therefore be regarded as an insulator. The conductivity of pure EtAc can be increased by saturation with an aqueous carrier electrolyte solution. As a consequence of the application of an electric field, transport of charge via the migration of ions originating from the aqueous phase takes place. The relationship between mass transfer and the electric current for an ionic species i is given by [21]

$$J_i = \frac{I_i}{Fz_i} = E\mu_i c_i S \quad (1)$$

where J_i is the ion flux across a capillary with cross section S, F the Faraday constant, z_i the ion charge, I_i the contribution of each type of ionic compound to the total current, E the electric field strength, μ_i the ion mobility and c_i the ion concentration; the subscript i refers to any ion in solution. The total current (I_{tot}) is the sum of the contributions of all ionic compounds:

$$I_{tot} = \sum_i I_i \quad (2)$$

The relationship between the current and the transfer of ions through an interface with cross-section S can be described as [21]

$$I = SFE \sum_i z_i \mu_i c_i \quad (3)$$

At low analyte concentrations, e.g., 10^{-8}–10^{-9} mol/l, no current was measured with the available equipment. Therefore, EtAc was saturated with a 10 mmol/l solution of β-alanine (pH 5), which acts as carrier electrolyte in order to conduct the current. This resulted in a significant increase in the amount of analyte extracted and an improvement in the overall reproducibility. Experiments in which β-alanine was replaced with crystal violet showed similar results with respect to analyte extraction recovery and reproducibility.

Compared with the buffer system, EtAc itself hardly induces a ζ potential and related to this hardly any electroosmotic flow (EOF). As a result of the EOF induced by the buffer system, EtAc is dragged into the capillary during EE. A counterflow is used during EE (step 3) to counterbalance the EOF in order to prevent further entry of EtAc into the capillary. To maintain a stable interface during the EE, a short EtAc zone should be present in the capillary inlet. However, when the EOF predominates over the counterflow, EtAc continues to enter the capillary. As the applied voltage (V) is constant, the electric current decreases gradually according to Ohm's law. The resistance of each zone is given by

$$R_{zone} = \frac{L_{zone}}{\pi r^2 \kappa_{zone}} \quad (4)$$

where L_{zone} is the zone length, r is the radius of the capillary and κ_{zone} is the specific conductivity in the zone. The total resistance over the three zones in the capillary with a constant radius is given by

$$R_{tot} = \left(\frac{L_E}{\kappa_E} + \frac{L_{TB}}{\kappa_{TB}} + \frac{L_{LB}}{\kappa_{LB}}\right)\frac{1}{\pi r^2} \quad (5)$$

Combining Eq. 5 with Ohm's law results in

$$I = \frac{\pi r^2 V \kappa_E \kappa_{TB} \kappa_{LB}}{\kappa_{TB}\kappa_{LB}L_E + \kappa_E\kappa_{LB}a + \kappa_E\kappa_{TB}[(1-a) - L_E]} \quad (6)$$

where L_E, L_{TB} and L_{LB} are the lengths of the EtAc zone, the terminating buffer zone and the leading buffer zone, respectively, and κ_E, κ_{TB}

and κ_{LB} are the specific conductivities of the EtAc zone, the terminating buffer zone and the leading buffer zone, respectively. In Eq. 6, L_{TB} is replaced by a, which equals 0.02 as the terminating buffer zone length is approximately 2% of the total capillary length (Section 2.3, step 1). The current, i.e., mass transfer, and the length of the organic solvent zone are related according to Eq. 6. Fig. 3 is a graphical representation of Eq. 6, each theoretical curve (A–E) representing a different specific conductivity of the organic solvent in relation to the ITP buffer system. An increase in the organic solvent zone length results in a decrease in the current. Fig. 3E is based on measured relative conductivity data. The relative conductivities for saturated EtAc, terminating buffer and leading buffer are 1, 1040 and 8640, respectively. A large difference in specific conductivity between the organic solvent and the terminating buffer strongly decreases the slope of the curve at short organic solvent zone lengths. Therefore, mass transfer is closely determined by the applied pressure-induced counterflow. As small differences in the organic solvent zone length affect the current dramatically, the mass transfer and the related reproducibility are influenced accordingly.

Fig. 4 shows the relationship between the pressure-induced counterflow and the peak area

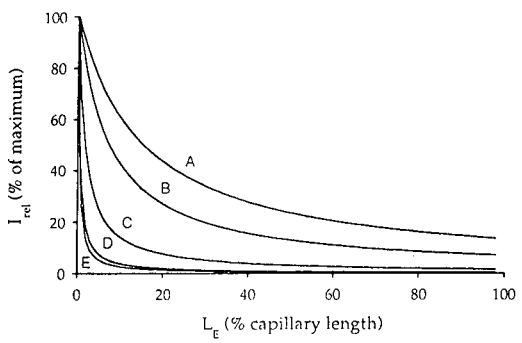

Fig. 3. Relationship between the current (I_{rel}) and the organic solvent zone length (L_E) during EE. The relative specific conductivities for the organic solvent zone, the terminating buffer zone and the leading buffer zone are as follows (κ_E, κ_{TB}, κ_{LB}), respectively: (A) 1000, 1040, 8640; (B) 500, 1040, 8640; (C) 100, 1040, 8640; (D) 10, 1040, 8640; (E) 1, 1040, 8640.

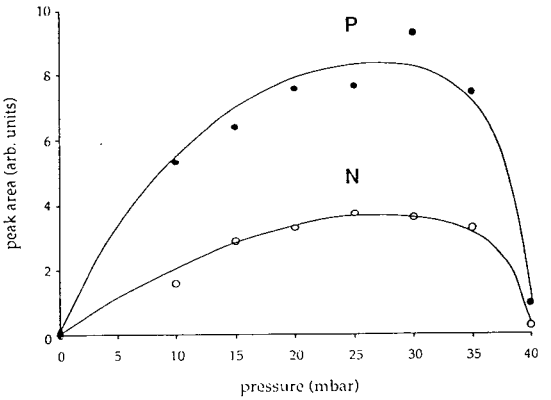

Fig. 4. Peak area vs. counterflow pressure using 300-μl samples of a 10^{-8} mol/l neostigmine (N) and propantheline (P) solution in saturated EtAc.

of neostigmine and propantheline obtained after EE–ITP–CZE of a 300-μl sample of a 10^{-8} mol/l mixture in saturated EtAc. The pressure used to induce a counterflow during EE at +10 kV (Section 2.3, step 3) is varied from 0 to 40 mbar. Three stages can be distinguished on each of the curves. In the first stage (0–5 mbar), the pressure-induced counterflow does not fully counterbalance the EOF. Hence EtAc is dragged into the capillary, resulting in a diminished mass transfer as explained above. In the second stage of the curve (15–35 mbar), a maximum is reached in which maximum mass transfer is obtained. Finally, above 35 mbar, the amount extracted is decreased dramatically as the EtAc zone together with the analyte molecules are pushed out of the capillary. At any given voltage during EE the pressure-induced counterflow should be chosen to compensate the EOF.

Based on the conductivity data mentioned above, the relationship of the electric field strengths in the three different zones (Fig. 5) can be calculated. The resistances of the three zones are related according to Eq. 4. Considering a constant current through the capillary applying a voltage of +10 kV over a 90-cm capillary, the electric field strengths in the EtAc zone, the terminating buffer zone and the leading buffer zone are 47250, 47 and 5 V/cm, respectively.

The number of ions $[N(t)]$ of a single species i

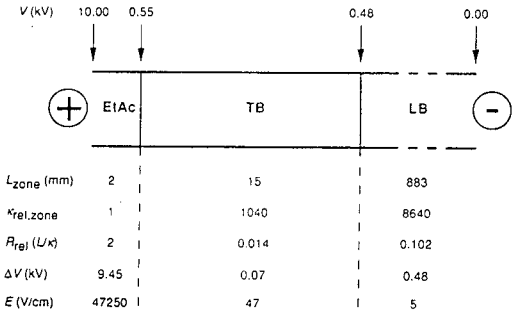

Fig. 5. Schematic representation of the ethyl acetate sample zone (EtAc), terminating buffer zone (TB) and leading buffer zone (LB) in a capillary, in which L_{zone} represents the zone length, $\kappa_{rel,zone}$ the relative conductivity of the zone, R_{rel} the relative resistance, ΔV the voltage drop over the zone and E the electric field strength in the zone.

extracted from the EtAc sample during time t is described by

$$N(t) = SE_{EtAc}\mu_i C_i t \quad (7)$$

This equation is similar to the relationship described by Chien and Burgi [22], considering a zero EOF, a constant EtAc zone length (2 mm) and a constant electric field strength over the EtAc zone, E_{EtAc}.

During the EE, the ion concentration in the EtAc zone will decrease owing to mass transport, which consequently enhances the E_{EtAc}. However, the electric field strength in the EtAc zone cannot exceed 50 kV/cm, which is an increase of approximately 6%. This extreme situation will only occur when the EtAc sample is completely exhausted. This justifies the assumption that the electric field strength in the EtAc zone is independent of time and can be considered constant.

Fig. 6 shows the relationship between the peak area and EE time, obtained after EE of a 300-μl sample of a 10^{-8} mol/l crystal violet solution in saturated EtAc for 0, 1, 3, 6, 12 and 20 min. In the first part of the curve the relationship between EE time and amount extracted is linear, which is in agreement with Eq. 7. During EE the analyte concentration and also the concentration of background electrolyte decrease gradually. A plateau is reached when the total ion concentration in the organic phase approaches zero.

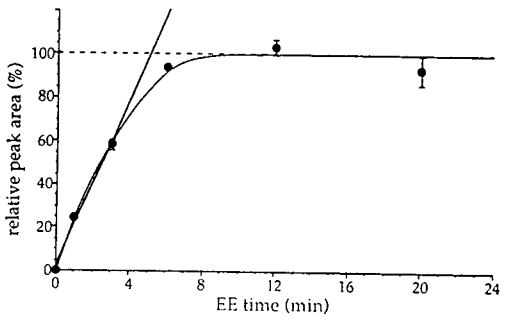

Fig. 6. Relative peak area vs. EE time using 300-μl samples of a 10^{-8} mol/l crystal violet solution in saturated EtAc ($n = 3$).

This was observed after 10 min of EE, applying a voltage of +15 kV combined with a 45-mbar pressure-induced counterflow.

In Fig. 7 the crystal violet recovery obtained after each of six repetitive extractions from an aliquot of 300 μl of 10^{-8} mol/l crystal violet solution in saturated EtAc at +15 kV and 45 mbar (Section 2.3, step 3) is presented. It shows that in the first EE cycle approximately 90% of the amount of crystal violet initially present in the sample is extracted from the organic phase. After five EE cycles no signal could be measured.

The amount of analyte extracted depends on several parameters, which simultaneously influence the electric current. These include local

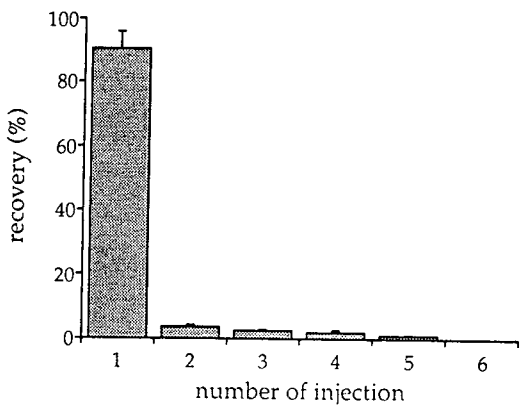

Fig. 7. Diagram of the recovery obtained after each of six repetitive extractions from a single 300-μl sample of a 10^{-8} mol/l crystal violet solution in saturated EtAc ($n = 3$).

differences in temperature, length of the EtAc plug in the capillary and variations in the EOF. These variables are difficult to control. During EE an alternating forward and backward movement of the interface was observed with 10^{-7} mol/l crystal violet in saturated EtAc. When the EtAc plug moves into the capillary, the electric field strength over the buffer zone diminishes and the EOF will be decreased accordingly. A steady state will be reached when the EOF is fully compensated by the pressure-induced counterflow. Fluctuations in the interface position in the capillary could be a consequence of an inhomogeneous distribution of anions and cations across the phase boundary [17]. Owing to electrophoresis, local accumulation of ions with the same charge occurs. The electric field over the capillary may induce an electrophoretic movement of the interface to the oppositely charged electrode. When the local accumulation of ions is neutralized, owing to repulsion and electromigration, the pressure-induced counterflow will predominate over the EOF. The capillary contents will be forced in the opposite direction hydrodynamically, until ions of the same charge sign accumulate again. Then the cycle starts all over.

The applied electric field strength has a significant influence on both the amount extracted and reproducibility. High electric field strengths will increase the amount of analyte extracted, but also disturb the interface and consequently affect the EE negatively. With 10^{-7} mol/l crystal violet in saturated EtAc a visible distortion and eventually segmentation of the interface zone in the capillary were observed using a voltage above +15 kV. In addition, a poorly conducting EtAc sample showed an identical distortion. This is in accordance with Thornton's theory, which suggests that droplet formation is enhanced in a system consisting of two immiscible phases that differ widely in conductivity [19].

In exhaustive EE the position and the geometry of the electrode with respect to the capillary inlet influence the EE recovery. Local exhaustion of the solution results in a dramatic decrease in conductivity and consequently a decrease in the ion transport in this section. The driving force behind analyte transport towards the exhausted section in the organic sample solution is determined by the concentration difference between the exhausted and the surrounding section, according to Fick's law. Important parameters are the viscosity of the organic solvent, the diffusion coefficient and diffusion path length, the vial geometry and the sample volume. The effects of these parameters are more pronounced when using large sample volumes for EE. EE of 3 pmol of crystal violet from a 300-μl saturated EtAc sample results in a three times larger peak area compared with the EE of 3 pmol of crystal violet from a 4-ml saturated EtAc sample with an equal EE time.

3.2. Quantitative aspects

Quantitative aspects of EE–ITP–CZE were investigated by generating calibration plots of crystal violet in the concentration range 10^{-10}–10^{-8} mol/l and of propantheline, neostigmine, salbutamol and terbutaline in the concentration range of 10^{-9}–10^{-7} mol/l. A typical calibration plot is characterized by $y = 1.5 \cdot 10^{12}x + 99$ ($r^2 = 0.999$), where y represents the peak area (arbitrary units) and x the analyte concentration (mol/l). The relative standard deviation (R.S.D.) of six extractions of a single batch of 10^{-8} mol/l crystal violet solution, without capillary conditioning between the runs, is 11.0%. Conditioning of the capillary between subsequent analyses shows no significant difference in reproducibility; the R.S.D. is 10.5% ($n = 6$).

Based on a signal-to-noise ratio of 3, the limit of detection (LOD) for EE–ITP–CZE of a 300-μl sample of crystal violet was 10^{-10} mol/l. The LOD for both neostigmine and propantheline was $5 \cdot 10^{-10}$ mol/l and for salbutamol and terbutaline 10^{-9} mol/l. Noise was measured peak-to-peak.

3.3. Application of EE–ITP–CZE

In Fig. 8, a comparison is made between (A) EE–ITP–CZE and electrokinetic injection CZE electropherograms from (B) water and (C) terminating buffer. Aliquots of 300 μl of a 10^{-8}

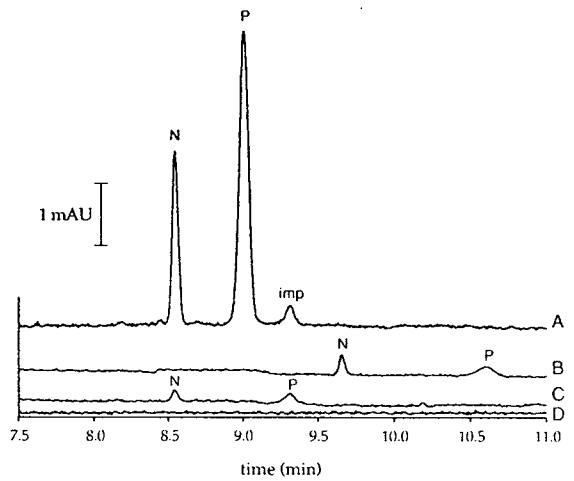

Fig. 8. Electropherograms obtained after (A) EE–ITP–CZE of a saturated EtAc solution, (B) ITP–CZE of a terminating buffer solution, (C) stacking of an aqueous solution and (D) electrokinetic injection for 20 s at +10 kV of 10^{-8} mol/l neostigmine (N) and propantheline (P) from a 300-μl sample. Electrokinetic sample injection, as used to obtain electropherograms A–C, was performed at +10 kV using an 8-mbar pressure-induced counterflow for 10 min. The peak marked "imp" is related to a chemical impurity. More experimental details are given in the text.

mol/l mixture of neostigmine and propantheline were used. Counterflow ITP [9,23] for 10 min at +10 kV combined with an 8-mbar pressure-induced counterflow was used to inject the analytes from a terminating buffer and water solution. Further, Fig. 8D shows an electropherogram obtained after an electrokinetic injection at +10 kV for 20 s from a 300-μl sample of a 10^{-8} mol/l mixture of propantheline and neostigmine in water. Owing to the different conditions in the three stacking procedures (Fig. 8A–C), different migration times of neostigmine and propantheline occur. A critical part of the EE procedure with respect to efficiency and resolution is the ITP step. A short ITP step results in poor efficiency and resolution, owing to the relatively long analyte zone prior to CZE. An optimum situation is obtained by increasing the duration of the ITP step until the steady-state situation is reached. Analyte recoveries in the counterflow ITP–CZE analyses from terminating buffer and water were significantly lower (approximately 10–30 times) than in the EE–ITP–CZE analyses from saturated EtAc, which can be explained by the difference in the conductivities and related large differences in the electric field strength.

Application of EE–ITP–CZE to the analysis of real samples containing high concentrations of matrix ions requires an additional sample clean-up step. However, this applies with any electrokinetic sample introduction technique, as discrimination between matrix ions and analyte ions during sample introduction occurs. Future research will be devoted to this subject.

4. Conclusions

It has been demonstrated that electroextraction in combination with isotachophoresis is a fast and effective technique for the on-line focusing of very large samples in capillary electrophoresis. Owing to the high concentrating power of electroextraction, the analytes are extracted in a small sample volume, just above the liquid–liquid interface, prior to ITP. As a result, ITP takes only a few minutes. Application of EE–ITP–CZE yields 10–30-fold higher sensitivities for the model compounds during equal time periods from equal sample volumes compared with sample stacking using a hydrodynamic counterflow. However, a requirement for the use of EE is that the analytes of interest should be dissolvable in the organic solvent used. In addition, a background electrolyte has to be added in order to obtain electric current, i.e., mass transfer.

Acknowledgement

The authors thank the Foundation for Quality Guarantee of the Veal Calf Sector (SKV, Netherlands) for funding.

References

[1] C.A. Monnig and R.T. Kennedy, *Anal. Chem.*, 66 (1994) 280R.

[2] V. Dolnik, K.A. Cobb and M. Novotny, *J. Microcol. Sep.*, 2 (1990) 127.
[3] F. Foret, V. Sustacek and P. Bocek, *J. Microcol. Sep.*, 2 (1990) 229.
[4] D. Kaniansky and J. Marák, *J. Chromatogr.*, 498 (1990) 191.
[5] D.S. Stegehuis, H. Irth, U.R. Tjaden and J. van der Greef, *J. Chromatogr.*, 538 (1991) 393.
[6] D.S. Stegehuis, U.R. Tjaden and J. van der Greef, *J. Chromatogr.*, 591 (1992) 341.
[7] F. Foret, E. Szoko and B.L. Karger, *J. Chromatogr.*, 608 (1992) 3.
[8] D. Kaniansky, J. Marák, V. Madajová and E. Simunicová, *J. Chromatogr.*, 638 (1993) 137.
[9] N.J. Reinhoud, U.R. Tjaden and J. van der Greef, *J. Chromatogr.*, 641 (1993) 155.
[10] N.J. Reinhoud, U.R. Tjaden and J. van der Greef, *J. Chromatogr. A*, 653 (1993) 303.
[11] V. Dolnik, M. Deml and P. Bocek, *J. Chromatogr.*, 320 (1985) 89.
[12] M. Mazereeuw, U.R. Tjaden and J. van der Greef, *J. Chromatogr. A*, 677 (1994) 151.
[13] T.C. Scott, *Sep. Purif. Methods*, 18 (1989) 65.
[14] P.V.R. Iyer and H. Sawistowski, *Proc. Int. Solvent Extr. Conf.*, 2 (1974) 1029.
[15] T. Usami, Y. Enokida and A. Suzuki, *J. Nucl. Sci. Technol.*, 30, No. 10 (1993) 51.
[16] G. Scibona, P.R. Danesi and C. Fabiani, *Ion Exch. Solvent Extr.*, 8 (1981) 95.
[17] P.J. Bailes, *Ind. Eng. Chem., Process Des. Dev.*, 20 (1981) 564.
[18] G. Stewart and J.D. Thornton, *AIChE Symp. Ser.*, 26 (1967) 29.
[19] J.D. Thornton, *Birmingham Univ. Chem. Eng. J.*, (1976) 6.
[20] M.H. Lamoree, N.J. Reinhoud, U.R. Tjaden, W.M.A. Niessen and J. van der Greef, *Biol. Mass Spectrom.*, 23 (1994) 339.
[21] P. Bocek, M. Deml, P. Gebauer and V. Dolnik, *Analytical Isotachophoresis*, VCH, Weinheim, 1988.
[22] R.L. Chien and D.S. Burgi, *Anal. Chem.*, 64 (1992) 489A.
[23] F.M. Everaerts, J.L. Beckers and T.P.E.M. Verheggen, *Isotachophoresis —Theory, Instrumentation and Practice*, Elsevier, Amsterdam, 1976.

ELSEVIER

Journal of Chromatography A, 687 (1994) 343–349

JOURNAL OF CHROMATOGRAPHY A

Separation of metallo–cyanide complexes by capillary zone electrophoresis

Wolfgang Buchberger, Paul R. Haddad*

Department of Chemistry, University of Tasmania, GPO Box 252C, Hobart, Tasmania 7001, Australia

First received 26 May 1994; revised manuscript received 29 August 1994

Abstract

The optimisation of electrolyte systems for the separation and detection of cyanide complexes of Au, Pt, Fe(II), Fe(III), Pd, Cu(I), Co, Ag, Cr and Ni using capillary zone electrophoresis is described. A phosphate–triethanolamine buffer at pH 8.5 was chosen for the separation. The factors affecting resolution and analysis time include the addition of ion-pairing reagents (which also act as electroosmotic mobility modifiers) as well as organic solvents to the carrier electrolyte. Less stable cyano complexes [such as those of copper(I)] require the presence of low concentrations of free cyanide in the electrolyte in order to achieve acceptable peak shapes. Direct UV detection at 214 nm is feasible for most of the metallo–cyanide complexes although some of them giver higher response in an indirect mode at 254 nm using trimellitate as the carrier electrolyte. Approaches for preconcentration are discussed in order to achieve detection limits necessary for environmental samples and other applications.

1. Introduction

Cyanide is used extensively in the mining industry for extraction of gold from its ores as well as in the metal processing industry for electroplating. Furthermore, certain metallurgical processes can lead to the generation of cyanide as an undesired by-product. In all these cases, rigorous control of waste solutions as well as monitoring of cyanide in environmental samples taken from the vicinity of industrial plants is essential in order to protect the environment. Cyanide in environmental samples is likely to be present in the form of metallo–cyanide complexes exhibiting varying persistence and toxicology. During recent years, ion-interaction chromatography has emerged as an efficient technique for separation of metallo–cyanides and has been employed for speciation analysis at μg/l levels [1].

Currently, capillary zone electrophoresis (CZE) is growing in significance as an analytical method for the separation of low-molecular-mass ionic species. It appears to be an attractive complementary technique to ion chromatography with promising features such as high separation efficiency, short analysis time and unique separation selectivity. CZE separation

* Corresponding author.

0021-9673/94/$07.00
SSDI 0021-9673(94)00826-4

procedures for a variety of small inorganic and organic anions and cations are already well documented in the literature, but its use for the separation of metallo–cyanides has not yet been fully exploited.

Aguilar et al. [2] have used CZE to separate hexacyanoferrate(II) and hexacyanoferrate(III) and have applied this method to the determination of iron cyanide complexes in zinc electroplating solutions. In another paper, Aguilar et al. [3] reported the separation of gold and silver cyanides in leaching solutions from ore. In both cases, a counterelectroosmotic mode was employed. The vectors of the electrophoretic mobilities of iron cyanides oppose the direction of the electroosmotic flow and exceed its magnitude. Therefore, these complexes were injected at the cathode and detected at the anode. Silver and gold cyanides show much lower electrophoretic mobilities and were injected at the anode and detected at the cathode.

In an attempt to improve the separation of metal ions by CZE, we have reported a precapillary derivatisation using cyanide with subsequent separation of the metallo–cyanides in a cyanide-containing carrier electrolyte [4]. This approach yielded satisfactory results for a range of metal ions, but the conditions are not suitable for the determination of metallo–cyanides in environmental samples since cyanide present in the carrier electrolyte could react with free metal ions in the sample, leading to erroneous results.

The aim of the work presented in this paper was the separation of a range of metallo–cyanides, preferably in a co-electroosmotic CZE mode, which would be applicable to complexes having either low or high electrophoretic mobility. Co-electroosmotic CZE of anionic species can only be carried out if the direction of the electroosmotic flow is reversed and directed to the anode. This reversal is generally accomplished by the addition of hydrophobic quaternary ammonium ions to the carrier electrolyte [5,6]. These electroosmotic flow modifiers can also act as ion-pairing reagents, and for this reason investigations into the potential of ion-pairing for manipulation of separation selectivity of metallo–cyanides have been included in our work.

2. Experimental

2.1. Instrumentation

The CZE instrument employed was a Quanta 4000 (Waters, Milford, MA, USA) interfaced to a Maxima 820 data station (Waters). Separations were carried out using an AccuSep (Waters) fused-silica capillary (60 cm × 75 μm I.D., effective length 52 cm). Injection was performed hydrostatically by elevating the sample at 10 cm for a specified time. Direct UV detection at 214 nm or indirect UV detection at 254 nm was used.

2.2. Carrier electrolytes

The following carrier electrolytes were used for direct UV detection: phosphate buffer at pH 11 (prepared from 5 m*M* Na_3PO_4 adjusted to pH 11 with phosphoric acid); phosphate buffer at pH 8 (prepared from 5 m*M* K_2HPO_4 adjusted to pH 8 with phosphoric acid); phosphate–triethanolamine buffer at pH 8.5 (prepared from 5 m*M* K_2HPO_4 and 5 m*M* triethanolamine, both adjusted to pH 8.5 with phosphoric acid). The carrier electrolyte for indirect UV detection consisted of 2.5 m*M* trimellitic acid adjusted to pH 9.5 with sodium hydroxide. The electroosmotic flow was adjusted by addition of varying amounts of hexamethonium bromide (Sigma, St. Louis, MO, USA). All carrier electrolytes were prepared from analytical-reagent grade chemicals using water purified with a Millipore (Bedford, MA, USA) Milli-Q water-treatment system.

2.3. Metallo–cyanide complexes

The following analytical-reagent grade metallo–cyanides were purchased: $KAu(CN)_2$ (Fluka, Buchs, Switzerland), $K_2Pt(CN)_4$ (Pfaltz & Bauer, Waterbury, CT, USA), $K_3Fe(CN)_6$ (Fluka), $K_4Fe(CN)_6 \cdot 3H_2O$ (Fluka). Other metallo–cyanides, namely $K_2Pd(CN)_4$, $K_3Cu(CN)_4$, $K_3Co(CN)_6$, $KAg(CN)_2$, $K_3Cr(CN)_6$ and $K_2Ni(CN)_4$ were synthesised using previously reported procedures [7].

3. Results and discussion

3.1. Control of the electroosmotic flow

The addition of hydrophobic trimethylalkylammonium salts is generally recommended for applications requiring suppression or reversal of the electroosmotic flow [5]. Unfortunately, attempts to use these salts for the separation of metallo–cyanides were unsuccessful because they tended to form precipitates with some of the complexes. Recently, 1,6-bis(trimethylammonium)hexane (hexamethonium bromide) has been introduced for control of the electroosmotic flow [6]. Our investigations indicated that carrier electrolytes consisting of phosphate buffers at pH 8 or 11 and up to 0.8 m*M* hexamethonium bromide can avoid the problem of precipitation. On the other hand, the electroosmotic flow was found not to be reversed but only decreased to a certain extent. Data for the electroosmotic mobility are shown in Fig. 1. These data suggest that a co-electroosmotic CZE mode cannot be employed as originally intended but the decrease in the electroosmotic flow might be sufficient to allow the separation of a broad range of metallo–cyanides using the anodic side for detection.

$Ag(CN)_2^-$ exhibits the lowest electrophoretic mobility of the metallo–cyanides included in this study. Its electrophoretic mobility was found to be $-5.75 \cdot 10^{-4}$ cm^2 V^{-1} s^{-1}. The observed mobility (being the vector sum of the electrophoretic and the electroosmotic mobility) of $Ag(CN)_2^-$ must exceed $-1.30 \cdot 10^{-4}$ cm^2 V^{-1} s^{-1} in order to obtain an analysis time of less than 20 min using the anode as the detection side. Therefore, the electroosmotic mobility must be decreased to at least $4.45 \cdot 10^{-4}$ cm^2 V^{-1} s^{-1}. Fig. 1 indicates that the necessary extent of decrease can be accomplished at pH 8 but not at pH 11, although the latter pH would be more favourable with respect to the stability of the metallo–cyanides.

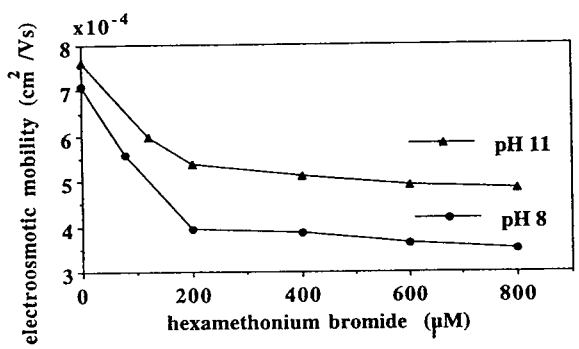

Fig. 1. Dependence of electroosmotic mobilities in phosphate buffers on the concentration of hexamethonium bromide.

3.2. Optimisation of separation selectivity

Initial experiments on optimisation of separation selectivity were performed employing a phosphate buffer at pH 8 as the carrier electrolyte. Under these conditions reproducible peaks could be obtained only if the electrolyte in the vial at the (anodic) detection side was replaced after each run. This behaviour was attributed to the fact that a phosphate buffer at pH 8 has a relatively low buffer capacity, so that after two or more consecutive runs hydrogen ions generated at the anode lower the pH to such an extent that considerable dissociation of metallo–cyanides occurs in the capillary during the run. Therefore, all further experiments were performed using a phosphate–triethanolamine buffer at pH 8.5 as the carrier electrolyte, since this mixture exhibits a much higher buffer capacity and avoids the necessity of frequent buffer replacement.

Fig. 2 shows a typical electropherogram of a mixture of metallo–cyanides using 0.8 m*M* hexamethonium bromide for controlling the electroosmotic flow. The solute concentrations used were in the range 5–15 μg/ml (calculated as the metal). Separation selectivity can easily be manipulated by varying the concentration of the hexamethonium bromide. Fig. 3 demonstrates the dependence of observed mobilities upon the concentration of hexamethonium bromide. It can be assumed that the observed changes in migration order are due predominantly to ion-pairing effects. Fig. 3 also indicates that different separation selectivities can be achieved at lower concentrations of hexamethonium bromide only if analysis time is sacrificed. A solution to this problem might be the use of electrolyte gra-

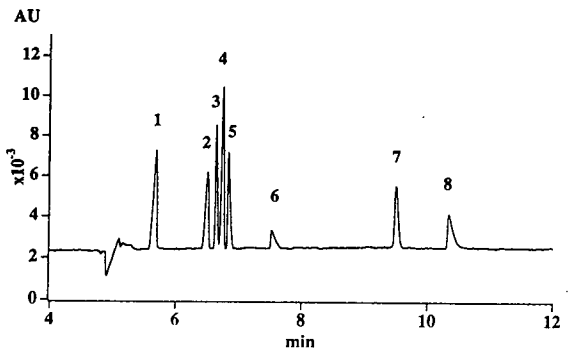

Fig. 2. Electropherogram of a mixture of metallo–cyanides. Carrier electrolyte: phosphate–triethanolamine buffer at pH 8.5 containing 0.8 m*M* hexamethonium bromide. Voltage: −20 kV. Injection time: 20 s. Detection: direct UV at 214 nm. Peaks: 1 = Fe(II); 2 = Pd; 3 = Co; 4 = Pt; 5 = Fe(III); 6 = Cr; 7 = Au; 8 = Ag.

dients. This technique is not yet widely used in CZE but its benefits have already been demonstrated by the work of Yeung and coworkers [8,9] who have employed a dynamic flow gradient induced by a step change in the concentration of cetyltrimethylammonium bromide (CTAB) in the carrier electrolyte. This step change was created by injecting the sample into the capillary containing a low concentration of CTAB, then running with buffer electrolyte containing a high concentration of CTAB. In this case, the electroosmotic flow, initially directed to the cathode, is monotonically reduced to zero. We have used a similar approach for the separation of metallo–cyanides, although in this case the electroosmotic flow is not reduced to zero because unlike CTAB, hexamethonium bromide does not reverse the electroosmotic flow (see above).

An electropherogram obtained in the gradient mode from 0.1 to 0.8 m*M* hexamethonium bromide is shown in Fig. 4. The changes in selectivity are in accordance with the trends shown in Fig. 3. The step change in the hexamethonium bromide concentration causes a step in the baseline at approximately 5.5–6 min. Therefore, the baseline obtained from a blank run was subtracted from the electropherogram given in Fig. 4, and some minor peaks appearing in this electropherogram are artefacts from the subtraction process. These baseline interferences can be avoided by using hexamethonium chloride instead of the bromide salt since the former does not show significant absorbance at the detection wavelength.

A further approach to manipulation of separation selectivity consists of employing carrier electrolytes containing organic solvents. Fig. 5 illustrates the dependence of observed mobilities

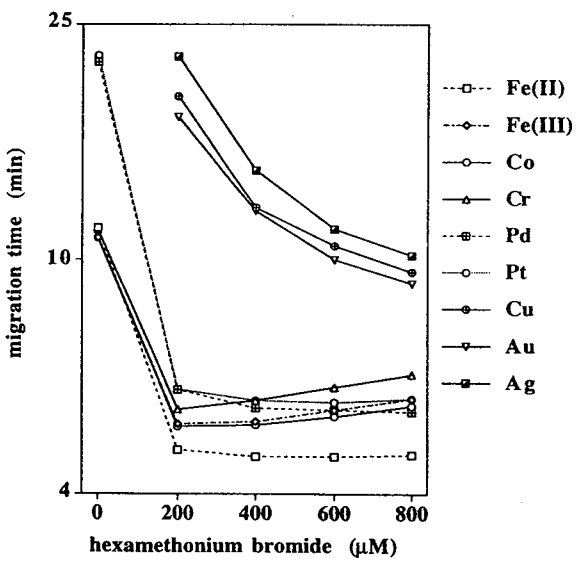

Fig. 3. Dependence of observed mobilities on the concentration of hexamethonium bromide (the *y*-axis is on a logarithmic scale).

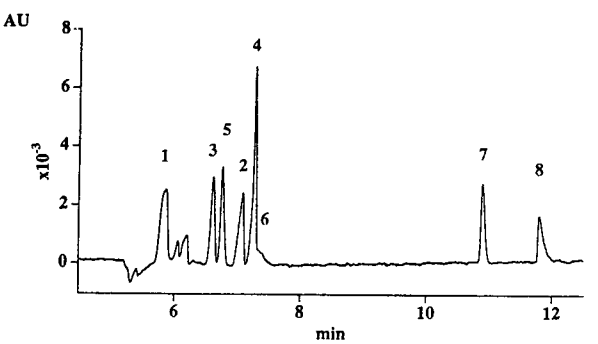

Fig. 4. Electropherogram of a mixture of metallo–cyanides using a gradient from 0.1 to 0.8 m*M* hexamethonium bromide. All other conditions and peaks as in Fig. 2.

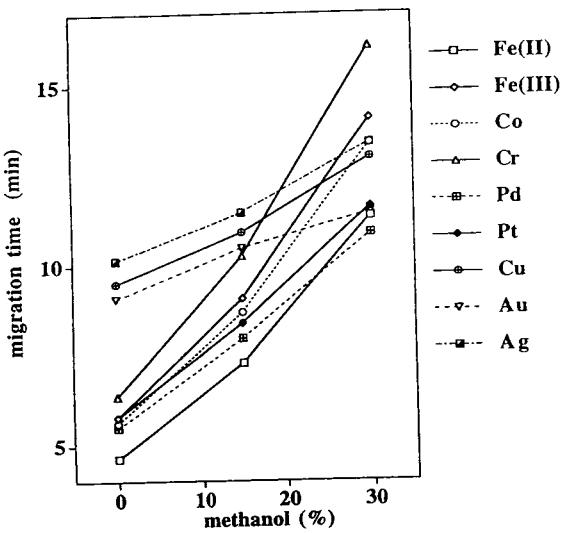

Fig. 5. Dependence of observed mobilities on the amount of methanol in the carrier electrolyte.

on the amount of methanol in the carrier electrolyte. The addition of methanol causes a general increase in the migration times of all complexes as a result of changes in the electroosmotic flow. Besides this general trend, there are several changes in migration order, as the slopes of the lines in Fig. 5 are lower for complexes with a low charge and higher for complexes with a high charge. The observed changes in separation selectivity may be a result of the change in hydration of the charged species in the presence of methanol.

Injection of the tetracyano complex of copper(I) resulted in a peak migrating between the cyanide complexes of gold and silver, but the peak shape was poor. Copper(I) forms cyano complexes containing 2 to 4 cyanide ions, so that during migration through the capillary different copper cyano species will be formed according to the respective dissociation constants and kinetics. The peak shape could be improved considerably by adding cyanide (0.02 to 0.3 m*M*) to the carrier electrolyte. Increasing the cyanide concentration in the carrier electrolyte also caused an increase in the electrophoretic mobility of the copper cyano complex. A speciation calculation based on stability constants from the literature [10,11] indicated that under the conditions chosen Cu(I) should form cyano complexes containing between 2 and 3 cyanide ligands and should therefore have an effective charge between −1 and −2. The increase in electrophoretic mobility is due mainly to the increase in charge as can be seen from Fig. 6. Slight deviations from linearity in Fig. 6 may be due to changes in the size and shape of the species.

3.3. Optimisation of detection

Most of the metallo–cyanide complexes investigated in this study exhibit UV absorption maxima in the wavelength range from 200 to 220 nm [1]. Therefore, a fixed-wavelength UV detector at 214 nm was employed. A 20-s hydrostatic injection yielded detection limits (defined as three times the signal-to-noise ratio and calculated as the metal) of 0.16 μg/ml for Fe(II), 0.64 μg/ml for Pd, 0.15 μg/ml for Co, 0.39 μg/ml for Pt, 0.21 μg/ml for Fe(III), 1.1 μg/ml for Cr, 1.2 μg/ml for Au and 2.5 μg/ml for Ag. Unfortunately, at 214 nm the chromium cyanide (which may be important in several environmental applications) has only a moderate molar extinction coefficient compared with cyano complexes of e.g. Fe(II) and Fe(III). For this reason, electrolytes were investigated which would permit the use of indirect UV detection as a more universal detection technique. Best results were obtained using 5 m*M* trimellitic acid adjusted to pH 9.5 as the carrier electrolyte, with

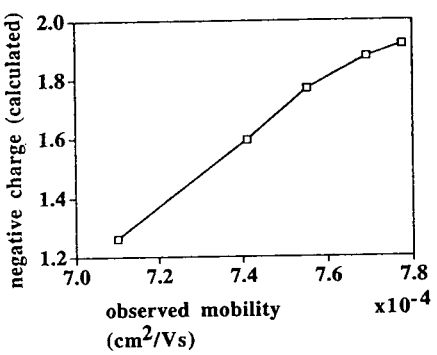

Fig. 6. Dependence of the observed mobility of the copper cyanide complex on the calculated charge.

detection at 254 nm. It must be taken into account that even at 254 nm some metallo–cyanides show molar extinction coefficients considerably higher than trimellitate. Therefore, the injection of a mixture of different metallo–cyanides may result in electropherograms comprising both negative and positive peaks. A typical example is given in Fig. 7 which shows the separation of the cyano complexes of Ni, Pd, Pt, Cr and Au. Here, the Pt peak is due to an increase in the absorbance resulting from the high absorptivity of the platinum complex, whereas all other peaks are caused by a decrease in the background absorbance. As one would anticipate, indirect detection improved the detectability of the chromium complex relative to other metallo–cyanides. Unfortunately, the absolute detection limit could not be improved significantly for chromium and was worse for other metallo–cyanides (1.0 μg/ml for Cr, 1.3 μg/ml for Pd, 1.6 μg/ml for Pt, 3.6 μg/ml for Au). The overall performance of the trimellitate carrier electrolyte in terms of resolution and efficiency was not as good as the carrier electrolyte described earlier for use with direct detection.

3.4. Approaches to sample preconcentration

The detection limits obtained with the proposed method are such that some environmental applications may require the use of preconcentration procedures in order to achieve sufficient sensitivity. Fortunately, CZE itself includes a preconcentration step (known as electrostacking) when the ionic strength of the introduced sample plug is lower than that of the carrier electrolyte. Under these conditions, solute ions from the injected sample are focused into a short band due to the higher electric field in the sample region. Nevertheless, a prediction of the influence of sample volume on separation efficiency for a given separation is difficult so that an experimental verification is appropriate. Fig. 8 shows the number of theoretical plates (measured for the Au–cyano complex in an aqueous standard) as a function of the injection time. An increase in the injection time from 20 to 200 s results in a loss of separation efficiency by approximately 40%. In some applications this decreased efficiency may be offset by an approximately tenfold increase in sensitivity (e.g. the detection limit for Au is decreased to 0.16 μg/ml). Larger volumes will sooner or later lead to losses of some of the injected species. This phenomenon can be explained by the fact that the hexamethonium bromide adsorbed to the capillary wall will dissolve into the water of the sample plug, so the ζ potential and the electroosmotic flow are increased in the sample region. Slow metal–cyano complexes cannot migrate fast enough to the boundary between the sample plug and the carrier electrolyte and are pumped

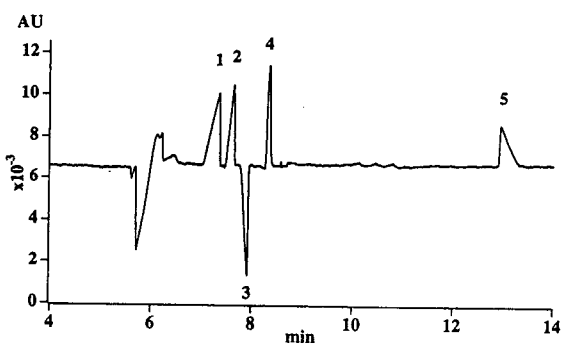

Fig. 7. Electropherogram of a mixture of metallo–cyanides using indirect UV detection at 254 nm. Carrier electrolyte: 2.5 m*M* trimellitate pH 9.5 containing 0.8 m*M* hexamethonium bromide. Voltage: −20 kV. Injection time: 30 s. Peaks: 1 = Ni; 2 = Pd; 3 = Pt; 4 = Cr; 5 = Au.

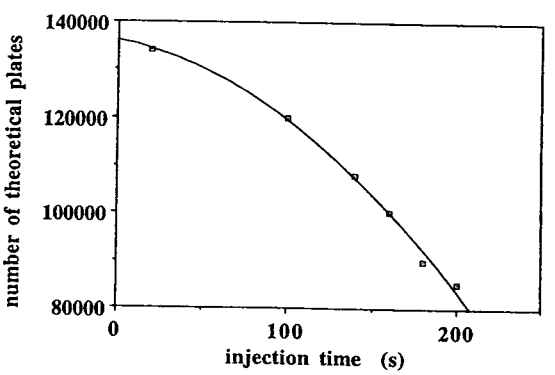

Fig. 8. Dependence of the number of theoretical plates (measured for the gold–cyanide complex) on the injection time.

out of the capillary by the increased electroosmotic flow and are therefore lost. These aspects of large volume electrostacking have also been discussed recently by Burgi [12].

Preconcentration of some metallo–cyanides can also be achieved using off-line solid-phase extraction on reversed-phase C_{18} silica. The complexes can be enriched efficiently from aqueous solutions if an ion-interaction mode is applied. The preconcentrated complexes may be eluted by a small volume of an organic solvent such as methanol. Preliminary experiments were carried out for the determination of the Au–cyano complex in leaching solutions from a gold mine. A Sep-Pak C_{18} cartridge was preconditioned with 2 ml of 5 m*M* PIC A (Waters) as the ion-interaction reagent. A 20-ml aliquot of the sample was passed through the cartridge and then eluted with 1 ml methanol and 1 ml water, and the eluate was used for CE without any further treatment. This procedure yielded a recovery of 103.6% for an aqueous standard containing 4 μg/ml Au (standard deviation 2.7%; $n = 6$). A real mine sample containing 1.3 μg/ml Au gave a recovery of 83%. This decreased recovery can be explained by the fact that the sample contained relatively high concentrations of anions, such as chloride and sulfate, which compete for the preconcentration sites on the Sep-Pak cartridge. Further investigations will have to include a careful optimisation of all steps involved in the sample preparation procedure, especially for samples with high ionic strengths.

4. Conclusions

The results obtained in this work indicate that CZE is an attractive technique for the separation of various metal–cyanide complexes. High efficiencies and short analysis times are some of the advantages of this method compared with the well-established technique of ion-interaction chromatography. The separation selectivity can be optimised for different applications by using ion-interaction reagents and/or organic solvents in the carrier electrolyte. Samples of high ionic strength are still a challenge for CZE as overloading effects are more pronounced than in chromatography. Adequate sample preparation procedures including preconcentration steps are crucial and will be the focus of further studies.

Acknowledgements

Financial support from Waters Corporation and the Australian Research Council are gratefully acknowledged.

References

[1] P.R. Haddad and C. Kalambaheti, *Anal. Chim. Acta*, 250 (1991) 21.
[2] M. Aguilar, X. Huang and R.N. Zare, *J. Chromatogr.*, 480 (1989) 427.
[3] M. Aguilar, A. Farran and M. Martinez, *J. Chromatogr.*, 635 (1993) 127.
[4] W. Buchberger, O.P. Semenova and A.R. Timerbaev, *J. High Resolut. Chromatogr.*, 16 (1993) 155.
[5] W.R. Jones and P. Jandik, *J. Chromatogr.*, 546 (1991) 445.
[6] M.P. Harrold, M.J. Wojtusik, J. Riviello and P. Henson, *J. Chromatogr.*, 640 (1993) 463.
[7] D.F. Hilton and P.R. Haddad, *J. Chromatogr.*, 361 (1986) 141.
[8] C.W. Whang and E.S. Yeung, *Anal. Chem.*, 64 (1992) 502.
[9] H.-T. Chang and E.S. Yeung, *J. Chromatogr.*, 608 (1992) 65.
[10] R.D. Hancock, N.P. Finkelstein and A. Evers, *J. Inorg. Nucl. Chem.*, 34 (1972) 3737.
[11] R.M. Izatt, G.D. Watt, D. Eatough and J.J. Christensen, *J. Chem. Soc. (A)*, (1967) 1304.
[12] D.S. Burgi, *Anal. Chem.*, 65 (1993) 3726.

ELSEVIER

Journal of Chromatography A, 687 (1994) 351–355

JOURNAL OF CHROMATOGRAPHY A

Short communication

Enantiomeric separation and determination of antiparkinsonian drugs by reversed-phase ligand-exchange high-performance liquid chromatography☆

Sajid Husain*, R. Sekar, R. Nageswara Rao

Analytical Chemistry Division, Indian Institute of Chemical Technology, Hyderabad 500 007, India

First received 11 May 1994; revised manuscript received 23 August 1994

Abstract

A simple and rapid high-performance liquid chromatographic method for the separation and determination of enantiomers of levodopa and carbidopa using a LiChrosper C_{18} column with aqueous copper–L-phenylalanine as mobile phase was developed. The separation between D- and L-enantiomers of levodopa and carbidopa was fairly good with separation factors of 1.63 and 2.38, respectively. The method was validated using synthetic mixtures and used for quality assurance of commercial formulations.

1. Introduction

Parkinson's disease, or paralysis agitans, is a degenerative nervous system disorder, characterized by progressive tremor, bradykinesia and muscular rigidity [1,2]. The causes of this disease are not known and its pathophysiology is poorly understood. However, it is known that the neuronal degeneration is difficult to arrest and hence leads to a significant depletion of dopamine. Therefore, any therapeutic attempt should involve correcting the dopamine depletion effectively. Dopamine is not administered directly because it does not cross the blood–brain barrier readily [3]. Therefore, its precursor levodopa (L-Dopa) is given orally for the treatment of Parkinson's disease. Levodopa is converted into dopamine by the enzyme decarboxylase and hence the concentration of dopamine is increased. This process of conversion of levodopa into dopamine is beneficial within the limits of the striatum but deleterious outside the blood–brain barrier because of the elevated levels of dopamine cause adverse reactions such as nausea, vomiting and cardiac arrhythmias (4). These side-effects are generally reduced by administering levodopa combined with a peripheral decarboxylase inhibitor, viz., carbidopa. Several combinations of levodopa and carbidopa are commercially available as different formulations. Although L-carbidopa is only used as a decarboxylase inhibitor, it may contain small amounts of the D-isomer owing to the procedures involved in its manufacture [5]. It has been reported that L-carbidopa is pharmacologically active whereas the D-form is not [6–9]. It may be noted that the use of racemic mixtures containing L-Dopa, D-Dopa, L-carbidopa and D-carbidopa may lead to serious side-effects such as dyskinesia and psy-

* Corresponding author.

☆ IICT Communication No. 3350.

0021-9673/94/$07.00
SSDI 0021-9673(94)00809-4

chosis owing to differences in the metabolism of the active and non-active components of the racemates [10]. Therefore, development of methods for the separation and determination of optical isomers of the antiparkinsonian drugs is of great importance.

Several gas and liquid chromatographic methods for the separation and determination of levodopa and carbidopa have been reported [11–13], but these methods are not specific for the separation of enantiomers of levodopa and carbidopa. Hence they are not suitable for monitoring the levels of D-Dopa and D-carbidopa which are generally present in low concentrations, i.e., 0.1–2.0%, in commercial formulations. Recently, high-performance liquid chromatography (HPLC) has opened up new opportunities in the resolution of optical isomers of drugs, pharmaceuticals and agrochemicals [14–16]. Chiral columns, chiral ligand-exchange stationary phases, chiral mobile additives and diastereomerization techniques have been used extensively. Gilon et al. [17] studied three-point interactions involved in the resolution of amino acids using chiral eluents. Olerich et al. [18] demonstrated the usefulness of aqueous copper(II)–L-phenylalanine complex as mobile phases with reverse-phased C_{18} columns for the separation of enantiomers of methyldopa, tryptophan and hydroxytryptophan. Gelber and Neumeyer [19] adopted the same conditions for the determination of enantiomers of L-Dopa and its analogues in individual dosage forms by HPLC. Several others have reported the enantiomeric separation of L-Dopa using a variety of columns such as cellulose, ion-exchange resins and modified silica with chiral eluents as mobile phases by HPLC [20–22]. However, the simultaneous determination of enantiomers of L-Dopa and carbidopa, as used in the treatment of Parkinson's disease, has not been reported so far. In this paper, we describe the simultaneous separation and determination of enantiomers of levodopa and carbidopa in combined formulations using a LiChrospher C_{18} column and an eluent containing 0.003 *M* aqueous $CuSO_4$ and 0.006 *M* L-phenylalanine at ambient temperature.

2. Experimental

2.1. Materials and reagents

All reagents were of analytical-grade unless stated otherwise. Glass-distilled water was deionized using Nanopure II D 3700 cartridge (Barnstead). L-Phenylalanine (Loba Chemie, Bombay, India), Copper sulphate (BDH, Poole, UK), L-Dopa (Loba Chemie), D-Dopa (Fluka, Buchs, Switzerland) and L-carbidopa (Sun Pharmaceuticals, Bombay, India) were used. D-Carbidopa was prepared and purified in the laboratory following published methods [23,24]. Commercial formulations of levodopa and carbidopa were obtained from local firms.

2.2. Apparatus

A high-performance liquid chromatograph (Shimadzu, Kyoto, Japan) with a 20-μl loop injector having a high-pressure six-way valve was used. A Shimadzu SPD-6AU variable-wavelength UV–Vis spectrophotometric detector was connected after the column. A LiChrospher C_{18} (Merck, Darmstadt, Germany) column (125 mm × 4.0 mm I.D., particle size 5 μm) was used for separation. The chromatograms and the integrated data were recorded with a Chromatopac C-R3A processing system.

2.3. Mobile phase

A 0.9912-g amount of L-phenylalanine and 0.7488 g of $CuSO_4 \cdot 5H_2O$ were dissolved in 100 ml of doubly distilled, deionized water to give 0.003 *M* copper(II)–0.006 *M* L-phenylalanine complex, which was used as the mobile phase.

2.4. Chromatographic conditions

The mobile phase was 0.003 *M* aqueous copper(II) sulphate–0.006 *M* L-phenylalanine. The analysis was carried out under isocratic conditions at a flow-rate of 1 ml/min and a chart speed of 5 mm/min at room temperature (27°C). Chromatograms were recorded; at 280 nm.

2.5. Analytical procedure

Samples (10 mg) were dissolved in the mobile phase (10 ml) and a 5-μl volume of each sample was injected and chromatographed under the above conditions. Synthetic mixtures and commercial formulations were analysed under identical conditions. The amounts of enantiomers of levodopa and carbidopa were calculated from the corresponding areas of the peaks.

3. Results and discussion

The HPLC separation of enantiomers of levodopa and carbidopa is shown in Fig. 1. The peaks were identified by injecting individual authentic compounds. It can be seen from Fig. 1 that the compounds are well resolved under the conditions used. The separation factors were 1.63 and 2.38 for enantiomers of levodopa and carbidopa, respectively. The peaks were resolved with excellent symmetry and reproducibility. The resolution factors were determined and found to be fairly high, viz., 4.46 and 11.28 for enantiomers of levodopa and carbidopa, respectively. The LiChrospher C_{18} column with 0.003 *M* $CuSO_4$–0.006 *M* L-phenylalanine (50:50, v/v) was found to be an ideal system for separation. The retention data, viz., retention times, capacity factors (k') and separation factors (α) for the compounds under investigation are given in Table 1.

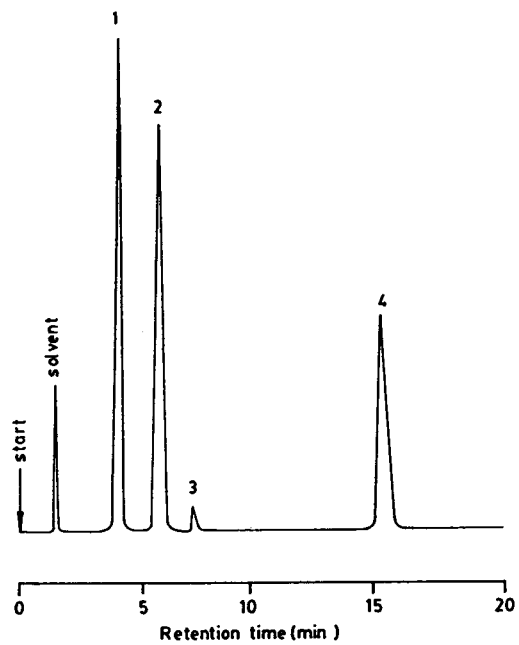

Fig. 1. Chromatogram of a typical mixture containing (1) D-Dopa (12 μg), (2) L-Dopa (10 μg), (3) D-carbidopa (0.1 μg) and (4) L-carbidopa (0.9 μg).

Table 1
Retention data

Compound	Retention time (min)	k'	α
D-Dopa	4.28	1.67	1.63
L-Dopa	5.96	2.73	
D-Carbidopa	7.55	3.72	2.38
L-Carbidopa	15.75	8.84	

The detector responses for D-Dopa and D-carbidopa were determined and the results are given in Table 2. The peak areas for $26.5 \cdot 10^{-9}$ g of D-Dopa and $10.4 \cdot 10^{-9}$ g of D-carbidopa were determined in triplicate and the average values for each were calculated. The relative standard deviations of these determinations were found to be 1.48% and 1.72% for D-Dopa and D-carbidopa, respectively. It is clear from Table 2 that the detector response for D-carbidopa was fairly high and it was found to be 4.5 times that of D-Dopa.

Standard mixtures containing different

Table 2
Detector response for D-Dopa and D-carbidopa

Compound	Amount (10^{-7} g)	Area	Relative standard deviation (%) ($n = 3$)
D-Dopa	0.2650	27114	1.48
D-Carbidopa	0.1040	47843	1.72

Table 3
Analytical data for standard mixtures

Sample No.	Compound	Taken (μg)	Found[a] (μg)	Error (%)	Compound	Taken (μg)	Found[a] (μg)	Error (%)
1	L-Dopa	98.04	97.18	−0.88	D-Dopa	1.96	2.01	+2.55
2	L-Dopa	94.59	95.92	+1.41	D-Dopa	5.41	5.33	−1.48
3	L-Dopa	90.43	89.26	−1.29	D-Dopa	9.57	9.82	+2.61
4	L-Carbidopa	97.25	98.79	+1.58	D-Carbidopa	2.75	2.67	−2.91
5	L-Carbidopa	95.38	96.25	+0.91	D-Carbidopa	4.62	4.73	+2.38
6	L-Carbidopa	91.24	90.17	−1.17	D-Carbidopa	8.76	8.58	+2.05

[a] Average of three determinations.

amounts of D-Dopa, D-carbidopa, L-Dopa and L-carbidopa were prepared and analysed by HPLC. The results are given in Table 3. It can be seen that the measured amounts of D-Dopa and D-carbidopa agreed well with the actual values to within 1.58% and 1.87%, respectively. The accuracy of the method was determined by the standard addition technique. Subsequent additions of D-Dopa and D-carbidopa were accurately reflected in their peak areas. Linear regression analysis data and the correlation coefficients are given in Table 4.

Fig. 2 shows the HPLC trace for a typical formulation of levodopa and carbidopa obtained commercially. It can be seen that very small amounts of D-Dopa and D-carbidopa which are known to be inactive are present in the formulations. The results are given in Table 5. These results show that the method is suitable for the determination of the enantiomeric excess of levodopa and carbidopa simultaneously using a reversed-phase C_{18} column with aqueous copper–L-phenylalanine as the mobile phase.

4. Conclusions

A simple and rapid HPLC method using a reversed-phase C_{18} column with aqueous copper–L-phenylalanine as the mobile phase has been developed for the simultaneous separation and determination of enantiomers of levodopa and carbidopa in mixtures. It is suitable for quality assurance of commercial formulations of levodopa and carbidopa used in the treatment of Parkinson's disease.

Acknowledgements

The authors thank Mr. R Narsimha and Mr. S.N. Alvi for technical assistance.

Table 4
Linearity data

Compound	Concentration range (μg)	Correlation equation[a]	Correlation coefficient
L-Dopa	90.43–99.56	$y = 1.015x - 0.072$	0.989
D-Dopa	1.96–9.97	$y = 0.997x + 0.014$	0.985
L-Carbidopa	91.24–99.85	$y = 1.012x - 0.108$	0.998
D-Carbidopa	0.51–8.76	$y = 0.989x + 0.025$	0.978

[a] y = Amount found (μg); x = amount taken (μg).

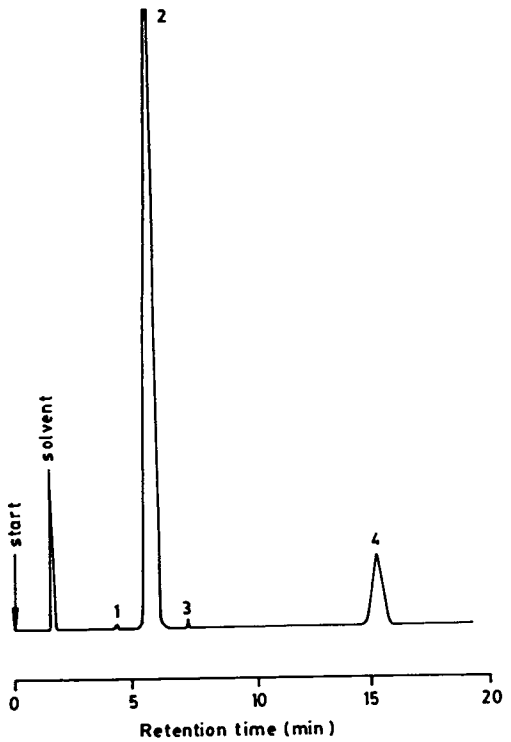

Fig. 2. Chromatogram of a commercial formulation containing L-Dopa (25 μg), L-carbidopa (2.5 μg), D-Dopa (0.15 μg) and D-carbidopa (0.02 μg). For identification of peaks, see Fig. 1.

Table 5
Levels of D-Dopa and D-carbidopa determined in samples of commercial formulations

Sample No.	Compound	Concentration (%)[a]	R.S.D. (%)
1	D-Dopa	0.89	1.6
	D-Carbidopa	–	–
2	D-Dopa	0.54	2.0
	D-Carbidopa	0.08	2.6
3	D-Dopa	0.27	2.4
	D-Carbidopa	0.15	2.2

[a] Average of three determinations.

References

[1] J.H. Stein (Editor), *Internal Medicine*, Little, Brown and Long, Boston, 1983, pp. 878–879.
[2] D.B. Clane, *N. Engl. J. Med.*, 329 (1993) 1021.
[3] L.S. Goodman and A. Gilman (Editors), *The Pharmacological Basis of Therapeutics* Macmillan, New York, 5th ed., 1975, pp. 227–229.
[4] E.F. Reynolds (Editor), *Martindale, The Extra Pharmacopoeia*, Pharmaceutical Press, London, 28th ed., 1982, pp. 883–890.
[5] B. Lausecker and F.M. Albert, *J. Chromatogr.*, 545 (1991) 115.
[6] L. Porter, *J. Pharmacol. Exper. Ther.*, 172 (1970) 406.
[7] S. Andreae, E. Schmitz, S. Schramm, F.M. Albert and D. Lohman, *GDR Pat.*, 230865 (1986); *C.A.*, 105 (1986) 227301j.
[8] S. Budavari (Editor), *The Merck Index*, Merck, Rahway, NJ, 11th ed., 1989, p. 1802.
[9] A.E. Harper, N.J. Benevenga and R.M. Wohlhueter, *Physiol. Rev.*, 50 (1970) 428.
[10] M. Goodall, *Adv. Neurol.*, 1 (1973) 517.
[11] S.T. Hamid and J. Walker, *Anal. Chim. Acta*, 105 (1979) 403.
[12] S. Ting, *J. Assoc. Off. Anal. Chem.*, 69 (1989) 169.
[13] L. Rihbany and M.F. Delaney, *J. Chromatogr.*, 248 (1982) 125.
[14] S.C. Chang, G.L. Reid, C.D. Chang and D.W. Armstrong, *Trends Anal. Chem.*, 12 (1993) 145.
[15] W.H. Pirkle, J.M. Finn, J.L. Schriner and B.C.H. Hamper, *J. Am. Chem. Soc.*, 103 (1981) 3964.
[16] S. Li and W.C. Purdy, *J. Chromatogr.*, 625 (1992) 109.
[17] C. Gilon, R. Leshem and E. Grushka, *J. Chromatogr.*, 203 (1981) 365.
[18] E. Olerich, H. Preusch and E. Wilhelm, *J. High Resolut. Chromatogr. Chromatogr. Commun.*, 3 (1980) 269.
[19] L.R. Gelber and J.L. Neumeyer, *J. Chromatogr.*, 257 (1983) 917.
[20] G. Gilbitz, W. Jellenz and D. Schonleber, *J. High Resolut. Chromatogr. Chromatogr. Commun.*, 3 (1980) 31.
[21] P.E. Hare and E. GilAv, *Science*, 204 (1979) 1226.
[22] H.G. Kicinski and A. Kettrup, *Fresenius' Z. Anal. Chem.*, 3200 (1985) 51.
[23] S. Karady, M.G. Ly Seemon, H. Pines and M. Sletzinger, *J. Org. Chem.*, 36 (1971) 1946.
[24] M. Sletzinger, J.M. Chemerda and F.W. Bollinger, *J. Med. Chem.*, 6 (1963) 101.

ELSEVIER

Journal of Chromatography A, 687 (1994) 356

JOURNAL OF CHROMATOGRAPHY A

Book Review

Time-of-Flight Mass Spectrometry and its Applications, edited by E.W. Schlag, Elsevier, Amsterdam, 1994, IX + 413 pp., price Dfl 215.00, US$ 122.75, ISBN 0-444-81875-8.

Mass spectrometry (MS) currently is busy enjoying a revolution in both its instrumentation and applications, like the continued, maturing growth of HPLC in the 1980s. Time-of-flight mass spectrometry (TOF-MS) is a significant part of this revolution thanks to several developments that are increasing its resolution and applicability. Typically these days (but with a variety of exceptions) the sample is volatilized into the flight tube with a laser pulse. From this pulse the entire mass spectrum is determined. This leads to the inherent advantages of TOF-MS: simplicity, low cost, speed, sensitivity, and "unlimited" mass range. Of course it is not possible to optimize all of these aspects at the same time for all applications. The special relevance of TOF-MS to separation scientists is pointed out nicely in the summary part of a specialized chapter on energy-isochronous TOF by H. Wollnik: "... TOF mass analyzers could improve the investigation of the composition of the effluent of gas- and liquid-chromatographs as well as of capillary zone electrophoresis systems. Especially in view of the fast transients of fast gas chromatographs or new capillary zone electrophoresis systems, TOF mass analyzers may become indispensible tools for chemical analysis."

This book comprehensively presents the various kinds of research work ongoing currently to advance the performance and utility of TOF-MS, with most of the chapters concerned with advanced, current, instrumental developments.

Examples of the more general topics that are covered are as follows: reflectrons (overview by B.M. Mamyrin), laser ion sources including multiple laser excitations (U. Boesl et al.); ion trap storage/reflectron combination (B.M. Chien et al.); decay energetics and dynamics of clusters (a chapter by H.J. Neusser and H. Krause focuses on aromatics, and one by S. Wei and A.W. Castleman, Jr., focuses on ammonia); photodissociation as a means to achieve tandem TOF (magnesium ion clusters were tested by M.A. Duncan et al.); resonance-enhanced two photon ionization (applied to aryl-tagged perfluorinated polyethers by D.S. Anex et al.); DNA sequencing (DNA fragments from the Sanger reaction) by laser-ablation of frozen aqueous films (P. Williams); factors affecting resolution in MALDI (A. Ingendoh et al.); and postsource decay following MALDI in peptide sequencing (R. Kaufmann et al.).

Boston, MA, USA R.W. Giese

SSDI 0021-9673(94)00914-7

ELSEVIER

Journal of Chromatography A, 687 (1994) 357

JOURNAL OF CHROMATOGRAPHY A

Book Review

Thin Layer Chromatography: Reagents and Detection Methods, vol. 1b, by H. Jork, W. Funk, W. Fischer and H. Wimmer, VCH, Weinheim, New York, Basle, 1994, xvi + 496 pp., price DM 198.00, £81.00, ISBN 3-527-28205-X.

This volume is the second in a series that provides a comprehensive treatment of detection methods for TLC. As in the first volume, this one is divided into two sections. Part 1 is devoted to specific detection methods, including activation reactions (photochemical, thermochemical and electrochemical) with some procedures tested, a selection of reagents for the recognition of functional groups with a recapitulary table and reagent sequences that describe the sequential application of a series of different reagents to the same chromatogram to increase the selectivity. The ranking through organic chemistry reactions is appreciated.

Part 1 is 140 pages long and is followed by Part 2 (about 300 pages), which consists of descriptions of 65 reagents in alphabetical order. Detailed descriptions of the preparation, use and chemical basis of these reagents are given, with relevant references. However the reader does not need to consult the original since all the necessary information is readily available in this book. For each reagent a worked example is provided with a representative chromatogram obtained through scanning densitometry. According to the authors, every procedure has been tested in their respective laboratories and I personally checked two successfully.

The book is well presented, has a pleasant typeface and good illustrations and photographs of high quality. A table of named reagents and reagent acronyms can be found at the end of the book. Most of the procedures involve TLC on silica gel, and applications dealing with alkyl-bonded or propylamino-bonded phases are scarce, which reflects the situation in the literature.

This book will be very useful not only to those practising TLC but also to any chromatographer practising liquid chromatography and looking for reliable detection through reagents. It will take its place among those books that one consults very often.

Marseille, France A.M. Siouffi

SSDI 0021-9673(94)00916-3

Author Index

PUBLICATION SCHEDULE FOR THE 1995 SUBSCRIPTION

Journal of Chromatography A and *Journal of Chromatography B: Biomedical Applications*

MONTH	O 1994	N 1994	D 1994	
Journal of Chromatography A	683/1 683/2 684/1	684/2 685/1 685/2 686/1	686/2 687/1 687/2 688/1 + 2	The publication schedule for further issues will be published later.
Bibliography Section				
Journal of Chromatography B: Biomedical Applications				

INFORMATION FOR AUTHORS

(Detailed *Instructions to Authors* were published in *J. Chromatogr. A*, Vol. 657, pp. 463–469. A free reprint can be obtained by application to the publisher, Elsevier Science B.V., P.O. Box 330, 1000 AH Amsterdam, Netherlands.)

Types of Contributions. The following types of papers are published: Regular research papers (full-length papers), Review articles, Short Communications and Discussions. Short Communications are usually descriptions of short investigations, or they can report minor technical improvements of previously published procedures; they reflect the same quality of research as full-length papers, but should preferably not exceed five printed pages. Discussions (one or two pages) should explain, amplify, correct or otherwise comment substantively upon an article recently published in the journal. For Review articles, see inside front cover under Submission of Papers.

Submission. Every paper must be accompanied by a letter from the senior author, stating that he/she is submitting the paper for publication in the *Journal of Chromatography A* or *B*.

Manuscripts. Manuscripts should be typed in **double spacing** on consecutively numbered pages of uniform size. The manuscript should be preceded by a sheet of manuscript paper carrying the title of the paper and the name and full postal address of the person to whom the proofs are to be sent. As a rule, papers should be divided into sections, headed by a caption (*e.g.*, Abstract, Introduction, Experimental, Results, Discussion, etc.). All illustrations, photographs, tables, etc., should be on separate sheets.

Abstract. All articles should have an abstract of 50–100 words which clearly and briefly indicates what is new, different and significant. No references should be given.

Introduction. Every paper must have a concise introduction mentioning what has been done before on the topic described, and stating clearly what is new in the paper now submitted.

Experimental conditions should preferably be given on a *separate* sheet, headed "Conditions". These conditions will, if appropriate, be printed in a block, directly following the heading "Experimental".

Illustrations. The figures should be submitted in a form suitable for reproduction, drawn in Indian ink on drawing or tracing paper. Each illustration should have a caption, all the *captions* being typed (with double spacing) together on a *separate sheet*. If structures are given in the text, the original drawings should be provided. Coloured illustrations are reproduced at the author's expense, the cost being determined by the number of pages and by the number of colours needed. The written permission of the author and publisher must be obtained for the use of any figure already published. Its source must be indicated in the legend.

References. References should be numbered in the order in which they are cited in the text, and listed in numerical sequence on a separate sheet at the end of the article. Please check a recent issue for the layout of the reference list. Abbreviations for the titles of journals should follow the system used by *Chemical Abstracts*. Articles not yet published should be given as "in press" (journal should be specified), "submitted for publication" (journal should be specified), "in preparation" or "personal communication".

Vols. 1–651 of the *Journal of Chromatography*; *Journal of Chromatography, Biomedical Applications* and *Journal of Chromatography, Symposium Volumes* should be cited as *J. Chromatogr.* From Vol. 652 on, *Journal of Chromatography A* (incl. Symposium Volumes) should be cited as *J. Chromatogr. A* and *Journal of Chromatography B: Biomedical Applications* as *J. Chromatogr. B*.

Dispatch. Before sending the manuscript to the Editor please check that the envelope contains four copies of the paper complete with references, captions and figures. One of the sets of figures must be the originals suitable for direct reproduction. Please also ensure that permission to publish has been obtained from your institute.

Proofs. One set of proofs will be sent to the author to be carefully checked for printer's errors. Corrections must be restricted to instances in which the proof is at variance with the manuscript.

Reprints. Fifty reprints will be supplied free of charge. Additional reprints can be ordered by the authors. An order form containing price quotations will be sent to the authors together with the proofs of their article.

Pharmaceutical and Biomedical Applications of Liquid Chromatography

Edited by
Christopher M. Riley, *Center for BioAnalytical Research, University of Kansas, Lawrence, USA*
W. John Lough, *School of Health Sciences, University of Sunderland, UK*
Irving W. Wainer, *Department of Oncology, McGill University, Montreal, Quebec, Canada*

Contents

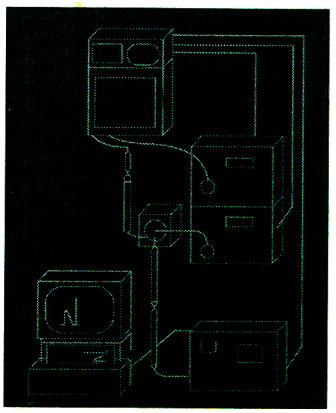

This volume reflects the changes that have taken place in the pharmaceutical industry over the last ten years, most notably the increased importance attached to the question of chirality, the growing influence of biotechnology and the need for more rigorous documentation and validation of analytical methods and procedures.
The first part of this book deals with the application of new technology to pharmaceutical and biomedical analysis, reflecting the present needs for increased speed, sensitivity and selectivity in the analysis of drugs. The second chapter provides an overview of capillary electophoresis, which represents one of the most inportant analytical developments to impact directly on pharmaceutical development in recent years. Although not a chromatographic technique, capillary electrophoresis was considered too important to be ignored.
Over the last 25 years, liquid chromatography has grown into a mature analytical technique and many of the fundamental issues concerned with retention and separation are well defined. The practitioners of modern liquid chromatography spend as much time in the development of techniques for sampling handling and automation as they do in the development of the separation. Therefore, Part Two of this book describes some of the recent advances in the areas of sample handling and the isolation of compounds from biological samples, including solid phase extraction, restricted access media for direct injection, coupled column technology and microdialysis. Similarily, Part Three contains two chapters concerned with liquid chromatographic methods for the isolation of drug substances, peptides and proteins from other complex media.
The pharmaceutical industry and the process of drug development are highly regulated and the increasing importance that the regulatory authorities attach to validation has had a significant impact on the analytical techniques used for the analysis of drugs. Although this has increased the workload of analysts in the pharmaceutical industry, it has also improved the quality of analytical methods used in the support of investigational and new drug applications as well as the quality of methods published more recently in the literature. Consequently, Part Four of this volume describes approaches to the optimization and validation of liquid chromatography methods for the analysis of drugs in the bulk form, in pharmaceutical formulations and biological fluids.

Audience

For undergraduate pharmacy students and chemistry students; post-graduate students and faculty in analytical chemistry, pharmaceutical chemistry, pharmaceutical analysis, pharmaceutics and medicinal chemistry; and analytical scientists in government, pharmaceutical industry and biotechnology industry.

1994 380 pages
ISBN 0-08-041009-X
Publication: October 1994
Hardbound
Price: £85.00/US$136.00
CH4A25 11/94

Sterling price quoted applies worlwide except in the Americas. US dollar price quoted applies in the Americas only.

Send your orders and enquiries to your nearest Elsevier Science office.
North America: Elsevier Science Inc., 660 White Plains Road, Tarrytown, NY10591-5153, USA
UK & all other countries: Elsevier Science Ltd, The Boulevard, Langford Lane Kidlington, Oxford, OX5 1GB

PERGAMON
An imprint of Elsevier Science

0021-9673(19941223)687:2;1-H